Partially Quenched Chiral Perturbation Theory and a Massless Up Quark: A Lattice Calculation of the Light-Quark-Mass Ratio

DISSERTATION

Presented in Partial Fulfillment of the Requirements for

the Degree Doctor of Philosophy in the

Graduate School of The Ohio State University

By

Daniel R. Nelson, B.A.

* * * * *

The Ohio State University

2002

<table>
<tr><td>Dissertation Committee:</td><td>Approved by</td></tr>
<tr><td>Professor Junko Shigemitsu, Adviser</td><td></td></tr>
<tr><td>Professor Gregory Kilcup</td><td></td></tr>
<tr><td>Professor Richard Furnstahl</td><td>Adviser</td></tr>
<tr><td>Professor Richard Hughes</td><td>Department of Physics</td></tr>
</table>

ABSTRACT

The nontrivial topological structure of the QCD gauge vacuum generates a CP breaking term in the QCD Lagrangian. However, measurements of the neutron electric dipole moment have demonstrated that the term's coefficient is unnaturally small, a dilemma known as the strong CP problem. A massless up quark has long been seen as a potential solution, as the term could then be absorbed through the resulting freedom to perform arbitrary chiral rotations on the up quark field.

Through the light-quark-mass ratio m_u/m_d, leading order Chiral Perturbation Theory appears to rule this scenario out. However, the Kaplan-Manohar ambiguity demonstrates that certain strong next-to-leading order corrections are indistinguishable from the effects of an up quark mass. Only a direct calculation of the Gasser-Leutwyler coefficient combination $2L_8 - L_5$ can resolve the issue.

New theoretical insights into partial quenched Chiral Perturbation Theory have revealed that a calculation of the low-energy constants of the partially quenched chiral Lagrangian is equivalent to a determination of the physical Gasser-Leutwyler coefficients. The coefficient combination in question is directly accessible through the pion mass's dependence on the valence quark mass, a dependence ripe for determination via Lattice Quantum Chromodynamics.

We carry out such a partially quenched lattice calculation using $N_f = 3$ staggered fermions and the recently developed smearing technique known as hypercubic blocking. Through the use of several ensembles, we make a quantitative assessment of our systematic error. We find $2L_8 - L_5 = \left(0.22 \pm 0.14\right) \times 10^{-3}$, which corresponds to a light-quark-mass ratio of $m_u/m_d = 0.408 \pm 0.035$. Thus, our study rules out the massless-up-quark solution to the strong CP problem.

This is the first calculation of its type to use a physical number of light quarks, $N_f = 3$, and the first determination of $2L_8 - L_5$ to include a comprehensive study of statistical error.

to Mom and Dad

for their unconditional love

ACKNOWLEDGMENTS

VITA

September 19, 1975 . . . . Born
                                        Pittsburgh, Pennsylvania

1997 . . . . B.A. Physics / Computer Science
                                        Juniata College

1997 - 2001 . . . . Teaching Assistant
                                        Department of Physics
                                        The Ohio State University

1999 . . . . Programmer
                                        Ohio Supercomputer Center

1999 - 2002 . . . . Physics Researcher
                                          Department of Physics
                                        The Ohio State University

PUBLICATIONS

Research Publications

D.R. Nelson, G.T. Fleming and G.W. Kilcup, Nucl. Phys. Proc. Suppl. 106 (2002) 221, hep-lat/0110112.

D.R. Nelson, G.T. Fleming and G.W. Kilcup, (2001), hep-lat/0112029.

G.T. Fleming, D.R. Nelson and G.W. Kilcup, (2002), hep-lat/0209141.

FIELDS OF STUDY

Major Field: Physics

    Studies in Lattice Quantum Chromodynamics: Professor Gregory Kilcup

TABLE OF CONTENTS

ix

LIST OF TABLES

LIST OF FIGURES

CHAPTER 1

INTRODUCTION

Since its inception, the low-energy dynamics of Quantum Chromodynamics (QCD) have been poorly understood. To date, the most successful framework for building an understanding of low-energy QCD has been Chiral Perturbation Theory, with the current large uncertainty in its NLO coefficients quantifying our lackluster understanding. These low-energy constants, the Gasser-Leutwyler coefficients, have error bars which range from 10% to 160% of their value. For many of these coefficients, their uncertainty has never been reduced below the magnitude determined at the first instance of their calculation some twenty years ago.

As an effective field theory, light-meson Chiral Perturbation Theory collects the interactions of QCD into a finite number of meson vertices. The complex low-energy dynamics of QCD are boiled down into the coefficients of these vertices, the Gasser-Leutwyler coefficients. Thus, while various theoretical and phenomenological methods have been used to estimate their values, the most direct determination of the Gasser-Leutwyler coefficients would be a calculation of these vertices' strength using the fundamental theory, QCD.

While perturbation theory clearly fails in this regard, as the strong coupling at these energy scales is of order one, lattice techniques have proven successful. In fact,

this may be a case in which lattice field theory can provide the physics community with the best results available.

We present here a lattice calculation of a single important combination of the Gasser-Leutwyler coefficients, $2L_8 - L_5$. The motivation behind this combination choice is twofold. First, it is the combination whose calculation on the lattice is most straightforward. Additionally, this combination provides insight into the NLO corrections to the light-quark-mass ratio m_u/m_d. Thus, determining $2L_8 - L_5$, even with moderate accuracy, allows one to lay to rest the possibility of a massless up quark.

While we calculate definitively only a single combination of the Gasser-Leutwyler coefficients, this study is only the first step in a larger effort by the lattice community to generate results for all accessible Gasser-Leutwyler coefficients.

Elements of this study have seen earlier publication [1]. A similar investigation, which uses an unphysical number of light quarks and less sophisticated analysis techniques, can be found in [2].

In Chapter 2, after a brief overview of QCD, the strong CP problem and its potential solutions are presented, including the directly relevant solution involving a massless up quark.

In Chapter 3 we introduce Chiral Perturbation Theory up to NLO, focusing on the insight it imparts into the light-quark-mass ratio m_u/m_d. The relationship between the quark-mass ratio and the light mesons is explored, and the importance of the Gasser-Leutwyler coefficient combination $2L_8 - L_5$ in that relationship is presented. An overview of past phenomenological and theoretical estimates for the coefficients L_5 and L_8 is given, including a discussion of the Kaplan-Manohar ambiguity, which

makes an experimental determination of $2L_8 - L_5$ impossible and theoretical estimates challenging.

In Chapter 4 the basics of Lattice Quantum Field Theory are presented.

In Chapter 5 we build on those basics, introducing Lattice Quantum Chromodynamics. The lattice techniques used in this study are covered, including staggered fermions, the conjugate gradient method, the R algorithm, hypercubic blocking, and the Sommer scale. We present in explicit detail the methods used to extract the pion mass and decay constant from staggered bilinear correlators.

In Chapter 6 we extend the concepts of Chiral Perturbation Theory to cover the partially quenched case, explaining how partially quenched Chiral Perturbation Theory allows physical results for the Gasser-Leutwyler coefficients to be generated from lattice calculations which use the unphysical partially quenched approximation.

In Chapter 7 our methods for data modeling and statistical error analysis are covered.

In Chapter 8 we detail the lattice ensembles generated for our study, explaining the motivation behind each ensemble's creation.

In Chapter 9 we present a step-by-step analysis of our lattice data, generating values for the Gasser-Leutwyler coefficient combinations $2L_8 - L_5$ and L_5 for each ensemble studied. A simultaneous analysis of several ensembles, which allows us to make a preliminary estimation of the coefficient combinations $2L_6 - L_4$ and L_4, is also presented.

In Chapter 10 our final result for $2L_8 - L_5$ is given, along with an analysis of our study's systematic error. Using Chiral Perturbation Theory we produce from our result a prediction for the light-quark-mass ratio. Secondary results are also given,

including values for the coefficients L_5, L_4, and L_6. The effects of quenching on results for the Gasser-Leutwyler coefficients is briefly discussed.

In Chapter 11 we summarize our results and discuss the rich potential for future work.

CHAPTER 2

QUANTUM CHROMODYNAMICS

Quarks are the fundamental building blocks of the universe. Bound together by gluon exchanges, they are the dominant constituents of hadrons. It is a hadron's quarks and the dynamics of the quark-gluon interactions which dictate that hadron's characteristics and behavior.

The physics of quarks and gluons is dominated by the strong force, Quantum Chromodynamics (QCD). Working in Euclidean space, QCD is governed by the partition function:

$$Z_{\text{QCD}} = \int [\mathcal{D}A_\mu][\mathcal{D}q][\mathcal{D}\bar{q}] \; e^{-\int_x \mathscr{L}_{\text{QCD}}} \tag{2.1}$$

where A_μ is the gluon field, and q and $\bar{q}$ are the quark and antiquark fields. The QCD Euclidean Lagrangian is:

$$\mathscr{L}_{\text{QCD}} = \frac{1}{2}\text{tr}\big[F_{\mu\nu}F^{\mu\nu}\big] + \bar{q}\big(\gamma^\mu D_\mu + \mathcal{M}\big)q \tag{2.2}$$

The quark field q is a vector in three spaces: flavor, color, and spin. The flavor index runs from 1 to N_f, while the color index runs from 1 to $N_c = 3$. Finally, quarks are Dirac spinors, four component vectors in spin space.

D_μ is the covariant derivative and a matrix in color space, while γ^μ is a Lorentz vector of spin space matrices. $\mathcal{M}$ is the quark mass matrix, a diagonal flavor-space

5

matrix with the quark masses along its diagonal:

$$\mathcal{M} \equiv \mathrm{diag}\big(\{m_i\}\big) \tag{2.3}$$

The gluon field A_μ makes its kinetic appearance in the Lagrangian through its field strength $F_{\mu\nu}$:

$$\begin{aligned}
F_{\mu\nu} &\equiv \frac{i}{g}\big[D_\mu, D_\nu\big] \\
&= \partial_\mu A_\nu - \partial_\nu A_\mu - ig\big[A_\mu, A_\nu\big]
\end{aligned} \tag{2.4}$$

The gluon field is both a Lorentz vector as well as a vector in adjoint color space. It has been written as a matrix in color space, with each component of the adjoint vector being multiplied by a generator of $SU(N_c)$:

$$A_\mu \equiv A_\mu^a \lambda^a \tag{2.5}$$

The gluon field acts as the parallel transporter of the quarks through color space, appearing in the covariant derivative:

$$D_\mu \equiv \partial_\mu - ig A_\mu \tag{2.6}$$

It is through D_μ that the quark-gluon interaction arises.

2.1   Symmetries of Quantum Chromodynamics

Of the symmetries respected by the QCD Lagrangian, two of them are of particular interest to us: color symmetry and flavor symmetry,

2.1.1 Color Symmetry

$SU(N_c)$ color symmetry is an exact and local symmetry of QCD under which the fields transform as:

$$q \rightarrow q' = \Omega(x)q \qquad (2.7)$$

$$\bar{q} \rightarrow \bar{q}' = \bar{q}\,\Omega^\dagger(x) \qquad (2.8)$$

$$A_\mu \rightarrow A'_\mu = \Omega(x)\left(A_\mu + \frac{i}{g}\partial_\mu\right)\Omega^\dagger(x) \qquad (2.9)$$

$$\Omega(x) = e^{-i\alpha^a(x)\lambda^a} \in SU(N_c) \qquad (2.10)$$

where $\alpha^a(x)$ is a set of $N_c^2 - 1$ real functions which parameterize the transformation. This transformation of A_μ results in the gluon field strength transforming as:

$$F_{\mu\nu} \rightarrow F'_{\mu\nu} = \Omega(x)F_{\mu\nu}\Omega^\dagger(x) \qquad (2.11)$$

2.1.2 Flavor Symmetry

In the case of degenerate quarks:

$$\mathcal{M} = m_q \mathbb{1} \qquad (2.12)$$

the Lagrangian respects a global $SU(N_f)$ flavor symmetry, under which the fields transform as:

$$q \rightarrow q' = Vq \qquad (2.13)$$

$$\bar{q} \rightarrow \bar{q}' = \bar{q}\,V^\dagger \qquad (2.14)$$

$$V = e^{-iv^a\tau^a} \in SU(N_f) \qquad (2.15)$$

where τ^a are the generators of $SU(N_f)$ flavor and v^a are real constants which parameterize the transformation.

In the case of massless quarks, $m_q = 0$, known as the chiral limit, the QCD Lagrangian exhibits an even larger $SU(N_f)_L \otimes SU(N_f)_R$ flavor symmetry. The quarks split into left- and right-handed pairs:

$$q = q_L + q_R \tag{2.16}$$

$$q_L \equiv P_+ q = \tfrac{1}{2}(1 + \gamma_5)q \tag{2.17}$$

$$q_R \equiv P_- q = \tfrac{1}{2}(1 - \gamma_5)q \tag{2.18}$$

$$\bar{q} = \bar{q}_L + \bar{q}_R \tag{2.19}$$

$$\bar{q}_L \equiv \bar{q}P_- = \tfrac{1}{2}\bar{q}(1 - \gamma_5) \tag{2.20}$$

$$\bar{q}_R \equiv \bar{q}P_+ = \tfrac{1}{2}\bar{q}(1 + \gamma_5) \tag{2.21}$$

each of which rotates independently under flavor symmetry:

$$q \quad \rightarrow \quad q' = Lq_L + Rq_R \tag{2.22}$$

$$\bar{q} \quad \rightarrow \quad \bar{q}' = \bar{q}_L L^\dagger + \bar{q}_R R^\dagger \tag{2.23}$$

$$L = e^{-il^a \tau^a} \in SU(N_f) \tag{2.24}$$

$$R = e^{-ir^a \tau^a} \in SU(N_f) \tag{2.25}$$

where l^a and r^a are sets of real constants which parameterize the transformation.

This symmetry can also be expressed in terms of a vector and an axial vector symmetry, $SU(N_f)_V \otimes SU(N_f)_A$. Here the vector symmetry corresponds to the smaller flavor symmetry discussed above, where left- and right-handed quarks transform equivalently, $L = R$. In contrast, a pure axial vector transformation rotates left- and right-handed quarks in opposite directions, $L = R^\dagger$. The currents associated with these symmetries are the non-singlet vector currents:

$$J^a_\mu \equiv \bar{q}\gamma_\mu \tau^a q \tag{2.26}$$

8

and the non-singlet axial vector currents:

$$J_\mu^{5a} \equiv \bar{q}\gamma_\mu\gamma_5\tau^a q \tag{2.27}$$

respectively.

In truth all quarks are neither massless nor degenerate. However, the two lightest quark flavors, up and down, have masses and a mass splitting which are quite small relative to the typical baryon mass. The next lightest quark flavor, strange, has a somewhat small mass, again relative to the typical baryon mass. So, if we restrict ourselves to the three lightest flavors of quarks, we would expect $SU(N_f = 3)_V \otimes SU(N_f = 3)_A$ flavor symmetry to be a good approximate symmetry of the strong interactions.

However, while $SU(N_f)_V$ flavor symmetry is manifest in QCD and its associated currents are conserved, $SU(N_f)_A$ flavor symmetry does not appear to be respected. There exist two possibilities when a theory's Lagrangian contains a symmetry, but the theory itself does not appear to respect that symmetry. Either the symmetry is still respected but also hidden via spontaneous symmetry breaking, or the symmetry is false, ruined by anomalous quantum corrections to the Lagrangian's classical solution. The $SU(N_f)$ axial vector flavor symmetry of QCD falls into the first category.

2.1.3 Spontaneous Symmetry Breaking

Spontaneous symmetry breaking occurs when a theory has not one ground state, but rather a set of ground states which transform into one another via the symmetry under discussion. In such a situation the theory's vacuum must choose its location from among these ground states and thus resides in a position which is not invariant under the symmetry. So, while the full theory retains the given symmetry, the state

space in the vicinity of the vacuum does not reflect that symmetry. Since this is the region important to low-energy interactions and the region explored by perturbation theory, the symmetry becomes hidden.

When the set of vacuum states is continuous, local fluctuations of the vacuum within that set are massless. Thus, the theory's spectrum will contain massless particles, known as Goldstone bosons, which correspond to those fluctuations. The number of spontaneously broken symmetries corresponds to the number of orthogonal directions within the set of ground states, and thus corresponds to the resulting number of Goldstone bosons.

It is the interactions of these Goldstone bosons, with one another and with the other particles of the theory, which enforces the now hidden symmetry.

2.1.4 Chiral Condensate

In massless QCD the energy required to create a quark-antiquark pair from the vacuum is small. Because such a pair must have zero total linear and angular momentum, they will contain a net chiral charge. Thus, the QCD vacuum includes a chiral condensate characterized by the non-zero vacuum expectation value of the operator:

$$\langle \bar{q}q \rangle = \langle \bar{q}_L q_R \rangle + \langle \bar{q}_R q_L \rangle \neq 0 \tag{2.28}$$

In truth, the vacuum expectation value includes an arbitrary $SU(N_f)_A$ rotation:

$$\langle \bar{q}_L L^\dagger R q_R \rangle + \langle \bar{q}_R R^\dagger L q_L \rangle = \langle \bar{q}_L A^{\dagger 2} q_R \rangle + \langle \bar{q}_R A^2 q_L \rangle \neq 0 \tag{2.29}$$

where $L = R^\dagger = A \in SU(N_f)_A$. The vacuum is forced to choose the $SU(N_f)_A$ alignment of this expectation value, thus spontaneously breaking $SU(N_f)_V \otimes SU(N_f)_A$ flavor symmetry down to $SU(N_f)_V$. Note that the chiral condensate is invariant under

$SU(N_f)_V$:

$$\langle \bar{q}q \rangle \quad \rightarrow \quad \langle \bar{q}_L L^\dagger R q_R \rangle + \langle \bar{q}_R R^\dagger L q_L \rangle$$

$$= \langle \bar{q}_L V^\dagger V q_R \rangle + \langle \bar{q}_R V^\dagger V q_L \rangle = \langle \bar{q}q \rangle \qquad (2.30)$$

where $L = R = V \in SU(N_f)_V$. Once the vacuum has made its choice for the condensate's alignment, we in turn can rotate the definition of our quark fields such that the vacuum expectation value does indeed take the form in (2.28). While the freedom for such a redefinition exists in massless QCD, the quark masses of true QCD would not allow it. However in that case, the vacuum expectation value will naturally align itself with the quark masses, again taking the form in (2.28).

Because the set of vacuum states is continuous, connected by elements of $SU(N_f)_A$ arbitrarily close to identity, we expect to find massless particles in the spectrum, the $N_f^2 - 1$ Goldstone bosons of the spontaneously broken symmetry. The spectrum of QCD does not contain any such massless particles. However, together the light pseudoscalar mesons — π^0, π^+, π^-, K^0, $\bar{K}^0$, K^+, K^-, and η — assume the role of the Goldstone bosons. Collected, they form an octet of very light particles, one for each of the eight generators of the spontaneously broken $SU(N_f = 3)_A$ flavor symmetry.

It is because the spontaneously broken $SU(N_f = 3)_A$ flavor symmetry is only an approximate symmetry of QCD, not an exact symmetry, that these Goldstone bosons are not exactly massless. In fact the squared masses of the light mesons are proportional to the parameters which break $SU(N_f)_A$ flavor symmetry: the quark masses. Thus, the light pseudoscalar mesons are often referred to as pseudo-Goldstone bosons.

2.2 $U(1)_A$ Problem

In addition to color and flavor symmetry, the QCD Lagrangian is classically invariant under two additional global $U(1)$ symmetries. The first is $U(1)_V$ vector symmetry, under which the quark fields transform by a simple phase rotation:

$$q \quad \rightarrow \quad q' = e^{i\alpha}q \tag{2.31}$$

$$\bar{q} \quad \rightarrow \quad \bar{q}' = \bar{q}e^{-i\alpha} \tag{2.32}$$

This symmetry is exact for arbitrary quark masses and corresponds to the conserved singlet vector current:

$$J_\mu \equiv \bar{q}\gamma_\mu q \tag{2.33}$$

$$\partial^\mu J_\mu = 0 \tag{2.34}$$

and to baryon number conservation, a phenomenon clearly observed in experiment. The second symmetry is $U(1)_A$ axial vector symmetry, under which left- and right-handed quarks undergo opposite phase rotations:

$$q \quad \rightarrow \quad q' = e^{i\alpha\gamma_5}q \tag{2.35}$$

$$\bar{q} \quad \rightarrow \quad \bar{q}' = \bar{q}e^{i\alpha\gamma_5} \tag{2.36}$$

Similar to the non-singlet flavor symmetries, this symmetry is only exact in the limit of massless quarks. The corresponding singlet axial vector current is:

$$J_\mu^5 \equiv \bar{q}\gamma_\mu\gamma_5 q \tag{2.37}$$

Assuming degenerate quarks, naive application of the equations of motion results in the divergence:

$$\partial^\mu J_\mu^5 = 2m_q\bar{q}\gamma_5 q \tag{2.38}$$

12

which equals zero in the chiral limit. Thus, we expect the symmetry to be an approximate symmetry of QCD. However, $U(1)_A$ symmetry calls for degenerate parity doublets which are not even approximately manifest in the QCD particle spectrum. The mystery of this missing symmetry is known as the $U(1)_A$ problem.

If the symmetry were spontaneously broken, the spectrum would contain a corresponding Goldstone boson. We could imagine combining the singlet axial vector symmetry with the non-singlet flavor symmetries:

$$U(N_f)_A = SU(N_f)_A \otimes U(1)_A \tag{2.39}$$

and having them spontaneously break together. This spontaneous breaking of $U(N_f = 3)_A$ would result in the eight light mesons mentioned above plus a new ninth light pseudoscalar meson. There exists a candidate pseudoscalar meson to fill the roll of this ninth light meson: the η'. However, it has been shown that, if the full $U(N_f = 3)_A$ symmetry were spontaneously broken, it would constrain the η' mass: $M_{\eta'} < \sqrt{3} M_\pi$ [3]. The actual η' is much heavier. $U(1)_A$ has no Goldstone boson, and thus spontaneous symmetry breaking can not explain the symmetry's disappearance. We must look for a second possibility.

2.2.1 Adler-Bardeen-Jackiw Anomaly

When a Lagrangian contains a given symmetry, its classical equations of motion will respect that symmetry. However, when the Lagrangian is placed within a path integral, that symmetry may be lost. For a given symmetry to survive the transition to quantum field theory, not only must the action be invariant under the transformation, but the measure of the path integral must also be invariant. When the measure is not invariant, the symmetry is said to be anomalously broken. In the context of

perturbation theory, this will manifest as a failure of the regularization of radiative corrections to respect the symmetry.

The conserved current corresponding to an unbroken symmetry has a divergence of zero. For an anomalously broken symmetry, the divergence of the corresponding current will be non-zero. This non-zero divergence is referred to as the anomaly. The anomaly which breaks the $U(1)_A$ symmetry of QCD is the Adler-Bardeen-Jackiw (ABJ) anomaly.

Under a $U(1)_A$ rotation, the measure of the QCD path integral transforms as:

$$[\mathcal{D}A_\mu][\mathcal{D}q][\mathcal{D}\bar{q}] \quad \rightarrow \quad [\mathcal{D}A_\mu][\mathcal{D}q][\mathcal{D}\bar{q}]e^{-\alpha\int_x \Theta} \tag{2.40}$$

where:

$$\Theta \equiv \frac{N_f g^2}{8\pi^2}\mathrm{tr}\left[F_{\mu\nu}\tilde{F}^{\mu\nu}\right] \tag{2.41}$$

and $\tilde{F}_{\mu\nu} \equiv \frac{1}{2}\epsilon_{\mu\nu\alpha\beta}F^{\alpha\beta}$. This results in the anomalous divergence of the axial vector current:

$$\partial^\mu J_\mu^5 = 2m_q\bar{q}\gamma_5 q + \Theta \tag{2.42}$$

which no longer equals zero in the massless quark limit. Thus, the $U(1)_A$ problem appears to be solved. The $U(1)_A$ symmetry of QCD is missing because it never existed; it is ruined by the ABJ anomaly. However, the situation is not that straightforward.

2.2.2 Gauge-Variant Axial Vector Current

The divergence of the axial vector current can also be written as a divergence of gauge fields:

$$\Theta = \frac{N_f g^2}{2\pi^2}\partial^\mu K_\mu \tag{2.43}$$

where:

$$K_\mu \equiv \frac{1}{2}\epsilon_{\mu\nu\alpha\beta}\mathrm{tr}\left[A^\nu\partial^\alpha A^\beta - \frac{2}{3}ig A^\nu A^\alpha A^\beta\right] \tag{2.44}$$

14

We can then define a new current $\tilde{J}_\mu^5$ which involves both quark and gauge fields:

$$\tilde{J}_\mu^5 \equiv J_\mu^5 - \frac{N_f g^2}{2\pi^2} K_\mu \tag{2.45}$$

For massless quarks this new current is then conserved:

$$\partial^\mu \tilde{J}_\mu^5 = 0 \tag{2.46}$$

and once again we find ourselves with a current that appears to be conserved, but whose associated symmetry is not manifest in the theory and with which there is no associated Goldstone boson.

The solution to the dilemma centers on the fact that K_μ is not a gauge invariant quantity. Because of this, if the symmetry associated with $\tilde{J}_\mu^5$ were spontaneously broken, the resulting Goldstone boson might decouple from the theory's physical states. When working with a gauge theory in a covariant gauge, the number of degrees of freedom in the theory is larger than the number of physical states. A condition must be applied to the states of the theory in order to remove unphysical states. It is during the application of that condition that the Goldstone bosons of a gauge-variant symmetry could decouple completely from the physical states. In fact, it has been shown that in QCD they do indeed decouple [4, 5]. The modified $U(1)_A$ symmetry is not observed because it is spontaneously broken, and the Goldstone boson which results decouples from QCD's physical states.

To summarize the fate of the chiral symmetries of QCD, we recall that the massless QCD Lagrangian classically respects the symmetry group $SU(N_f)_V \otimes SU(N_f)_A \otimes U(1)_V \otimes U(1)_A$, while only the smaller group of vector symmetries $SU(N_f)_V \otimes U(1)_V$ is manifest in the theory. The two chiral symmetries have each met a separate fate. $SU(N_f)_A$ is spontaneously broken by the chiral condensate, resulting in the light

pseudoscalar mesons as Goldstone bosons of this hidden symmetry. $U(1)_A$, on the other hand, is gone entirely, forced to gauge variance by the ABJ anomaly.

2.3 θ Vacua

Generally a quantum field theory which does not experience spontaneous symmetry breaking has a single vacuum, the one field configuration with minimum action. This is the case when all other field configurations can be smoothly deformed into the vacuum state.

However, if the field theory contains field configurations which can not be smoothly deformed into one another, the theory will have multiple vacua. In such a case, the space of field states can be grouped into sets of configurations which are smoothly connected. In each of these sets, there will be some configuration with minimal action. It is these field configurations which are the multiple vacua of the theory. They are analogous to multiple local minima in quantum mechanics, separated by infinitely high barriers.

This phenomenon of multiple vacua occurs for certain gauge theories, including the $SU(N_c = 3)$ gluon fields of QCD.

It is possible to write down gluon field configurations which have finite action and localized action density, but where the gauge field does not go to zero as we approach infinity. This is because a region of space in which the gauge field has the form:

$$A_\mu(x) = \frac{i}{g}\Omega(x)\partial_\mu\Omega^\dagger(x) \tag{2.47}$$

contains zero action density. Here $\Omega(x)$ is an arbitrary smooth function mapping x onto the gauge group. As evident from (2.9), the form in (2.47) is simply the gauge transform of $A_\mu = 0$. When constructing such a field configuration where the action

16

density goes to zero at infinity but the gauge field does not, we must choose $\Omega(x)$ as we approach infinity in each direction. In effect we are choosing a smooth mapping of the sphere at infinity S_{d-1} onto the gauge group, where d is the dimension of the Euclidean space.

As an example, take the case of a $U(1)$ gauge field in $d = 2$ dimensions. When we write down a field configuration, we are choosing a mapping of S_1, a simple circle, onto $U(1)$. Since $U(1)$ is also described by a circle, one is mapping a circle onto a circle. Denoting both circles as the phase of a unit vector in the complex plane, we can write down examples of such mappings:

$$\mathcal{H}: \qquad e^{i\phi} \quad \mapsto \quad e^{i\phi'} \tag{2.48}$$

The simplest example is the constant mapping:

$$\mathcal{H}_0: \qquad e^{i\phi} \quad \mapsto \quad 1 \tag{2.49}$$

The next simplest is the identity mapping:

$$\mathcal{H}_1: \qquad e^{i\phi} \quad \mapsto \quad e^{i\phi} \tag{2.50}$$

By visualizing the mappings as vectors located at each point on a circle, we realize that it is impossible to deform one of the above mappings into the other using only smooth gauge transformations. At some point on the circle, one of the vectors will turn clockwise during the deformation, while its neighbor will be required to turn counterclockwise.

A set of mappings which can be smoothly deformed into one another is labeled a homotopy class. Thus, the two mappings of (2.49) and (2.50) are representative members of two separate homotopy classes. In fact, we can easily write down an

17

infinite number of mappings, each of which belongs to a new homotopy class:

$$\mathcal{H}_\nu : \qquad e^{i\phi} \quad \mapsto \quad e^{i\nu\phi} \tag{2.51}$$

where ν is an integer which enumerates the classes. For any $U(1)$ gauge field config-uration we write down, there is one and only one mapping among those above such that the configuration can be smoothly deformed so that its gauge field orientation at infinity is described by the mapping.

The analog for QCD is mappings of $SU(N_c = 3)$ onto S_3. In this case as well, the gauge group is rich enough for there to be an infinite number of homotopy classes. In each homotopy class there is a field configuration with the minimum action. These are the infinite vacuum states of an $SU(N_c = 3)$ gauge theory. For the homotopy class which contains the constant mapping $\mathcal{H}_0$, the vacuum state will correspond to the traditional vacuum: a constant zero gauge field. However, for all other homotopy classes, the minimum action configurations will contain local kinks in the gauge field. These kinks are known as instantons, and each will have a local non-zero action density associated with it.

The winding number ν of a field configuration, which is used to label its homotopy class, can be shown to equal:

$$
\begin{aligned}
\nu &= \frac{1}{16\pi^2} \int_x \text{tr}\left[F_{\mu\nu} \tilde{F}^{\mu\nu} \right] \\
&= \frac{1}{2N_f g^2} \int_x \Theta
\end{aligned}
\tag{2.52}
$$

Thus, we see that the vacuum of QCD is not simple, but rather there is an infinite number of potential vacua $|\nu\rangle$. The true vacuum $|\theta\rangle$ is then a linear combination of

the $|\nu\rangle$. In order for this vacuum to have the correct behavior under gauge transformations, the coefficients of the combination must have the form:

$$|\theta\rangle = \sum_{\nu} e^{i\nu\theta} |\nu\rangle \tag{2.53}$$

where θ is a new arbitrary parameter of the theory. Incorporating this linear combination of vacua into the path integral of QCD effectively adds an additional term to the Lagrangian:

$$Z_{\text{QCD}} = \sum_{\nu} e^{i\nu\theta} \int [\mathcal{D}A_\mu]_\nu [\mathcal{D}q][\mathcal{D}\bar{q}] \; e^{-\int_x \mathscr{L}_{\text{QCD}}} \tag{2.54}$$

$$= \int [\mathcal{D}A_\mu][\mathcal{D}q][\mathcal{D}\bar{q}] \; e^{-\int_x \mathscr{L}_{\text{QCD eff}}} \tag{2.55}$$

where $[\mathcal{D}A_\mu]_\nu$ represents a functional integral over field configurations with winding number ν and:

$$\mathscr{L}_{\text{QCD eff}} = \mathscr{L}_{\text{QCD}} + \mathscr{L}_\theta$$

$$= \mathscr{L}_{\text{QCD}} + i\frac{\theta}{16\pi^2} \text{tr}\left[F_{\mu\nu}\tilde{F}^{\mu\nu}\right] \tag{2.56}$$

From (2.40) we can see that the ABJ anomaly has the same form as this new term. Thus, if we are assuming massless quarks, we have the freedom to absorb θ via a $U(1)_A$ rotation of the quark fields. However, for massive quarks, we lose that freedom. Because the quark mass eigenstates of QCD are not the same as those of the full Standard Model, the actual quark mass matrix $\tilde{\mathcal{M}}$ will include some chiral phase. In order to remove this chiral phase and put the mass matrix into the form standard for QCD, we apply a $U(1)_A$ rotation to the quark fields with a magnitude equal to $\arg \det \tilde{\mathcal{M}}$. This binds us to that specific rotation, and restricts us from absorbing θ. After this rotation, the physical value $\bar{\theta}$ for the coefficient in $\mathscr{L}_\theta$ becomes:

$$\bar{\theta} = \theta + \arg \det \tilde{\mathcal{M}} \tag{2.57}$$

19

Each choice of value for θ corresponds to a unique vacuum choice for QCD. Such a continuous set of vacuum states is reminiscent of spontaneous symmetry breaking. In fact the θ vacua are the multiple vacua of the spontaneously broken $\tilde{J}_\mu^5$ symmetry discussed above. This concurs with the fact that $U(1)_A$ rotations move one among the θ vacua.

2.4   Strong CP

As demonstrated by (2.43), $\mathscr{L}_\theta$ is a total divergence and thus can have no effect on perturbation-theory calculations. However, it still generates non-perturbative symptoms. In particular, $\mathscr{L}_\theta$ breaks CP symmetry and leads to CP violating effects. The most significant of these violations is a correction to the zero neutron dipole moment. However, the neutron dipole moment is strongly bound by experiment, $d_n < 6.3 \times 10^{-26}$ e cm [6]. This in turn leads to a bound on $\bar{\theta}$ [7]:

$$\bar{\theta} < 10^{-10} \tag{2.58}$$

This extreme smallness of $\bar{\theta}$ is known as the strong CP problem.

Were $\bar{\theta}$ the only parameter in the Standard Model to break CP symmetry, its extreme smallness would be of no particular concern. In such a situation, $\bar{\theta}$ can only be multiplicatively renormalized, and thus can remain small over a broad range of scales. However, CP is also broken by weak interactions. Thus, even if $\bar{\theta}$ were small at some given scale, at other scales it would be drastically additively renormalized by the other CP-breaking elements of the theory. Therefore, the observed smallness of $\bar{\theta}$ is deemed unnatural [8], and there is likely some as-yet-unknown structure which enforces this smallness. As such, the strong CP problem has traditionally been seen

as a chink in the armor of the Standard Model, and as a fertile starting point for beyond-the-Standard-Model theoretical work.

One proposed solution to the strong CP problem is through the introduction of an additional particle: the axion [9]. This field σ would couple to the quarks as a phase factor on the quark mass matrix:

$$\mathscr{L}_{\text{axion}} = \frac{1}{2}\partial_\mu\sigma\partial^\mu\sigma + \bar{q}\tilde{\mathcal{M}}e^{-i\sigma}q \qquad (2.59)$$

In such a situation both θ and the chiral phase of $\tilde{\mathcal{M}}$ can be absorbed via a field redefinition of the axion. However, thus far experimental and astrophysical searches for the axion have been unsuccessful.

A second possible solution is the Nelson-Barr mechanism [10, 11]. In this scenario, CP is a symmetry of the fundamental theory and CP violations are due to a spontaneous breaking of CP at the GUT scale. Included in the theory are several beyond-the-Standard-Model particles, including flavors of heavy fermions. Below the GUT scale, $\bar{\theta}$ gains a non-zero value proportional to the heavy fermion mass divided by the GUT scale. The smallness of this ratio, and therefore $\bar{\theta}$, is no longer unnatural because, if these fermion flavors were massless, new chiral symmetries would be introduced into the theory. In other words, the ratio obtains only a multiplicative renormalization as we change scales, and can thus remain small for all scales.

Another potential solution to the strong CP problem requires that a single flavor of quark remain massless. This is in fact the only proposed solution which does not require physics from beyond the Standard Model. The obvious candidate for this massless quark is the lightest flavor: the up quark. If the up quark were massless, we would regain the freedom to apply $U(1)_A$ rotations to it, and through the ABJ anomaly we could absorb the CP violating term. Surprisingly, current experimental

data does not rule out a massless up quark. However, through the lattice calculations presented here, we show that a massless up quark is unlikely.

It should be noted that a massless up quark would not be the end of the dilemma. It would simply shift the focus from an explanation of the smallness of $\bar{\theta}$ to an explanation of the masslessness of the up quark. However, several beyond-the-Standard-Model scenarios for the dynamic generation of quark masses, in which a massless up quark is a natural consequence, have been proposed [12, 13, 14].

CHAPTER 3

CHIRAL PERTURBATION THEORY

As a consequence of QCD's non-Abelian nature, it has two important characteristics: asymptotic freedom and confinement. Asymptotic freedom signifies that at very high energies the coupling of the strong force is greatly reduced, and quarks behave as if free. In this regime perturbation theory is successful. Conversely, confinement indicates that at low energies the interactions are strong enough to confine quarks and gluons within bound states. It is for this reason that only color singlet states are directly observed, never free quarks or gluons. These low energies are beyond the radius of convergence of perturbation theory, and the method becomes useless.

While it is impossible at low energies to apply perturbation theory to QCD's fundamental degrees of freedom, we can use clues from QCD to build an effective quantum field theory of its bound states. Such an effective theory is known as Chiral Perturbation Theory (ChPT). We focus our attention on to the lightest bound states of QCD, the octet of light pseudoscalar mesons. However, the ideas discussed here can also be used to construct an effective theory for the baryons.

Clues as to the appropriate form for our effective field theory come from QCD in the form of symmetries. The Lagrangian of ChPT must respect any symmetries respected by QCD. Confinement insures that all bound states are singlets under color.

Thus, color symmetry does not restrict the form of our chiral Lagrangian. Both flavor and Lorentz symmetry, on the other hand, place strong restrictions on the terms which the Lagrangian may include. For the moment we will assume massless quarks, so that $SU(N_f)_V \otimes SU(N_f)_A$ flavor symmetry is an exact symmetry of QCD.

Because we have no information other than the symmetries of QCD, we are forced to include in our chiral Lagrangian every possible term which respects both flavor and Lorentz symmetry. Of course, there are an infinite number of such terms. So, we order the terms by their importance and then ignore those whose importance is beyond our chosen sensitivity. The effective Lagrangian is thus an expansion in some parameter which establishes the importance of each term:

$$\mathscr{L}_{\text{ChPT}} = \mathscr{L}_{\text{ChPT}}^{(2)} + \mathscr{L}_{\text{ChPT}}^{(4)} + \mathscr{L}_{\text{ChPT}}^{(6)} + \cdots \tag{3.1}$$

Because we are attempting to build a low-energy theory for the light pseudoscalar mesons, we will take terms with lower powers of meson momentum to be of greater importance.

We collect the meson fields π^a into a flavor-space matrix Φ, multiplying each meson field by its corresponding broken flavor-symmetry generator:

$$\Phi \equiv \pi^a \tau^a = \frac{1}{\sqrt{2}} \left(\mathfrak{Q}\bar{\mathfrak{Q}} - \frac{1}{3}\mathbb{1}\text{Tr}\left[\mathfrak{Q}\bar{\mathfrak{Q}}\right] \right)$$

$$= \frac{1}{\sqrt{2}} \begin{bmatrix} \frac{2}{3}u\bar{u} - \frac{1}{3}d\bar{d} - \frac{1}{3}s\bar{s} & u\bar{d} & u\bar{s} \\ d\bar{u} & -\frac{1}{3}u\bar{u} + \frac{2}{3}d\bar{d} - \frac{1}{3}s\bar{s} & d\bar{s} \\ s\bar{u} & s\bar{d} & -\frac{1}{3}u\bar{u} - \frac{1}{3}d\bar{d} + \frac{2}{3}s\bar{s} \end{bmatrix} \tag{3.2}$$

where:

$$\mathfrak{Q} = \begin{bmatrix} u \\ d \\ s \end{bmatrix} \qquad\qquad \bar{\mathfrak{Q}} = \begin{bmatrix} \bar{u} & \bar{d} & \bar{s} \end{bmatrix} \tag{3.3}$$

The singlet piece of Φ has been subtracted, effectively removing η' from the matrix. The fields π^a are known as the Cartesian components of the mesons and do not correspond to the physical eigenstates of the light-pseudoscalar-meson fields, which can be identified as:

$$\Phi = \pi^a \tau^a = \frac{1}{\sqrt{2}} \begin{bmatrix} \frac{1}{\sqrt{2}}\pi^0 + \frac{1}{\sqrt{6}}\eta & \pi^+ & K^+ \\ \pi^- & -\frac{1}{\sqrt{2}}\pi^0 + \frac{1}{\sqrt{6}}\eta & K^0 \\ K^- & \bar{K}^0 & -\frac{2}{\sqrt{6}}\eta \end{bmatrix} \tag{3.4}$$

The unitary matrix Σ is then built from the meson-field matrix:

$$\Sigma \equiv e^{2i\pi^a\tau^a/f} \in SU(N_f) \tag{3.5}$$

We now define how the meson fields transform under flavor symmetry:

$$\Sigma \quad \rightarrow \quad \Sigma' = L\Sigma R^\dagger \tag{3.6}$$

using L and R from (2.24) and (2.25). With this definition Φ transforms linearly under pure vector transformations:

$$\Phi \quad \rightarrow \quad \Phi' = V\Phi V^\dagger \tag{3.7}$$

where $L = R = V$. Otherwise, the transformation of the meson fields is non-linear.

3.1 Leading Order Chiral Perturbation Theory

Considering all terms allowed by symmetry considerations and then expanding in terms of p^2/Λ_χ^2 — where p is the meson momentum and Λ_χ is some scale beyond which the expansion, and ChPT, breaks down — we find only one meaningful term at lowest order:

$$\mathscr{L}_{\text{ChPT}}^{\text{LO}'} = \frac{f^2}{4}\text{Tr}\big[\partial_\mu \Sigma^\dagger \partial^\mu \Sigma\big] \tag{3.8}$$

25

Note that derivatives of Σ correspond to powers of meson momentum. While the structure of the term is determined by symmetry, its coefficient f is not. The value of f is set by the behind-the-scenes dynamics of QCD, which ChPT hides from us. In the chiral limit, f equals the pion decay constant:

$$f = f_\pi + O(m_q) \tag{3.9}$$

where we are using the normalization $f_\pi \simeq 92.4\,\text{MeV}$. Expanding $\mathscr{L}_{\text{ChPT}}^{\text{LO}'}$ in terms of the meson fields π^a reveals a conventional scalar kinetic term for the mesons as well as a tower of interactions involving an increasing number of meson fields.

Non-zero quark mass breaks the flavor symmetry of QCD, an important building block of our chiral Lagrangian. However, there are two critical points which allow us to include the effects of quark mass in ChPT. First, we know the form through which the quark masses break flavor symmetry: the quark mass matrix $\mathcal{M}$. Thus, we can correctly break the symmetry in our effective theory by adding terms to the Lagrangian which break $SU(N_f)_V \otimes SU(N_f)_A$ only via insertions of $\mathcal{M}$. Secondly, the quark masses are small, presumably with respect to Λ_χ. So, the most important of such terms will be those with a low power of $\mathcal{M}$.

While the form of $\mathcal{M}$ is known, it is scaled by an unknown constant μ with units of mass:

$$\chi \equiv 2\mu\mathcal{M} = 2\mu\,\text{diag}\big(\{m_i\}\big) \tag{3.10}$$

In the chiral limit, μ is directly related to the chiral condensate:

$$\mu = -\frac{\langle\bar{q}q\rangle}{f_\pi^2 N_f} + O(m_q) \tag{3.11}$$

Now, considering all terms which respect Lorentz and flavor symmetry, except via insertions of $\mathcal{M}$, and expanding simultaneously to $O(p^2/\Lambda_\chi^2)$ and $O(\mu\mathcal{M}/\Lambda_\chi^2)$, we

26

determine the LO Euclidean chiral Lagrangian:

$$\mathscr{L}_{\text{ChPT}}^{\text{LO}} = \mathscr{L}_{\text{ChPT}}^{(2)} \tag{3.12}$$

$$= \frac{f^2}{4}\text{Tr}\left[\partial_\mu \Sigma^\dagger \partial^\mu \Sigma\right] - \frac{f^2}{4}\text{Tr}\left[\Sigma^\dagger \chi + \chi \Sigma\right] \tag{3.13}$$

The low-energy non-perturbative dynamics of QCD have been boiled down, at this order, to two unknown constants: f and μ.

The arrangement of the meson fields in Σ seems quite arbitrary. In fact there are an infinite number of other arrangements and corresponding representations of $SU(N_f)_V \otimes SU(N_f)_A$, each of which would result in a new form for the chiral Lagrangian. However, any such representation will result in exactly the same meson physics as the representation presented here. This is due to a fundamental characteristic of effective quantum field theories known as universality. For a low-energy effective theory, the symmetries of the theory alone determine the resultant physics, and the details of the symmetries' representation are unimportant.

3.2 Leading Order Quark Mass Ratios

With the LO chiral Lagrangian in hand, predictions can be made for quantities in which the constants of the Lagrangian cancel away, such as ratios of semi-leptonic decay rates. The meson masses can not be predicted, but their dependence on the quark masses can. By inverting those relationships and using experimental values for the meson masses, we can calculate the light-quark-mass ratios.

The LO ChPT expressions for the meson masses are straightforward:

$$\tilde{M}_{\pi^0}^2 = \tilde{M}_{\pi^+}^2 = \tilde{M}_{\pi^-}^2 = \mu(m_u + m_d) \tag{3.14}$$

$$\tilde{M}_{K^+}^2 = \tilde{M}_{K^-}^2 = \mu(m_u + m_s) \tag{3.15}$$

$$\tilde{M}_{K^0}^2 = \tilde{M}_{\bar{K}^0}^2 = \mu(m_d + m_s) \tag{3.16}$$

These masses $\tilde{M}_X$ are often referred to as the mesons' QCD masses. They are related to the physical meson masses by a Quantum Electrodynamics (QED) correction. However at lowest order, only the masses of the charged mesons are corrected and all by the same amount, a result known as Dashen's theorem [15]:

$$\delta_{E_\pi} = \delta_{E_K} = \delta_E$$

$$= M_{\pi^+}^2 - M_{\pi^0}^2 + O(e^2 m_q) \tag{3.17}$$

where M_X represents a meson's physical mass. Thus, QED adds only one additional unknown parameter to the picture:

$$M_{\pi^0}^2 = \mu(m_u + m_d) \tag{3.18}$$

$$M_{\pi^+}^2 = M_{\pi^-}^2 = \mu(m_u + m_d) + \delta_E \tag{3.19}$$

$$M_{K^+}^2 = M_{K^-}^2 = \mu(m_u + m_s) + \delta_E \tag{3.20}$$

$$M_{K^0}^2 = M_{\bar{K}^0}^2 = \mu(m_d + m_s) \tag{3.21}$$

We are ignoring and will continue to ignore a small correction to $M_{\pi^0}^2$ due to the mixing of the physical π^0 and η states. The above relationships can be inverted to predict the quark-mass ratios [16]:

$$\frac{m_u}{m_d} = \frac{M_{K^+}^2 - M_{K^0}^2 + 2M_{\pi^0}^2 - M_{\pi^+}^2}{M_{K^0}^2 - M_{K^+}^2 + M_{\pi^+}^2} = 0.55 \tag{3.22}$$

$$\frac{m_s}{m_d} = \frac{M_{K^0}^2 + M_{K^+}^2 - M_{\pi^+}^2}{M_{K^0}^2 - M_{K^+}^2 + M_{\pi^+}^2} = 20.1 \tag{3.23}$$

This LO calculation clearly suggests that the up quark mass is non-zero. However, we will see that the NLO calculation muddy the water.

3.3   Next-To-Leading Order Chiral Perturbation Theory

When we venture beyond tree-level and attempt to calculate one-loop corrections with our LO chiral Lagrangian, we find that the corrections have new matrix structures, and thus the divergences can not be absorbed into our LO terms. As it turns out, these new terms are the same terms which we would have included in our Lagrangian had we decided to go out to NLO in meson momentum and quark mass. Thus, if we would like to work at one-loop using our LO Lagrangian, we must also include tree-level effects from NLO terms. The one-loop corrections will then renormalize the coefficients of our NLO terms. This behavior is a direct consequence of ChPT being an effective field theory and will occur order by order.

Adding the NLO terms, the Euclidean chiral Lagrangian becomes [17]:

$$
\begin{aligned}
\mathscr{L}_{\text{ChPT}}^{\text{NLO}} &= \mathscr{L}_{\text{ChPT}}^{(2)} + \mathscr{L}_{\text{ChPT}}^{(4)} \\
&= \frac{f^2}{4}\text{Tr}\big[\partial_\mu \Sigma^\dagger \partial^\mu \Sigma\big] - \frac{f^2}{4}\text{Tr}\big[\Sigma^\dagger \chi + \chi\Sigma\big] \\
&\quad - L_1\Big(\text{Tr}\big[\partial_\mu \Sigma^\dagger \partial^\mu \Sigma\big]\Big)^2 \\
&\quad - L_2\Big(\text{Tr}\big[\partial_\mu \Sigma^\dagger \partial_\nu \Sigma\big]\text{Tr}\big[\partial^\mu \Sigma^\dagger \partial^\nu \Sigma\big]\Big) \\
&\quad - L_3\Big(\text{Tr}\big[\partial_\mu \Sigma^\dagger \partial^\mu \Sigma \partial_\nu \Sigma^\dagger \partial^\nu \Sigma\big]\Big) \\
&\quad + L_4\Big(\text{Tr}\big[\partial_\mu \Sigma^\dagger \partial^\mu \Sigma\big]\text{Tr}\big[\Sigma^\dagger \chi + \chi\Sigma\big]\Big) \\
&\quad + L_5\Big(\text{Tr}\big[\partial_\mu \Sigma^\dagger \partial^\mu \Sigma(\Sigma^\dagger \chi + \chi\Sigma)\big]\Big) \\
&\quad - L_6\Big(\text{Tr}\big[\Sigma^\dagger \chi + \chi\Sigma\big]\Big)^2 \\
&\quad - L_7\Big(\text{Tr}\big[\Sigma^\dagger \chi - \chi\Sigma\big]\Big)^2 \\
&\quad - L_8\Big(\text{Tr}\big[\Sigma^\dagger \chi \Sigma^\dagger \chi\big] + \text{Tr}\big[\chi\Sigma\chi\Sigma\big]\Big) \qquad (3.24)
\end{aligned}
$$

where L_i are additional unknown constants known as the Gasser-Leutwyler (GL) coefficients. They are not constrained by chiral symmetry. Rather, they parameterize our ignorance concerning the low-energy dynamics of QCD. Terms which couple the mesons to a background gauge field have been dropped. Note that each term in $\mathscr{L}_{\text{ChPT}}^{(4)}$ contains either four derivatives, two derivatives and one power of χ, or two powers of χ.

The magnitude of the chiral scale Λ_χ is an important element in determining the validity of ChPT. By looking at the loop corrections to the NLO terms in the chiral Lagrangian, we can develop an estimate for Λ_χ. We find that when the meson momentum in loops is cutoff at $\Lambda = 4\pi f$, the radiative corrections from the LO Lagrangian are on the same order at the contributions from tree-level NLO diagrams.

So, we can only reasonably expect ChPT to be useful below that scale, and thus:

$$\Lambda_\chi \simeq 4\pi f \tag{3.25}$$

Since $f = f_\pi$ at lowest order, we find that $\Lambda_\chi \simeq 1.2$ GeV. We are now in a position to evaluate the validity of our expansion in the quark mass. At lowest order $\mu\mathcal{M} \simeq M_{K^0}^2$, and thus $(\mu\mathcal{M}/\Lambda_\chi^2) \simeq 0.2$. The quark mass expansion is sound. Therefore, if we restrict ourselves to meson momentum below 500 MeV, we can expect ChPT to produce accurate predictions.

3.4   Next-To-Leading Order Quark Mass Ratios

The NLO expressions for the meson masses are calculable from the NLO Lagrangian. Using notation similar to the literature, $\tilde{M}_\pi$ represents the pion mass without QED corrections, while $\tilde{M}_K$ represents the kaon mass neglecting the mass difference $m_d - m_u$ and without QED corrections. These uncorrected masses are related to the physical meson masses via:

$$\tilde{M}_\pi^2 = \tilde{M}_{\pi^0}^2 = M_{\pi^0}^2 \tag{3.26}$$

$$2\tilde{M}_K^2 = \tilde{M}_{K^0}^2 + \tilde{M}_{K^+}^2 = M_{K^0}^2 + M_{K^+}^2 - \left(1 + \Delta_E\right)\left(M_{\pi^+}^2 - M_{\pi^0}^2\right) \tag{3.27}$$

The above equalities are corrected by terms of order $O(e^2 m_q)$ and $O\big((m_d - m_u)^2\big)$, as well as by NNLO ChPT. The parameter Δ_E allows for a difference between the QED contributions to the pion and kaon masses:

$$\frac{\delta_{E_K}}{\delta_{E_\pi}} = 1 + \Delta_E \tag{3.28}$$

Use of Dashen's theorem, as was done in the LO case, is equivalent to using $\Delta_E = 0$. A comprehensive study of experimental data [18, 19] suggests a significant deviation

from Dashen's theorem and gives the result:

$$\Delta_E = 0.84 \pm 0.25 \tag{3.29}$$

This is the value which will be used in subsequent calculations, unless stated otherwise.

Using the NLO chiral Lagrangian, the uncorrected NLO meson masses are calculated [17]:

$$\begin{aligned}
\tilde{M}_\pi^2 = \mu\big(m_u + m_d\big)\bigg\{ & 1 + \mathcal{I}_\pi - \tfrac{1}{3}\mathcal{I}_\eta \\
& + \frac{8}{f^2}\mu\big(m_u + m_d\big)\big(2L_8 - L_5\big) \\
& + \frac{16}{f^2}\mu\big(m_u + m_d + m_s\big)\big(2L_6 - L_4\big)\bigg\}
\end{aligned} \tag{3.30}$$

$$\begin{aligned}
\tilde{M}_K^2 = \mu\big(\hat{m} + m_s\big)\bigg\{ & 1 + \tfrac{2}{3}\mathcal{I}_\eta \\
& + \frac{8}{f^2}\mu\big(\hat{m} + m_s\big)\big(2L_8 - L_5\big) \\
& + \frac{16}{f^2}\mu\big(m_u + m_d + m_s\big)\big(2L_6 - L_4\big)\bigg\}
\end{aligned} \tag{3.31}$$

where $\hat{m} = \tfrac{1}{2}(m_u + m_d)$ and $\mathcal{I}_X$ represent chiral logs which arise from divergent loop corrections. We choose to cut these loops off at $\Lambda = \Lambda_\chi = 4\pi f$:

$$\mathcal{I}_X \equiv \frac{\tilde{M}_X^2}{2(4\pi f)^2} \ln \frac{\tilde{M}_X^2}{(4\pi f)^2} \tag{3.32}$$

The additional correction terms involving GL coefficients come from NLO tree-level interactions.

We can use these expressions to construct two combinations of the meson masses which experience an equal correction Δ_M at NLO [17]:

$$\frac{\tilde{M}_K^2}{\tilde{M}_\pi^2} = \frac{m_s + \hat{m}}{m_d + m_u}\left\{1 + \Delta_M + O(m_q^2)\right\} \tag{3.33}$$

$$\frac{\tilde{M}_{K^0}^2 - \tilde{M}_{K^+}^2}{\tilde{M}_K^2 - \tilde{M}_\pi^2} = \frac{m_d - m_u}{m_s - \hat{m}}\left\{1 + \Delta_M + O(m_q^2)\right\} \tag{3.34}$$

where:

$$\Delta_M = -\mathcal{I}_\pi + \mathcal{I}_\eta + \frac{8}{f^2}\mu\left(m_s - \hat{m}\right)\left(2L_8 - L_5\right)$$

$$= -\mathcal{I}_\pi + \mathcal{I}_\eta + \frac{8}{f_\pi^2}\left(\tilde{M}_K^2 - \tilde{M}_\pi^2\right)\left(2L_8 - L_5\right) \tag{3.35}$$

Thus, a ratio independent of NLO corrections can be defined:

$$Q^2 \equiv \frac{m_s^2 - \hat{m}^2}{m_d^2 - m_u^2} = \frac{\tilde{M}_K^2}{\tilde{M}_\pi^2}\frac{\tilde{M}_K^2 - \tilde{M}_\pi^2}{\tilde{M}_{K^0}^2 - \tilde{M}_{K^+}^2} + O(m_q^2) \tag{3.36}$$

Replacing the QCD meson masses with physical masses results in:

$$Q^2 = \frac{1}{4M_{\pi^0}^2}\frac{M_{K^0}^2 + M_{K^+}^2 - (1 + \Delta_E)M_{\pi^+}^2 + (1 + \Delta_E)M_{\pi^0}^2}{M_{K^0}^2 - M_{K^+}^2 + (1 + \Delta_E)M_{\pi^+}^2 - (1 + \Delta_E)M_{\pi^0}^2}$$

$$\times \left(M_{K^0}^2 + M_{K^+}^2 - (1 + \Delta_E)M_{\pi^+}^2 - (1 - \Delta_E)M_{\pi^0}^2\right)$$

$$= \left(22.01 \pm 0.57\right)^2 \tag{3.37}$$

where experimental error in the meson masses is overwhelmed by uncertainty in Δ_E. Use of Dashen's Theorem instead of (3.29) results in a central value of $Q = 24.18$. The quark-mass ratios can be represented as an ellipse [20] which conforms to the equation:

$$\left(\frac{m_u}{m_d}\right)^2 + \frac{1}{Q^2}\left(\frac{m_s}{m_d}\right)^2 = 1 \tag{3.38}$$

where $\hat{m}$ has been taken to be small relative to m_s.

We now can solve for the quark-mass ratios, but only in terms of the unknown NLO correction Δ_M [21]:

$$\frac{m_s}{\hat{m}} = \frac{2\tilde{M}_K^2}{\tilde{M}_\pi^2\left(1 + \Delta_M\right)} - 1 \tag{3.39}$$

$$\frac{m_u}{\hat{m}} = 1 - \frac{\tilde{M}_K^2}{\tilde{M}_\pi^4}\frac{\tilde{M}_K^2 - \left(1 + \Delta_M\right)\tilde{M}_\pi^2}{Q^2\left(1 + \Delta_M\right)^2} \tag{3.40}$$

Setting m_u equal to zero and solving (3.40) for Δ_M, we find:

$$\Delta_M = \frac{\tilde{M}_K^2}{4Q^2\tilde{M}_\pi^2}\left(-1 \pm \sqrt{1 + 4Q^2}\right) - 1$$

$$= -0.404 \pm 0.002 \pm 0.015 \pm 0.16 \tag{3.41}$$

where the first uncertainty is due to experimental error in the meson masses, the second is due to uncertainty in Δ_E, and the third comes from an assumption that unaccounted for NNLO corrections are on the order of Δ_M^2. Use of Dashen's theorem instead of (3.29) results in the value $\Delta_M = -0.455 \pm 0.002 \pm 0.21$, for which no uncertainly due to Δ_E is given. The value for Δ_M from (3.41) corresponds, via (3.35), to $2L_8 - L_5 = (-1.25 \pm 0.77) \times 10^{-3}$, or the range:

$$-2.02 \times 10^{-3} < 2L_8 - L_5 < -0.48 \times 10^{-3} \tag{3.42}$$

Using Dashen's theorem corresponds to $2L_8 - L_5 = (-1.49 \pm 0.98) \times 10^{-3}$. Sharpe quotes a range similar to (3.42) in [22]. The second root of (3.40) is not considered as it requires the corrections to be even more improbably large.

From (3.41) we see that if the NLO corrections to ChPT are quite large, the massless up quark remains a possibility.

At times, an alternative normalization of the GL coefficients is used:

$$\alpha_i = 8(4\pi)^2 L_i \tag{3.43}$$

34

This is a more natural normalization in that each α_i can be expected to be on the order of one. Under this normalization the range consistent with a massless up quark is:

$$-2.6 \quad < \quad 2\alpha_8 - \alpha_5 \quad < \quad -0.6 \tag{3.44}$$

As discussed above, one-loop graphs generated by the LO chiral Lagrangian renormalize the GL coefficients. Thus, the GL coefficients are functions of the renormalization scale. That scale dependence has a simple form [17]:

$$L_i(\Lambda_2) = L_i(\Lambda_1) + \frac{\Gamma_i}{(4\pi)^2} \ln \frac{\Lambda_1}{\Lambda_2} \tag{3.45}$$

where:

$$\Gamma_5 = \frac{3}{8} \qquad\qquad \Gamma_8 = \frac{5}{48} \tag{3.46}$$

L_7 is scale invariant, with $\Gamma_7 = 0$. The full set of scaling coefficients Γ_i can be found in [23]. Unless otherwise stated, we report all GL coefficients at $\Lambda = 4\pi f_\pi$.

3.5 Phenomenological Results

In order to unquestionably rule out a massless up quark, the value of $2L_8 - L_5$ must be determined. Because the GL coefficients encapsulate the low energy dynamics of QCD, they could in principle be analytically calculated directly from the QCD Lagrangian. However, the limitations of perturbation theory at these low energy scales has stymied such efforts. Thus, the primary source of information about these constants is phenomenological studies.

3.5.1 Meson Decay Constants

Calculating NLO expressions for the meson decay constants using the NLO chiral Lagrangian, we find [17]:

$$f_\pi = f\left\{1 - 2\mathcal{I}_\mu - \mathcal{I}_K\right.$$
$$+ \frac{4}{f^2}\mu(m_u + m_d)L_5$$
$$\left. + \frac{8}{f^2}\mu(m_u + m_d + m_s)L_4\right\} \tag{3.47}$$

$$f_K = f\left\{1 - \tfrac{3}{4}\mathcal{I}_\pi - \tfrac{3}{2}\mathcal{I}_K - \tfrac{3}{4}\mathcal{I}_\eta\right.$$
$$+ \frac{4}{f^2}\mu(\hat{m} + m_s)L_5$$
$$\left. + \frac{8}{f^2}\mu(m_u + m_d + m_s)L_4\right\} \tag{3.48}$$

Their ratio isolates L_5:

$$\frac{f_\pi}{f_K} = 1 + \Delta_f + O(m_q^2) \tag{3.49}$$

where:

$$\Delta_f = \tfrac{5}{4}\mathcal{I}_\pi - \tfrac{1}{2}\mathcal{I}_K - \tfrac{3}{4}\mathcal{I}_\eta + \frac{4}{f^2}\mu(m_s - \hat{m})L_5$$
$$= \tfrac{5}{4}\mathcal{I}_\pi - \tfrac{1}{2}\mathcal{I}_K - \tfrac{3}{4}\mathcal{I}_\eta + \frac{4}{f_\pi^2}(\tilde{M}_K^2 - \tilde{M}_\pi^2)L_5 \tag{3.50}$$

We can then fix L_5 using experimental values:

$$L_5 = (0.51 \pm 0.47) \times 10^{-3} \tag{3.51}$$

where the uncertainty comes from both experimental error and an assumption that the unknown NNLO corrections to (3.49) are on the order of Δ_f^2. Use of Dashen's theorem instead of (3.29) has very little effect on the value, resulting in $L_5 = (0.50 \pm 0.47) \times 10^{-3}$.

3.5.2 Gell-Mann-Okubo Relation

At leading order ChPT confirms the traditional Gell-Mann-Okubo relation:

$$\tilde{M}_\pi^2 + 3\tilde{M}_\eta^2 = 4\tilde{M}_K^2 \tag{3.52}$$

At NLO, ChPT predicts a correction which accounts for the meson masses' observed deviation from the relation:

$$\Delta_{\text{GMO}} \equiv \frac{4\tilde{M}_K^2 - \tilde{M}_\pi^2 - 3\tilde{M}_\eta^2}{\tilde{M}_\eta^2 - \tilde{M}_\pi^2} = 0.218 \tag{3.53}$$

This NLO correction is:

$$\Delta_{\text{GMO}} = -2\frac{4\tilde{M}_K^2 \mathcal{I}_K - \tilde{M}_\pi^2 \mathcal{I}_\pi - 3\tilde{M}_\eta^2 \mathcal{I}_\eta}{\tilde{M}_\eta^2 - \tilde{M}_\pi^2}$$
$$- \frac{6}{f_\pi^2}\left(\tilde{M}_\eta^2 - \tilde{M}_\pi^2\right)\left(12L_7 + 6L_8 - L_5\right) \tag{3.54}$$

Using the observed deviation we can bind a linear combination of the GL coefficients:

$$12L_7 + 6L_8 - L_5 = \left(-1.08 \pm 0.24\right) \times 10^{-3} \tag{3.55}$$

where uncertainty in Δ_E and the light meson masses is dwarfed by an assumption that the unknown NNLO corrections to the Gell-Mann-Okubo relation are on the order of Δ_{GMO}^2. Use of Dashen's theorem instead of (3.29) results in the value $12L_7 + 6L_8 - L_5 = (-1.10 \pm 0.26) \times 10^{-3}$.

With L_7 unknown, the combination $2L_8 - L_5$ remains undetermined.

3.6 Kaplan-Manohar Ambiguity

We will find that it is impossible to fix the value of $2L_8 - L_5$ using only expressions from ChPT combined with experimental measurements. The chiral Lagrangian

contains an ambiguity among its parameters which prevents us from using the predictions of ChPT to determine L_6, L_7, L_8, and the quark-mass ratios. This ambiguity is known as the Kaplan-Manohar (KM) ambiguity [20].

The chiral Lagrangian is invariant under a certain redefinition of its coefficients. To see this we shift the quark masses in the following way:

$$m_u \longmapsto \mathring{m}_u = m_u + \lambda m_d m_s \tag{3.56}$$

$$m_d \longmapsto \mathring{m}_d = m_d + \lambda m_u m_s \tag{3.57}$$

$$m_s \longmapsto \mathring{m}_s = m_s + \lambda m_u m_d \tag{3.58}$$

where λ has units of inverse mass. Stated in terms of χ, this redefinition has the form:

$$\chi \longmapsto \mathring{\chi} = \chi + \hat{\lambda} \chi^{-1} \det \chi \tag{3.59}$$

where:

$$\hat{\lambda} = \frac{\lambda}{2\mu} \tag{3.60}$$

Using the Cayley-Hamilton theorem for a 3×3 matrix $\mathcal{B}$:

$$\mathbb{1} \det \mathcal{B} = \mathcal{B}^3 - \mathcal{B}^2 \operatorname{Tr} \mathcal{B} - \tfrac{1}{2} \mathcal{B} \operatorname{Tr} \mathcal{B}^2 - \tfrac{1}{2} \mathcal{B} \big(\operatorname{Tr} \mathcal{B} \big)^2 \tag{3.61}$$

we can write the shift in χ as:

$$\hat{\lambda} \chi^{-1} \det \chi = \hat{\lambda} \chi^{-1} \det[\chi \Sigma]$$
$$= \hat{\lambda} \Big\{ \Sigma \chi \Sigma \chi \Sigma - \Sigma \chi \Sigma \operatorname{Tr}[\chi \Sigma] - \tfrac{1}{2} \Sigma \operatorname{Tr}[\chi \Sigma \chi \Sigma] - \tfrac{1}{2} \Sigma \big(\operatorname{Tr}[\chi \Sigma] \big)^2 \Big\} \tag{3.62}$$

where $\det \Sigma = 1$ has been used. From this we find:

$$\operatorname{Tr}\big[\Sigma^\dagger \mathring{\chi} \big] = \operatorname{Tr}\big[\Sigma^\dagger \chi \big] - \frac{\hat{\lambda}}{2} \Big\{ \operatorname{Tr}[\chi \Sigma \chi \Sigma] - \big(\operatorname{Tr}[\chi \Sigma] \big)^2 \Big\} \tag{3.63}$$

Thus, the mass term in the chiral Lagrangian becomes:

$$
\begin{aligned}
\mathrm{Tr}\big[\Sigma^\dagger \mathring{\chi} + \mathring{\chi}\Sigma\big] = \; & \mathrm{Tr}\big[\Sigma^\dagger \chi + \chi\Sigma\big] \\
& + \frac{\hat{\lambda}}{4}\Big(\mathrm{Tr}\big[\Sigma^\dagger \chi + \chi\Sigma\big]\Big)^2 \\
& + \frac{\hat{\lambda}}{4}\Big(\mathrm{Tr}\big[\Sigma^\dagger \chi - \chi\Sigma\big]\Big)^2 \\
& - \frac{\hat{\lambda}}{2}\Big(\mathrm{Tr}\big[\Sigma^\dagger \chi \Sigma^\dagger \chi + \chi\Sigma\chi\Sigma\big]\Big)
\end{aligned}
\tag{3.64}
$$

From (3.24) we see that a redefinition of three GL coefficients will absorb these additional terms:

$$
L_6 \;\rightarrowtail\; \mathring{L}_6 = L_6 - \tilde{\lambda} \tag{3.65}
$$

$$
L_7 \;\rightarrowtail\; \mathring{L}_7 = L_7 - \tilde{\lambda} \tag{3.66}
$$

$$
L_8 \;\rightarrowtail\; \mathring{L}_8 = L_8 + 2\tilde{\lambda} \tag{3.67}
$$

where:

$$
\tilde{\lambda} = \frac{f^2}{32\mu}\lambda \tag{3.68}
$$

Stated explicitly, the KM ambiguity is the invariance in form of the chiral Lagrangian under the redefinitions (3.59), (3.65), (3.66), and (3.67). While we had believed that there was only one well-defined Lagrangian for ChPT, we now discover that there exists a family of Lagrangians, all equally valid and connected via the above transformations.

The KM ambiguity implies that all expressions for physical quantities obtained from the chiral Lagrangian will be invariant under the parameter redefinitions. Thus, combining these expressions with experimental results can never allow us to distinguish between one coefficient set (χ, L_6, L_7, L_8) and another $(\mathring{\chi}, \mathring{L}_6, \mathring{L}_7, \mathring{L}_8)$. For example, the combinations of GL coefficients L_5 and $12L_7 + 6L_8 - L_5$, which we were

able to determine using expressions from ChPT, are both clearly invariant under the redefinitions. The ratio Q^2 defined in (3.36), which was also fixed using ChPT, is invariant to this order under the redefinitions. This becomes clear when we note that the squares of the quark masses transform as:

$$\mathring{m}_i^2 = m_i^2 + 2\lambda m_u m_d m_s + O(m_q^4) \tag{3.69}$$

Even the meson mass expressions are invariant to the order at which we are working:

$$\begin{aligned}
\tilde{M}_\pi^2 &= \mu\big(\mathring{m}_u + \mathring{m}_d\big)\Big\{1 + \mathcal{I}_\pi - \tfrac{1}{3}\mathcal{I}_\eta \\
&\qquad\qquad + \frac{8}{f^2}\mu\big(\mathring{m}_u + \mathring{m}_d\big)\big(2\mathring{L}_8 - L_5\big) \\
&\qquad\qquad + \frac{16}{f^2}\mu\big(\mathring{m}_u + \mathring{m}_d + \mathring{m}_s\big)\big(2\mathring{L}_6 - L_4\big)\Big\} \\
&= \tilde{M}_\pi^2 + 2\lambda\mu m_s \hat{m} + 2\mu\hat{m}\Big\{\frac{8}{f^2}\mu\hat{m}\big(4\tilde{\lambda}\big) + \frac{16}{f^2}\mu\big(2\hat{m} + m_s\big)\big(-2\tilde{\lambda}\big)\Big\} + \cdots \\
&= \tilde{M}_\pi^2 + 2\lambda\mu m_s \hat{m} - \tilde{\lambda}\frac{64\mu}{f^2}\mu m_s \hat{m} + \cdots \\
&= \tilde{M}_\pi^2 + \cdots \tag{3.70}
\end{aligned}$$

Note that while some measurable quantities appear to break invariance at higher order, they in fact continue to be invariant order by order.

The quark-mass ratios, as well as the quantity $2L_8 - L_5$, are not invariant under the redefinition. Thus, using ChPT alone, they can not be fixed. We can only hope to determine a one-parameter family of allowed values.

The KM ambiguity does not represent a symmetry of either QCD or ChPT. It is nothing more than an ambiguity in the effective theory's couplings. Thus, true values for the quark-mass ratios and the GL coefficients do exist. We have simply found that determining those quantities requires theoretical input from outside ChPT.

ChPT does place one constraint on L_6, L_7, and L_8. The GL coefficients must be of natural order. If they were not, it would imply that ChPT is based on a poor expansion, and ChPT would have proven useless. Yet, ChPT's accurate predictions in other contexts imply otherwise. We are curious what sort of bounds this naturalness places on the up quark mass. If we assume that the maximum reasonable shift in an α_i is on the order of one:

$$\mathring{\alpha}_i = \alpha_i + \frac{(4\pi f)^2}{4\mu}\lambda = \alpha_i + O(1) \tag{3.71}$$

we find an estimate for the largest reasonable value for λ:

$$\lambda \approx \frac{4\mu}{(4\pi f)^2} \approx 4\frac{M_{K^0}^2}{m_s}\frac{1}{\Lambda_\chi^2} \approx \frac{1}{m_s} \tag{3.72}$$

This λ corresponds to a shift in m_u on the order of the down quark mass:

$$\mathring{m}_u - m_u = \lambda m_d m_s \approx m_d \tag{3.73}$$

Thus, we find that a massless up quark is within the natural range and is not shown by this argument to be beyond the scope of possibility.

In light of the KM ambiguity, we see that we were somewhat naive in our construction of the chiral Lagrangian. We had stated previously that we knew exactly the form of the chiral symmetry breaking structure, and that we could account for that breaking via insertions of $\mathcal{M}$. Yet, we now find that there exists a continuous set of matrices:

$$\mathring{\mathcal{M}}(\lambda) = \mathcal{M} + \lambda \mathcal{M}^{-1} \det \mathcal{M} \tag{3.74}$$

each of which is an equally valid choice for breaking the chiral symmetry of our Lagrangian. If fact, even if the up quark were massless, the form of the chiral symmetry

41

breaking term could naively be mistaken for a non-zero up quark mass:

$$\mathring{\mathcal{M}}(\lambda)\Big|_{m_u=0} = \begin{bmatrix} \lambda m_d m_s & & \\ & m_d & \\ & & m_s \end{bmatrix} \tag{3.75}$$

It is impossible for ChPT to distinguish between the effects of a non-zero up quark mass and certain large NLO corrections.

3.7 Theoretical Estimates

Various theoretical approximations can be made in an attempt to estimate Δ_M and the Gasser-Leutwyler coefficients.

3.7.1 Resonance Saturation

While each interaction term in an effective field theory such as ChPT occurs at a point, in the full theory they correspond to short-distance interactions, each encompassing a tower of graphs involving heavier particles. These particles are heavy in the sense that they are more massive than the scale of the effective theory. In the case of our ChPT, these heavy particles include all bound states of QCD heavier than the light mesons. When the transition is made from the full theory to an effective theory, the heavy states are integrated out. This integration shrinks the short-distance interaction to a point and condenses the effects of the heavy particle exchanges into the coefficient of the effective theory's corresponding coupling term.

Thus, if we can identifying the most significant of the heavy particle exchanges corresponding to a given coupling term, we can estimate the full integration process by merely integrating over the identified important exchanges. This leads to a rough estimate of the coupling's coefficient in the effective theory.

For certain simple coupling terms, the most significant of the contributing interactions is the exchange of a single heavy particle, the lightest of the heavy particles with the correct quantum numbers to mediate the coupling. In such a case the resulting estimate for the coupling constant is proportional to the inverse square of the heavy particle's mass.

Both L_5 and L_7 are examples of coupling constants whose value can be estimated as described. We can model their corresponding vertices as being saturated by exchange of the members of the scalar octet and η' respectively [24, 25]. Adding factors which arise from the integration, the estimates become:

$$L_5 \simeq \frac{f_\pi^2}{4M_S^2} \simeq 2.3 \times 10^{-3} \qquad L_7 \simeq -\frac{f_\pi^2}{48M_{\eta'}^2} = -0.2 \times 10^{-3} \tag{3.76}$$

with $M_S \simeq 980 \, \text{MeV}$. Comparing with the determined value of L_5 (3.51), we can see that the estimate is off but is of the correct order of magnitude. This allows us to approximate the uncertainty of the L_7 estimate:

$$L_7 = \left(-0.2 \pm 2.5\right) \times 10^{-3} \tag{3.77}$$

Combined with (3.51) and (3.55), (3.77) leads to estimates for $2L_8 - L_5$, Δ_M, and the light-quark-mass ratio:

$$\frac{m_u}{m_d} = 0.4 \pm 2.1 \tag{3.78}$$

We can see that the uncertainly in the resonance saturation estimate is too far significant to rule out a massless up quark.

3.7.2 Large N_c

In the large-N_c limit the ABJ anomaly is suppressed and massless QCD has a full $U(N_f = 3)_V \otimes U(N_f = 3)_A$ flavor symmetry. If we assume that this symmetry

43

spontaneously breaks to $U(N_f = 3)_V$, it would result in nine Goldstone bosons as discussed in Section 2.2. A now light η' would join the ranks of the light mesons and take on the role of the ninth Goldstone boson. At NLO in $1/N_c$, the anomaly and the η' mass return.

The perspective of large N_c can be incorporated into ChPT by constructing a Lagrangian which is not only an expansion in p^2/Λ_χ^2 and $\mu\mathcal{M}/\Lambda_\chi^2$, but also in $1/N_c$ [26]. Additionally, the now light η' can no longer be excluded from the low-energy theory. Instead, we include it as the trace of our meson field matrix Φ, making Σ an element of $U(N_f)$. This procedure is complicated by the fact that, while the ABJ anomaly is suppressed, it is not absent. Correspondingly, the η' is light, yet the symmetry group which must be respected by our Lagrangian is the anomalously-broken chiral symmetry, $U(N_f)_V \otimes SU(N_f)_A$. Under this reduced group, $\mathrm{Tr}\big[\ln\Sigma\big] \propto \mathrm{Tr}\,\Phi$ is invariant. Thus, the symmetry leaves the Lagrangian's dependence on $\mathrm{Tr}\big[\ln\Sigma\big]$ unconstrained, and the Lagrangian must incorporate arbitrary functions of the η' field. In the end, however, we are saved from these arbitrary functions by the fact that their Taylor expansion is an expansion in $1/N_c$. Thus, large N_c truncates the functions to simple forms.

An analysis of the η and η' masses in large-N_c ChPT out to order $O(N_c p^2/\Lambda_\chi^2)$, $O(N_c \mu\mathcal{M}/\Lambda_\chi^2)$, and $O(N_c^0 = 1)$ implies a constraint on Δ_M [27]:

$$\Delta_M > -\frac{4\tilde{M}_K^2 - 3\tilde{M}_\eta^2 - \tilde{M}_\pi^2}{4\tilde{M}_K^2 - 4\tilde{M}_\pi^2} = -0.07 \tag{3.79}$$

Comparing the constraint to (3.41), we can see that large-N_c considerations suggest that a massless up quark is unlikely.

3.8 Indirect Phenomenological Results

To continue our attempt to determine Δ_M via phenomenological results, we are forced to draw from evidence beyond the light-meson sector. These results are often introduced to light-meson ChPT in the form of the quantity R, the ratio of the strength of $SU(N_f = 3)$ breaking over the strength of isospin breaking:

$$R \equiv \frac{m_s - \hat{m}}{m_d - m_u} \tag{3.80}$$

Via (3.34), knowledge of R allows for a determination of Δ_M.

Results from other systems tend to give somewhat consistent values for R at leading order. However, consistency in LO results does not preclude large NLO corrections. Additionally, spread in the LO results is significant enough to suggest somewhat sizable NLO corrections, perhaps sizable enough to allow for a massless up quark. Unfortunately, each of the phenomenological results available requires theoretical assumptions in order to tackle their own NLO corrections. Thus, none of them provide a model-free determination of the light-meson sector's NLO corrections.

3.8.1 ψ' Branching Ratios

In the limit of degenerate quarks, the decays:

$$\psi' \to J/\psi + \pi^0 \tag{3.81}$$

$$\psi' \to J/\psi + \eta \tag{3.82}$$

vanish. The first decay is allowed by isospin breaking, while the second is allowed by $SU(N_f = 3)$ breaking. Thus, at leading order the ratio of their amplitudes allows for a measure of R [28]:

$$\frac{T(\psi' \to J/\psi + \pi^0)}{T(\psi' \to J/\psi + \eta)} = \frac{3\sqrt{3}}{4R}(1 + \Delta_{\psi'}) \tag{3.83}$$

where $\Delta_{\psi'}$ represents NLO corrections. Attempts have been made to account for the NLO corrections [29], resulting in the value:

$$R_{\psi'} = 30 \pm 4 \tag{3.84}$$

However, the methods are not direct and various theoretical assumptions are required. In fact doubts have been raised concerning one of the primary assumptions [30].

3.8.2 ρ^0-ω Mixing

In the limit of perfect isospin symmetry, the ω would be a pure isospin singlet. However, isospin is broken and thus the ρ^0 and ω mix. The strength of this mixing allows for a measurement of R based on the decay:

$$\omega \to \pi^+\pi^- \tag{3.85}$$

This results in the value [31]:

$$R_\omega = 41 \pm 4 \tag{3.86}$$

which does not account for NLO corrections to the vector meson masses.

3.8.3 Baryon Masses

At leading order the mass splitting of the baryon octet leads to three independent measurements of R. Corrections out to order $O(m_q^2)$ have been accounted for [32], although theoretical assumptions were required. The nucleon, Σ, and Ξ splittings result in the values:

$$R_N = 51 \pm 10 \tag{3.87}$$

$$R_\Sigma = 43 \pm 4 \tag{3.88}$$

$$R_\Xi = 42 \pm 6 \tag{3.89}$$

respectively.

3.8.4 Accepted Values

L_8 has a generally accepted value, often quoted in reviews and first presented in [17]. This value is based on the R obtained by averaging the baryon mass splitting predictions and the ρ^0-ω mixing prediction:

$$R = 42.6 \pm 2.5 \tag{3.90}$$

where the value used for R_ω is more recent than that used in [17]. This value for R results in:

$$\Delta_M = 0.179 \pm 0.097 \tag{3.91}$$

$$2L_8 - L_5 = \left(1.50 \pm 0.46\right) \times 10^{-3} \tag{3.92}$$

$$L_7 = \left(-0.55 \pm 0.14\right) \times 10^{-3} \qquad L_8 = \left(1.00 \pm 0.33\right) \times 10^{-3} \tag{3.93}$$

$$\frac{m_u}{m_d} = 0.608 \pm 0.056 \tag{3.94}$$

where equations (3.34), (3.35), (3.40), (3.51), and (3.55) have been used. The uncertainty in Δ_M due to NNLO corrections has been assumed to be on the order of Δ_M^2. Because (3.34) is sensitive to the value of Δ_E, use of Dashen's theorem instead of (3.29) results in significantly different values:

$$\Delta_M = -0.022 \pm 0.057 \tag{3.95}$$

$$2L_8 - L_5 = \left(0.55 \pm 0.27\right) \times 10^{-3} \tag{3.96}$$

$$L_7 = \left(-0.31 \pm 0.12\right) \times 10^{-3} \qquad L_8 = \left(0.53 \pm 0.31\right) \times 10^{-3} \tag{3.97}$$

$$\frac{m_u}{m_d} = 0.539 \pm 0.043 \tag{3.98}$$

Any attempts to calculate m_u/m_d through a determination of R will encounter this sensitivity to the poorly understood QED mass contributions to the light meson masses.

A recent comprehensive study of the relevant experimental data can be found in [19]. The analysis culminates in the result:

$$\frac{m_u}{m_d} = 0.46 \pm 0.09 \tag{3.99}$$

Although the analysis of the data is sophisticated, it still requires the use of indirect phenomenological results and various theoretical assumptions in order to determine the strength of $SU(N_f)$ breaking.

All of these results clearly suggest that the up quark is massive. However, the value for R was determined using model-dependent assumptions about NLO corrections to quantities outside the light-meson sector. We then used this value to calculate the NLO correction to the light meson masses. The validity of this process is somewhat questionable.

3.9   First Principles Calculation

The strong consequences of a massless up quark and the importance of the strong CP problem make a first principles calculation of $2L_8 - L_5$, free of model-dependent assumptions, very desirable. Currently the only context in which such a calculation can be attempted is Lattice Quantum Chromodynamics. Lattice QCD allows for a direct and non-perturbative measurement of the Gasser-Leutwyler coefficients, numerically evaluating the underlying QCD dynamics from which they obtain their values.

3.10   Degenerate Quark Masses

As will be discussed in Chapter 5, in the context of a Lattice QCD calculation, we have the freedom to choose the masses of our quarks. For our study, we have chosen to use $N_f = 3$ degenerate light quarks. Thus we present here, assuming $m_q \equiv m_u = m_d = m_s$ and cutting off loops at $\Lambda = 4\pi f$, ChPT's NLO expressions for the chiral pseudo-Goldstone boson mass:

$$\tilde{M}_\pi^2 = zm_q(4\pi f)^2 \left\{ 1 + \frac{zm_q}{N_f} \ln zm_q \right.$$
$$\left. + zm_q\big(2\alpha_8 - \alpha_5\big) + zm_q N_f\big(2\alpha_6 - \alpha_4\big) \right\} \tag{3.100}$$

and decay constant:

$$f_\pi = f\left\{ 1 + \frac{zm_q N_f}{2} \ln zm_q + zm_q \frac{\alpha_5}{2} + zm_q N_f \frac{\alpha_4}{2} \right\} \tag{3.101}$$

where we introduce:

$$z \equiv \frac{2\mu}{(4\pi f)^2} \tag{3.102}$$

and we have made use of the alternative normalization of the GL coefficients. Note that, other than the fact that we have now left N_f unspecified, these expressions follow directly from (3.30) and (3.47).

CHAPTER 4

LATTICE QUANTUM FIELD THEORY

Lattice Quantum Field Theory (LQFT) is a first-principles non-perturbative numerical approach to Euclidean-space quantum field theory.

4.1 Discretization

It begins with the Euclidean-space partition function of a field theory:

$$Z = \int \left(\prod_a [\mathcal{D}\phi_a] \right) e^{-S[\phi_a]} \tag{4.1}$$

where the theory contains some set of fields ϕ_a, and $S[\phi_a]$ is the Euclidean action for a given field configuration $[\phi_a]$. Any physical observable of the theory can be expressed as the expectation value of an operator: the value of the operator evaluated under the distribution defined by the partition function:

$$\langle \mathcal{O} \rangle = Z^{-1} \int \left(\prod_a [\mathcal{D}\phi_a] \right) \mathcal{O}[\phi_a] \, e^{-S[\phi_a]} \tag{4.2}$$

where the operator $\mathcal{O}[\phi_a]$ is some mapping of field configurations into real numbers.

In order to manage the theory numerically, continuous space is replaced by a discrete lattice of points, and the infinite extent of space is made finite and compact. The number of lattice sites along a given direction μ is denoted by L_μ, which in all

cases we will take to be even, while the distance between lattice sites is denoted by a. The theory's fields are attributed values only on the discrete set of locations x_i:

$$\phi_{a;n_i} \equiv \phi_a(x_i)$$

$$n_{i;\mu} \equiv a^{-1}x_{i;\mu} \in \mathbb{Z}^4 \tag{4.3}$$

where each component of n_i is confined to integers in the range $[0, L_\mu - 1]$. Derivatives within $S[\phi_a]$ must also be discretized, (A.17) and (A.18). A single field configuration now contains a finite number of degrees of freedom, and the functional integral is replaced by a finite product of standard integrals:

$$\langle \mathcal{O} \rangle = Z^{-1} \prod_a \prod_i \left(\int_{-\infty}^{\infty} d\phi_{a;n_i} \right) \mathcal{O}[\phi_a] \, e^{-S[\phi_a]} \tag{4.4}$$

where Z has been redefined accordingly. In the limit of a small spacing between the lattice sites, $a \to 0$, and a large lattice extent, $L_\mu \to \infty$, the results of the lattice theory will coincide with the continuum theory.

While our express motivation for discretization is to allow for a numerical approach to quantum field theory, it is worth noting that the discretization procedure is also a valid regularization scheme. The finite lattice spacing results in a Lorentz-variant ultraviolet momentum cutoff at $p_\mu = \pi/a$, removing infinities which arise in a perturbative formulation due to loop corrections. Renormalized physical quantities become functions of the lattice spacing and remain finite in the continuum limit. However, because the regulator breaks Lorentz invariance, it is cumbersome to work with and has a narrow range of practical applications.

While a single field configuration contains a finite number of degrees of freedom, the integral in (4.4) runs over an infinite number of such configurations. Thus, in order to attempt the integral numerically, we must apply Monte Carlo techniques. A finite

sampling of the infinite field-configuration space is generated, where the probability that a given field configuration $[\phi_a]$ is included in the sample is:

$$P\big([\phi_a]\big) \equiv Z^{-1}W[\phi_a]$$

$$= Z^{-1}e^{-S[\phi_a]} \tag{4.5}$$

where $W[\phi_a]$ is the Boltzmann weight of the configuration. Such a set of field configurations is referred to as an ensemble. In the limit of having a large number of configurations in an ensemble, the expectation value of an operator is simply the average of its value evaluated on each configuration in the ensemble:

$$\langle \mathcal{O} \rangle = \frac{1}{N}\sum_n \langle \mathcal{O} \rangle_{[\phi_a]_n} \tag{4.6}$$

where the ensemble contains N configurations and $\langle \mathcal{O} \rangle_{[\phi_a]_n} \equiv \mathcal{O}[\phi_a]_n$ denotes the evaluation of the operator on the fixed field configuration $[\phi_a]_n$, the n-th field configuration of the ensemble.

A given quantum field theory contains some number of fundamental constants. In order to fix these constants in the context of LQFT, an equal number of observables must be calculated. The results of these calculations are then set to experimentally measured values, binding the fundamental constants. From that point on, LQFT is predictive. Any additional calculated observables must match experiment. This procedure is analogous to choosing the renormalization conditions when implementing a continuum regularization scheme.

4.2 Ensemble Creation

Much of the computation time required to numerically implement LQFT is consumed generating the weighted ensemble of field configurations. Thus, identifying efficient algorithm is of paramount importance.

Any algorithm for generating an ensemble with the proper field-configuration distribution will involve the iteration of a two-step update process. This process consists of proposing the addition of a configuration to the ensemble, and then accepting or rejecting that proposal based on an appropriate probability. Such an algorithm will generate the correct ensemble if we insure that the probability of proposing a given configuration times the probability of accepting that configuration results in the correct probability for that configuration's inclusion in the ensemble.

The most straightforward update process involves proposing field configurations generated randomly, with a distribution that is flat relative the measure of the partition function. A configuration $[\phi_a]$ is then accepted into the ensemble with a probability based directly on its Boltzmann weight $W[\phi_a] = e^{-S[\phi_a]}$. If a random number in the range $[0, 1]$ is less than $W[\phi_a]$, the configuration is added to the ensemble.

However, the volume of field-configuration space is quite large, and $W[\phi_a]$ tends to be very sharply peaked at a specific set of field configurations. Thus, while this procedure generates the correct configuration distribution in a straightforward manner, it is very inefficient. Much of the computation time will be spent generating configurations which are subsequently rejected by the acceptance step.

4.2.1 Markov Chains

We require an algorithm which allows us to primarily propose configurations which are in the vicinity of the peak, but which does not skew the probability of each configuration's inclusion in the ensemble.

In order to propose configurations near the peak in $W[\phi_a]$, we will generate our proposal based on the last configuration accepted into the ensemble. The proposal configuration is produced by introducing some change in the previous configuration. The magnitude of that change must be small enough that we do not stray too far from the peak, but large enough that we can hope to sample a substantial volume of configuration space with a reasonably sized ensemble. An ensemble generated using such a chain of configurations, each one spawned from the previous, is known as a Markov chain.

Most algorithms for generating Markov chains satisfy two conditions: ergodicity and detailed balance. While ergodicity is required for any Markov algorithm, detailed balance is sufficient, but not necessary, to insure the creation of the correct configuration distribution.

4.2.2 Ergodicity

As we step along our Markov chain, we must insure that the update algorithm does not restrict us to some subset of field-configuration space. Rather, whatever process we develop for changing the previous configuration and generating a proposal must, given an arbitrary number of iterations, span all of configuration space. This condition on the update process is known as ergodicity.

4.2.3 Detailed Balance

To correctly construct our Markov chain, we must determine the proposal-acceptance probability which leads to our desired distribution. We begin by noting that, once an ensemble has the correct distribution, the configuration densities must be in equilibrium. That is, the correct distribution is a fixed point of the update process. Therefore, for such an ensemble, the probability of adding field configuration $[\phi_a]_B$ to the ensemble, given that configuration $[\phi_a]_A$ was the previous configuration accepted, must be equal to the probability of adding field configuration $[\phi_a]_A$ to the ensemble, given that $[\phi_a]_B$ was the previous configuration accepted:

$$P\big([\phi_a]_A \to [\phi_a]_B\big) = P\big([\phi_a]_B \to [\phi_a]_A\big) \tag{4.7}$$

This condition is known as detailed balance.

Three distinct factors combine to determine $P\big([\phi_a]_A \to [\phi_a]_B\big)$: the probability of $[\phi_a]_A$ being the previous configuration accepted into the ensemble $P_W\big([\phi_a]_A\big)$; the probability of proposing $[\phi_a]_B$, given that $[\phi_a]_A$ was the previous configuration $P_P\big([\phi_a]_A \to [\phi_a]_B\big)$; and the probability of accepting $[\phi_a]_B$, given that $[\phi_a]_A$ was the previous configuration $P_A\big([\phi_a]_A \to [\phi_a]_B\big)$:

$$P\big([\phi_a]_A \to [\phi_a]_B\big) = P_W\big([\phi_a]_A\big)P_P\big([\phi_a]_A \to [\phi_a]_B\big)P_A\big([\phi_a]_A \to [\phi_a]_B\big) \tag{4.8}$$

Equilibrium dictates that:

$$P_W\big([\phi_a]_A\big)P_P\big([\phi_a]_A \to [\phi_a]_B\big)P_A\big([\phi_a]_A \to [\phi_a]_B\big)$$
$$= P_W\big([\phi_a]_B\big)P_P\big([\phi_a]_B \to [\phi_a]_A\big)P_A\big([\phi_a]_B \to [\phi_a]_A\big) \tag{4.9}$$

If we require that the equilibrium point corresponds to an ensemble with our desired configuration distribution, then the probability of a configuration being the

55

latest configuration accepted is proportional to its Boltzmann weight:

$$P_W([\phi_a]_A) = Z^{-1}W[\phi_a]_A \qquad\qquad P_W([\phi_a]_B) = Z^{-1}W[\phi_a]_B \qquad (4.10)$$

We have said very little about the process which generates a proposal configuration from the previous configuration. However, placing a simple condition on it will allow us to determine the acceptance probability. We require that the probability of making any given change is equal to the probability of making the reverse change:

$$P_P([\phi_a]_A \to [\phi_a]_B) = P_P([\phi_a]_B \to [\phi_a]_A) \qquad (4.11)$$

Bound by such a condition, we can easily see that an appropriate acceptance probability would be:

$$
\begin{aligned}
P_A([\phi_a]_A \to [\phi_a]_B) &= \min\left\{1, \frac{W[\phi_a]_B}{W[\phi_a]_A}\right\} \\
&= \min\left\{1, e^{S[\phi_a]_A - S[\phi_a]_B}\right\} \qquad (4.12)
\end{aligned}
$$

If the proposed configuration has a larger Boltzmann weight than the previous configuration, it is always accepted into the ensemble. If it has a smaller weight than the previous configuration, it is accepted with a probability based on the change in the action.

Such a Markov process, which accepts or rejects a proposal configuration with a probability based on its difference in weight from the previous configuration, is known as a Metropolis algorithm.

4.2.4 Autocorrelation Length

Because each new configuration is generated by making changes to the previously accepted configuration, any given configuration in a Markov chain will have similarities to the configurations which come before it. This correlation between ensembles along a Markov chain is known as autocorrelation.

Due to autocorrelation, a single update step does not sample configuration space with the correct weight. Instead, a number of update steps must be performed in order to generate only a single independent and correctly weighted sample of configuration space. The length that must be moved along a Markov chain in order to go from one independent configuration to the next is known as the autocorrelation length.

We can estimate the autocorrelation length by choosing some observable and watching its evolution as we evaluate it on individual configurations along the Markov chain. The observable will experience fluctuations whose frequency can be taken to suggest the order of the autocorrelation length. Clearly, the perceived autocorrelation length will depend heavily on the observable chosen. Because two configurations are only truly decorrelated after an infinite number of update steps, any estimation of autocorrelation length will always involve a somewhat arbitrary cutoff decision.

Reducing the autocorrelation length is desirable, as it allows us to sample a larger region of configuration space using a shorter Markov chain. The autocorrelation length can be reduced by increasing the magnitude of the changes made when generating a proposal configuration. However, such gains can be offset by a reduction in the acceptance rate.

4.2.5 Acceptance Rate

In order to minimize the computation time spent generating configurations which ultimately go unused, the acceptance rate of a Markov chain process must be kept reasonably large. This can be done by reducing the magnitude of the changes which are made when generating a proposal configuration, and thus reducing the chances of straying significantly from the peak in $W[\phi_a]$. However, as discussed above, such a reduction causes a corresponding increase in the autocorrelation length. Thus, the optimal magnitude of the update step can be elusive, but is generally one which results in an acceptance rate of approximately 50%.

In order to retain a reasonable acceptance rate, but still allow large changes in the proposal configuration, update methods which move through configuration space along, or nearly along, lines of constant action can be used. Minimizing the change in action increases the acceptance rate without ruining detailed balance, and conversely allows for larger update steps. By interspersing such constant-action update steps with standard update steps, ergodicity is retained.

4.2.6 Thermalization

When beginning a Markov chain, one must choose an initial field configuration. Because this choice for the head of the chain is arbitrary, and not chosen by the Markov process itself, that first configuration, and any configurations which are correlated with it, will not have the correct distribution. Thus, the ensemble will only obtain the correct distribution in the limit of an infinitely large ensemble, when the effects of the earliest configurations have washed out.

This process of decorrelation from the initial configuration is known as thermalization. The number of update steps required by thermalization is obviously closely related to an ensemble's autocorrelation length. Since we can only work with finite ensembles, configurations generated before the Markov chain is thermalized will be dropped from the ensemble. We refer to the point on the Markov chain at which we first begin to retain configurations as the thermalization point, with N_T denoting the number of configurations dropped. Unfortunately, an estimation of the thermalization point involves the same uncertainties and arbitrariness as an estimation of the autocorrelation length.

4.3 Two-Point Correlation Functions

A particularly useful observable in LQFT is the two-point correlation function:

$$C(x) \equiv \langle \mathcal{O}(x)\mathcal{O}(0)\rangle \tag{4.13}$$

where the operator $\mathcal{O}(x)$ is some function of the fields local to x and corresponds to a set of values for the theory's quantum numbers. The Euclidean-space two-point correlation function is analogous to the two-point Green's function of Minkowski space. $\mathcal{O}(x)$ creates or annihilates at x every eigenstate of the theory with matching quantum numbers, each with an amplitude that is dependent upon the operator's exact form. Thus, the correlation function gives the amplitude for creating that tower of states at the origin, having them propagate to x, and then annihilating them.

The Euclidean-space states of a quantum field theory are defined to be the eigenstates of the time component of the translation operator, also known as the transfer matrix. These states decay exponentially with time, each picking up a factor equal

to its eigenvalue e^{-Et} after propagating a distance t in time, where E is the state's energy. This corresponds directly to the phase oscillation of a Minkowski-space state with a frequency proportional to its energy. Knowing this factor, the tower of states created by $\mathcal{O}(x)$ can be made explicit:

$$C(\vec{x} = \vec{0}, t) = \sum_n \frac{1}{2E_n V} \langle 0|\mathcal{O}|n\rangle \langle n|\mathcal{O}|0\rangle \, e^{-E_n t} \tag{4.14}$$

where the sum is over all states with appropriate quantum numbers, both single- and multi-particle, and $\langle n|\mathcal{O}|0\rangle$ represents the amplitude for the operator $\mathcal{O}(x)$ creating the state $|n\rangle$ from the vacuum. The factor $(2E_n V)^{-1}$ comes from a relativistic normalization of the states, where V is the spatial volume of a time slice.

Because $\mathcal{O}(x)$ is local in space, the tower of created states includes states of all momenta. We can restrict the states created to those with a specific momentum $\vec{p}$ by Fourier transforming the annihilation operator:

$$\mathcal{O}(\vec{p}, t) = \sum_{\vec{x}} e^{-i\vec{p}\cdot\vec{x}} \mathcal{O}(\vec{x}, t) \tag{4.15}$$

Choosing only states with zero total momentum, we simply sum over all spatial positions of a time slice:

$$\mathcal{O}(\vec{p} = \vec{0}, t) = \sum_{\vec{x}} \mathcal{O}(\vec{x}, t) \tag{4.16}$$

At zero momentum the energy E_n of a state is reduced to its mass M_n. Thus, using a zero-momentum annihilation operator, the correlation function becomes:

$$C(t) \equiv C(\vec{p} = \vec{0}, t) = \left\langle \sum_{\vec{x}} \mathcal{O}(\vec{x}, t)\mathcal{O}(\vec{0}, 0) \right\rangle$$
$$= \sum_n \frac{1}{2M_n} |\langle n|\mathcal{O}|0\rangle|^2 e^{-M_n t} \tag{4.17}$$

where the sum is now only over zero-momentum states, and the sum over $\vec{x}$ has canceled with the factor of V^{-1}. Note that restricting the annihilation operator to

60

zero momentum is sufficient. There is no need to Fourier transform the creation operator.

If the creation and annihilation points are well separated in time, and assuming that there is an energy gap between the lightest and second-lightest states, all states will be exponentially damped relative to the lowest energy state $|1\rangle$. Thus:

$$\lim_{t\to\infty} C(t) = \frac{1}{2M_1}|\langle 1|\mathcal{O}|0\rangle|^2 e^{-M_1 t} \tag{4.18}$$

At this point the correlation function has been expressed in terms of only two unknowns: the operator's overlap with the lightest state $\langle 1|\mathcal{O}|0\rangle$ and the mass of that state M_1.

Using the techniques of LQFT, we can numerically calculate, for a given set of quantum numbers, the two-point correlation function $C(t)$ at large time separations. Then, analyzing the t dependence of our result, we can extract the creation amplitude and mass of the lowest energy state. By repeating this process for all appropriate combinations of quantum numbers, LQFT allows us to non-perturbatively calculate from first principles the low-energy spectrum of a quantum field theory.

CHAPTER 5

LATTICE QUANTUM CHROMODYNAMICS

The study of QCD using the techniques of LQFT is known as Lattice Quantum Chromodynamics (LQCD).

5.1 Gluon Fields

We first describe the discretization of gluon fields.

5.1.1 Gauge Discretization

Many of the symmetries of a quantum field theory, the most significant of which is Poincaré symmetry, are lost during discretization and are only regained in the continuum limit. Because local $SU(N_c)$ gauge symmetry is the defining symmetry of QCD, the discretization process for the gluon fields will focus on preserving this symmetry at non-zero lattice spacing.

The gluon fields act as a parallel transporter, describing the color transformation of the quarks as they move through space. A color vector moving through some path C picks up a unitary rotation U_C:

$$U_C = \mathcal{P} \exp\left(ig \int_C dx A_\mu(x) \right) \tag{5.1}$$

where $\mathcal{P}$ denotes path-ordering within the exponentiated integral. In order to retain gauge symmetry at non-zero lattice spacing, and to preserve the parallel-transporting nature of the gluon fields, we choose to work, not with the gluon fields A_μ themselves, but instead with unitary color-transformation matrices which we assign to the links connecting neighboring lattice sites. These matrices transport a color vector from one lattice site to the next, and thus are defined using (5.1), where the path C is now the straight line linking neighboring sites:

$$U_{\mu;n} \equiv \mathcal{P} \exp\left(ig \int_x^{x+a\hat{\mu}} dx' A_\mu(x') \right) \tag{5.2}$$

where $U_{\mu;n}$ denotes the matrix which transports a vector from the site at x to the site at $x + a\hat{\mu}$, and $\hat{\mu}$ denotes a unit vector in the direction μ. Correspondingly, $U_{\mu;n-\hat{\mu}}^\dagger$ is the matrix which transports a vector from x to $x - a\hat{\mu}$. Recall that the four-vector n has been defined such that its elements are integers at the lattice sites:

$$n_\mu \equiv a^{-1} x_\mu \tag{5.3}$$

At lowest order in a, $U_{\mu;n}$ can be expressed in terms of only the parallel component of the gauge field at a point halfway along the relevant link:

$$U_{\mu;n} = \exp\left(iag A_\mu(x + \tfrac{a}{2}\hat{\mu}) + \cdots \right) \tag{5.4}$$

Using link matrices $U_{\mu;n}$ to describe our gauge fields allows for the preservation of a discretized local color symmetry. The associated gauge transformation is:

$$U_{\mu;n} \quad \rightarrow \quad U'_{\mu;n} = \Omega_{n+\hat{\mu}} U_{\mu;n} \Omega_n^\dagger \tag{5.5}$$

$$\Omega_n \in SU(N_c) \tag{5.6}$$

where Ω_n is ascribed values only on the lattice sites.

5.1.2 Gauge Action

It is clear that, under the gauge transformation described in (5.5), any closed loop of link matrices will be invariant. The simplest of such loops is a square with sides one link in length. This loop in known as the plaquette:

$$P_{\mu\nu;n} \equiv W^{1\times 1}_{\mu\nu;n} = U^\dagger_{\nu;n} U^\dagger_{\mu;n+\hat\nu} U_{\nu;n+\hat\mu} U_{\mu;n} \tag{5.7}$$

Expressing the plaquette in terms of the gluon field and expanding around its center:

$$
\begin{aligned}
P_{\mu\nu;x} &= e^{-a\mathcal{A}_\nu(x+\frac{\bar\nu}{2})} e^{-a\mathcal{A}_\mu(x+\bar\nu+\frac{\bar\mu}{2})} e^{a\mathcal{A}_\nu(x+\bar\mu+\frac{\bar\nu}{2})} e^{a\mathcal{A}_\mu(x+\frac{\bar\mu}{2})} + \cdots \\
&= e^{-a\mathcal{A}_\nu(x+\frac{\bar\nu}{2})} e^{-a\mathcal{A}_\mu(x+\frac{\bar\mu}{2})-a^2\Delta_\nu\mathcal{A}_\mu(x+\frac{\bar\mu}{2}+\frac{\bar\nu}{2})} \\
&\qquad \times e^{a\mathcal{A}_\nu(x+\frac{\bar\nu}{2})+a^2\Delta_\mu\mathcal{A}_\nu(x+\frac{\bar\nu}{2}+\frac{\bar\mu}{2})} e^{a\mathcal{A}_\mu(x+\frac{\bar\mu}{2})} + \cdots \\
&= e^{-a\mathcal{A}_\nu(x+\frac{\bar\nu}{2})-a\mathcal{A}_\mu(x+\frac{\bar\mu}{2})-a^2\Delta_\nu\mathcal{A}_\mu(x+\frac{\bar\mu}{2}+\frac{\bar\nu}{2})+\frac{a^2}{2}\left[\mathcal{A}_\nu(x+\frac{\bar\nu}{2}),\mathcal{A}_\mu(x+\frac{\bar\mu}{2})\right]} \\
&\qquad \times e^{a\mathcal{A}_\nu(x+\frac{\bar\nu}{2})+a^2\Delta_\mu\mathcal{A}_\nu(x+\frac{\bar\nu}{2}+\frac{\bar\mu}{2})+a\mathcal{A}_\mu(x+\frac{\bar\mu}{2})+\frac{a^2}{2}\left[\mathcal{A}_\nu(x+\frac{\bar\nu}{2}),\mathcal{A}_\mu(x+\frac{\bar\mu}{2})\right]} + \cdots \\
&= e^{a^2\left(\Delta_\mu\mathcal{A}_\nu(x+\frac{\bar\mu}{2}+\frac{\bar\nu}{2})-\Delta_\nu\mathcal{A}_\mu(x+\frac{\bar\mu}{2}+\frac{\bar\nu}{2})-\left[\mathcal{A}_\mu(x+\frac{\bar\mu}{2}),\mathcal{A}_\nu(x+\frac{\bar\nu}{2})\right]\right)} + \cdots \\
&= e^{a^2\left(\Delta_\mu\mathcal{A}_\nu(x+\frac{\bar\mu}{2}+\frac{\bar\nu}{2})-\Delta_\nu\mathcal{A}_\mu(x+\frac{\bar\mu}{2}+\frac{\bar\nu}{2})-\left[\mathcal{A}_\mu(x+\frac{\bar\mu}{2}+\frac{\bar\nu}{2}),\mathcal{A}_\nu(x+\frac{\bar\mu}{2}+\frac{\bar\nu}{2})\right]\right)} + \cdots \\
&= e^{ia^2 g F_{\mu\nu}(x+\frac{\bar\mu}{2}+\frac{\bar\nu}{2})} + \cdots \\
&= \mathbb{1} + ia^2 g F_{\mu\nu}(x + \tfrac{a}{2}\hat\mu + \tfrac{a}{2}\hat\nu) - \frac{a^4 g^2}{2}\left(F_{\mu\nu}(x + \tfrac{a}{2}\hat\mu + \tfrac{a}{2}\hat\nu)\right)^2 + \cdots \tag{5.8}
\end{aligned}
$$

where $\mathcal{A}_\mu(x) \equiv ig A_\mu(x)$, $\bar\mu \equiv a\hat\mu$, the matrix identity:

$$e^{\mathcal{A}} e^{\mathcal{B}} = e^{\mathcal{A}+\mathcal{B}+\frac{1}{2}[\mathcal{A},\mathcal{B}]} + \cdots \tag{5.9}$$

has been used, and terms higher order in a have been dropped at each step. Thus, at lowest order in a, the real trace of the plaquette gives us access to the gauge field strength at its center:

$$\mathrm{Re\,tr}\left[\mathbb{1} - P_{\mu\nu;n}\right] = \frac{a^4 g^2}{2}\,\mathrm{tr}\left[\left(F_{\mu\nu}(x + \tfrac{a}{2}\hat\mu + \tfrac{a}{2}\hat\nu)\right)^2\right] + O(a^6) \tag{5.10}$$

We are now able to assemble an action which is dependent only on the degrees of freedom which remain in our gluon field after discretization, and equals the continuum action at lowest order in a. Using $\int_x \to a^4 \sum_n$:

$$S_g[U] = \int_x \frac{1}{2} \mathrm{tr}\left[F_{\mu\nu}(x)F^{\mu\nu}(x)\right] \quad \to$$

$$a^4 \sum_n \frac{1}{2} \mathrm{tr}\left[F_{\mu\nu}(an + \tfrac{a}{2}\hat{\mu} + \tfrac{a}{2}\hat{\nu})F^{\mu\nu}(an + \tfrac{a}{2}\hat{\mu} + \tfrac{a}{2}\hat{\nu})\right]$$

$$= a^4 \sum_n \sum_\mu \sum_{\nu<\mu} \mathrm{tr}\left[\left(F_{\mu\nu}(an + \tfrac{a}{2}\hat{\mu} + \tfrac{a}{2}\hat{\nu})\right)^2\right]$$

$$= \frac{2}{g^2} \sum_n \sum_\mu \sum_{\nu<\mu} \mathrm{Re}\,\mathrm{tr}\left[\mathbb{1} - P_{\mu\nu;n}\right] + O(a^2) \tag{5.11}$$

Finally:

$$S_g[U] = \beta \sum_n \sum_\mu \sum_{\nu<\mu} \frac{1}{N_c} \mathrm{Re}\,\mathrm{tr}\left[\mathbb{1} - P_{\mu\nu;n}\right] \tag{5.12}$$

$$\beta \equiv \frac{2N_c}{g^2} \tag{5.13}$$

Because the action is constructed only of closed gauge-link loops, we can be sure that gauge symmetry has been preserved.

5.1.3 Gauge Coupling

It is evident from (5.12) that, for any lattice calculation which includes only gauge fields, there is only one free parameter in the action, the strong coupling constant g. We might expect the lattice space a to also appear in the action, but in fact it does not. This is because the lattice spacing is not a physical parameter, but rather must be thought of as a momentum cutoff for our quantum field theory. Thus, the action should depend on our cutoff a only through the renormalization-scale dependence of the true parameters of the action.

We see then that the strong coupling constant and the lattice spacing are not independently free parameters. Once β is chosen for a pure-gauge lattice calculation, both g and a are fixed, related by the strong coupling's renormalization group equation. It is this dependence of the strong coupling on the lattice spacing which allows us to conceptualize a continuum limit, and which distinguishes a LQFT calculation from a standard statistical mechanics system.

In more concrete terms, when doing such a lattice calculation, we first choose a value for β. Then we calculate some dimensionful physical observable whose value has been determined experimentally. The units in our lattice calculation of the observable will appear as powers of a. Thus, by setting our calculated value equal to the experimentally measured value, the lattice spacing is fixed. This procedure corresponds directly to the application of a renormalization condition in continuum field theory.

5.1.4 Gauge Updates

The gauge action (5.12) has the very convenient property of locality. That is, any given field degree of freedom couples directly only to other degrees of freedom in close spatial vicinity. Thus, calculating the shift in action due to some change in the field variables requires only information local to that change, and Markov-chain update steps can be made with relatively little computational effort.

In the case of a pure gauge calculation, the update step would involve making a change to an individual link in such a manner as to preserve detailed balance. Only the plaquettes that contain the changed link need to be recalculated in order to determine the shift in the action. The update is then accepted or rejected based on

the size of that shift. By doing a number of these individual updates to each link in the lattice, we can quickly generate a new configuration to add to the Markov chain.

Unfortunately, the introduction of quarks to our lattice calculation will destroy locality, significantly increasing the computation time required for an update.

5.2 Quark Fields

We will now bring quarks into our lattice theory. The process will be complicated significantly by the fact that they are Dirac spinors, and that the Dirac action is linear in momentum.

5.2.1 Fermion Discretization

First we define a discretized quark field, attributing it values only on the lattice sites:

$$q_n \equiv a^{3/2} q(x) \qquad\qquad \bar{q}_n \equiv a^{3/2} \bar{q}(x) \qquad\qquad (5.14)$$

The powers of a which appear in the definition cancel units contained by the continuum quark field, making the discretized field suitable for use in numerical calculations.

To construct a lattice quark action, we must first discretize the covariant derivative:

$$
\begin{aligned}
D_\mu q(x) &= \partial_\mu q(x) - ig A_\mu(x) q(x) \\
&= \frac{1}{2a}\Big[q(x+\hat{\mu}) - q(x-\hat{\mu}) \Big] \\
&\quad - \frac{ig}{2}\Big[A_\mu(x+\tfrac{\bar{\mu}}{2}) q(x+\hat{\mu}) + A_\mu(x-\tfrac{\bar{\mu}}{2}) q(x-\hat{\mu}) \Big] + \cdots \\
&= \frac{1}{2a}\Big\{ \Big[1 - ig a A_\mu(x+\tfrac{\bar{\mu}}{2}) \Big] q(x+\hat{\mu}) \\
&\quad - \Big[1 + ig a A_\mu(x-\tfrac{\bar{\mu}}{2}) \Big] q(x-\hat{\mu}) \Big\} + \cdots \\
&= \frac{1}{2a^{5/2}}\Big[U^\dagger_{\mu;n} q_{n+\hat{\mu}} - U_{\mu;n-\hat{\mu}} q_{n-\hat{\mu}} \Big] + \cdots
\end{aligned}
\tag{5.15}
$$

Note that in order to calculate the finite difference at site n, the value of the quark field at neighboring sites is first parallel transported to n via the appropriate gauge link matrices. In this way the quark-gluon interaction manifests in our lattice theory.

5.2.2 Fermion Action

The quark action can now be discretized:

$$
\begin{aligned}
S_q^N[U, q, \bar{q}] &= \int_x \bar{q}(x) \big(\gamma^\mu D_\mu + \mathcal{M} \big) q(x) \quad \rightarrow \\
&\quad a^4 \sum_n \frac{1}{a^4} \Big\{ \frac{1}{2} \sum_\mu \bar{q}_n \gamma_\mu \Big[U^\dagger_{\mu;n} q_{n+\hat{\mu}} - U_{\mu;n-\hat{\mu}} q_{n-\hat{\mu}} \Big] + a \bar{q}_n \mathcal{M} q_n \Big\} \\
&= \sum_n \sum_m \bar{q}_n M^N_{n,m}[U] q_m
\end{aligned}
\tag{5.16}
$$

where, if we assume degenerate quarks, the interaction matrix $M[U] = M^N[U]$ is:

$$
\begin{aligned}
M^N_{n,m}[U] &\equiv \frac{1}{2} \sum_\mu \gamma_\mu \Big[U^\dagger_{\mu;n} \delta_{n,m-\hat{\mu}} - U_{\mu;n-\hat{\mu}} \delta_{n,m+\hat{\mu}} \Big] + m_Q \delta_{n,m} \\
&= D^N_{n,m}[U] + m_Q \delta_{n,m}
\end{aligned}
\tag{5.17}
$$

Note that the action includes an implied sum over color, spin, and flavor indices and that $M_{n,m}[U]$ is a matrix in those three indices, as well as in position. We represent the

kinetic term of $M_{n,m}[U]$ using $D_{n,m}[U]$. The lattice quark mass m_Q absorbs one power of a and becomes a unitless parameter, suitable for use in a numerical calculation. It is related to the dimensionful quark mass by:

$$m_Q = \breve{m}_q \equiv a m_q \tag{5.18}$$

Now including both quarks and gluons in our LQCD action, $S'_{\text{LQCD}}[U, q, \bar{q}] = S_g[U] + S_q[U, q, \bar{q}]$, our partition function is:

$$Z_{\text{LQCD}} = \int [\mathcal{D}U][\mathcal{D}q][\mathcal{D}\bar{q}] \; e^{-S_g[U]} \; e^{-\sum_{nm} \bar{q}_n M_{n,m}[U] q_m} \tag{5.19}$$

As a fermion, the quark field is expressed in terms of Grassmann numbers. Because there is no simple way to numerically account for the anticommutating property of Grassmann numbers, we will integrate out the quark degrees of freedom analytically. The result is the determinant of the interaction matrix:

$$\begin{aligned} Z_{\text{LQCD}} &= \int [\mathcal{D}U] \; e^{-S_g[U]} \; \det M[U] \\ &= \int [\mathcal{D}U] \; e^{-S_{\text{LQCD}}[U]} \end{aligned} \tag{5.20}$$

where

$$\begin{aligned} S_{\text{LQCD}}[U] &= S_g[U] - \ln \det M[U] \\ &= S_g[U] - \text{Tr} \ln M[U] \end{aligned} \tag{5.21}$$

This determinant, or trace, is over all indices of $M[U]$. In the case of $M^N[U]$, it is over color, spin, flavor, and position indices. Note that if the interaction matrix is diagonal in flavor space, as is true for $M^N[U]$, the determinant can be factored into a product of distinct flavor determinants.

69

5.2.3 Color Symmetry

The full LQCD action continues to have local color symmetry at non-zero lattice spacing:

$$q_n \quad \rightarrow \quad q'_n = \Omega_n q_n \tag{5.22}$$

$$\bar{q}_n \quad \rightarrow \quad \bar{q}'_n = \bar{q}_n \Omega_n^\dagger \tag{5.23}$$

$$U_{\mu;n} \quad \rightarrow \quad U'_{\mu;n} = \Omega_{n+\hat{\mu}} U_{\mu;n} \Omega_n^\dagger \tag{5.24}$$

$$\Omega_n \in SU(N_c) \tag{5.25}$$

5.2.4 Quark Propagators

In order to calculate a quark-antiquark correlator, we again must first analytically integrate over the fermion degrees of freedom. Via the integration, the quark and antiquark insertions generate an inverse of the interaction matrix:

$$
\begin{aligned}
\langle \bar{q}_{a\alpha i;n} q_{b\beta j;m} \rangle &= Z_{\mathrm{LQCD}}^{-1} \int [\mathcal{D}U][\mathcal{D}q][\mathcal{D}\bar{q}] \; e^{-S'_{\mathrm{LQCD}}[U,q,\bar{q}]} \; \bar{q}_{a\alpha i;n} \; q_{b\beta j;m} \\
&= Z_{\mathrm{LQCD}}^{-1} \int [\mathcal{D}U] \; e^{-S_{\mathrm{LQCD}}[U]} \; M[U]_{a\alpha in, b\beta jm}^{-1} \\
&= Z_{\mathrm{LQCD}}^{-1} \int [\mathcal{D}U] \; e^{-S_g[U]} \; \det M[U] \; M[U]_{a\alpha in, b\beta jm}^{-1} \tag{5.26}
\end{aligned}
$$

where the correlator's color, spin, flavor, and position indices respectively are shown explicitly. We see that $M[U]^{-1}$ is acting as the quark propagator.

Because the interaction matrix is constructed to take quarks into antiquarks, its transpose appears as the antiquark propagator:

$$
\begin{aligned}
&\langle q_{a\alpha i;n} \bar{q}_{b\beta j;m} \rangle \\
&\qquad = Z_{\mathrm{LQCD}}^{-1} \int [\mathcal{D}U] \; e^{-S_g[U]} \; \det M[U] \; (M[U]^T)_{a\alpha in, b\beta jm}^{-1} \tag{5.27}
\end{aligned}
$$

Inspection of the adjoint of the interaction matrix allows us to express the antiquark propagator in terms of the quark propagator:

$$
\begin{aligned}
M^N[U]^\dagger_{n,m} &= \frac{1}{2}\sum_\mu \gamma_\mu \Big[U_{\mu;m}\delta_{m,n-\hat\mu} - U^\dagger_{\mu;m-\hat\mu}\delta_{m,n+\hat\mu} \Big] + m_Q\delta_{m,n} \\
&= \frac{1}{2}\sum_\mu (-\gamma_\mu)\Big[U^\dagger_{\mu;m-\hat\mu}\delta_{m,n+\hat\mu} - U_{\mu;m}\delta_{m,n-\hat\mu} \Big] + m_Q\delta_{n,m} \\
&= \gamma_5 \left\{ \frac{1}{2}\sum_\mu \gamma_\mu \Big[U^\dagger_{\mu;n}\delta_{n,m-\hat\mu} - U_{\mu;n-\hat\mu}\delta_{n,m+\hat\mu} \Big] + m_Q\delta_{n,m} \right\} \gamma_5 \\
&= \gamma_5 M^N_{n,m}[U]\gamma_5
\end{aligned}
\tag{5.28}
$$

Thus, for this interaction matrix:

$$
\begin{aligned}
&\langle q_{a\alpha i;n}\bar q_{b\beta j;m}\rangle \\
&\quad = Z^{-1}_{\mathrm{LQCD}}\int [\mathcal{D}U]\, e^{-S_g[U]}\,\det M[U]\,\Big(\gamma_5 M^N[U]^{-1}\gamma_5\Big)^*_{a\alpha in,b\beta jm}
\end{aligned}
\tag{5.29}
$$

Note that γ_5 is its own inverse.

While it is instructive to consider the calculation of a quark-antiquark correlator due to its simplicity, it is worth noting that, because it is not a gauge-invariant quantity, its expectation value on each configuration includes a random phase and thus equals zero after the ensemble average. Quark operators with a non-zero expectation value are more complex than the simple two-point quark correlator. Using Wick contractions, operators with four or more quark insertions can be reduced to a sum of products of quark and antiquark propagators. If the operator is such that these products of propagators form closed loops, their expectation value with be gauge invariant and potentially non-zero.

5.2.5 Quenched Approximation

The quark fields have introduced the determinant of their interaction matrix into the Boltzmann weight. From the perspective of the gauge fields, this determinant acts as a non-local interaction, coupling each link to every other link in the lattice. While it is still possible to account for this complicated Boltzmann weight in our Markov process, the computation time required will be significantly increased.

In order to avoid this increase, and to return to the simplicity of the pure gauge action, an approximation is often made within the partition function known as the quenched approximation. The quenched approximation assumes that:

$$\det M[U] \propto e^{-S_g} \tag{5.30}$$

Thus, the determinant can be accounted for by a simple shift in β, and the partition function reverts to that for pure gauge. Calculation of a quark-antiquark correlator under the quenched approximation amounts to the expression:

$$\langle \bar{q}_{a\alpha i;n} q_{b\beta j;m} \rangle = Z_{\mathrm{qQCD}}^{-1} \int [\mathcal{D}U] \, e^{-S_g[U]} \, M[U]_{a\alpha in,b\beta jm}^{-1} \tag{5.31}$$

where Z_{qQCD} is appropriately defined.

While the quenched partition function does not correspond to any well-defined unitary field theory, the resulting system of interactions is often referred to as quenched QCD (qQCD).

From the perspective of perturbation theory, removal of the interaction matrix determinant from the QCD partition function corresponds to the removal of quark loops from Feynman diagrams.

5.2.6 Partially Quenched Approximation

Even when the interaction-matrix determinant is included in the Boltzmann weight during a Markov process, a second approximation known as the partially quenched approximation is often made.

The partially quenched approximation arises from the fact that the quark interaction matrix is a function of the quark mass, $M_{(m_Q)}[U]$. Thus, if we wish to calculate the expectation value of an operator at a variety of quark masses, we must generate a separate ensemble for each quark mass. However, the creation of a Markov chain is computationally expensive, much more so than the calculation of a quark propagator under that Markov chain.

In the partially quenched approximation we generate only a single Markov chain using a single quark mass known as the sea, or dynamical, quark mass m_S. Observables, such as a quark propagator, are then calculated under that ensemble using a number of different quark mass values. The quark mass used in the observable is known as the valence quark mass m_V. Partial quenching is thus an approximation of the interaction-matrix determinant at the valence quark mass by that determinant evaluated at the dynamical quark mass.

Calculation of a quark-antiquark correlator under the partially quenched approximation amounts to the expression:

$$\langle \bar{q}_{a\alpha i;n} q_{b\beta j;m} \rangle$$
$$= Z_{\mathrm{pqQCD}}^{-1} \int [\mathcal{D}U]\; e^{-S_g[U]}\; \det M_{(m_S)}[U]\; M_{(m_V)}[U]^{-1}_{a\alpha in, b\beta jm} \tag{5.32}$$

where Z_{pqQCD} is appropriately defined.

In a similar fashion to quenching, partial quenching does not result in a unitary field theory. Nonetheless, the system of interactions which results from partial quenching is referred to as partially quenched QCD (pqQCD).

From the perspective of partial quenching, qQCD is the special case of pqQCD in which the dynamical quark mass is taken to infinity. The mass term in the quark action $S_q[U, q, \bar{q}]$ dominates, and the dynamical quarks decouple from the gauge fields, affecting the partition function only as an irrelevant constant factor.

Here we have presented pqQCD as a convenient approximation of full QCD. However, we will find that extensions to the concepts behind ChPT will take partial quenching beyond a mere approximation, allowing us to calculate physical results incalculable within unquenched QCD.

5.2.7 Fermion Doubling Problem

In order to determine the particles contained in our discretized quark action, we must identify the zeros of the momentum-space action.

Introducing the momentum-space quark fields:

$$q_n = \int_k e^{iak \cdot n} q(k) \qquad\qquad \bar{q}_n = \int_k e^{iak \cdot n} \bar{q}(k) \qquad (5.33)$$

allows for a Fourier transformation of the free-field action:

$$\begin{aligned}
S_q^N[\mathbb{1}, q, \bar{q}] &= \sum_n \left\{ \frac{1}{2} \sum_\mu \bar{q}_n \gamma_\mu \left[q_{n+\hat{\mu}} - q_{n-\hat{\mu}} \right] + m_Q \bar{q}_n q_n \right\} \\
&= \int_k \left\{ \frac{1}{2} \sum_\mu \bar{q}(k) \gamma_\mu \left[e^{iak_\mu} - e^{-iak_\mu} \right] q(k) + m_Q \bar{q}(k) q(k) \right\} \\
&= \int_k \bar{q}(k) M_{(k)}^N[\mathbb{1}] q(k) \qquad (5.34)
\end{aligned}$$

where:

$$M^N_{(k)}[\mathbb{1}] = i\sum_\mu \gamma_\mu \sin ak_\mu + m_Q \tag{5.35}$$

As in the continuum case, the free-field action is diagonal in momentum space.

For the remainder of this section, we will assume $m_Q = 0$.

Using an infinitely large lattice volume has resulted in a continuous momentum space. However, our discretization of position space has resulted in an action which is periodic with respect to momentum. Additionally, momentum space itself is periodic, with each component confined to a Brillouin zone of length $2\pi a^{-1}$. We choose the range of allowed momenta to be $-{}^\pi/_{2a} < k_\mu \leq {}^{3\pi}/_{2a}$, such that the maxima of the action occur on the limits of the Brillouin zone.

Each zero of the momentum-space action corresponds to a pole in the propagator, and thus a particle of the theory. We expect one particle, the particle corresponding to the zero at $k = 0$. However, the periodicity of the action results in fifteen additional zeros, generating fifteen additional species of quarks. This unexpected proliferation of quark species is known as the fermion doubling problem.

The fermion doubling problem is a direct consequence of the linear nature of the Dirac action. Had the action been quadratic, as is the case for scalar fields, the additional zeros would have been pushed beyond the Brillouin zone.

Any of these additional quark species can be shifted to the origin via the redefinition:

$$k_\mu \quad \rightarrow \quad k'_\mu = k_\mu + A_\mu \frac{\pi}{a} \tag{5.36}$$

where A is one of sixteen possible binary four-vectors, each of which corresponds to a single quark species. We define a binary vector to be a vector whose components

take on only the values zero and one. Under this redefinition of momentum:

$$
\begin{aligned}
M^N_{(k)}[\mathbb{1}] \quad &\rightarrow \quad i \sum_\mu (-)^{A_\mu} \gamma_\mu \sin a k_\mu \\
&= i \sum_\mu \gamma^A_\mu \sin a k_\mu
\end{aligned}
\tag{5.37}
$$

where, for each quark species, the Dirac matrices have been redefined in order to return $M^N_{(k)}[\mathbb{1}]$ to its proper form:

$$
\gamma^A_\mu \equiv (-)^{A_\mu} \gamma_\mu
\tag{5.38}
$$

$$
\gamma^A_5 \equiv \gamma^A_1 \gamma^A_2 \gamma^A_3 \gamma^A_4 = \gamma_5 \prod_\mu (-)^{A_\mu}
\tag{5.39}
$$

For half of the quark species, γ_5 has switched sign, resulting in a corresponding switch in the definition of chirality. Thus, not only does the fermion doubling problem introduce unexpected quark species to the theory, but it also hopelessly entangles the theory's left- and right-handed degrees of freedom, making impossible their independent rotation. Thus, the definition of a discretized version of chiral symmetry becomes impossible.

The inevitability of fermion doubling for any naive action is demonstrated by the Nielsen-Ninomiya theorem and is detailed in [33, 34, 35]

5.3 Staggered Fermions

There are several ways of handling the fermion doubling problem, each of which has its own advantages and disadvantages. The original and perhaps most commonly used method is known as Wilson fermions [36]. A term is added to the fermion action which grants the extra quark species a large mass, effectively decoupling them from the theory. However, this term also destroys all chiral symmetry. Because of the importance of chiral symmetry to our study, such a trampling of the symmetry is

unacceptable. Thus, we make use of a second fermion formulation: Kogut-Susskind, or staggered, fermions [37, 38, 39], a formulation in which a subset of chiral symmetry is retained at non-zero lattice spacing.

5.3.1 Staggered Action

The staggered fermion formulation begins with a realization that, through a redefinition of the quark fields, we can diagonalize the fermion action with respect to spin. Once each spin component is independent, we drop three of the four components, reducing the degrees of freedom within the quark species by a factor of four. Finally, the resulting sixteen single-spin-component quark species are collected together to form four flavors of Dirac quarks.

The formulation of staggered fermions makes use of several phase functions, which we define now:

$$\eta_{\mu;n} \equiv \prod_{\nu<\mu}(-)^{n_\nu} \qquad\qquad \zeta_{\mu;n} \equiv \prod_{\nu>\mu}(-)^{n_\nu} \qquad (5.40)$$

$$\epsilon_n \equiv \prod_{\mu}(-)^{n_\mu} \qquad (5.41)$$

The staggered fermion fields are defined by a redefinition of the quark fields:

$$\chi_n \equiv \Gamma_n q_n \qquad\qquad \bar\chi_n \equiv \bar q_n \Gamma_n^\dagger \qquad (5.42)$$

where Γ_n is a spin-space matrix, defined by:

$$\Gamma_n \equiv \prod_{\mu}\gamma_\mu^{n_\mu} = \gamma_1^{n_1}\gamma_2^{n_2}\gamma_3^{n_3}\gamma_4^{n_4} \qquad (5.43)$$

Recall that the components of n are integers and that $\gamma_\mu\gamma_\mu = \mathbb{1}$. Thus, Γ_n traverses only sixteen possible values.

77

Substituting χ and $\bar{\chi}$ into the single-flavor fermion action:

$$S_q^N[U, q, \bar{q}] = \sum_n \left\{ \frac{1}{2} \sum_\mu \bar{q}_n \gamma_\mu \left[U_{\mu;n}^\dagger q_{n+\hat{\mu}} - U_{\mu;n-\hat{\mu}} q_{n-\hat{\mu}} \right] + m_Q \bar{q}_n q_n \right\}$$

$$= \sum_n \left\{ \frac{1}{2} \sum_\mu \bar{\chi}_n \Gamma_n^\dagger \gamma_\mu \left[U_{\mu;n}^\dagger \Gamma_{n+\hat{\mu}} \chi_{n+\hat{\mu}} - U_{\mu;n-\hat{\mu}} \Gamma_{n-\hat{\mu}} \chi_{n-\hat{\mu}} \right] + m_Q \bar{\chi}_n \Gamma_n^\dagger \Gamma_n \chi_n \right\}$$

$$= \sum_n \left\{ \frac{1}{2} \sum_\mu \eta_{\mu;n} \bar{\chi}_n \Gamma_n^\dagger \gamma_\mu \gamma_\mu \Gamma_n \left[U_{\mu;n}^\dagger \chi_{n+\hat{\mu}} - U_{\mu;n-\hat{\mu}} \chi_{n-\hat{\mu}} \right] + m_Q \bar{\chi}_n \chi_n \right\}$$

$$= \sum_n \left\{ \frac{1}{2} \sum_\mu \eta_{\mu;n} \bar{\chi}_n \left[U_{\mu;n}^\dagger \chi_{n+\hat{\mu}} - U_{\mu;n-\hat{\mu}} \chi_{n-\hat{\mu}} \right] + m_Q \bar{\chi}_n \chi_n \right\} \tag{5.44}$$

where the following identities have been used:

$$\Gamma_n^\dagger \Gamma_n = \mathbb{1} \tag{5.45}$$

$$\Gamma_{n+\hat{\mu}} = \Gamma_{n-\hat{\mu}} = \eta_{\mu;n} \gamma_\mu \Gamma_n = \zeta_{\mu;n} \Gamma_n \gamma_\mu \tag{5.46}$$

The Dirac spin matrix γ_μ in the fermion action has been replaced by a simple scalar phase function $\eta_{\mu;n}$. Thus, the action is now diagonal with respect to spin, and the spin components of the redefined fields have decoupled. We now drop three of the four spin components, leaving χ_n a scalar in spin space and a vector only in color space. The result is the staggered fermion action:

$$S_q^S[U, \chi, \bar{\chi}] = \sum_n \sum_m \bar{\chi}_n M_{n,m}^S[U] \chi_m \tag{5.47}$$

$$M_{n,m}^S[U] = \frac{1}{2} \sum_\mu \eta_{\mu;n} \left[U_{\mu;n}^\dagger \delta_{n,m-\hat{\mu}} - U_{\mu;n-\hat{\mu}} \delta_{n,m+\hat{\mu}} \right] + m_Q \delta_{n,m}$$

$$= D_{n,m}^S[U] + m_Q \delta_{n,m} \tag{5.48}$$

where $M^S[U]$ is now a matrix in only color and position.

5.3.2   Shift Symmetry

In general, a lattice field theory will have a discrete translation symmetry in which the fields are translated multiples of the lattice spacing along directions flush with

the lattice. In the continuum limit this discrete symmetry becomes the continuum's continuous translation symmetry.

In the case of staggered fermions, however, the appearance of the phase factor $\eta_{\mu;n}$ in the action, whose value varies between lattice sites, does not allow for a straightforward definition of translation symmetry. Instead, the action has the more complex shift symmetry, sometimes referred to as ζ-shift symmetry, defined by the transformation:

$$\chi_n \quad \to \quad \chi'_n = \zeta_{\nu;n}\chi_{n+\hat{\nu}} \tag{5.49}$$

$$\bar{\chi}_n \quad \to \quad \bar{\chi}'_n = \zeta_{\nu;n}\bar{\chi}_{n+\hat{\nu}} \tag{5.50}$$

where $\hat{\nu}$ points in the direction of the shift. It is easy to verify that this is a symmetry of the staggered action through use of the identity:

$$\eta_{\mu;\hat{\nu}} = \zeta_{\nu;\hat{\mu}} \tag{5.51}$$

Noting $\zeta_{\nu;n}\zeta_{\nu;n+\hat{\nu}} = \zeta_{\nu;\hat{\nu}} = 1$ reveals that the standard translation symmetries can still be defined, yet only for translation lengths which are a multiple of two lattice spacings.

The transfer matrix, which propagates states through time and whose eigenstates define the states of a theory, is equivalent to the time component of the translation operator. Thus, a staggered transfer matrix which propagates states forward a single lattice step can not be defined. Rather, the transfer matrix can only be constructed such that it propagates states forward two time steps per application.

5.3.3 Even-Odd Symmetry

We define even sites to be those for which summing the components of n results in an even number. Conversely, odd sites are defined as those for which the sum is odd.

Inspection of $M^S[U]$ reveals that, for $m_Q = 0$, χ on even sites couples only to $\bar{\chi}$ on odd sites. Similarly, χ on odd sites couples only to $\bar{\chi}$ on even sites. Thus, the staggered fermion action has a $U(1)_e \otimes U(1)_o$ symmetry, defined by the transformation:

$$\chi_n \quad \rightarrow \quad \chi'_n = \begin{cases} e^{i\alpha_e} \chi_n & \text{even } n \\ e^{i\alpha_o} \chi_n & \text{odd } n \end{cases} \tag{5.52}$$

$$\bar{\chi}_n \quad \rightarrow \quad \bar{\chi}'_n = \begin{cases} \bar{\chi}_n e^{-i\alpha_o} & \text{even } n \\ \bar{\chi}_n e^{-i\alpha_e} & \text{odd } n \end{cases} \tag{5.53}$$

For $m_Q \neq 0$, only a subset of the symmetry remains, that for which $\alpha_e = \alpha_o$.

The symmetry can also be expressed in terms of a $U(1)_1 \otimes U(1)_\epsilon$ symmetry:

$$\chi_n \quad \rightarrow \quad \chi'_n = e^{i(\alpha_1 + \epsilon_n \alpha_\epsilon)} \chi_n \tag{5.54}$$

$$\bar{\chi}_n \quad \rightarrow \quad \bar{\chi}'_n = \bar{\chi}_n e^{-i(\alpha_1 + \epsilon_n \alpha_\epsilon)} \tag{5.55}$$

where the connection to even-odd symmetry is made via $\alpha_1 = \frac{1}{2}(\alpha_e + \alpha_o)$ and $\alpha_\epsilon = \frac{1}{2}(\alpha_e - \alpha_o)$. For $m_Q \neq 0$, the $U(1)_\epsilon$ symmetry is broken, and only $U(1)_1$ remains. This $U(1)_\epsilon$ symmetry is the one component of chiral symmetry which survives the discretization process and is the reason we use the staggered fermion formulation.

One other consequence of even-odd symmetry is that the square of the interaction matrix $M^S[U]^\dagger M^S[U]$ couples only even sites to even sites and odd sites to odd sites. This becomes useful in simplifying certain calculations.

5.3.4   Quarks

The staggered fermion action leaves us with sixteen species of particles, each of which has a single spin and flavor component. Collecting these degrees of freedom, we define our quark field such that the result is four flavors of Dirac spinors.

One option is to make the definition in momentum space [40, 41, 42], assigning each of the zeros of the momentum-space action a distinct spin and flavor index. However, such a procedure leads to a highly non-local definition of the quark field. Instead, we chose to define the quark field in position space, constructing the quark field Q at a single point by gathering together nearby degrees of freedom in χ.

We divide the lattice into hypercubes. A subset of our full lattice, to which each hypercube contributes its lowest member site, makes up a lattice with a spacing of $2a$. We label the sites on this lattice with the index h, such that $h/2 \in \mathbb{Z}^4$, and define our quark field Q such that it takes on values only at the sites of this coarser lattice. Each spin- and flavor-component combination of Q_h is built from a unique linear combination of χ at the sixteen corners of the hypercube h. The quark field $(Q_h)_{\alpha i}$ is constructed as a 4×4 matrix which mixes spin and flavor space, with one spin index α and one flavor index i:

$$(Q_h)_{\alpha i} \equiv \frac{1}{2} \sum_A (\Gamma_A)_{\alpha i} \chi_{h+A} \qquad (\bar{Q}_h)_{i\alpha} \equiv \frac{1}{2} \sum_A \bar{\chi}_{h+A} (\Gamma_A^\dagger)_{i\alpha} \qquad (5.56)$$

where the summation is over all possible binary four-vectors, and visiting each corner of the hypercube h in turn. Note that the normalization of this definition varies in the literature.

We will find that this spatial separation between the various spin and flavor degrees of freedom in our quark field breaks a majority of spin and flavor symmetry. Since the different spin and flavor degrees of freedom of the quark field couple to different gauge links, they each experience a distinct gauge environment. Only in the continuum limit, where the lattice spacing goes to zero and the spatial separation is removed, will the full spin and flavor symmetries of our theory return.

5.3.5 Quark Bilinears

With our quark field defined, we can construct quark bilinears, operators consisting of local quark-antiquark pairs with a specific spin and flavor structure. It is through bilinears that we will access the spin and flavor structure of the staggered formalism, using them as the creation and annihilation operators of two-quark bound states, our lattice mesons.

In the continuum we represented bilinears with the notation $\mathcal{J}_\Gamma^a = \bar{q}\Gamma\tau^a q$, where Γ was some set of spin-space Dirac matrices which determined the bilinear's spin structure and τ^a was some generator of flavor-space rotations which determined the bilinear's flavor structure.

In the context of staggered quarks, bilinears are represented using the notation:

$$
\begin{aligned}
\mathcal{J}_{\mathcal{S},\mathcal{F};h} &= \bar{Q}_h\big(\gamma_\mathcal{S} \otimes \xi_\mathcal{F}\big)Q_h \\
&\equiv (\bar{Q}_h)_{i\alpha}(\gamma_\mathcal{S})_{\alpha\beta}(\xi_\mathcal{F})_{ij}(Q_h)_{\beta j} \\
&= \mathrm{Tr}\big[\bar{Q}_h\gamma_\mathcal{S}Q_h\xi_\mathcal{F}^T\big]
\end{aligned}
\tag{5.57}
$$

where $\gamma_\mathcal{S}$ is a matrix which contracts the quark field's spin indices and represents the spin structure of the bilinear, and $\xi_\mathcal{F}$ is a matrix which contracts the quark field's flavor indices and represents the flavor structure of the bilinear.

Because the number of quark flavors equals the number of spin components, similar bases can be used for the bilinears' spin and flavor matrices. Each matrix takes on

the value of one of the sixteen members of a Clifford algebra:

$$\gamma_{\mathcal{S}} \in \begin{cases} \mathbb{1} \\ \gamma_{\mu} \\ \gamma_{\mu}\gamma_{\nu} \\ \gamma_{\mu}\gamma_5 \\ \gamma_5 \end{cases} \qquad \xi_{\mathcal{F}} \in \begin{cases} \mathbb{1} \\ \gamma_{\mu}^* \\ \gamma_{\mu}^*\gamma_{\nu}^* \\ \gamma_{\mu}^*\gamma_5^* \\ \gamma_5^* \end{cases} \tag{5.58}$$

The members of a Clifford algebra can be expressed in a manner which parallels the definition of Γ_n. Treating $\mathcal{S}$ and $\mathcal{F}$ as binary four-vectors which encode a bilinear's spin and flavor structure:

$$\gamma_{\mathcal{S}} \equiv \Gamma_{\mathcal{S}} = \prod_{\mu} \gamma_{\mu}^{\mathcal{S}_{\mu}} = \gamma_1^{\mathcal{S}_1}\gamma_2^{\mathcal{S}_2}\gamma_3^{\mathcal{S}_3}\gamma_4^{\mathcal{S}_4} \tag{5.59}$$

$$\xi_{\mathcal{F}}^* \equiv \gamma_{\mathcal{F}} = \Gamma_{\mathcal{F}} = \prod_{\mu} \gamma_{\mu}^{\mathcal{F}_{\mu}} = \gamma_1^{\mathcal{F}_1}\gamma_2^{\mathcal{F}_2}\gamma_3^{\mathcal{F}_3}\gamma_4^{\mathcal{F}_4} \tag{5.60}$$

With this notation in place, we can express bilinears in terms of the χ and $\bar{\chi}$ fields:

$$\bar{Q}_h\big(\gamma_{\mathcal{S}} \otimes \xi_{\mathcal{F}}\big)Q_h = \text{Tr}\big[\bar{Q}_h\gamma_{\mathcal{S}}Q_h\xi_{\mathcal{F}}^T\big]$$

$$= \frac{1}{4}\sum_{A}\sum_{B}\text{Tr}\big[\Gamma_A^{\dagger}\gamma_{\mathcal{S}}\Gamma_B\gamma_{\mathcal{F}}^{\dagger}\big]\bar{\chi}_{h+A}\chi_{h+B} \tag{5.61}$$

Thus, a bilinear at a hypercube consists of a linear combination of all possible contractions of χ and $\bar{\chi}$ within that hypercube, where the coefficients of the linear combination depend on the spin and flavor structure of the bilinear.

In truth (5.61) is somewhat oversimplified. The definition of the quark bilinears is complicated by the fact that link matrices live in the hypercube over which the bilinear is defined. Thus, in order for the quark bilinear definition to have the correct color structure, link matrices must be included between non-local contractions of χ and $\bar{\chi}$:

$$\bar{Q}_h\big(\gamma_{\mathcal{S}} \otimes \xi_{\xi_{\mathcal{F}}}\big)Q_h = \frac{1}{4}\sum_{A}\sum_{B}\text{Tr}\big[\Gamma_A^{\dagger}\gamma_{\mathcal{S}}\Gamma_B\gamma_{\mathcal{F}}^{\dagger}\big]\bar{\chi}_{h+A}\mathcal{U}_{A,B;h}\chi_{h+B} \tag{5.62}$$

83

where $\mathcal{U}_{A,B;h}$ represents an equal weighting of all possible shortest gauge link chains connecting the corner B to the corner A of the hypercube h. Note that because $\mathcal{U}_{A,B;h}$ is in general a sum of unitary matrices, it is not itself unitary.

Returning again to the free-field case, we can solve for the coefficients of the linear combination:

$$
\begin{aligned}
\bar{Q}_h\big(\gamma_{\mathcal{S}} \otimes \xi_{\mathcal{F}}\big)Q_h &= \frac{1}{4}\sum_A \sum_B \operatorname{Tr}\big[\Gamma_A^\dagger \gamma_{\mathcal{S}} \Gamma_B \gamma_{\mathcal{F}}^\dagger\big]\bar{\chi}_{h+A}\chi_{h+B} \\
&= \sum_A \sum_B \delta_{A+\mathcal{S},B+\mathcal{F}}(-)^{A\cdot\bar{\eta}_{A+\mathcal{S}}}(-)^{B\cdot\bar{\zeta}_{B+\mathcal{F}}}\bar{\chi}_{h+A}\chi_{h+B} \\
&= \sum_A (-)^{\varphi_{\mathcal{S},\mathcal{F};A}}\bar{\chi}_{h+A}\chi_{h+A+\mathcal{S}+\mathcal{F}}
\end{aligned} \tag{5.63}
$$

where:

$$
\varphi_{\mathcal{S},\mathcal{F};A} \equiv A \cdot \big(\bar{\zeta}_{\mathcal{S}} + \bar{\eta}_{\mathcal{F}}\big) + \mathcal{S} \cdot \bar{\eta}_{\mathcal{S}+\mathcal{F}} \tag{5.64}
$$

and we have used the following definitions:

$$
\eta_{\mu;A} = (-)^{\bar{\eta}_{\mu;A}} \qquad\qquad \bar{\eta}_{\mu;A} \equiv \sum_{\nu<\mu} A_\nu \tag{5.65}
$$

$$
\zeta_{\mu;A} = (-)^{\bar{\zeta}_{\mu;A}} \qquad\qquad \bar{\zeta}_{\mu;A} \equiv \sum_{\nu>\mu} A_\nu \tag{5.66}
$$

and identities:

$$
A \cdot \bar{\eta}_B = B \cdot \bar{\zeta}_A \tag{5.67}
$$

$$
\operatorname{Tr}\big[\Gamma_A^\dagger \Gamma_B\big] = 4\delta_{A,B} \tag{5.68}
$$

$$
\Gamma_A^\dagger \Gamma_B = (-)^{A\cdot\bar{\eta}_{A+B}}\Gamma_{A+B} \qquad\qquad \Gamma_A \Gamma_B^\dagger = (-)^{A\cdot\bar{\zeta}_{A+B}}\Gamma_{A+B}^\dagger \tag{5.69}
$$

We define the addition of binary vectors modulo two, such that the sum of two binary vectors is itself a binary vector. When adding binary and standard vectors together, as per the case $h + A + \mathcal{S} + \mathcal{F}$, the addition of the binary vectors is carried out first.

From (5.63) we see that, for any given $\mathcal{S}$ and $\mathcal{F}$ combination, only sixteen of the sum's coefficients are non-zero. Also, those which are non-zero equal a simple sign factor.

The second term in $\varphi_{\mathcal{S},\mathcal{F};A}$ can be factored out of the hypercubic sum, and contributes only an overall sign:

$$\bar{Q}_h\big(\gamma_{\mathcal{S}} \otimes \xi_{\mathcal{F}}\big)Q_h = (-)^{\mathcal{S}\cdot\bar{\eta}_{\mathcal{S}}+\mathcal{F}} \sum_A (-)^{\varphi'_{\mathcal{S},\mathcal{F};A}} \bar{\chi}_{h+A}\chi_{h+A+\mathcal{S}+\mathcal{F}} \tag{5.70}$$

where:

$$\varphi'_{\mathcal{S},\mathcal{F};A} \equiv A \cdot \big(\bar{\zeta}_{\mathcal{S}} + \bar{\eta}_{\mathcal{F}}\big) \tag{5.71}$$

For a given bilinear $\mathcal{J}_{\mathcal{S},\mathcal{F}}$ we define the binary four-vector $\mathcal{D}_{\mathcal{S},\mathcal{F}} = \mathcal{S} + \mathcal{F}$, and we define the distance of that bilinear to be the number of non-zero elements of $\mathcal{D}_{\mathcal{S},\mathcal{F}}$. Inspection of (5.63) reveals that the non-zero contractions within a bilinear are always between corners of the hypercube separated by an offset equal to $\mathcal{D}_{\mathcal{S},\mathcal{F}}$, and thus the number of links separating those corners always equals the distance of the bilinear.

The simplest bilinears are those in which $\mathcal{S} = \mathcal{F}$. They are known as local bilinears as they have a distance of zero, and thus all of their contractions are local:

$$\bar{Q}_h\big(\gamma_{\mathcal{S}} \otimes \xi_{\mathcal{S}}\big)Q_h = \sum_A (-)^{A\cdot(\bar{\zeta}_{\mathcal{S}}+\bar{\eta}_{\mathcal{S}})} \bar{\chi}_{h+A}\chi_{h+A} \tag{5.72}$$

In the more specific cases of $\gamma_{\mathcal{S}} = \xi_{\mathcal{F}}^* = \mathbb{1}$ and $\gamma_{\mathcal{S}} = \xi_{\mathcal{F}}^* = \gamma_5$, the phase factors become quite simple:

$$\bar{Q}_h\big(\mathbb{1} \otimes \mathbb{1}\big)Q_h = \sum_A \bar{\chi}_{h+A}\chi_{h+A} \tag{5.73}$$

$$\bar{Q}_h\big(\gamma_5 \otimes \xi_5\big)Q_h = \sum_A \epsilon_A \bar{\chi}_{h+A}\chi_{h+A} \tag{5.74}$$

We can generalize our perspective on the structure $\big(\gamma_{\mathcal{S}} \otimes \xi_{\mathcal{F}}\big)$ beyond its use in the notation of bilinears by viewing it as a position- and color-space matrix which operates on χ and $\bar{\chi}$ field configurations, also referred to as fermion field vectors. For the local case the matrix is diagonal, and simply applies a sign factor to the χ and

$\bar\chi$ field at each lattice site. In the non-local case the matrix also swaps the fermion degrees of freedom around within each hypercube, shifting the χ field at corner A on each hypercube to corner $A + \mathcal{S} + \mathcal{F}$ and applying gauge link matrices as appropriate. Stated explicitly as a matrix operating on χ and $\bar\chi$ field vectors, $\left(\gamma_{\mathcal{S}} \otimes \xi_{\mathcal{F}}\right)$ has the form:

$$\left(\gamma_{\mathcal{S}} \otimes \xi_{\mathcal{F}}\right)_{n,m} = (-)^{\mathcal{S}\cdot\bar\eta_{\mathcal{S}+\mathcal{F}}}(-)^{A\cdot(\bar\zeta_{\mathcal{S}}+\bar\eta_{\mathcal{F}})}\delta_{h+A+\mathcal{S}+\mathcal{F},m}\mathcal{U}_{A,A+\mathcal{S}+\mathcal{F};h} \tag{5.75}$$

where h denotes the hypercube containing n, and A denotes its position within that hypercube:

$$h = 2\left\lfloor \frac{n}{2} \right\rfloor \qquad\qquad A = n - h \tag{5.76}$$

The first two terms on the right-hand side of (5.75) apply a sign factor to χ, the second of which is position dependent, the third term swaps the χ degrees of freedom around within each hypercube, and the fourth term applies the appropriate color matrices for that movement. From this perspective, a bilinear is seen as the application of such a matrix to a fermion field vector which is non-zero only at all corners of a single hypercube, and then the contraction of the result with the adjoint of the original vector.

5.3.6 Meson States

Each bilinear corresponds to a set of values for the spin and flavor quantum numbers of our staggered lattice theory and thus create and annihilate all states with like quantum numbers. The lightest state created by a bilinear will be a two-quark bound state with appropriate quantum numbers, a staggered lattice meson. By determining a correspondence between lattice and continuum quantum numbers,

we can identify what continuum mesons our lattice mesons become as we move to the continuum limit.

We choose to label each staggered lattice meson using the name of the lightest Standard Model meson which has corresponding spin quantum numbers. Flavor structure takes a backseat to spin structure when labeling our staggered states because our staggered theory contains four degenerate light quarks, while the Standard Model contains three non-degenerate light quarks. Thus, there is no direct correspondence between the flavor quantum numbers of our staggered mesons and the mesons of the Standard Model.

The staggered meson states, each listed with a bilinear having matching quantum numbers, include:

$$\text{pion:} \quad \bar{Q}\big(\gamma_5 \otimes \xi_{\mathcal{F}}\big)Q \tag{5.77}$$

$$\text{rho:} \quad \bar{Q}\big(\gamma_i \otimes \xi_{\mathcal{F}}\big)Q \tag{5.78}$$

$$\text{scalar:} \quad \bar{Q}\big(\mathbb{1} \otimes \xi_{\mathcal{F}}\big)Q \tag{5.79}$$

where $i \in \{1, 2, 3\}$ chooses the polarization of the rho and the flavor structure of the states has been left unspecified.

The flavor structure $\xi_{\mathcal{F}}$ of each listed bilinear takes on one of sixteen possible values. In the continuum limit the degeneracy of the four staggered quark flavors causes these sixteen states to be themselves degenerate. However, at non-zero lattice spacing, all but one of the flavor structures becomes non-local, flavor symmetry is broken, and the masses of the sixteen states split.

For each spin structure, one of the flavor structure choices will correspond to a local bilinear. In the case of the staggered pion, that state is:

$$\text{local pion:} \qquad \bar{Q}\big(\gamma_5 \otimes \xi_5\big)Q \qquad\qquad (5.80)$$

At non-zero lattice spacing only this local pion remains light, while the other fifteen non-local pions gain a mass contribution dependent upon the lattice spacing.

Thus far, we have ignored two complications which are inherent in the correspondence between the bilinear operators and the staggered meson states.

The first complication relates to the time component of a state's spin. Recall that the spin of a particle is defined relative to its momentum four-vector. In the case of states with zero spatial momentum, which we create by summing over a time slice as described in Section 4.3, the state's momentum four-vector points along the time direction. Thus, the time component of our state's spin is undefined, and there exist more bilinears than there are states to create. As a consequence, the bilinears $\bar{Q}\big(\gamma_{\mathcal{S}} \otimes \xi_{\mathcal{F}}\big)Q$ and $\bar{Q}\big(\gamma_4\gamma_{\mathcal{S}} \otimes \xi_{\mathcal{F}}\big)Q$ both couple to the same state.

The second complication arises because states decay exponentially as they propagate through time, and thus the use of creation operators, or sources, which are distributed in time, such as bilinears, is not straightforward. We will find that each bilinear couples to states with two sets of quantum numbers, one set which was naively unexpected.

Looking at the two bilinears $\bar{Q}\big(\gamma_{\mathcal{S}} \otimes \xi_{\mathcal{F}}\big)Q$ and $\bar{Q}\big(\gamma_4\gamma_5\gamma_{\mathcal{S}} \otimes \xi_4\xi_5\xi_{\mathcal{F}}\big)Q$ and comparing the sign factors of their χ with $\bar{\chi}$ contractions, we find the factors the same on a given time slice. The difference between their sign factors only arises when we compare neighboring time slices. The sign factors of one bilinear will be constant between time slices, while the other's factors will flip in sign each time step.

By defining the binary four-vector $\mathcal{K}$ such that $\gamma_\mathcal{K} = \gamma_5\gamma_4$, we can state the above explicitly:

$$\varphi'_{\mathcal{S}+\mathcal{K},\mathcal{F}+\mathcal{K};A} = \varphi'_{\mathcal{S},\mathcal{F};A} + A_4 \tag{5.81}$$

The only distinction between $\varphi'_{\mathcal{S}+\mathcal{K},\mathcal{F}+\mathcal{K};A}$ and $\varphi'_{\mathcal{S},\mathcal{F};A}$ is an oscillation along the time direction represented by the A_4 term.

If we choose to use a creation source for our mesons which is limited to a single time slice, we will always in effect be choosing a source which is an equal linear combination of the bilinears $\bar{Q}(\gamma_\mathcal{S} \otimes \xi_\mathcal{F})Q$ and $\bar{Q}(\gamma_4\gamma_5\gamma_\mathcal{S} \otimes \xi_4\xi_5\xi_\mathcal{F})Q$. The alternating in time of one of the bilinear's sign factors will cause their combined contribution to cancel on one of the two time slices of the hypercube. The result of this cancellation is a single-time-slice source.

In an effort to generate only one set of quantum numbers, we might consider adding a second time slice to our source. This allows us to use exactly the bilinear $\bar{Q}(\gamma_\mathcal{S} \otimes \xi_\mathcal{F})Q$ as our source. However, doing so only suppresses, but does not eliminate, the coupling to states having the quantum numbers of the bilinear $\bar{Q}(\gamma_4\gamma_5\gamma_\mathcal{S} \otimes \xi_4\xi_5\xi_\mathcal{F})Q$. This continued coupling is because states decay exponentially as they propagate in time. Thus, in order to overlap only with states of one quantum number set or another, the exponential decay of states which occurs within our source, which is distribute in time, must be accounted for. Yet, such an accounting can only be done if we have complete knowledge of the spectrum for the two sets of quantum numbers in question. Thus, in practice it is impossible.

The quantum number sets of the bilinears $\bar{Q}(\gamma_\mathcal{S} \otimes \xi_\mathcal{F})Q$ and $\bar{Q}(\gamma_4\gamma_5\gamma_\mathcal{S} \otimes \xi_4\xi_5\xi_\mathcal{F})Q$ each have an associated lowest energy state, their respective staggered mesons. These two mesons are often referred to as parity partners, as they have the same

quantum numbers up to opposite parity. If, instead of attempting to project out the entire tower of states of one of the quantum number sets, we wish merely to project out its associated meson state, only knowledge of the time evolution of those two lowest-energy states is required. That is, we must know the meson masses ahead of time.

If no attempt is made to account for the time evolution of the meson states, and instead the exact two-time-slice bilinear $\bar{Q}(\gamma_S \otimes \xi_F)Q$ is used as our source, the amplitude of the parity-partner meson is suppressed by a factor of $\tanh \frac{1}{2}aM$, where the two mesons are assumed to have similar masses and M is the average of those masses. Note that in the continuum limit, $a \to 0$, the suppression is complete. This is not surprising as the operators are then local in time.

For any two parity partners, the positive parity state will propagate through time in a straightforward fashion. Its negative parity partner, however, will alternate in sign each time step. This unorthodox behavior is a direct consequence of the staggered transfer matrix being defined only for time translations of two lattice steps. If we consider the states only on every other time step, the sign oscillation of the negative-parity state is hidden, and both states behave as expected.

To summarize the core issue, when the bilinear $\bar{Q}(\gamma_S \otimes \xi_F)Q$ is used to create states, it will invariably couple both to states with its own quantum numbers and to states with quantum numbers associated with the bilinear $\bar{Q}(\gamma_4\gamma_5\gamma_S \otimes \xi_4\xi_5\xi_F)Q$. Thus, the direct connection between bilinears and meson states is blurred.

The local pion is free from this second complication, as it has no parity partner. The bilinear $\bar{Q}(\gamma_5 \otimes \xi_5)Q$ creates only states with the quantum numbers of the local pion, and creates no negative-parity states.

5.3.7 Quark Action

Using our definition of quark bilinears, we can express the free-field staggered fermion action in terms of Q and $\bar{Q}$:

$$
\begin{aligned}
S^S[\mathbb{1}, \chi, \bar{\chi}] &= \sum_n \left\{ \frac{1}{2} \sum_\mu \eta_{\mu;n} \bar{\chi}_n \left[\chi_{n+\hat{\mu}} - \chi_{n-\hat{\mu}} \right] + m_Q \bar{\chi}_n \chi_n \right\} \\
&= \sum_h \sum_A \left\{ \frac{1}{2} \sum_\mu \eta_{\mu;A} \bar{\chi}_{h+A} \left[\chi_{h+A+\hat{\mu}} - \chi_{h+A-\hat{\mu}} \right] + m_Q \bar{\chi}_{h+A} \chi_{h+A} \right\} \\
&= \sum_h \left\{ \frac{1}{4} \sum_\mu \left[\bar{Q}_h \left(\gamma_\mu \otimes \mathbb{1} \right) \left(Q_{h+2\hat{\mu}} - Q_{h-2\hat{\mu}} \right) \right. \right. \\
&\quad \left. \left. + \bar{Q}_h \left(\gamma_5 \otimes \xi_\mu \xi_5 \right) \left(Q_{h+2\hat{\mu}} - 2Q_h + Q_{h-2\hat{\mu}} \right) \right] + m_Q \bar{Q}_h \left(\mathbb{1} \otimes \mathbb{1} \right) Q_h \right\}
\end{aligned}
\tag{5.82}
$$

where we have used the following identities:

$$
\bar{\chi}_{h+A} = \text{Tr} \left[\bar{Q}_h \Gamma_A \right]
\tag{5.83}
$$

$$
\chi_{h+A+\hat{\mu}} = \text{Tr} \left[\left(\delta_{0,A_\mu} Q_h + \delta_{1,A_\mu} Q_{h+2\hat{\mu}} \right) \Gamma_{A+\hat{\mu}}^\dagger \right]
\tag{5.84}
$$

$$
\chi_{h+A-\hat{\mu}} = \text{Tr} \left[\left(\delta_{0,A_\mu} Q_{h-2\hat{\mu}} + \delta_{1,A_\mu} Q_h \right) \Gamma_{A-\hat{\mu}}^\dagger \right]
\tag{5.85}
$$

$$
\sum_A \text{Tr} \left[\bar{Q}_h \Gamma_A \right] \text{Tr} \left[Q_h \Gamma_{\mathcal{F}}^\dagger \Gamma_A^\dagger \Gamma_{\mathcal{S}} \right] = 4 \text{Tr} \left[\bar{Q}_h \Gamma_{\mathcal{S}} Q_h \Gamma_{\mathcal{F}}^\dagger \right]
\tag{5.86}
$$

$$
\epsilon_A \Gamma_A = \gamma_5 \Gamma_A \gamma_5 \qquad\qquad \delta_{0,A_\mu} = \tfrac{1}{2} \left(1 + \epsilon_A \eta_{\mu;A} \zeta_{\mu;A} \right)
\tag{5.87}
$$

$$
\eta_{\mu;A} \zeta_{\mu;A} \Gamma_A = \gamma_\mu \Gamma_A \gamma_\mu \qquad\qquad \delta_{1,A_\mu} = \tfrac{1}{2} \left(1 - \epsilon_A \eta_{\mu;A} \zeta_{\mu;A} \right)
\tag{5.88}
$$

The first term in (5.82) is expected. It is a discretization of the standard flavor-diagonal kinetic term of the continuum quark action. However, the second term corresponds to the lattice spacing a times a discretization of the second derivative of the quark field (A.18). Thus, this second term is a lattice artifact. In the continuum limit, $a \to 0$, it disappears and the staggered quark action becomes the standard continuum action.

Yet at non-zero lattice spacing, this term remains, and as the term is not diagonal in flavor space, it demonstrates explicitly the flavor symmetry breaking present within the staggered formalism.

5.3.8 Flavor Symmetry

A continuum four-flavor massless QCD theory classically has a $U(4)_V \otimes U(4)_A$ flavor symmetry. However, in our staggered discretization of that four-flavor theory, the second kinetic term in the staggered quark action (5.82) breaks much of the flavor symmetry, and at finite lattice spacing only a remnant is preserved.

For massive quarks, the staggered quark action has a $U(1)_{\mathbb{1}}$ symmetry, defined by the transformation:

$$Q \quad \rightarrow \quad Q' = e^{i\alpha_1(\mathbb{1}\otimes\mathbb{1})}Q \tag{5.89}$$

$$\bar{Q} \quad \rightarrow \quad \bar{Q}' = \bar{Q}e^{-i\alpha_1(\mathbb{1}\otimes\mathbb{1})} \tag{5.90}$$

For massless quarks, the symmetry expands to $U(1)_{\mathbb{1}}\otimes U(1)_{\gamma_5}$, where $U(1)_{\gamma_5}$ is defined by the transformation:

$$Q \quad \rightarrow \quad Q' = e^{i\alpha_\epsilon(\gamma_5\otimes\xi_5)}Q \tag{5.91}$$

$$\bar{Q} \quad \rightarrow \quad \bar{Q}' = \bar{Q}e^{i\alpha_\epsilon(\gamma_5\otimes\xi_5)} \tag{5.92}$$

This $U(1)_{\mathbb{1}}\otimes U(1)_{\gamma_5}$ symmetry is equivalent to the $U(1)_1\otimes U(1)_\epsilon$ symmetry described by (5.54) and (5.55), simply reexpressed in terms of the staggered quark fields. In the continuum limit, the $U(1)_1$ symmetry becomes the flavor-singlet vector symmetry $U(1)_V$. The $U(1)_\epsilon$ symmetry becomes a single $U(1)$ subgroup of the continuum's flavor non-singlet axial vector symmetry. Following its role as a non-singlet axial vector symmetry, $U(1)_\epsilon$ is spontaneously broken, with the resulting Goldstone boson being

a two-particle bound state created and annihilated by the bilinear $\bar{Q}(\gamma_5 \otimes \xi_5)Q$. When we move away from the chiral limit, $U(1)_\epsilon$ becomes an approximate symmetry, and the bound state becomes a pseudo-Goldstone boson with a squared mass proportional to the quark mass.

The form of the creation bilinear reveals that the Goldstone boson of the spontaneously broken $U(1)_\epsilon$ symmetry is the local staggered pion. It is clear now that the local pion remains light at non-zero lattice spacing because a remnant of the continuum's non-singlet axial symmetry is preserved. It is also not surprising that the fifteen other non-local pions gain a mass, as the staggered formulation breaks the flavor symmetries for which they would have been Goldstone bosons.

It is the existence of this robust Goldstone boson, still present an non-zero lattice spacing, which will prove to make the staggered fermion formulation a valuable tool in our study. Because the local pion is a Goldstone boson, Chiral Perturbation Theory allows us to calculate its mass and decay constant in terms of certain GL coefficients. By evaluating these quantities using a lattice calculation, we can determine the value of those GL coefficients.

5.3.9 $N_f \neq 4$

One remaining stumbling block is that the number of quark flavors is restricted by the staggered fermion formulation to a multiple of four. Yet, the Standard Model contains three light flavors. We resolve this issue by taking the interaction-matrix determinant to a fractional power.

As discussed in Section 5.3.7, the staggered interaction matrix $M^S[U]$ becomes flavor-space diagonal in the continuum limit. Thus in that limit, its determinant can

be factored into the product of four equivalent determinants, one associated with each quark flavor:

$$\det M^S[U] = \left(\sqrt[4]{\det M^S[U]} \right)^4 \tag{5.93}$$

If we desire some number of quark flavors N_f other than four, we need only to include N_f powers of the fourth root of the interaction-matrix determinant in our partition function. In terms of the effective gauge action, this choice of flavors becomes a simple factor:

$$\begin{aligned} S^S_{\text{LQCD}}[U] &= S_g[U] - \ln\left[\left(\sqrt[4]{\det M^S[U]} \right)^{N_f} \right] \\ &= S_g[U] - \frac{N_f}{4} \operatorname{Tr} \ln M^S[U] \end{aligned} \tag{5.94}$$

Of course at finite lattice spacing, the staggered action is not flavor diagonal and its determinant will not factor. Thus, this procedure for choosing N_f clearly becomes invalid. Yet, the inclusion of the $N_f/4$ factor in a numerical calculation proves to be straightforward and, whatever effect that factor has at non-zero lattice spacing, as a becomes small that effect will become an improving approximation of N_f flavors. Thus, in our lattice calculations we will use this method to approximate $N_f = 3$ quark flavors, the same number of light flavors as is present in the Standard Model.

5.4   Conjugate Gradient

At their core most lattice calculations involve the inverse of the fermion interaction matrix. In the case of our study, the inverse is required during both the generation of our ensemble configurations and during the calculation of our meson propagators.

The staggered fermion interaction matrix $M^S[U]$ is very large, $L^4 N_c \times L^4 N_c$, but since it only connects each site to its neighbors, it is also quite sparse, with only

$L^4N_c(4N_c+1)$ non-zero elements. In both cases, we use L^4 to represent $L_1L_2L_3L_4$. Because of this sparseness, the memory required to store the interaction matrix grows only linearly with the lattice volume. Its inverse $M^S[U]^{-1}$, however, is not sparse. Thus, we make no attempt to calculate and store the inverse interaction matrix directly. Rather, we use a numerical algorithm which allows us to apply the inverse matrix to a vector via repeated application of the original matrix. This algorithm, which finds use in a broad range of fields, is known as the Conjugate Gradient (CG) method [43]. For a clear yet complete explanation of CG, we refer the reader to [44].

We use CG to apply the inverse interaction matrix to some field vector W, calculating X, where X has the form:

$$X = M^S[U]^{-1}W \tag{5.95}$$

In practice however, we can not use CG to apply $M^S[U]^{-1}$ to a vector directly because $M^S[U]$ is not positive definite, a characteristic required by CG. Yet the square of the interaction matrix $M^S[U]^\dagger M^S[U]$ is positive definite. Thus, we are able to calculate X by first applying $M^S[U]^\dagger$ to W, and then using CG to apply the inverse of $M^S[U]^\dagger M^S[U]$:

$$X = \left(M^S[U]^\dagger M^S[U]\right)^{-1}M^S[U]^\dagger W \tag{5.96}$$

Recalling Section 5.3.3, the calculation is simplified by the fact that the square of the interaction matrix, and thus its inverse, couples only even sites to even sites and odd sites to odd sites. The even components of X can be calculated by inverting a matrix which consists of only the even-to-even elements of $M^S[U]^\dagger M^S[U]$, a smaller

matrix which is thus easier to invert:

$$X_e = \left(M^S[U]^\dagger M^S[U]\right)^{-1}_{e,e} \left(M^S[U]^\dagger W\right)_e$$

$$= \left(M^S[U]^\dagger M^S[U]\right)^{-1}_{e,e} \left(-D^S[U]_{e,o} W_o + m_Q W_e\right) \tag{5.97}$$

where the subscript e (o) denotes the even (odd) half of the lattice sites. We have used $D[U]^\dagger = -D[U]$. From (5.95) we know that:

$$W_o = \left(M^S[U]X\right)_o$$

$$= D^S[U]_{o,e} X_e + m_Q X_o \tag{5.98}$$

Thus, the odd elements of X can be put in terms of its even elements:

$$X_o = \frac{1}{m_Q} \left(W_o - D^S[U]_{o,e} X_e\right) \tag{5.99}$$

We see that both the even and odd components of our resulting field vector X can be computed by inverting only the even half of the interaction matrix. This procedure is known as preconditioning and will significantly speed up our numerical calculations.

5.5 R Algorithm

The advent of fermion fields in our lattice field theory results in a non-local effective gauge action:

$$Z^S_{\mathrm{LQCD}} = \int [\mathcal{D}U]\, e^{-S^S_{\mathrm{LQCD}}[U]} \tag{5.100}$$

$$S^S_{\mathrm{LQCD}}[U] = S_g[U] + \frac{N_f}{4} \operatorname{Tr} \ln M^S[U] \tag{5.101}$$

where the $\operatorname{Tr} \ln M^S[U]$ term mixes all gauge degrees of freedom. This non-locality significantly increases the computational effort required to generate an ensemble. When producing a Markov chain using the local pure-gauge action, determining the change

in action due to some local modification requires only information in the neighborhood of the modification. With our non-local action, however, determining the change in action due to any modification requires a full recalculation of the configuration's action. As such, we can no longer afford to grow our Markov chain via a large number of small localized changes.

Instead, we require a procedure which permits large steps through configuration space during which all gauge field degrees of freedom are updated simultaneously. These update steps must change the equilibrium ensemble distribution either not at all or very slightly, such that there is either no chance, or only a very small chance, of rejection. Additionally, the algorithm must permit simulation of $N_f = 3$ flavors of dynamical fermions.

The R algorithm [45], also known as Hybrid Molecular Dynamics (HMD), fits all of these criteria. The strong point of HMD is that it chooses the next configuration in our Markov chain with the correct probability distribution. No acceptance step is required. Additionally, the simulation of any number of dynamical flavors is straightforward. Unfortunately, the effective probability distribution used by the R algorithm is only accurate to within a certain uncorrectable error.

5.5.1 Hybrid Molecular Dynamics

The first conceptual step towards HMD is the introduction of an auxiliary field $H_{\mu;n}$ to the theory. This field consists of traceless Hermitian color matrices, four of which live on each lattice site. They are parameterized as:

$$H_{\mu;n} = \sum_a \lambda^a h^a_{\mu;n} \tag{5.102}$$

97

where λ^a are the generators of $SU(3)$ color. Being an auxiliary field, $H_{\mu;n}$ has a trivial action:

$$Z_{\text{HMD}}^S = \int [\mathcal{D}H][\mathcal{D}U] \ e^{-S_{\text{HMD}}^S[H,U]} \tag{5.103}$$

$$S_{\text{HMD}}^S[H,U] = S_H[H] + S_{\text{LQCD}}^S[U] \tag{5.104}$$

$$S_H[H] = \frac{1}{2} \sum_n \sum_\mu \text{tr}\, H_{\mu;n}^2 \tag{5.105}$$

As there are no interaction terms between the auxiliary field $H_{\mu;n}$ and the gauge field $U_{\mu;n}$, its introduction into the theory does not affect the expectation value of gauge or fermion field operators. The quark and gluon physics of the HMD partition function is the same as that of the LQCD partition function.

With its simple action, updating the auxiliary field is effortless. A heat-bath update can be used, in which the next $H_{\mu;u}$ field configuration is simply chosen using the proper probability distribution. This field configuration choice is made by setting each $h_{\mu;n}^a$ to a Gaussian random number with appropriate normalization. No acceptance step is required.

Given that $[U]_A$ was the last gauge configuration added to our Markov chain, after including a heat-bath updated auxiliary field $[H]_A$, we have the HMD configuration $[H,U]_A$. What we now require is a procedure which will take us from $[H,U]_A$ to a new configuration $[H,U]_B$ with equal HMD action $S_{\text{HMD}}^S[H,U]$ in a deterministic and reversible manor. Once $[H,U]_B$ is found, $[U]_B$ can be added to our ensemble with no acceptance step, as there has been no change in the HMD action. The procedure used by HMD to generate $[H,U]_B$ from $[H,U]_A$ is based on classical molecular dynamics. This is from where HMD draws its name.

In the context of HMD, the gauge field configuration $[U]$ is thought of as denoting the position of a classical particle in the very-large-dimensional configuration space. The LQCD action $S^S_{\text{LQCD}}[U]$ is taken to be a static potential through which the particle moves. Finally, the auxiliary field configuration $[H]$ acts as the particle's canonical momentum. With these identifications, the HMD action $S^S_{\text{HMD}}[H, U]$ has the same form as the one-particle system's Hamiltonian $\mathscr{H}$.

The configuration $[H, U]_A$ is treated as the initial condition for a trajectory through configuration space. Using the Hamiltonian's classical equations of motion, we move the configuration along the trajectory for some interval in artificial HMD time. By the time we reach the endpoint of the trajectory $[H, U]_B$, the gauge field degrees of freedom have changed significantly. We have taken a large directed step through configuration space. Additionally, $[H, U]_B$ has the same HMD action as our starting point $[H, U]_A$. This is because, along a classical trajectory through a time-independent potential, a system's Hamiltonian is conserved. Thus, we can safely add the gauge configuration $[U]_B$ to our ensemble with no acceptance step. In a sense, when a heat-bath update is applied to the auxiliary field, HMD is choosing, with the proper distribution, our ensemble's next gauge configuration. It is then simply a matter of calculating, via the classical equations of motion, which configuration the R algorithm has chosen.

5.5.2 Ensemble Equilibrium

To see clearly that this sort of update process is valid, we can investigate the ensemble equilibrium condition discussed in Section 4.2.3. That is, an ensemble with the desired configuration distribution must sit in equilibrium during the update process:

$$P([U]_A \rightarrow [U]_B) = P([U]_B \rightarrow [U]_A) \tag{5.106}$$

As before, $P([U]_A \rightarrow [U]_B)$ has three factors:

$$P([U]_A \rightarrow [U]_B) = P_W([U]_A) P_P([U]_A \rightarrow [U]_B) P_A([U]_A \rightarrow [U]_B) \tag{5.107}$$

where:

$$P_W([U]_A) = Z_{\text{LQCD}}^{-1} e^{-S_{\text{LQCD}}^S [U]_A} \tag{5.108}$$

and as we have asserted that no acceptance step is required:

$$P_A([U]_A \rightarrow [U]_B) = 1 \tag{5.109}$$

The remaining factor $P_P([U]_A \rightarrow [U]_B)$ is essentially the probability that the heat-bath update of the auxiliary field will choose a certain trajectory, the trajectory which takes us from the position $[U]_A$ in configuration space to the position $[U]_B$. Conversely, $P_P([U]_B \rightarrow [U]_A)$ is the probability of choosing that same trajectory in the reverse direction. Associated with the trajectory is a value for the conserved Hamiltonian $\mathscr{H}$ which is independent of the direction the trajectory is traversed.

The probability of choosing a given trajectory is based solely on the kinetic energy $S_H[H]$ required to take the trajectory. The kinetic energy must make up the difference between the trajectory's Hamiltonian $\mathscr{H}$ and the static potential at the trajectory's starting point $S_{\text{LQCD}}^S [U]_A$:

$$S_H[H] = \mathscr{H} - S_{\text{LQCD}}^S [U]_A \tag{5.110}$$

Thus, the probability of choosing to take the trajectory in the forward direction over choosing to take that same trajectory in the reverse direction is:

$$\frac{P_P([U]_A \rightarrow [U]_B)}{P_P([U]_B \rightarrow [U]_A)} = \frac{e^{-\mathscr{H} + S_{\text{LQCD}}^S [U]_A}}{e^{-\mathscr{H} + S_{\text{LQCD}}^S [U]_B}} = e^{S_{\text{LQCD}}^S [U]_A - S_{\text{LQCD}}^S [U]_B} \tag{5.111}$$

This is exactly the probability required to generate the desired configuration distribution:

$$
\begin{aligned}
P\big([U]_A \to [U]_B\big) &= P_W\big([U]_A\big) P_P\big([U]_A \to [U]_B\big) \\
&= Z_{\text{LQCD}}^{-1} e^{-S_{\text{LQCD}}^S[U]_A} P_P\big([U]_B \to [U]_A\big) e^{S_{\text{LQCD}}^S[U]_A - S_{\text{LQCD}}^S[U]_B} \\
&= Z_{\text{LQCD}}^{-1} e^{-S_{\text{LQCD}}^S[U]_B} P_P\big([U]_B \to [U]_A\big) \\
&= P_W\big([U]_B\big) P_P\big([U]_B \to [U]_A\big) \\
&= P\big([U]_B \to [U]_A\big)
\end{aligned}
\tag{5.112}
$$

5.5.3 Finite Step-Size Error

We numerically evolve an auxiliary and gauge field configuration along its trajectory using finite steps in HMD time of some chosen size. Preceding each step, the gradient of the static potential $S_{\text{LQCD}}^S[U]$ is calculated in order to determine the magnitude and direction of the step. Each such calculation requires an application of the inverse interaction matrix, the most numerically demanding aspect of the algorithm. As such, it may be tempting to use a large time step in the interests of efficiency. However, the finite size of these steps introduces error into the R algorithm's ensemble distribution. The finite steps cause the numerical evolution to stray from the true trajectory. Thus, the end-point configuration will not be exactly the configuration chosen by the heat-bath update of the auxiliary field. We must insure that the step size used is sufficiently small such that our ensemble's configuration distribution is not significantly skewed.

5.5.4 $N_f \neq 4$

When simulating $N_f = 4$ dynamical staggered quarks, the Φ algorithm [45], also known as Hybrid Monte Carlo (HMC), can be used. This algorithm uses molecular dynamics in the same fashion as the R algorithm. The difference between the two lies in how they handle the interaction-matrix determinant in the effective gauge action $S_{\mathrm{LQCD}}^S[U]$.

In the case of the Φ algorithm, the determinant is replaced by a set of pseudo-fermion fields whose interaction matrix is the inverse of the staggered quark interaction matrix. Such a pseudo-fermion interaction matrix generates the appropriate determinant factor in the ensemble average. As the pseudo-fermions are not Grassmann fields, we can work with them numerically, and as their action is straightforward, they are easily updated at the start of each trajectory using a heat-bath method similar to that used for the auxiliary field.

A particularly noteworthy feature of the Φ algorithm is that the use of the pseudo-fermion fields allows the HMC action to be known exactly. As a result, the error introduced by finite step size can be accounted for with an acceptance step at the end of each trajectory. While the numerical evolution will stray from the correct trajectory before it reaches its endpoint, we can make up for this error by accepting or rejecting the entire trajectory based on the difference between the the HMC action at the beginning and end points of the trajectory

In the case of the R algorithm, because we are taking the fermion interaction-matrix determinant to a fractional power in order to simulate at $N_f \neq 4$, the determinant can not be replaced with a functional integral over pseudo-fermionic degrees of freedom. Instead, the determinant is evaluated using a noisy estimator. Such a

procedure does not allow for an exact determination of the HMD action, and thus the error introduced by finite step size can not be accounted for via an acceptance step.

In summary, the R algorithm allows us to take large directed steps through configuration space with no chance of losing numerical effort due to an acceptance test. Additionally, it allows us to operate at $N_f \neq 4$. Its primary disadvantage is that the algorithm is inexact, as the finite step-size errors can not be accounted for.

For the specifics of the R algorithm, including the exact form of the classical equations of motion, the reader is referred to [45].

5.6 Hypercubic Blocking

In order to gain access to the GL coefficients, we are studying the local pion mass's dependence on the quark mass. At NLO in ChPT, the local pion propagator includes graphs with non-local pion loops. Thus, its mass gains a dependence on the masses of the non-local pions, and through them a NLO dependence on the strength of the staggered fermion formulation's flavor symmetry breaking. Because this is the same order at which the GL coefficients appear, flavor symmetry breaking has the potential to introduce significant systematic error in the values we observe for the GL coefficients.

If the lattice spacing of our ensembles were small enough, flavor symmetry breaking would become negligible. However, as is always the case in lattice calculations, due to limited computer resources our lattice spacing is not as small as we would like. Thus, some other method for controlling flavor symmetry breaking is required.

An oft-used method for reducing lattice artifacts is the smearing of gauge links. Each of a configuration's gauge links is replaced by a linear combination of itself and other local gauge paths which connect the same endpoints. The result is a smeared, or fat, link configuration. Such a process does not affect long distance behavior, but reduces lattice artifacts by smoothing out short-distance gauge fluctuations. A reduction in statistical error, especially in quantities sensitive to short-distance fluctuations, is often seen, as well as an improvement in rotational symmetry.

In the context of staggered fermions, flavor symmetry breaking is the result of the various corners of a hypercube experiencing distinct gauge backgrounds. Smearing the gauge links reduces these differences, and thus reduces flavor symmetry breaking. This has been demonstrated in both quenched [46] and full LQCD [47], and is also supported by perturbation theory [48]. It is not surprising that a procedure which in general improves rotational symmetry would, in the context of staggered fermions, improve flavor symmetry as well, as the Lorentz and flavor symmetries have been tightly entangled.

Often multiple iterations, or levels, of a smearing process are applied to an ensemble, as the effects of smearing become more pronounced with the number of levels applied. However, a large number of smearing levels results in a highly non-local definition of the fat link and significantly alters short distance behavior. Thus, there is a trade-off between using a large number of smearing levels to greatly reduce short-distance gauge noise, and using a moderate number of smearing levels to preserve short-distance physics.

From the perspective of reducing flavor symmetry breaking in staggered fermions, the optimal point in this trade-off is a smearing procedure which maximally smears

a gauge link without reaching beyond that link's hypercubes. A procedure developed for this exact purpose is hypercubic blocking [49, 50]. It constructs a fat link by smearing it only with links contained by the eight hypercubes of which that link is an edge.

In the application of a standard smearing level, a link is replaced by a projected linear combination of itself and the six three-link gauge paths, known as staples, which connect the same endpoints. With hypercubic blocking, three levels similar to this manner of smearing are applied. The defining feature is that staples which reach beyond the hypercube of the resulting fat link are not used. As such, the staples used in a given smearing level must be orthogonal to the fat link and to the staples used in all previous levels. With only three directions orthogonal to the original link, hypercubic blocking stops after three levels.

Taking $U_{\mu;n}$ to be the original thin links of a configuration and $V_{\mu;n}$ to be the resulting fat links of the hypercubic-blocked configuration, we layout the definition of hypercubic blocking explicitly:

$$V_{\mu;n} \equiv V_{\mu;n}^{(1)} \equiv \operatorname*{proj}_{SU(3)}\left[\left(1-\alpha_1\right)U_{\mu;n} + \frac{\alpha_1}{6}\sum_{\nu\neq\mu}\sum_{\pm} V_{\mp\nu;n+\hat{\mu}\pm\hat{\nu}}^{(2;\mu)} V_{\mu;n\pm\hat{\nu}}^{(2;\nu)} V_{\pm\nu;n}^{(2;\mu)}\right] \tag{5.113}$$

$$V_{\mu;n}^{(2;\nu)} \equiv \operatorname*{proj}_{SU(3)}\left[\left(1-\alpha_2\right)U_{\mu;n} + \frac{\alpha_2}{4}\sum_{\substack{\rho\neq\mu \\ \rho\neq\nu}}\sum_{\pm} V_{\mp\rho;n+\hat{\mu}\pm\hat{\rho}}^{(3;\mu\nu)} V_{\mu;n\pm\hat{\rho}}^{(3;\nu\rho)} V_{\pm\rho;n}^{(3;\mu\nu)}\right] \tag{5.114}$$

$$V_{\mu;n}^{(3;\nu\rho)} \equiv \operatorname*{proj}_{SU(3)}\left[\left(1-\alpha_3\right)U_{\mu;n} + \frac{\alpha_3}{2}\sum_{\substack{\sigma\neq\mu \\ \sigma\neq\nu \\ \sigma\neq\rho}}\sum_{\pm} U_{\mp\sigma;n+\hat{\mu}\pm\hat{\sigma}} U_{\mu;n\pm\hat{\sigma}} U_{\pm\sigma;n}\right] \tag{5.115}$$

where $X_{-\nu;n} \equiv X_{\nu;n-\hat{\nu}}^{\dagger}$. The parameters α_1, α_2, and α_3 are the adjustable parameters of the procedure. Throughout our work we use values for these parameters suggested

by early hypercubic blocking literature [49]:

$$\alpha_1 = 0.75 \qquad\qquad \alpha_2 = 0.6 \qquad\qquad \alpha_3 = 0.3 \qquad (5.116)$$

Because the sum of a set of unitary matrices is not itself unitary, the result of each level of smearing must be projected back into the space of unitary matrices. This projection process must result in a unitary matrix which is as close as possible to the original non-unitary matrix so that the resulting fat link characterizes as well as possible the sum over local paths. It is not obvious, however, what metric this measure of closeness should use. As such, we simply define a reasonable method for identifying the closest unitary matrix, and do not trouble ourselves with the exact form of the resulting metric. For the definition of the $SU(3)$ projection and details of the procedure used to implement that definition, see Appendix C.

It has been demonstrated that hypercubic blocking reduces the mass splitting between the local and lightest non-local staggered pions [49] and thus clearly reduces flavor symmetry breaking. As such, we use hypercubic blocking to both estimate and reduce the effects of flavor symmetry breaking on our results.

We generate our ensembles using the standard thin-link staggered fermion action (5.47). We then apply hypercubic blocking to our ensembles and proceed with our analysis using both the thin-link and hypercubic-blocked ensembles. We have a greater trust in results arising from hypercubic-blocked ensembles, but by comparing those results to the thin-link results, we can estimate the magnitude of the systematic error that flavor symmetry breaking introduces.

By using hypercubic blocking in this way, we are in effect using a different interaction matrix for our dynamical and valence quarks. Calculation of a partially quenched

quark-antiquark correlator after hypercubic blocking amounts to the expression:

$$\langle \bar{q}_{a\alpha i;n} q_{b\beta j;m} \rangle$$

$$= Z_{\text{pqQCD}}^{-1} \int [\mathcal{D}U] \; e^{-S_g[U]} \; \det M_{(m_S)}[U] \; M_{(m_V)}[V]_{a\alpha in,b\beta jm}^{-1} \qquad (5.117)$$

While we admit that it is neither clear that this procedure has a clean continuum limit, nor that it corresponds to a well-defined field theory, it should at least prove useful in estimating the magnitude of flavor-symmetry-breaking effects.

It should be noted that, while we do not use hypercubic blocked links in our dynamical interaction matrix, an algorithm for doing so has since been proposed [50, 51, 52].

5.7   Sommer Scale

When the creation of an ensemble begins, a set of values for the parameters in the lattice Lagrangian must be chosen. In our case these parameters are the gauge coupling, via β, and the unitless quark mass m_Q. As discussed in Section 5.1.3, the lattice spacing a is not chosen directly, but rather is related to the other parameters by their renormalization group equations. In order to determine a, we use the ensemble to calculate some dimensionful quantity and then match the result to a physical measurement.

A quantity which proves to be particularly useful for this purpose is the Sommer scale [53, 54], also known as r_0. Its popularity as a scale-setting quantity arises from the fact that it can be calculated on the lattice easily and with small statistical error, its physical value is well determined, and its definition is equally valid in both quenched and unquenched simulations. No other quantity combines all of these advantages.

5.7.1 Static Quark Potential

The definition of the Sommer scale is based on the static quark potential $V(r)$, the potential energy function between two static quarks. The Sommer scale r_0 is defined to be the separation distance r between two static quarks at which:

$$r^2 F(r) = c = 1.65 \tag{5.118}$$

where $F(r)$ is the force between the two quarks:

$$F(r) = \frac{d}{dr} V(r) \tag{5.119}$$

The dimensionless parameter $c = 1.65$ is chosen so as to correspond to an inter-quark distance which is both convenient for calculation on the lattice and well explored phenomenologically. A second common choice is $c = 1$ which defines an alternative scale known as r_1.

The static quark potential dominates the internal physics of heavy quark mesons. Thus, its form can be gleaned from the spectra of both J/ψ and Υ. All successful phenomenological potentials are in agreement as to the behavior of the static quark potential near the Sommer scale, giving:

$$r_0 = 0.49 \, \text{fm} \tag{5.120}$$

5.7.2 Wilson Loops

On the lattice we calculate the static quark potential, and from it r_0, using the expectation value of rectangular Wilson loops $W^{s \times t}$. In general a Wilson loop is any closed path of gauge-link matrices. In the case of rectangular Wilson loops, we define $W^{s \times t}_{\mu\nu;n}$ to be a loop with its lowest corner at site n and with a length of s gauge links

in the direction μ and a breadth of t gauge links in the direction ν:

$$W_{\mu\nu;n}^{s\times t} \equiv \left(\prod_{\ell=1}^{t}U_{\nu;n+(\ell-1)\hat{\nu}}^{\dagger}\right)\left(\prod_{\ell=1}^{s}U_{\mu;n+(\ell-1)\hat{\mu}+t\hat{\nu}}^{\dagger}\right)$$
$$\times \left(\prod_{\ell=t}^{1}U_{\nu;n+s\hat{\mu}+(\ell-1)\hat{\nu}}\right)\left(\prod_{\ell=s}^{1}U_{\mu;n+(\ell-1)\hat{\mu}}\right) \tag{5.121}$$

The action associated with a heavy point-like color charge is simply the path-ordered integral of the gauge field along its trajectory. From this perspective the real trace of the Wilson loop, $\operatorname{Re}\operatorname{tr}\left[W_{i4;0}^{s\times t}\right]$, is thought of as the action associated with creating a quark-antiquark pair at the origin and instantaneously separating them a distance as, having the resulting states propagate an interval of time at, and finally instantaneously reuniting the pair. If we go to the limit of large time separations, the state which dominates the expectation value of the Wilson loop is two static quarks separated by a distance as. By its very definition, the static quark potential $V(r=as)$ corresponds to the energy of this state:

$$\lim_{t\to\infty}\left\langle\operatorname{Re}\operatorname{tr}\left[W^{s\times t}\right]\right\rangle = \mathscr{A}e^{-aV(as)t} \tag{5.122}$$

where $\mathscr{A}$ is the amplitude for creating and annihilating the state. In practice, in order to maximize the information extracted from each configuration and thus minimize statistical error, we calculate the Wilson-loop expectation value by summing over all possible positions and allowed orientations of the loop:

$$W^{s\times t} \equiv \sum_{n}\sum_{\mu\neq 4}W_{\mu 4;n}^{s\times t} \tag{5.123}$$

5.7.3 Corrected Cornell Potential

A standard ansatz for the continuum static quark potential is the Cornell potential:

$$aV_C(as) = v_0 + v_1 s + v_2 \frac{1}{s} \tag{5.124}$$

This ansatz is based on two of the defining features of QCD: confinement and asymptotic freedom. The second term is a string-tension term, which dominates at large s and causes the potential to be confining. The third term is a Coulomb term, which dominates at small s and results in asymptotic freedom. In our case we have expressed the potential in terms of the unitless parameters v_i in order to facilitate our numerical analysis.

The form for the continuum's Coulomb potential follows directly from the continuum's gluon propagator $G_C(\vec{k})$:

$$\left[\frac{1}{s}\right]_C \equiv \frac{1}{s} = 4\pi \int_{-\infty}^{\infty} \frac{d^3k}{(2\pi)^3} G_C(\vec{k}) \cos sk_\mu \tag{5.125}$$

where:

$$G_C(\vec{k}) = \frac{1}{\vec{k} \cdot \vec{k}} \tag{5.126}$$

and the momentum integration variable $\vec{k}$ is unitless. Recall that we have defined the displacement s to be in the direction μ.

On the lattice, finite lattice spacing and the loss of rotational invariance alter the form of the gluon propagator at tree level, and thus modify the Coulomb potential. We denote the tree-level Coulomb potential for a system as:

$$\left[\frac{1}{s}\right]_X \equiv 4\pi \int_{-\pi}^{\pi} \frac{d^3k}{(2\pi)^3} G_X(\vec{k}) \cos sk_\mu \tag{5.127}$$

where X becomes L for the thin-link lattice and H for the hypercubic-blocked lattice. The corresponding tree-level gluon propagators are [55]:

$$G_L(\vec{k}) = \frac{1}{\vec{p} \cdot \vec{p}} \qquad\qquad G_H(\vec{k}) = \frac{\mathfrak{H}(\vec{k})}{\vec{p} \cdot \vec{p}} \qquad (5.128)$$

where:

$$p_i \equiv 2 \sin \frac{k_i}{2} \qquad (5.129)$$

The factor $\mathfrak{H}(\vec{k})$ accounts for the effects of the hypercubic blocking:

$$\mathfrak{H}(\vec{k}) \equiv \left(1 - \frac{\alpha_1}{6} \vec{p} \cdot \vec{\omega}\right)^2 \qquad (5.130)$$

where:

$$\omega_i \equiv p_i \left[1 + \alpha_2(1 + \alpha_3) - \frac{\alpha_2}{4}(1 + 2\alpha_3)(\vec{p} \cdot \vec{p} - p_i^2) + \frac{\alpha_2 \alpha_3}{4} \prod_{j \neq i} p_j^2\right] \qquad (5.131)$$

and α_i are the hypercubic-blocking coefficients.

The values used for the corrected Coulomb potentials are shown in Table 5.1. They were determined using a simple Monte Carlo integration of the momenta integrals (5.127).

We can now introduce a corrected potential:

$$aV_X(as) = v_0 + v_1 s + v_2 \frac{1}{s} + \tilde{v}_2 \left(\left[\frac{1}{s}\right]_X - \frac{1}{s}\right) \qquad (5.132)$$

where the parameter $\tilde{v}_2$ allows for a correction of the continuum's Coulomb term.

Once an ensemble's Wilson-loop expectation values have been calculated, we fit that two-dimensional data to the form:

$$\left\langle \mathrm{Re\,tr}\left[W^{s \times t}\right]\right\rangle = \mathscr{A}_s \exp\left\{-\left[v_0 + v_1 s + v_2 \frac{1}{s} + \tilde{v}_2 \left(\left[\frac{1}{s}\right]_X - \frac{1}{s}\right)\right] t\right\} \qquad (5.133)$$

The range of s and t used in the fit must be chosen carefully in order that t remains large enough that the static-quark state dominates, while both s and t remain small

111

s	$\left[\frac{1}{s}\right]_X$		
	C	L	H
1	1	1.0817(12)	0.7330(12)
2	0.5	0.53793(73)	0.48464(73)
3	0.33333	0.34572(54)	0.33359(53)
4	0.25	0.25513(68)	0.25187(68)
5	0.2	0.20176(43)	0.20071(43)
6	0.16667	0.16868(71)	0.16827(71)
7	0.14286	0.14337(46)	0.14319(46)
8	0.125	0.12597(43)	0.12586(43)
9	0.11111	0.11157(38)	0.11523(38)
10	0.1	0.10009(46)	0.10006(46)
11	0.09091	0.09139(61)	0.09137(61)
12	0.08333	0.08355(66)	0.08355(66)

Table 5.1: Tree-level Coulomb potential for the continuum C, thin-link lattice L, and hypercubic-blocked lattice H. The error listed is the statistical error of the Monte Carlo integration through which the values were determined. Because the same set of sample points was used for the Monte Carlo integration of the thin-link and hypercubic-blocked propagators, their error is highly correlated.

enough that the finite extent of the lattice does not come into play. The results of the fit are values for its free parameters: v_0, v_1, v_2, $\tilde{v}_2$, and an amplitude $\mathscr{A}_s$ for each value of s included in the fit range.

With these values in hand, the ensemble's lattice spacing can be determined via the Sommer scale. The Sommer scale r_0 is defined to be the distance at which the continuum static quark potential meets the criteria of (5.118). Thus after fitting, we drop the correction term from our potential [56], determining r_0 to be:

$$r_0 = a\sqrt{\frac{1.65 + v_2}{v_1}} \tag{5.134}$$

Matching with phenomenological results (5.120), we find:

$$a = \left(0.49\sqrt{\frac{v_1}{1.65 + v_2}}\right) \text{fm} \tag{5.135}$$

or:

$$a^{-1} = \left(395\sqrt{\frac{1.65 + v_2}{v_1}}\right) \text{MeV} \tag{5.136}$$

It is worth noting that, because the GL coefficients are unitless parameters, their calculation does not involve the lattice spacing directly. However, knowledge of the lattice spacing is still critical in that it allows access to such important values as the physical extent of an ensemble's lattice, the physical mass of the pseudo-Goldstone boson, and the expected strength of finite-lattice-spacing errors.

5.8 Meson Propagators

The lightest states produced by each quark bilinear are that bilinear's corresponding staggered meson and its parity partner. A two-point correlation function which

uses a bilinear as its creation and annihilation operator will thus, at large time separa-
tions, be dominated by the propagator of these two states. Therefore, in the manner
outlined in Section 4.3, the bilinear correlators allow us access to the masses of the
staggered mesons, and in the case of the local pion, the decay constant as well.

5.8.1 Bilinear Correlators

In order to analyze meson propagators using lattice techniques, we must first
express the bilinear correlators in a form which leaves them vulnerable to lattice
investigation.

We discuss here only local-bilinear correlators, $\mathcal{S} = \mathcal{F}$, as they are significantly
simpler than more general non-local correlators and are of primary importance in our
study. For a similar discussion which encompasses non-local bilinears, see Appendix
B.3.

We begin with a simple correlator of the form presented in Section 4.3. For
our creation operator, or source, we use the bilinear with the quantum numbers of
whatever meson we have chosen for study. For our annihilation operator, or sink, we
use a wall of the same bilinear, summing over all positions on a time slice in order to
restrict the annihilated states to those with zero spatial momentum:

$$\left\langle \sum_{\substack{\vec{g} \\ g_4=t}} \mathcal{J}_{\mathcal{S},\mathcal{S};g} \mathcal{J}_{\mathcal{S},\mathcal{S};0} \right\rangle \tag{5.137}$$

The large time behavior of this correlator will be dominated by the propagator of the
corresponding staggered meson and its parity partner. We denote the time separation
of the correlator with the unitless parameter t, which takes on the integer values
$[0, L_4 - 1]$

We replace the single bilinear in our source with a linear combination of all local bilinears:

$$\frac{1}{16}\Big\langle \sum_{\substack{\vec{g} \\ g_4=t}} \mathcal{J}_{\mathcal{S},\mathcal{S};g} \sum_{\mathcal{R}} \mathcal{J}_{\mathcal{R},\mathcal{R};0} \Big\rangle \tag{5.138}$$

Our source now overlaps with significantly more states, including all local mesons. However, with the bilinear form of the sink unchanged, only our desired states are annihilated, and thus the correlator continues to measure only the states we desire. Furthermore, we will find that this change allows us to calculate all local correlators simultaneously, minimizing our computational effort.

For our source we switch from a single bilinear to a wall of bilinears at the appropriate time slice. This reduces the statistical error of our calculation without significantly increasing the computation time. The resulting factor of $V \equiv L_1 L_2 L_3$ is accounted for in Appendix 5.8.3.

$$C_{\mathcal{S},\mathcal{S};t} = \frac{1}{16}\Big\langle \sum_{\substack{\vec{g} \\ g_4=t}} \mathcal{J}_{\mathcal{S},\mathcal{S};g} \sum_{\substack{\vec{h} \\ h_4=0}} \sum_{\mathcal{R}} \mathcal{J}_{\mathcal{R},\mathcal{R};h} \Big\rangle \tag{5.139}$$

The sum of all local bilinears has a simple form in terms of χ and $\bar{\chi}$, as demonstrated in Appendix B.1. Only a single contraction over the hypercube is non-zero, that at the lowest corner of the hypercube:

$$\sum_{\mathcal{R}} \mathcal{J}_{\mathcal{R},\mathcal{R};h} = 16 \bar{\chi}_h \chi_h \tag{5.140}$$

Using (5.72) and (5.140), we put the correlator in terms of the fundamental lattice fermion degrees of freedom, χ and $\bar{\chi}$:

$$C_{\mathcal{S},\mathcal{S};t} = \Big\langle \sum_{\substack{\vec{g} \\ g_4=t}} \sum_{B} (-)^{\varphi'_{\mathcal{S},\mathcal{S};B}} \bar{\chi}_{g+B} \chi_{g+B} \sum_{\substack{\vec{h} \\ h_4=0}} \bar{\chi}_h \chi_h \Big\rangle \tag{5.141}$$

115

The situation is complicated slightly by the fact that the fermion field at each site is not a scalar but rather a color vector. Within each bilinear these color vectors are contracted with an implied sum over color. That is, taking χ_a^n to be the fermion degree of freedom with color a at site n:

$$C_{\mathcal{S},\mathcal{S};t} = \left\langle \sum_{\substack{\vec{g} \\ g_4=t}} \sum_B (-)^{\varphi'_{\mathcal{S},\mathcal{S};B}} \sum_a \bar{\chi}_{g+B} \chi_{g+B} \sum_{\substack{\vec{h} \\ h_4=0}} \sum_c \bar{\chi}_h \chi_h \right\rangle \tag{5.142}$$

Via Wick contractions we compute the Grassmann integral over the fermion fields analytically, putting our correlator in terms of only gauge degrees of freedom. We do not allow the bilinears to self-contract by asserting that we only wish to investigate flavor-non-singlet mesons. The contracted χ and $\bar{\chi}$ fields are transformed by the integral into the inverse of the fermion interaction matrix:

$$C_{\mathcal{S},\mathcal{S};t} = \left\langle \sum_{a,c} \sum_{\substack{\vec{g} \\ g_4=t}} \sum_B (-)^{\varphi'_{\mathcal{S},\mathcal{S};B}} \sum_{\substack{\vec{h} \\ h_4=0}} \overline{\bar{\chi}_{g+B} \chi_{g+B} \bar{\chi}_h \chi_h} \right\rangle$$

$$= \left\langle \sum_{a,c} \sum_{\substack{\vec{g} \\ g_4=t}} \sum_B (-)^{\varphi'_{\mathcal{S},\mathcal{S};B}} \sum_{\substack{\vec{h} \\ h_4=0}} M^S[U]^{-1}_{g+B,h} (M^S[U]^T)^{-1}_{g+B,h} \right\rangle$$

$$= \left\langle \sum_{a,c} \sum_{\substack{\vec{g} \\ g_4=t}} \sum_B (-)^{\varphi'_{\mathcal{S},\mathcal{S};B}} \sum_{\substack{\vec{h} \\ h_4=0}} \epsilon_{g+B} \epsilon_h \left| M^S[U]^{-1}_{g+B,h} \right|^2 \right\rangle$$

$$= \left\langle \sum_{a,c} \sum_{\substack{\vec{g} \\ g_4=t}} \sum_B (-)^{\varphi'_{\mathcal{S}+5,\mathcal{S}+5;B}} \sum_{\substack{\vec{h} \\ h_4=0}} \left| M^S[U]^{-1}_{g+B,h} \right|^2 \right\rangle \tag{5.143}$$

where $(M^S[U]^T)^{-1}$ has been put in terms of $M^S[U]^{-1}$ as described in (B.6), and 5 is taken to be the binary four-vector with all elements set to one, such that γ_5 has the proper value under the definition (5.59).

The bilinear correlator is now in terms of quantities which are calculable on the lattice: elements of the inverse of the fermion interaction matrix. Because we do not have access to the inverse interaction matrix itself, but rather use CG to apply the

inverse to a fermion field vector, calculating the individual elements of the inverse matrix, as appears to be required by the correlator, requires a prohibitive number $N_c V$ of applications of the inverse interaction matrix.

In order to reduce the number of inversions required, we calculate the field vectors $X^{(c)\ell}$:

$$X_n^{(c)\ell} = \sum_{\substack{\vec{h} \\ h_4=0}} M^S[U]_{n,h}^{-1} \eta_h^\ell \underset{a,c}{} \tag{5.144}$$

each of which requires only a single application of the inverse interaction matrix.

η^ℓ is a set of noise field vectors for which each element equals a random unit-length phase. The introduction of this random-phase vector eliminates unwanted cross terms from the square of $X^{(c)\ell}$. In the limit of an infinite number of noise vectors N_ℓ:

$$\lim_{N_\ell \to \infty} \frac{1}{N_\ell} \sum_\ell^{N_\ell} \eta_n^{\ell*} \eta_m^\ell = \delta_{n,m} \tag{5.145}$$

The sum for the off-diagonal elements is over an infinite number of random phases and washes out to zero. Thus:

$$\sum_\ell^{N_\ell} \left| X_n^{(c)\ell} \right|^2 = \sum_\ell^{N_\ell} \sum_{\substack{\vec{h} \\ h_4=0}} M^S[U]_{n,h}^{-1*} \eta_h^{\ell*} \sum_{\substack{\vec{f} \\ f_4=0}} M^S[U]_{n,f}^{-1} \eta_f^\ell$$

$$= \sum_{\substack{\vec{h} \\ h_4=0}} \left| M^S[U]_{n,h}^{-1} \right|^2 \tag{5.146}$$

The use of the random-phase vector has contracted $M^S[U]^{-1}$ with itself, allowing us to avoid the calculation of its individual elements.

In practice, we use only a single noise vector, $N_\ell = 1$. This is allowed as the random phases between the cross terms within a single element of the sum over noise vectors is enough to wash out the position-off-diagonal terms in the square of $X^{(c)}$. This single noise vector is effectively provided by the random phase which is automatically present at each lattice site due to the gauge link's local gauge freedom.

Our correlator becomes:

$$C_{\mathcal{S},\mathcal{S};t} = \left\langle \sum_c \sum_{\substack{\vec{g} \\ g_4=t}} \sum_B (-)^{\varphi'_{\mathcal{S}+5,\mathcal{S}+5;B}} \sum_a \left| X^{(c)}_{g+B} \right|_a^2 \right\rangle \tag{5.147}$$

where we have one field vector $X^{(c)}$ for each color:

$$X_n^{(c)} = \sum_{\substack{\vec{h} \\ h_4=0}} M^S[U]^{-1}_{n,h}{}_{a,c} \tag{}$$

$$= \left(M^S[U]^{-1} W^{(c)} \right)_n{}_a \tag{5.148}$$

These N_c field vectors $X^{(c)}$ each require an application of the inverse of the interaction matrix to calculate. To do so, we construct the field vector $W^{(c)}$, which equals one only at color c in the lowest corner of each hypercube on the time slice $n_4 = 0$ and zero elsewhere. The result of applying the inverse interaction matrix to $W^{(c)}$ is $X^{(c)}$.

From inspection it is clear that the calculation of $X^{(c)}$ is independent of both $\mathcal{S}$ and t. Thus, due to our use of the sum of all local bilinears as our source, we are able to calculate the correlator between all local bilinears at all time separations using only N_c inversions per configuration.

In the case of the local pion, $\mathcal{S} = 5$ and $\varphi'_{\mathcal{S}+5,\mathcal{S}+5;B} = \varphi'_{0,0;B} = 0$ for all B. The correlator becomes quite simple:

$$C_{5,5;t} = \left\langle \sum_c \sum_{\substack{\vec{g} \\ g_4=t}} \sum_B \sum_a \left| X^{(c)}_{g+B} \right|_a^2 \right\rangle \tag{5.149}$$

In practice we calculate the correlator multiple times, shifting our origin's time component and averaging over the results. For our study we repeated the calculation every four lattice steps in time. This allows us to extract the maximum amount of information from each configuration, minimizing our statistical error.

5.8.2 Meson Masses

For large time separations the bilinear correlator will be dominated by the propagator of the lightest states it creates. In our case those are the appropriate staggered meson and its parity partner. For the moment we will ignore the parity partner.

For a bilinear correlator with its source contained on the time slice $n_4 = 0$ and its sink contained on the time slice $n_4 = t$, we see from (4.18) that the large t behavior will be:

$$\mathscr{A} e^{-aMt} \tag{5.150}$$

where M is the mass of the staggered meson and $\mathscr{A}$ is the amplitude for creating and annihilating the meson state. Note that we can define a unitless mass $\check{M} = aM$ by absorbing into M the factor of a. Such unit-free quantities prove useful, as numerical procedures can only be used to determine dimensionless values. Throughout, we use the notation $\check{X}$ to indicate some quantity X after the appropriate powers of lattice spacing have been absorbed so as to make $\check{X}$ dimensionless.

The lattice's periodic boundary conditions allow states to propagate from source to sink along both time directions. Accounting for this in our propagator, we find:

$$\mathscr{A} \left(e^{-aMt} + e^{-aM(L_4 - t)} \right) \tag{5.151}$$

As discussed in Section 5.8.1, we do not use a single-time-slice sink, but rather a full-bilinear sink which lives both on time slice $n_4 = t$ and $n_4 = t + 1$. Thus, in addition to this approximately doubling the magnitude of our correlator, the states must propagate different distances when being annihilated at the two time slices of

our sink:

$$\mathscr{A}\left[\left(e^{-aMt} + e^{-aM(L_4-t)}\right) + \left(e^{-aM(t+1)} + e^{-aM(L_4-1-t)}\right)\right]$$

$$= \mathscr{A}\left(1 + e^{-aM}\right)\left(e^{-aMt} + e^{-aM(L_4-1-t)}\right) \tag{5.152}$$

Accounting now for the negative-parity state, whose propagator oscillates in sign each time step, the final form for our large-time bilinear correlator is:

$$C_{\mathcal{S},\mathcal{F};t} = \mathscr{A}_+\left(1 + e^{-aM_+}\right)\left(e^{-aM_+t} + e^{-aM_+(L_4-1-t)}\right)$$

$$+ \mathscr{A}_-(-)^t\left(1 - e^{-aM_-}\right)\left(e^{-aM_-t} - e^{-aM_-(L_4-1-t)}\right) \tag{5.153}$$

where $\mathscr{A}_+$ and $\mathscr{A}_-$ are the amplitude for the creation and annihilation of the positive and negative parity states, and M_+ and M_- are those states' masses. Recall that L_4 has been defined to be even.

In the case of the local pion, there is no overlap with the negative parity state, $\mathscr{A}_- = 0$:

$$C_{5,5;t} = \mathscr{A}_{\pi_5}\left(1 + e^{-aM_{\pi_5}}\right)\left(e^{-aM_{\pi_5}t} + e^{-aM_{\pi_5}(L_4-1-t)}\right) \tag{5.154}$$

where $\mathscr{A}_{\pi_5}$ is the amplitude for creating and annihilating the local pion state using our source and sink operators, and M_{π_5} is the mass of the local pion.

Thus, after completing a lattice calculation of $C_{5,5;t}$, we can fit the results to the form described by (5.154) and extract the mass of the local pion.

5.8.3   Meson Decay Constants

While the local pion mass can be extracted without any consideration for the correlator's amplitude $\mathscr{A}_{\pi_5}$, the local pion decay constant f_{π_5} can not. Thus, careful attention must be given to the normalization of the source and sink operators.

Recalling (4.18), we put our large-time correlator's amplitude in terms of our source and sink operator's overlap with the local pion state:

$$C_{5,5;t} = \frac{1}{2\check{M}_{\pi_5}V} \langle 0|\mathcal{O}_{\text{sink}}|\pi_5\rangle\langle\pi_5|\mathcal{O}_{\text{source}}|0\rangle\mathfrak{C}_{5,5;t} \tag{5.155}$$

where $|\pi_5\rangle$ is the dimensionless zero-momentum staggered local-pion state and:

$$\mathfrak{C}_{5,5;t} \equiv \left(1 + e^{-\check{M}_{\pi_5}}\right)\left(e^{-\check{M}_{\pi_5}t} + e^{-\check{M}_{\pi_5}(L_4-1-t)}\right) \tag{5.156}$$

From (5.141) we identify our source and sink operators as:

$$\mathcal{O}_{\text{source}} = \sum_{\substack{\vec{h} \\ h_4=0}} \bar{\chi}_h\chi_h = \sum_{\substack{\vec{n}\ \text{even} \\ n_4=0}} \bar{\chi}_n\chi_n$$

$$= \sum_{\substack{\vec{n}\ \text{even} \\ n_4=0}} \epsilon_n\bar{\chi}_n\chi_n \tag{5.157}$$

and:

$$\mathcal{O}_{\text{sink}} = \sum_{\substack{\vec{g} \\ g_4=t}}\sum_{\substack{\vec{B} \\ B_4=0}} (-)^{\varphi'_{5,5;B}}\bar{\chi}_{g+B}\chi_{g+B}$$

$$= \sum_{\substack{\vec{n} \\ n_4=t}} \epsilon_n\bar{\chi}_n\chi_n \tag{5.158}$$

Our addition of an ϵ_n factor to the source is allowed as the source is only non-zero at even sites. We consider only a single time slice, $B_4 = 0$, of our two-time-slice sink operator, as the form of $\mathfrak{C}_{5,5;t}$ already accounts for a second time slice.

We can now put our correlator in terms of $\langle 0|\epsilon_n\bar{\chi}_n\chi_n|\pi_5\rangle$, the overlap between the local pion state and a single-site operator with the local pion's quantum numbers. We find:

$$\langle 0|\mathcal{O}_{\text{source}}|\pi_5\rangle = \frac{V}{2^3}\langle 0|\epsilon_n\bar{\chi}_n\chi_n|\pi_5\rangle \tag{5.159}$$

$$\langle 0|\mathcal{O}_{\text{sink}}|\pi_5\rangle = V\langle 0|\epsilon_n\bar{\chi}_n\chi_n|\pi_5\rangle \tag{5.160}$$

121

and, thus:

$$C_{5,5;t} = \frac{V}{16\check{M}_{\pi_5}}|\langle 0|\epsilon_n\bar{\chi}_n\chi_n|\pi_5\rangle|^2\mathfrak{C}_{5,5;t} \tag{5.161}$$

In the continuum, a meson's decay constant can be defined by the meson state's overlap with the appropriate weak interaction bilinear. In the case of the continuum pion, this definition is:

$$\sqrt{2}f_\pi M_\pi^2 = (m_u + m_d)\langle 0|\bar{u}\gamma_5 d|\pi^+\rangle \tag{5.162}$$

where $|\pi^+\rangle$ is the continuum's zero-momentum π^+ state. Recall that we are using the pion decay constant normalization in which $f_\pi \simeq 92.4\,\text{MeV}$. In order to put our correlator in terms of the pion decay constant, we use the discretization correspondence [57]:

$$\langle 0|\bar{u}\gamma_5 d|\pi^+\rangle \quad \rightarrow \quad \frac{1}{a^2\sqrt{4}}\langle 0|\epsilon_n\bar{\chi}_n\chi_n|\pi_5\rangle \tag{5.163}$$

Thus, combining (5.161), (5.162), and (5.163), our correlator becomes:

$$\begin{aligned}
C_{5,5;t} &= \frac{f_{\pi_5}^2 M_{\pi_5}^3(a^3 V)}{8m_q^2}\mathfrak{C}_{5,5;t} \\
&= \frac{\check{f}_{\pi_5}^2 \check{M}_{\pi_5}^3 V}{8m_Q^2}\mathfrak{C}_{5,5;t}
\end{aligned} \tag{5.164}$$

where f_{π_5} is the local pion decay constant and $\check{f}_{\pi_5}$ is the corresponding dimensionless value.

Knowing the normalization of our correlator, we now have the ability to extract both the local pion mass and decay constant.

The local pion decay constant is protected by the staggered formulation's even-odd symmetry. This protection does not occur for any of the other fifteen staggered pions, as the staggered action breaks their corresponding axial vector symmetries. Thus, making a connection between the lattice propagator of one of these pions and

its continuum decay constant requires the calculation of a renormalization factor. The process is thus much more involved than for the local pion case.

CHAPTER 6

PARTIALLY QUENCHED CHIRAL PERTURBATION THEORY

In Chapter 3 we presented ChPT's prediction for the quark mass dependence of the chiral pseudo-Goldstone boson's mass and decay constant. In Chapter 5 we detailed lattice techniques for calculating that mass and decay constant. However, performing a set of lattice calculations using different values for the quark mass is extremely computationally cumbersome. As we are constrained by finite computer resources, we find it easier to vary only the valence quark mass. That is, we make use of the partially quenched approximation of Section 5.2.6.

ChPT is the low-energy effective field theory for the light bound states of unquenched QCD. Thus, its predictions are not valid in the context of our partially quenched calculations. In order to bridge this gap between ChPT and partial quenching, we must make quantitative sense of the effects of partial quenching. The culmination of this process is partially quenched Chiral Perturbation Theory (pqChPT), a low-energy effective field theory for the light bound states of pqQCD [58, 59].

Note that throughout this chapter, as in Chapter 3, we work in an infinite volume continuum.

6.1 Partially Quenched Quantum Chromodynamics

As discussed in Section 5.2.6, pqQCD is not a well-behaved unitary field theory. Nonetheless, we are not prevented from proposing a quark content for pqQCD, nor from discussing pqQCD in a Lagrangian context.

Partially quenched QCD clearly contains two types of fermionic quark flavors: dynamical quarks and valence quarks. As is illustrated by (5.32), the dynamical quark field appears in the partition function's Boltzmann weight but does not appear in the operators whose expectation value we calculate. The valence quark field, on the other hand, appears only in these operators and does not contribute to the Boltzmann weight. The challenge before us is to construct a quark content for pqQCD in which these abnormal attributes are a natural consequence.

Eliminating dynamical quarks from external operators is a simple matter of restricting ourselves to calculating only the expectation value of operators which involve valence quarks. By definition, this was our intent from the beginning.

Eliminating the valence quarks' natural contribution to the theory's Boltzmann weight is more involved. We introduce a set of ghost quark flavors, scalar quark fields with incorrect spin statistics, with an interaction matrix equivalent to the valence quarks'. As the ghost quarks are bosons, their functional integral results in the inverse of the interaction-matrix determinant. If, for each valence quark flavor, we include a ghost quark flavor of equal mass, the two contributions to the theory's Boltzmann weight will cancel. The valence quark interaction-matrix determinant, which would naturally appear in the Boltzmann weight, is effectively eliminated.

Thus, pqQCD can be thought of as having three types of quark flavors: dynamical quarks, valence quarks, and ghost quarks. The first two are standard fermionic

quarks and the last is bosonic. In our study, we use dynamical and valence quark flavors which are independently degenerate. The mass of the ghost quarks is then set equal to the valence quark mass. We represent the number of dynamical quarks as N_f and the number of valence quarks, and therefore ghost quarks as well, as N_v. From the perspective of this quark content, the pqQCD partition function, before the integration over quark degrees of freedom, is seen to be:

$$Z_{\mathrm{pqQCD}} = \int [\mathcal{D}A_\mu][\mathcal{D}q_v][\mathcal{D}\bar{q}_v][\mathcal{D}q_s][\mathcal{D}\bar{q}_s][\mathcal{D}\tilde{q}_g][\mathcal{D}\bar{\tilde{q}}_g] \; e^{-\int_x \mathscr{L}_{\mathrm{pqQCD}}} \qquad (6.1)$$

where:

$$\begin{aligned}
\mathscr{L}_{\mathrm{pqQCD}} &= \frac{1}{2}\mathrm{tr}\big[F_{\mu\nu}F^{\mu\nu}\big] \\
&+ \bar{q}_v\big(\gamma^\mu D_\mu + m_v\big)q_v + \bar{q}_s\big(\gamma^\mu D_\mu + m_s\big)q_s + \bar{\tilde{q}}_g\big(\gamma^\mu D_\mu + m_v\big)\tilde{q}_g
\end{aligned} \qquad (6.2)$$

We use q_v to represent the vector of N_v fermionic valence quark flavors with mass m_v, q_s to represent the vector of N_f fermionic dynamical quark flavors with mass m_s, and $\tilde{q}_g$ to represent the vector of N_v bosonic ghost quark flavors with mass m_v. Our use of m_s here to denote the dynamical quark mass, and elsewhere to denote the Standard Model's strange quark mass, should remain clear via context.

Performing the functional integral over quark degrees of freedom results in the cancellation discussed above:

$$\begin{aligned}
Z_{\mathrm{pqQCD}} &= \int [\mathcal{D}A_\mu] \; e^{-\int_x \mathscr{L}_g} \; \frac{\det\big[\gamma^\mu D_\mu + m_v\big]}{\det\big[\gamma^\mu D_\mu + m_v\big]} \det\big[\gamma^\mu D_\mu + m_s\big] \\
&= \int [\mathcal{D}A_\mu] \; e^{-\int_x \mathscr{L}_g} \; \det\big[\gamma^\mu D_\mu + m_s\big]
\end{aligned} \qquad (6.3)$$

We can see by comparison to (5.32) that the pqQCD partition function (6.3) has the appropriate form to correspond to the calculation of partially quenched expectation values.

The above construction of the quark content of pqQCD can also be understood in the context of perturbation theory. From this perspective, dynamical quarks appear only in closed quark loops, and not in the external legs of Feynman diagrams. Valence quarks, on the other hand, appear only in external legs and never in loops. To insure that dynamical quarks appear only in loops, we restrict ourselves to calculating matrix elements between valence-quark external states. To remove valence-quark loops, we again introduce ghost quarks. For every Feynman diagram which includes a valence-quark loop, there will be an identical diagram in which that loop is replaced by a ghost-quark loop. As bosons, the ghost-quark loops will appear with opposite sign. Thus, all diagrams which include valence-quark loops are canceled.

It should be noted that, although we have conceived of a quark content and constructed a Lagrangian for pqQCD, the theory remains pathological. The advent of scalar quarks, with incorrect spin statistics, spoils unitarity. Furthermore, we are artificially restricting the physical states of the theory, removing dynamical- and ghost-quark external states. This effectively sets elements of the S matrix to zero, further ruining unitary. However, because it is the partially quenched approximation itself which is non-unitary, we can not hope to construct a unitary field theory with the necessary partition function.

6.2 Partially Quenched Flavor Symmetry

Just as the flavor symmetry group of QCD dictates the form of ChPT, so will the flavor symmetry group of pqQCD dictate the form of pqChPT.

The flavor symmetry group of massless QCD, $SU(N_f)_L \otimes SU(N_f)_R$, follows directly from its quark content. Massless pqQCD has an analogous flavor symmetry

group which also follows from the quark content proposed above. First, we collect the standard and ghost quarks into a single vector:

$$q = \begin{bmatrix} q_v \\ q_s \\ \tilde{q}_g \end{bmatrix} \qquad\qquad \bar{q} = \begin{bmatrix} \bar{q}_v & \bar{q}_s & \bar{\tilde{q}}_g \end{bmatrix} \qquad (6.4)$$

This mixture of fermions and bosons causes the flavor symmetry group to be a graded group, $SU(N_v+N_f|N_v)_L \otimes SU(N_v+N_f|N_v)_R$. In truth, there are subtleties which arise in the identification of pqQCD's flavor symmetry group. However, Sharpe demonstrates in [60] that the above graded group generates the correct Ward identities for pqQCD. Thus, while it is not the exact flavor symmetry group of pqQCD, it is still appropriate to use in constructing pqChPT.

6.3 Graded Groups

Matrices which are elements of a graded group have the following distinguishing properties. The graded group element $\Sigma \in SU(N|M)$ can be written in block form:

$$\Sigma = \begin{bmatrix} A & C \\ D & B \end{bmatrix} \qquad (6.5)$$

where A and B are respectively $N \times N$ and $M \times M$ matrices of standard commuting numbers, while C and D are respectively $N \times M$ and $M \times N$ matrices of anticommuting numbers. In order to preserve the correct behavior of the adjoint, the complex conjugate of a product of these anticommuting numbers is defined to switch their order:

$$(ab)^* \equiv b^* a^* \qquad (6.6)$$

128

where a and b are elements of C or D. Finally, the super trace of a graded group element is defined as:

$$\mathrm{sTr}\,\Sigma \equiv \mathrm{Tr}\,A - \mathrm{Tr}\,B \tag{6.7}$$

from which the definition of the super determinant is based:

$$\mathrm{sdet}\,\Sigma \equiv \exp\Big\{\mathrm{sTr}\big[\ln\Sigma\big]\Big\} = \frac{\det\big[A - CB^{-1}D\big]}{\det B} \tag{6.8}$$

Using these properties for graded group elements, the graded group $SU(N_v + N_f|N_v)_L \otimes SU(N_v + N_f|N_v)_R$ has the appropriate behavior to act as the flavor symmetry group for pqQCD's mixture of fermionic and bosonic quarks.

6.4 Partially Quenched Chiral Lagrangian

With the flavor symmetry group for pqQCD in hand, we are now in a position to develop a low-energy effective field theory for the light bound states of pqQCD, mirroring closely the process in Chapter 3.

We begin with an assumption that the full flavor symmetry of pqQCD is spontaneously broken by a chiral condensate, from $SU(N_v + N_f|N_v)_L \otimes SU(N_v + N_f|N_v)_R$ down to $SU(N_v + N_f|N_v)_V$, just as occurs in full QCD as discussed in Section 2.1.4. The result is set of Goldstone particles, pqQCD's light mesons. Note that we use the term mesons loosely, as several of these particles are fermions. The fermionic subset of Goldstone particles are those which correspond to broken symmetries whose generator's non-zero elements are contained by the sub-matrices C and D.

Partially quenched ChPT will be a low-energy effective field theory for these Goldstone particles. We collect the partially quenched mesons into a flavor-space matrix

Φ, multiplying each meson field π^a by its corresponding broken flavor symmetry generator:

$$\Phi \equiv \pi^a \tau^a = \begin{bmatrix} \phi_{q\bar{q}} & \phi_{q\tilde{\bar{q}}} \\ \phi_{\tilde{q}\bar{q}} & \phi_{\tilde{q}\tilde{\bar{q}}} \end{bmatrix} \tag{6.9}$$

where $\phi_{q\bar{q}}$ is an $N_v + N_f \times N_v + N_f$ matrix containing bosonic bound states of ordinary quark-antiquark pairs, $\phi_{\tilde{q}\tilde{\bar{q}}}$ is an $N_v \times N_v$ matrix containing bosonic bound states of ghost quark-antiquark pairs, and $\phi_{q\tilde{\bar{q}}}$ and $\phi_{\tilde{q}\bar{q}}$ are respectively $N_v + N_f \times N_v$ and $N_v \times N_v + N_f$ matrices containing fermionic bound states of mixed quark-antiquark pairs. We further subdivide the matrix $\phi_{q\bar{q}}$, making its dynamical- and valence-quark blocks explicit:

$$\phi_{q\bar{q}} = \begin{bmatrix} \phi_{v\bar{v}} & \phi_{v\bar{s}} \\ \phi_{s\bar{v}} & \phi_{s\bar{s}} \end{bmatrix} \tag{6.10}$$

where the $N_v \times N_v$ matrix $\phi_{v\bar{v}}$ holds the mesons which contain a valence quark-antiquark pair. As only valence-quark fields are used in the operators whose expectation values we calculate, it is only this block of mesons whose masses we measure directly in our partially quenched lattice calculations. From the perspective of pqChPT, all other mesons appear only at one-loop order and higher. From now on we will refer to a valence quark-antiquark meson as a pion, as it coincides with the state in our partially quenched staggered calculation to which we have designated that name. We define the unitary field matrix Σ as:

$$\Sigma \equiv e^{2i\pi^a \tau^a / f} \in SU(N_v + N_f | N_v) \tag{6.11}$$

The quark masses break pqQCD's flavor symmetry explicitly, granting the Goldstone particles a light mass. We incorporate this symmetry breaking into pqChPT using a factor whose matrix structure is equivalent to the quark mass matrix:

$$\chi \equiv 2\mu\mathcal{M} = 2\mu \, \mathrm{diag}(\underbrace{m_v, \ldots,}_{N_v} \underbrace{m_s, \ldots,}_{N_f} \underbrace{m_v, \ldots}_{N_v}) \tag{6.12}$$

130

As stated above, we use N_v valence quarks of mass m_v, N_f dynamical quarks of mass m_s, and N_v ghost quarks of mass m_v.

Considering all terms which respect both Lorentz and pqQCD's graded flavor symmetry, except via insertion of $\mathcal{M}$, and expanding simultaneously in both meson momentum and meson mass, we construct the NLO partially quenched chiral Euclidean Lagrangian:

$$
\begin{aligned}
\mathscr{L}_{\text{pqChPT}}^{\text{NLO}} \;=\; & \frac{f^2}{4}\text{sTr}\big[\partial_\mu\Sigma^\dagger\partial^\mu\Sigma\big] - \frac{f^2}{4}\text{sTr}\big[\Sigma^\dagger\chi + \chi\Sigma\big] \\
& - L_1\Big(\text{sTr}\big[\partial_\mu\Sigma^\dagger\partial^\mu\Sigma\big]\Big)^2 \\
& - L_2\Big(\text{sTr}\big[\partial_\mu\Sigma^\dagger\partial_\nu\Sigma\big]\text{sTr}\big[\partial^\mu\Sigma^\dagger\partial^\nu\Sigma\big]\Big) \\
& - L_3\Big(\text{sTr}\big[\partial_\mu\Sigma^\dagger\partial^\mu\Sigma\partial_\nu\Sigma^\dagger\partial^\nu\Sigma\big]\Big) \\
& + L_4\Big(\text{sTr}\big[\partial_\mu\Sigma^\dagger\partial^\mu\Sigma\big]\text{sTr}\big[\Sigma^\dagger\chi + \chi\Sigma\big]\Big) \\
& + L_5\Big(\text{sTr}\big[\partial_\mu\Sigma^\dagger\partial^\mu\Sigma\big(\Sigma^\dagger\chi + \chi\Sigma\big)\big]\Big) \\
& - L_6\Big(\text{sTr}\big[\Sigma^\dagger\chi + \chi\Sigma\big]\Big)^2 \\
& - L_7\Big(\text{sTr}\big[\Sigma^\dagger\chi - \chi\Sigma\big]\Big)^2 \\
& - L_8\Big(\text{sTr}\big[\Sigma^\dagger\chi\Sigma^\dagger\chi\big] + \text{sTr}\big[\chi\Sigma\chi\Sigma\big]\Big) \qquad (6.13)
\end{aligned}
$$

Note that this Lagrangian has the same form as that for standard ChPT (3.24), with the only differences arising from our use of a graded flavor symmetry group.

As long as we restrict our choice for the dynamical and valence quark masses such that they remain within the radius of convergence of pqChPT, the partially quenched chiral Lagrangian will accurately describe the two-dimensional quark mass dependence of the mesons' characteristics and behavior.

6.5 Next-to-Leading Order Meson Properties

Using the NLO partially quenched chiral Lagrangian, we determine NLO expressions for the mass [61]:

$$M_{vv}^2 = z m_v (4\pi f)^2 \left\{ 1 + \frac{z}{N_f} \left(2m_v - m_s \right) \ln z m_v + \frac{z}{N_f} \left(m_v - m_s \right) \right.$$
$$\left. + z m_v \left(2\alpha_8 - \alpha_5 \right) + z m_s N_f \left(2\alpha_6 - \alpha_4 \right) \right\} \tag{6.14}$$

and decay constant:

$$f_{vv} = f \left\{ 1 + \frac{z N_f}{4} \left(m_v + m_s \right) \ln \frac{z}{2} \left(m_v + m_s \right) + z m_v \frac{\alpha_5}{2} + z m_s N_f \frac{\alpha_4}{2} \right\} \tag{6.15}$$

of the partially quenched chiral pseudo-Goldstone boson containing two degenerate valence quarks, our pion. The quantity z is defined in (3.102). Note that in the unquenched case, $m_q = m_v = m_s$, these expressions correspond exactly to those from ChPT: (3.100) and (3.101).

For the pqChPT expressions for the pion mass and decay constant in the case of arbitrary quark masses, the reader is referred to [62].

Note that in the limit of zero valence quark mass, $m_v \to 0$, the logarithmic term in M_{vv}^2 diverges. Such divergent log terms in pqChPT expressions are often referred to as quenched chiral logs, or sometimes simply as quenched logs. They are directly analogous to the chiral logs of standard ChPT. The appearance of quenched chiral logs makes it clear that the true chiral limit of pqQCD is reached only by taking the dynamical and valence quark masses to zero simultaneously. In that case, the quenched log terms remain finite.

Quenched logs also appear in expressions derived from the low-energy chiral theory of fully quenched QCD, quenched Chiral Perturbation Theory (qChPT). We will not
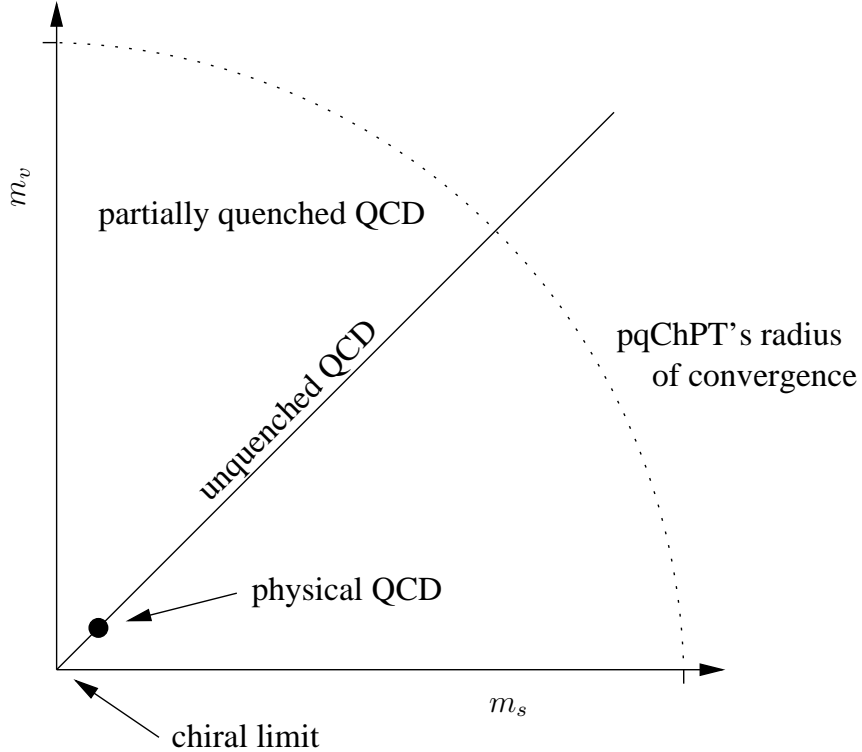
Figure 6.1: The quark-mass plane of pqQCD.

discuss qChPT in detail, noting only that such logs are divergent when the only quark mass available for adjustment, the valence quark mass, is taken to zero. Thus, doubt is thrown onto the very existence of a chiral limit under the quenched approximation.

6.6 Physical Results from Partially Quenched Calculations

There are two critical points which allow pqChPT to act as a bridge between our unphysical partially quenched calculations and the physical GL coefficients.

The first is that unquenched QCD is a subset of pqQCD. If we visualize all possible dynamical- and valence-quark-mass choices as defining the plane of pqQCD, as shown in Figure 6.1, unquenched QCD is seen to lie on the diagonal line at which $m_v = m_s$.

The second point is that the two-dimensional quark mass dependence of pqChPT's Lagrangian is known and explicitly included up to whatever order we have chosen to work. Thus, the GL coefficients are not functions of quark mass, but rather are constants throughout the quark-mass plane. Most importantly, they are constants as we move across the line of unquenched QCD.

Thus, the GL coefficients of pqChPT and standard ChPT are the same. If we perform a partially quenched calculation and, via pqChPT, determine from the calculation values for the GL coefficients, we have in fact generated valid results for the GL coefficients of the physical world.

Additionally, in a unquenched calculation, we are restricted to exploring quark mass dependence only along the unquenched line. In the case of the pion mass, it is clear from (3.100) that such an exploration would grant us access only to the GL coefficient combination $2\alpha_8 - \alpha_5 + 2N_f\alpha_6 - N_f\alpha_4$. On the other hand, the use of partial quenching grants us additional moment arms with which to extract information from our calculated quantities. In the case of the pion mass, varying the dynamical and valence quark masses independently allows for the determination of two coefficient combinations: $2\alpha_8 - \alpha_5$ and $2\alpha_6 - \alpha_4$.

It should be noted that the dependence of the partially quenched chiral Lagrangian on the number of dynamical quark flavors N_f is not known. Thus, the GL coefficients are functions of N_f. As a consequence, in order for our partially quenched results to be considered valid results for the physical coefficients, we are forced to use a physical number of dynamical light quarks, $N_f = 3$, in our calculations. We in fact do just that.

In standard QCD, the η' can be thought of as obtaining its large mass via the summation over quark-loop chains which appear in its propagator. From this perspective it is evident that the η' of fully quenched QCD will be lighter than expected, as any such quark loops have been removed. Thus, the η' must be included in any low-energy effective theory for qQCD such as qChPT. This inclusion introduces additional couplings to qChPT and destroys any correspondence of its couplings to the couplings of physical ChPT. While it was not initially known whether partially quenched QCD suffers from this same flaw, Sharpe demonstrates in [60] that the η' of pqQCD is in fact heavy, and can be safely left out of pqChPT. Thus, the correspondence between the GL coefficients of pqChPT and ChPT is retained.

6.7 Calculation of the Gasser-Leutwyler Coefficients

A basic outline of our procedure for the calculation of the GL coefficients is as follows. We calculate the local pion's bilinear correlator, using $N_f = 3$ staggered lattice techniques as detailed in Chapter 5, for a range of dynamical and valence quark masses. We then fit those results, using the techniques described in Chapter 7 and over a fit range contained by the radius of convergence of pqChPT, to pqChPT's corresponding predictions for the correlator's quark-mass dependence.

In order to facilitate a numerical fit of the lattice results to the predicted forms from pqChPT, those forms must be expressed in terms of dimensionless parameters. Making use of (5.164), we build pqChPT's prediction for the correlator's form:

$$C_{5,5;t} = \frac{\check{f}_{\pi_5}^2 \check{M}_{\pi_5}^3 V}{8 m_V^2} \left(1 + e^{-\check{M}_{\pi_5}}\right)\left(e^{-\check{M}_{\pi_5} t} + e^{-\check{M}_{\pi_5}(L_4 - 1 - t)}\right) \qquad (6.16)$$

where, using (6.14):

$$\check{M}_{\pi_5}^2 = \check{z}m_V(4\pi\check{f})^2 \left\{ 1 + \frac{\check{z}}{N_f}(2m_V - m_S)\ln \check{z}m_V + \frac{\check{z}}{N_f}(m_V - m_S) \right.$$
$$\left. + \check{z}m_V\big(2\alpha_8 - \alpha_5\big) + \check{z}m_S N_f\big(2\alpha_6 - \alpha_4\big) \right\} \qquad (6.17)$$

using (6.15):

$$\check{f}_{\pi_5} = \check{f}\left\{ 1 + \frac{\check{z}N_f}{4}(m_V + m_S)\ln\frac{\check{z}}{2}(m_V + m_S) + \check{z}m_V\frac{\alpha_5}{2} + \check{z}m_S N_f\frac{\alpha_4}{2} \right\} \qquad (6.18)$$

and $\check{z}$ and $\check{f}$ are dimensionless parameters related to z and f by appropriate powers of the lattice spacing. The unitless dynamical and valence quark masses are denoted by m_S and m_V.

The products of this fit are values for the physical GL coefficients of ChPT.

6.8 Constant Dynamical Quark Mass

As discussed in Section 5.2.6, changing the valence quark mass is significantly less computationally demanding than changing the dynamical quark mass. Thus, for those ensembles which have the smallest expected systematic error, and thus those which are the most computationally demanding, we use a single dynamical-quark-mass value, and vary only the valence quark mass. Fortunately, variation of the valence quark mass grants us access to the GL coefficient combination we are most interested in, the combination $2\alpha_8 - \alpha_5$.

The GL coefficient combination $2\alpha_8 - \alpha_5$ originally became of interest because it is the unknown term in Δ_M (3.35), where Δ_M is the difference in the NLO contributions to the physical pion and kaon masses (3.34). Clearly, any such differences in the NLO terms arise due to the contrasting valence-quark content of the pion and kaon. Thus,

it is of no surprise that variation of only the valence quark mass grants access to the coefficient combination critical in the determination of Δ_M.

Without variation of the dynamical quark mass, the terms in (6.17) and (6.18) which depend on m_S can not be accounted for. Thus, in cases where we have calculated the local-bilinear correlator only along a line of constant dynamical quark mass, we absorb the unknown NLO m_S dependence into the LO coefficients $\check{z}$ and $\check{f}$. This change results in a deviation from the original expressions only when $\check{z}$ and $\check{f}$ appear in NLO terms, and thus the error due to this change occurs at NNLO. The resulting expression for the pion mass is:

$$\check{M}_{\pi_5}^2 = \check{z}m_V(4\pi\check{f})^2\left\{1 + \frac{\check{z}}{N_f}(2m_V - m_S)\ln\check{z}m_V + \frac{\check{z}}{N_f}(m_V - m_S)\right.$$
$$\left. + \check{z}m_V(2\alpha_8 - \alpha_5)\right\} \tag{6.19}$$

and for the pion decay constant is:

$$\check{f}_{\pi_5} = \check{f}\left\{1 + \frac{\check{z}N_f}{4}(m_V + m_S)\ln\frac{\check{z}}{2}(m_V + m_S) + \check{z}m_V\frac{\alpha_5}{2}\right\} \tag{6.20}$$

These forms are then used in (6.16) in place of (6.17) and (6.18).

CHAPTER 7

DATA MODELING

Throughout our study, in order to extract information from our lattice calculations, we model the results to theoretical predictions. We present here details of that process.

7.1 Lattice Measurements

The product of a lattice calculation is the value of some operator evaluated under each gauge configuration of an ensemble. We refer to such an operator evaluation as a measurement, using the term in the loosest sense, as no actual experimental measurement is taking place.

An operator's form will contain some number of adjustable parameters x_n, which we label as measure parameters. For each measurement a value is be chosen for each of these measure parameters. We codify the results of the measurements as:

$$y_a(x_1, x_2, x_3, \ldots) \equiv \langle \mathcal{O}(x_1, x_2, x_3, \ldots) \rangle_{[U]_a} \tag{7.1}$$

where a denotes the configuration under which the operator was evaluated, and runs from 1 to N, where N is the number of configurations in the ensemble, and the various x_n designate the location in the operator's adjustable-parameter space at

which the measurement is made. Each measure parameter x_n takes on a discrete set of values $x_{n;i}$, where i enumerates the values for that measure parameter at which we have chosen to make measurements, running from 1 to $N_{M;n}$. As an example, in the evaluation of a single bilinear correlator, there is one measure parameter, the bilinears' time separation, which takes on integer values in the range $[0, L_4 - 1]$.

We generally use the more compact notation $y_{a;x}$, where the index x enumerates all possible combinations of allowed values for the measure parameters. It runs from 1 to N_M, where:

$$N_M = \prod_n N_{M;n} \tag{7.2}$$

representing the total number of measurements made on each configuration.

7.2 Data Blocking

As a result of autocorrelation, as described in Section 4.2.4, measurements on neighboring configurations of a Markov chain are correlated. However, to correctly account for the statistical error in our data, we require that each measurement be independent. In order to meet this requirement, we divide the Markov chain into N_K blocks, each of which contains $N_B = N/N_K$ neighboring configurations. We choose an N_B larger than the Markov chain's autocorrelation length. Thus, the average measurement within each block can be treated as a single uncorrelated measurement, independent of the results from other blocks.

From now on we work only with this blocked data:

$$y_{B;x} = \frac{1}{N_B} \sum_{a \in B} y_{a;x} \tag{7.3}$$

It is worth noting that, for Gaussian distributed data, the standard error of our result is independent of the value chosen for N_B, assuming N_B is larger than the

chain's autocorrelation length but is still small enough that N_K remains large. Increasing N_B reduces the variance between blocks but also reduces our sample size. For Gaussian distributed data, the two effects cancel exactly.

7.3   Data Correlation

We visualize all of the measurements on a single block as defining the location of a single point in a large-dimensional measurement space, where each possible combination of measure-parameter values represents a dimension of the space. From this perspective, the index x of each measurement $y_{B;x}$ is seen as indexing the components of the point's position.

The full set of measurements for an ensemble is seen as a cloud of points in this measurement space. We expect the data points to cluster around some central value and their density to die off as a Gaussian in all directions. The shape of this cloud, in addition to the rate of its falloff along the various directions, characterize the statistical error of our measurements.

For each measurement there is an ensemble-average value:

$$\overline{y}_x = \langle y_x \rangle = \frac{1}{N_K} \sum_B y_{B;x} \tag{7.4}$$

which corresponds to the expectation value of the operator $\mathcal{O}_x$.

Additionally, each measurement has a variance:

$$\sigma_x^2 = \left\langle \left(y_x - \overline{y}_x \right)^2 \right\rangle$$
$$= \frac{1}{N_K} \sum_B \left(y_{B;x} - \overline{y}_x \right)^2 \tag{7.5}$$

which expresses the width of the cloud along the measurement-space coordinate x. However, σ_x^2 only effectively characterizes the measurements' error if the cloud is an

ellipse with axes that are flush with the coordinate directions of the measurement space. In such a case the width of the cloud along each coordinate direction is all that is needed to characterize the shape of the cloud. Yet, if the measurements are correlated, we will find that the axes of the ellipse do not fall along the coordinate directions.

Invariably, measurements are correlated. That is, the measurements vary coherently between blocks. If, when a given measurement on a given block is found to be above the ensemble average, another nearby measurement tends to also be above the ensemble average, then those two measurements are said to be correlated. If the second measurement tends to be on the opposite side of the ensemble average as the first, the two measurements are anticorrelated. If the two measurements move above and below the ensemble average in an independent fashion, they are uncorrelated.

The correlations between the N_M measurements are quantified by the covariance matrix C:

$$
\begin{aligned}
C_{x,y} &= \left\langle \left(y_x - \overline{y}_x \right) \left(y_y - \overline{y}_y \right) \right\rangle \\
&= \frac{1}{N_K} \sum_B \left(y_{B;x} - \overline{y}_x \right) \left(y_{B;y} - \overline{y}_y \right)
\end{aligned}
\tag{7.6}
$$

Along the diagonal, the covariance matrix corresponds to the standard variance of a measurement, $C_{x,x} = \sigma_x^2$, while the off-diagonal elements represent correlations between measurements. A large positive off-diagonal value corresponds to a strong correlation, while a large negative off-diagonal value corresponds to a strong anticorrelation. Completely uncorrelated data will have a diagonal covariance matrix.

Often literature refers to a correlation matrix ρ rather than a covariance matrix. The correlation matrix is constructed to specify only the correlation between

measurements, with all information concerning their error removed:

$$\rho_{x,y} = \frac{1}{\sigma_x \sigma_y} C_{x,y} \tag{7.7}$$

If two measurements are correlated, their value will tend to vary coherently. From the perspective of the data cloud, measurement points will tend to fall along a line diagonal to the coordinate directions of the two measurements. Thus, the data will form an ellipse with diagonal axes.

The eigenvectors of the covariance matrix correspond to the off-diagonal axes of this ellipse. Additionally, the eigenvalues of the matrix correspond to the width of the cloud along those directions, effectively giving the data's standard error measured along the ellipse's axes.

It is possible in certain pathological situations that data could form shapes more complex than a simple ellipse. The most common example is a boomerang-like shape, where the cloud may actually miss the ensemble average completely. Correct statistical error analysis of such data requires the use of moments higher than the second, and is beyond the scope of this discussion.

7.4 Theoretical Models

For each set of measurements taken, we have some theoretical form which we expect the data to match. Included in this theory function are some number of fit parameters c_ℓ whose value we hope to glean from the data:

$$f(c_1, c_2, c_3, \ldots; x_1, x_2, x_3, \ldots) \tag{7.8}$$

We also make use of the more compact notation $f_x(c_1, c_2, c_3, \ldots)$ or $f_x(c)$.

Given a set of values for the fit parameters, the theory function $f_x(c)$ specifies a point in measurement space. We would like to find the set of fit parameters which result in that point being as close as possible to the data's ensemble average. Additionally, we would like to use a metric for this measure of closeness which accounts for the variation in magnitude of the data's statistical error with the direction of the distance in question.

The correct metric for this purpose is the inverse of the covariance matrix. It weights distance in a given direction with a strength inversely proportional to the variance of the data along that direction. Using this metric the squared distance between our ensemble average and the theory function for a given set of fit parameters is:

$$\chi^2 = \sum_x \sum_y \left(\overline{y}_x - f_x(c)\right) C^{-1}_{x,y} \left(\overline{y}_y - f_y(c)\right) \tag{7.9}$$

We are now left to minimize χ^2 with respect to the fit parameters, and thus determine the optimal set of fit parameter values.

By the nature of its definition, the covariance matrix is symmetric, and must be positive definite in the limit of a large number of configurations, $N_K \to \infty$. Thus, Cholesky decomposition [63] can be used to determine a triangular matrix L such that:

$$LL^T = C \tag{7.10}$$

or equivalently:

$$(L^{-1})^T L^{-1} = C^{-1} \tag{7.11}$$

By applying L^{-1} to our vector of correlated distances, we generate a vector of uncorrelated distances weighted by the inverse of their uncertainty:

$$r_x = L_{x,y}^{-1}\big(\overline{y}_y - f_y(c)\big) \tag{7.12}$$

In terms of r_x, χ^2 is now simply:

$$\chi^2 = \sum_x r_x^2 \tag{7.13}$$

In cases where the number of data blocks N_K is not large relative to the number of measurements N_M, there is no guarantee that the covariance matrix will be positive definite. When it is not, we have no choice other than to set the matrix's off-diagonal elements to zero, effectively disregarding measurement correlation in the context of the fit. We find that this is often required in our study, as many of the fits have two, or even three, measurement parameters. Additionally, increasing our available data requires lengthening our Markov chains, a process which is exceedingly computationally intensive. These two factors often lead us to a very large N_M relative to our available N_K.

Minimizing χ^2 can be done using a nonlinear least-squares fitting technique. We begin each fit with the downhill simplex method [63, 64], also known as the amoeba method, and complete it using the Levenberg-Marquardt method [63, 65].

7.5 Jackknife Error

We determine the statistical error of our fit parameters via a jackknife procedure. This involves repeating the entire fit process N_K times, each time leaving out a different block of data from the data set. The result is a vector of values $c_{\ell;j}$, where j runs from 1 to N_K, for each fit parameter c_ℓ. The standard error for each fit parameter

is then:

$$\sigma_{c_\ell}^2 = \frac{N_K - 1}{N_K} \sum_j \left(c_{\ell;j} - \overline{c}_\ell \right)^2 \tag{7.14}$$

where:

$$\overline{c}_\ell = \frac{1}{N_K} \sum_j c_{\ell;j} \tag{7.15}$$

When reporting the value of a fit parameter, we quote the statistical error using the form:

$$c_\ell \pm \sqrt{\sigma_{c_\ell}^2} \tag{7.16}$$

where c_ℓ is the optimal fit parameter value found in the full fit and $\sigma_{c_\ell}^2$ is given by (7.14).

When our desired result is some function of the fit parameters $g(c_1, c_2, c_3, \ldots)$, the variation in the fit parameters may be correlated such that the subsequent variation in the result is larger or smaller than what would be expected. In such a case we apply the jackknife procedure to the result itself:

$$\sigma_g^2 = \frac{N_K - 1}{N_K} \sum_j \left(g(c_{1;j}, c_{2;j}, c_{3;j}, \ldots) - \overline{g} \right)^2 \tag{7.17}$$

where:

$$\overline{g} = \frac{1}{N_K} \sum_j g(c_{1;j}, c_{2;j}, c_{3;j}, \ldots) \tag{7.18}$$

The result is then reported in the form:

$$g(c_1, c_2, c_3, \ldots) \pm \sqrt{\sigma_g^2} \tag{7.19}$$

7.6   Specific Applications

We applied the data modeling techniques described above in six aspects of our study. For clarity we present explicitly the measure parameters x_n, fit parameters c_ℓ, measurement operator $\mathcal{O}_x$, and theory function $f_x(c)$ used in each fit.

145

Because we are only able to manipulate dimensionless quantities in our numerical fit procedure, measure and fit parameters must be unitless. Often we absorb into dimensionful quantities some number of powers of the lattice spacing a in order to construct a fit's required unitless quantities. We remind the reader of our use of $\check{X}$ to denote the unitless version of some quantity X.

7.6.1 Static Quark Potential

We determine the static quark potential at a single spatial separation by fitting the rectangular Wilson-loop expectation value to an exponential:

$$x_n : t \qquad\qquad\qquad \mathcal{O}_x : (9.3)$$

$$c_\ell : \mathscr{A}, aV(as) \qquad\qquad\qquad f_x(c) : (9.3)$$

7.6.2 Spatial Dependence of Static Quark Potential

We extracted the form of the static quark potential by fitting the rectangular Wilson loop expectation value to its predicted form:

$$x_n : s, t \qquad\qquad\qquad \mathcal{O}_x : (5.133)$$

$$c_\ell : \mathscr{A}_s, v_0, v_1, v_2, \tilde{v}_2 \qquad\qquad\qquad f_x(c) : (5.133)$$

Note that a unique fit parameter $\mathscr{A}_s$ is used for each value of s in the fit range.

7.6.3 Single Correlator

In order to determine the mass and decay constant of the local pion for a single value of the valence quark mass, we fit the local-bilinear correlator to an exponential:

$$x_n : t \qquad\qquad\qquad \mathcal{O}_x : (5.149)$$

$$c_\ell : \check{f}_{\pi_5}, \check{M}_{\pi_5} \qquad\qquad\qquad f_x(c) : (5.164)$$

7.6.4 Quadratic Valence-Quark-Mass Dependence

To determine the valence quark mass value at which the local pion mass equals the physical kaon mass, we fit the local-bilinear correlator at various valence quark masses to a phenomenologically motivated quadratic form for the local pion mass:

$$x_n : t, m_V \qquad\qquad \mathcal{O}_x : (5.149)$$

$$c_\ell : \mathscr{A}_{m_V}, a_0, a_1, a_2 \qquad\qquad f_x(c) : (9.5), (9.6)$$

Note that an independent fit parameter $\mathscr{A}_{m_V}$ is used for each value of m_V studied.

For illustrative purposes, in one case we also fit the correlator to a cubic form, using the fit characteristics described above, but replacing (9.6) with (9.9).

7.6.5 Chiral Valence-Quark-Mass Dependence

To determine the GL coefficient combinations $2\alpha_8 - \alpha_5$ and α_5, we fit the local-bilinear correlator at various valence quark masses to the form for the local pion mass and decay constant predicted by pqChPT:

$$x_n : t, m_V \qquad\qquad \mathcal{O}_x : (5.149)$$

$$c_\ell : \check{z}, \check{f}, 2\alpha_8 - \alpha_5, \alpha_5 \qquad\qquad f_x(c) : (6.16), (6.19), (6.20)$$

For small volume ensembles, we are forced to add a constant term to the pion-mass form in the above fit. For these ensembles we use the fit characteristics described above, but replace (6.19) with (9.10).

7.6.6 Chiral Dynamical- and Valence-Quark-Mass Dependence

In order to determine the GL coefficient combinations $2\alpha_8 - \alpha_5$, $2\alpha_6 - \alpha_4$, α_5, and α_4, we fit the local-bilinear correlator at various dynamical and valence quark masses

to the form for the local pion mass and decay constant predicted by pqChPT:

$$x_n : t, m_V, m_S \qquad\qquad \mathcal{O}_x : (5.149)$$

$$c_\ell : \check{z}, \check{f}, 2\alpha_8 - \alpha_5, 2\alpha_6 - \alpha_4, \alpha_5, \alpha_4 \qquad f_x(c) : (6.16), (6.17), (6.18)$$

In this case the measurement operator is not a function of one of the measure parameters, the dynamical quark mass m_S. Instead, m_S is a parameter of the ensemble itself. Thus, measurements at different values of m_S come from different ensembles, and there can be no correlation between them. The elements of the covariance matrix which correspond to measurements at different dynamical quark masses are simply zero.

CHAPTER 8

ENSEMBLE DETAILS

We present here the ensembles used in our study, revealing the motivation behind and the parameters used in the generation of each ensemble. Table 8.1 displays a summary of this information.

For all dynamical ensembles, a configuration was added to the ensemble every ten HMD trajectories along the Markov chain, with the first configuration in each ensemble being ten trajectories from the ensemble's starting condition.

8.1 Primary Ensemble

We refer to our primary ensemble as ensemble A, or after hypercubic blocking as ensemble A hyp. This ensemble has our largest lattice extent, $16^3 \times 32$, and reasonable lattice spacing. As such, it is from A hyp that we will generate our quoted results. This is our only ensemble to include two Markov chains, one of which has an ordered starting condition, and the second of which has a disordered starting condition. Such a set of Markov chains is very helpful in determining the thermalization point, as in a sense the chains begin on opposite sides of the desired equilibrium ensemble.

149

	L_1	L_2	L_3	L_4	β	m_S	N_f	start	N	N_T	N_B	N_K
A	16	16	16	32	5.3	0.01	3	O	2250	250	200	20
								D	2250	250		
B	12	12	16	32	5.3	0.01	3	O	2250	250	200	10
C	8	8	8	32	5.3	0.01	3	O	10050	250	200	49
W	8	8	8	32	5.115	0.015	3	O	10300	300	100	100
X	8	8	8	32	5.1235	0.02	3	O	10300	300	100	100
Y	8	8	8	32	5.132	0.025	3	T	10000	0	100	100
Z	8	8	8	32	5.151	0.035	3	T	10000	0	100	100
Q	16	16	16	32	5.8	-	0	144 configurations				

Table 8.1: The lattice parameters for the ensembles used in our study. The starting conditions are denoted as O for an ordered start, D for a disordered start, and T for a thermal start. The values for Markov chain length N, thermalization point N_T, and block length N_B are given as trajectory counts. N_K corresponds to the number of blocks available in an ensemble.

8.2   Finite-Volume Ensembles

In order to study the magnitude of finite-volume error in our results, we use two ensembles with smaller lattice extent than our primary ensemble, leaving all other lattice parameters unchanged. We hope that results from the $12^2 \times 16 \times 32$ ensemble, or ensemble B, deviate only slightly from those of our primary ensemble, demonstrating that the finite-volume error in ensemble A is under control. We expect that results from the $8^3 \times 32$ ensemble, or ensemble C, will deviate significantly from our primary ensemble's results, as its physical volume is thought to be too small for our study. This should, however, make clear the effects of finite volume. Both of these finite-volume ensembles have ordered starting conditions.

8.3 Varying-Dynamical-Quark-Mass Ensembles

To determine the GL coefficient combination $2\alpha_6 - \alpha_4$, we require a set of ensembles between which the dynamical quark mass varies, but all other ensemble parameters are constant. In order to vary the dynamical quark mass, but leave the lattice spacing unchanged, we have made use of results from the Columbia group [66]. They have mapped out the $N_f = 3$, $L_4 = 4$ finite temperature transition, determining several critical β and m_Q value pairs [67]. We have generated four ensembles using these values, and refer to them as ensembles W, X, Y, and Z. Ensembles W and X have ordered starting conditions, while ensembles Y and Z have thermalized starting conditions, using initial configurations from the ensembles of [67].

Because of the significant computational effort required to generate four distinct ensembles, we have used a small lattice extent. A reasonable physical volume is still obtained, as the lattice spacing corresponding to the ensemble parameters used is rather large.

We also make use of ensemble W to study the magnitude of finite-lattice-spacing effects on our results. This ensemble has approximately twice the lattice spacing of our primary ensemble, yet has approximately equal physical volume. Thus, the deviation of its results from those of our primary ensemble give an indication of the effects of finite lattice spacing.

8.4 Quenched Ensemble

Quenched ChPT predicts a different functional form than pqChPT for the pion mass and decay constant's dependence on the valence quark mass [58]. Thus, it may be possible to distinguish a quenched ensemble from a partially quenched ensemble

via a study of that dependence. To this end, we include in our study a fully quenched ensemble with the same lattice extent as our primary ensemble and approximately equal lattice spacing. We refer to this ensemble as ensemble Q hyp, studying it only after hypercubic blocking. We do not make use of the predictions of qChPT, but instead treat the quenched ensemble as though it were partially quenched, with $N_f = 3$ and $m_Q = 0.01$. If the effects of quenching are strong, the results from ensemble Q hyp should deviate significantly from those of ensemble A hyp.

CHAPTER 9

ANALYSIS

We present here the analysis of our ensembles and the processes which lead to our results.

9.1 Thermalization and Block Length

Figures D.1 through D.7 show the local pion's bilinear correlator $C_{5,5;t}$ calculated on the individual configurations of our ensembles. Such a plot makes obvious the effects of both thermalization and autocorrelation. For each ensemble we present the bilinear correlator at two time separations: $t = 0$ and $t = 15$.

The vertical dotted line in each plot demonstrates the value used for that ensemble's thermalization point N_T as described in Section 4.2.6. The vertical range represents the block length N_B used for that ensemble as described in Section 7.2.

In the case of ensemble A, with its pair of Markov chains, we overlay the evolution of the two chains on a single plot. This makes the appropriate thermalization point quite clear.

9.2 Sommer Scale

As described in Section 5.7, the lattice spacing of each ensemble is set via the Sommer scale. We present here our calculation of the lattice spacings, as well as a study of the effects of our fit-range choices on the results. We calculate the lattice spacing of the thin-link and hypercubic-blocked versions of each ensemble independently.

In all cases a value of $s_{\min} = 1$ is used as the lower spatial bound of our fit ranges.

9.2.1 Effective Potential

In order to determine an appropriate minimum time separation $t_{\min}$ to use for our fit range, we calculate the effective potential $V_{\text{eff}}(s)$ for a range of time separations. The value of the effective potential between t and $t + 1$ is the exponential decay constant which describes the falloff of the Wilson-loop expectation value considering only those two time separations. Explicitly, the effective potential at $t + \frac{1}{2}$ is defined as:

$$aV_{\text{eff}}(s)\Big|_{t+\frac{1}{2}} \equiv \ln \frac{\big\langle \text{Re}\,\text{tr}\big[W^{s \times t}\big]\big\rangle}{\big\langle \text{Re}\,\text{tr}\big[W^{s \times t+1}\big]\big\rangle} \tag{9.1}$$

The effective potential is expected to vary rapidly for small t, where the asymptotic static quark state is infected by higher-energy states. Beyond some larger t the value is expected to plateau at the static quark potential. We chose $t_{\min}$ such that our fit range spans only the region in which the static quark potential is uncontaminated.

Figures D.8 through D.15 show the effective potential over a range of time separations t and at two spatial separations s for each ensemble. The chosen spatial separations bracket, or nearly bracket, that ensemble's result for r_0/a. The dotted vertical line in each plot represents the value of $t_{\min}$ chosen for the final fit. The error

bars displayed are the result of a jackknife analysis. Those points whose error bars span their plot's vertical range have been dropped.

For ensembles W through Z, and their hypercubic blocked counterparts, our choice of $t_{\min} = 2$ may not seem optimal in light of the effective potential plots. However, $t_{\min}$ must be low enough so that the statistical errors of the static quark potential are under control out to a spatial separation of $s = 4$. This requirement arises from the fact that we are using a four-parameter form for the s dependence of the Wilson-loop expectation value (5.132). Thus, without four well-determined values for the static quark potential along the s direction, the fit is under-determined. Choosing $t_{\min} = 3$, which would perhaps seem advisable based on the effective potential's behavior, causes the statistical error of the static quark potential at $s = 4$ to be very large. Thus, we choose $t_{\min} = 2$. In Section 9.2.3 we present the dependence of the resulting value of r_0/a on our choice of $t_{\min}$. This dependence demonstrates that our choice of $t_{\min} = 2$ for ensembles W through Z in not unreasonable.

If we were not using a corrected ansatz for the static quark potential, an under-determined spatial dependence would not be as significant an issue. When calculating jackknife error for such an under-determined potential, the results for the fit parameters will vary wildly. However, as long as the statistical error in the vicinity of the Sommer scale is under control, these variations will be correlated such that the corresponding variation in r_0/a will remain small. For our corrected potential, we do not have this luxury. In this case, we ignore a term in the static quark potential's fit form when determining the Sommer scale. It is critical that the coefficient for that term $\tilde{v}_2$ be well determined by the fit, as the correlation of its error with that of the other fit parameters is discarded, and thus is not available to stabilize r_0/a.

It follows from the definition of the rectangular Wilson loop that its expectation value has a symmetric dependence on s and t. Based on our ansatz for the static quark potential (5.132), we can only expect the expectation value to fall off in time as a single exponential for time separations t larger than some value s_{str}, where s_{str} is the spatial separation beyond which the static quark potential is dominated by its string-tension term. The Sommer scale r_0 is specifically defined so that it falls in the transition region between a Coulomb-like and a string-like quark potential. Thus, it is clear that one should choose a value for t_{min} which is just greater than r_0/a. In all cases we choose t_{min} to be just greater than the value determined for r_0/a on the corresponding hypercubic blocked ensemble.

9.2.2 Static Quark Potential

For each ensemble the Wilson-loop expectation value is fit to our ansatz (5.133) over the range of spatial and time separations bound by s_{min}, s_{max}, t_{min}, and t_{max}. The value of r_0/a is then determined via (5.134).

In Figures D.16 through D.30 we display the results of these fits, plotting the determined corrected static quark potential, defined as:

$$aV_{\text{corr}}(as) \equiv v_0 + v_1 s + v_2 \frac{1}{s} \tag{9.2}$$

The parameters v_0, v_1, and v_2 are determined by the fit. The parameter $\tilde{v}_2$ is also determined by the fit, but its term is dropped when calculating the corrected static quark potential.

Included in the plots are the results of independent fits of the Wilson-loop expectation value along lines of constant s. The Wilson-loop expectation value is fit to the

form:

$$\left\langle \operatorname{Re} \operatorname{tr}\left[W^{s \times t}\right]\right\rangle = \mathscr{A} e^{-aV(as)t} \tag{9.3}$$

for a single spatial separation s and over the range of time separations t from $t_{\min}$ to $t_{\max}$. The result is a value for the static quark potential at a single spatial separation $aV(as)$. These values are represented on the plots by $\times$'s. The plots' diamonds correspond to the corrected static quark potential, which in this case is defined as:

$$aV_{\mathrm{corr}}(as) \equiv aV(as) - \tilde{v}_2\left(\left[\frac{1}{s}\right]_X - \frac{1}{s}\right) \tag{9.4}$$

where $\tilde{v}_2$ is determined by the full fit as discussed above.

It should be stressed that the corrected static-quark-potential curve is not the result of a fit to the corrected static-quark-potential points. The curve and points are only related in that they are both the result of fits to the same expectation-value data. Agreement between the corrected static-quark-potential curve and points demonstrates that our ansatz for the s dependence of the Wilson-loop expectation value is appropriate.

The error bars are determined via a jackknife analysis. For clarity, error bars are only shown on the corrected potential points, although equivalent error bars on the corresponding uncorrected potential points would be appropriate. Each fit curve's one-sigma range is bound by dotted lines. This range is the result of a jackknife analysis of the curve's value at each point along the horizontal axis. Due to the large number of Wilson-loop expectation values used for the fit, the data's covariance matrix fails to be positive definite for all ensembles. Thus, in all cases we use a diagonal covariance matrix.

157

On each plot the vertical dashed line corresponds to the ensemble's determined value of r_0/a, while the shaded region corresponds that result's jackknife error bars.

9.2.3 Dependence on $t_{\min}$

In order to directly study the $t_{\min}$ dependence of our results, we repeat the fits using a range of values for $t_{\min}$. All other fit range parameters are left unchanged. The fruits of this analysis are presented in Figures D.31 through D.34. In each plot the $t_{\min}$ used in the final fit is denoted by a filled diamond, which thus corresponds to that ensemble's determined value for r_0/a. For several ensembles, especially the thin-link ensembles, very few points are given. For those values of $t_{\min}$ at which a point is not given, the fit either fails entirely, results in an imaginary value for r_0/a, or produces statistical error bars which span the plot's vertical axis.

9.2.4 Dependence on $t_{\max}$

In order to directly study the $t_{\max}$ dependence of our results, we repeat the fits using a range of values for $t_{\max}$. All other fit range parameters are left unchanged. The products of this analysis are presented in Figures D.35 through D.38. In each plot the $t_{\max}$ used in the final fit is denoted by a filled diamond, which thus corresponds to that ensemble's determined value for r_0/a. Due to increasingly large statistical error in the Wilson-loop expectation value for large time separations, the fit results have a weak dependence on $t_{\max}$. Ensemble C hyp shows the strongest dependence, most likely due to significant finite-volume effects.

	$s_{\max}$	$t_{\min}$	$t_{\max}$	v_0	v_1	v_2	$\tilde{v}_2$
A hyp	7	4	10	0.243(16)	0.1031(31)	−0.336(21)	−0.352(31)
B hyp	5	4	10	0.293(24)	0.0924(41)	−0.396(33)	−0.432(48)
C hyp	4	4	10	0.374(15)	0.0649(33)	−0.479(19)	−0.523(26)
A	7	4	10	0.77(13)	0.097(45)	−0.16(11)	−2.4(24)
B	5	4	10	0.81(16)	0.081(55)	−0.30(17)	−1.0(33)
C	4	4	10	0.81(10)	0.074(36)	−0.33(13)	−0.6(23)
W hyp	4	2	10	−0.239(50)	0.4715(99)	−0.026(64)	−0.119(89)
X hyp	4	2	10	−0.129(40)	0.4393(76)	−0.152(52)	−0.278(74)
Y hyp	4	2	10	−0.144(47)	0.4322(90)	−0.114(61)	−0.205(86)
Z hyp	4	2	10	−0.128(43)	0.4190(79)	−0.129(57)	−0.233(82)
W	4	2	10	0.65(21)	0.384(72)	0.05(18)	−4.9(38)
X	4	2	10	0.33(19)	0.487(67)	−0.10(17)	−0.4(36)
Y	4	2	10	−0.05(20)	0.613(69)	−0.48(17)	7.4(36)
Z	4	2	10	0.11(20)	0.548(72)	−0.39(16)	5.1(37)
Q hyp	7	4	10	0.169(12)	0.1043(22)	−0.261(15)	−0.290(22)

Table 9.1: Fit-range limits and the results for a subset of the fit parameters from the corrected static-quark-potential fits.

9.2.5 Dependence on $s_{\max}$

In order to directly study the $s_{\max}$ dependence of our results, we repeat the fits using a range of values for $s_{\max}$. All other fit range parameters are left unchanged. The outcome of this analysis is presented in Figures D.39 through D.42. In each plot the $s_{\max}$ used in the final fit is denoted by a filled diamond, which thus corresponds to that ensemble's determined value for r_0/a. Due to increasingly large statistical error in the Wilson-loop expectation value for large spatial separations, the fit results have a weak dependence on $s_{\max}$. Again, ensemble C hyp shows the strongest dependence.

9.2.6 Results

Tables 9.1 and 9.2 compile the results of the corrected static-quark-potential fits. Table 9.1 presents the fit ranges used, and displays each ensemble's determined values for a relevant subset of the fit parameters. Table 9.2 presents the corresponding values for r_0/a and the inverse lattice spacing. The quoted uncertainties are from a jackknife analysis of the statistical error.

In order to gauge the effects of using a corrected potential, we repeat the fits using an uncorrected static quark potential, fixing the correction term's parameter to zero, $\tilde{v}_2 = 0$. The results of these uncorrected fits are given in Table 9.2.

Note that between the thin-link ensembles W through Z, the results of the corrected fit show uncontrolled variation. This is most obvious in the values obtained for the correction term's parameter $\tilde{v}_2$, and can be seen clearly in Figures D.26 through D.29 and in Table 9.1. This is the result of a poorly determined s dependence for the static quark potential, resulting in an extremely flat minimum for χ^2 along a path through fit-parameter space. This leads to large, but highly correlated, variations in the fit parameters. Because we ignore the correction term when determining r_0/a, these correlated errors do not have a chance to counteract one another. The end result for r_0/a is large statistical errors within each ensemble and large variations in the value between ensembles. For the corresponding uncorrected static-quark-potential fits, the situation is improved twofold. The ansatz for the potential contains fewer terms, and thus the resulting fit parameters are better determined. Additionally, all terms are retained when determining r_0/a, and thus any correlated error has an opportunity to cancel in the final result for r_0/a. This improved situation is clear

	r_0/a		$a^{-1}\,(\mathrm{MeV})$	
	uncorr	corr	uncorr	corr
A hyp	3.507(23)	3.570(27)	1384.1(90)	1409(10)
B hyp	3.581(68)	3.684(44)	1414(27)	1454(17)
C hyp	3.757(28)	4.248(78)	1483(11)	1677(31)
A	3.17(12)	3.9(10)	1251(49)	1550(400)
B	3.69(24)	4.1(17)	1457(95)	1610(670)
C	3.94(29)	4.2(12)	1560(110)	1670(480)
W hyp	1.8809(37)	1.856(19)	742.4(15)	732.5(73)
X hyp	1.9076(33)	1.847(17)	752.9(13)	728.9(69)
Y hyp	1.9293(35)	1.885(19)	761.5(14)	744.2(75)
Z hyp	1.9547(40)	1.905(19)	771.5(16)	751.9(75)
W	1.766(12)	2.10(30)	697.2(47)	830(120)
X	1.763(11)	1.78(21)	696.0(44)	704(84)
Y	1.7809(93)	1.38(17)	702.9(37)	545(68)
Z	1.812(10)	1.51(19)	715.1(41)	598(76)
Q hyp	3.570(12)	3.650(19)	1409.2(47)	1440.5(76)

Table 9.2: The final results for the Sommer scale and lattice spacing from the corrected and uncorrected static-quark-potential fits.

from the relative consistency between the uncorrected results for the Sommer scale of ensembles W through Z, as shown in Table 9.2.

One advantage of hypercubic blocking, a reduction in statistical error, is evident in our results for the Sommer scale. As such, we have a greater trust in our hypercubic-blocked results. In following sections we use an ensemble's hypercubic-blocked lattice spacing for both the thin-link and hypercubic-blocked versions of the ensemble.

We suspect the variation in the determined lattice spacing for ensembles A through C is due not to true changes in the lattice spacing, but rather to our limited ability to determine the lattice spacing on the smaller-volume ensembles. Thus, in order to clarify the effects of finite volume in other quantities, we use, in the following sections, the lattice spacing determined for ensemble A hyp for ensembles B and C as well.

9.3 Effective Mass

We can extract the value of the local pion mass and decay constant from the bilinear correlator $C_{5,5;t}$ because, for large time separations t, it contains only a single state, the static local pion. Thus, we must determine some time separation $t_{\min}$ beyond which we will assume the pion state is uncontaminated.

In order to make this choice for each ensemble, we calculate the effective mass of the local pion over a range of time separations. The effective mass M_{eff} at $t + \frac{1}{2}$ is the mass which describes the exponential falloff of the correlator, considering only the correlator's value at the time separations t and $t + 1$. In practice we determine the effective mass by fitting the correlator at a single valence quark mass to the form in (5.164), using the value of the correlator only at four time separations: t, $t + 1$, $L_4 - 2 - t$, and $L_4 - 1 - t$.

The resulting values for the effective mass are presented in Figures D.43 through D.46. The error bars shown are the result of a jackknife analysis. In each case the effective mass is high for small t, where the correlator still contains higher-energy states, and then plateaus for large t. The value of $t_{\min}$ chosen for each ensemble is represented in the plots by a vertical dotted line. Those values can also be found in Table 9.3. All other fits of the correlator in this study use these values for $t_{\min}$, fitting the correlator only over the range from $t_{\min}$ to $L_4 - 1 - t_{\min}$.

9.4 Pion Mass

Once we have determined an appropriate $t_{\min}$, the local pion mass at a given valence quark mass can be ascertained by fitting the bilinear correlator $C_{5,5;t}$ to its expected exponential falloff (5.164) in t. Table 9.3 shows the results of these fits

	$t_{\min}$	$m_V = 0.01$		$m_V = m_S$	
		aM_{π_5}	M_{π_5} (MeV)	aM_{π_5}	M_{π_5} (MeV)
A hyp	7	0.19769(57)	278.5(21)		
B hyp	7	0.20235(93)	285.1(24)		
C hyp	7	0.335(11)	471(16)		
A	7	0.29704(31)	418.5(30)		
B	7	0.29792(37)	419.8(30)		
C	7	0.3483(32)	490.8(57)		
W hyp	4	0.25189(19)	184.5(18)	0.30659(19)	224.6(22)
X hyp	4	0.25143(25)	183.3(17)	0.35134(24)	256.1(24)
Y hyp	4	0.25098(23)	186.8(19)	0.39029(25)	290.5(29)
Z hyp	4	0.25091(26)	188.7(19)	0.45804(26)	344.4(34)
W	4	0.258565(96)	189.4(19)	0.315645(98)	231.2(23)
X	4	0.25955(11)	189.2(18)	0.36470(11)	265.8(25)
Y	4	0.260230(99)	193.7(20)	0.40742(11)	303.2(31)
Z	4	0.26140(12)	196.5(20)	0.48119(12)	361.8(36)
Q hyp	7	0.19472(70)	280.5(18)	-	-

Table 9.3: Minimum time separation and local pion mass at $m_V = 0.01$ and $m_V = m_S$. For those ensembles in which $m_S = 0.01$, the results are not repeated.

using the valence-quark-mass values $m_V = 0.01$ and $m_V = m_S$. For those ensembles in which $m_S = 0.01$, the results are not repeated. The uncertainties quoted are the result of a jackknife analysis of the statistical error. In the case of the dimensionful result, the statistical error of the inverse lattice spacing is added in quadrature. We use a diagonal correlation matrix for these fits.

Ensembles A and B generate very similar pion masses, indicating that the local pion mass is relatively free of finite-volume effects. The pion mass of ensemble C is significantly larger. This indicates that the small volume of the ensemble is constricting the pion, preventing it from relaxing to its lowest energy state.

As discussed in Section 6.4, pqChPT is only valid for quark masses within some radius of convergence from the chiral limit. In order to gain some insight into the

physical magnitude of our quark masses, we compare our calculated pion masses to the experimental mass of the the Standard Model's light mesons. The experimental mass of the Standard Model's pion is $M_{\pi^0} = 135.0\,\text{MeV}$, while the kaon mass is $M_{K^+} = 493.7\,\text{MeV}$ [68]. From Table 9.3, it is clear that the quark masses we use are larger than those of the up and down quarks. Yet, the ensembles' pion masses remain below the kaon mass. In the case of ensemble A hyp, the pion mass is well below the kaon mass. This leaves us hopeful that pqChPT is valid within the quark-mass range of our study. It should be noted that our coarse lattice spacings, especially in ensembles W through Z, are a large part of why our pion masses remain low.

9.5 Kaon Quark-Mass Threshold

For staggered lattice fermions the quark mass is multiplicatively renormalized. While we do not wish to calculate the renormalization factors exactly, we do require some method for comparing the quark mass between ensembles. Thus, for each ensemble we calculate what we identify as the kaon quark-mass threshold m_{Q_K}, the valence quark mass at which the local pion mass equals the Standard Model's kaon mass. At that point, the physical valence quark mass should be on the order of half the strange quark mass.

In order to determine m_{Q_K}, we require an ansatz for the pion mass's valence-quark-mass dependence which is accurate up to large valence quark mass. While pqChPT predicts a form for the pion mass, it is not appropriate to use it in this case, as the fit includes valence quark masses which are beyond the expected radius of convergence of pqChPT. Instead, we simply fit the squared pion mass to a quadratic polynomial, a form which it follows very well up to the largest valence quark mass we investigate.

The phenomenological fit form we use for this purpose alone is:

$$C_{5,5;t} = \mathscr{A}_{m_V} \left(e^{-\check{M}_{\pi_5} t} + e^{-\check{M}_{\pi_5}(L_4 - 1 - t)} \right) \tag{9.5}$$

where:

$$\check{M}_{\pi_5}^2 = a_0 + a_1 m_V + a_2 m_V^2 \tag{9.6}$$

and $\mathscr{A}_{m_V}$ is a set of independent fit parameters, one for each valence-quark-mass value studied. We should stress that this is clearly not the form predicted by pqChPT. We use it here only because we require a good fit of the local pion mass up to large valence quark mass. The results of these fits are used for nothing other than an interpolation

	a_0	a_1	a_2	m_{Q_K}
A hyp	0.00223(11)	3.684(20)	−1.99(22)	0.03331(13)
B hyp	0.00401(29)	3.694(37)	−2.15(54)	0.03276(20)
C hyp	0.0671(76)	4.59(21)	−10.1(25)	0.0125(17)
A	0.00435(18)	8.558(15)	−21.99(24)	0.014365(21)
B	0.00503(20)	8.547(15)	−21.85(24)	0.014295(27)
C	0.0359(25)	8.744(49)	−27.49(52)	0.01027(27)
W hyp	0.00378(12)	6.0518(72)	−2.778(47)	0.077151(55)
X hyp	0.00395(13)	6.0084(71)	−2.654(45)	0.078381(63)
Y hyp	0.00406(12)	5.9758(73)	−2.617(49)	0.075492(63)
Z hyp	0.00434(15)	5.9523(81)	−2.669(51)	0.074160(64)
W	0.001263(59)	6.6238(40)	−4.911(28)	0.072242(28)
X	0.001388(55)	6.6679(40)	−5.100(30)	0.072598(25)
Y	0.001509(56)	6.6935(40)	−5.204(28)	0.069284(26)
Z	0.001612(72)	6.7502(43)	−5.456(29)	0.067282(27)
Q hyp	0.00269(22)	3.524(21)	−2.25(27)	0.03327(12)

Table 9.4: Kaon quark-mass threshold and results for a subset of the fit parameters from the quadratic fits of the pion mass's valence-quark-mass dependence.

to determine the point at which the local pion mass crosses the Standard Model's physical kaon mass:

$$m_{Q_K} = \frac{-a_1 + \sqrt{a_1^2 - 4a_2\big(a_0 - (a \times 493.7\,\text{MeV})^2\big)}}{2a_2} \tag{9.7}$$

where a is the lattice spacing used for the ensemble.

Figures D.47 through D.50 display, and Table 9.4 summarizes, the results of these fits. The curve in each plot demonstrates the valence-quark-mass dependence determined by the fit, and is generated by using (9.6) and the resultant values for the fit parameters. The diamonds are the result of independent fits of the correlator at separate valence quark masses, using the same method as was used in Section 9.4. It should be stressed that the full quadratic fit of the valence-quark-mass dependence is not a fit to these points. The points are related to the fit only in that they are

both derived from the same correlator data. Agreement between the fit curve and the diamonds demonstrates that our phenomenological ansatz for the local pion mass's valence-quark-mass dependence is appropriate. The valence-quark-mass values at which pion-mass points are given correspond to the values used in the quadratic fit.

The error bars were determined via a jackknife analysis. Each fit curve's one-sigma range is bound by dotted lines. This range is the result of a jackknife analysis of the curve's value at each point along the horizontal axis. In most cases this region is thinner than the curve's line, and thus is not easily visible. Uncertainty in the lattice spacing is not taken into account. Instead, the plots' vertical axes are simply rescaled using the lattice spacing's central value. We use a diagonal correlation matrix in the fit, as the full correlation matrix is not positive definite for several of the ensembles.

The dashed vertical line appearing in the plots corresponds to that ensemble's determined value for m_{Q_K}, while the shaded region corresponds to the uncertainty in that result, as determined by a jackknife analysis of the statistical error. In many cases this region is thiner than the line itself, and is not readily visible. This error, which is repeated in Table 9.4, does not take into account uncertainty in the ensembles' lattice spacings.

Because finite-volume effects inflate the pion mass in ensembles C hyp and C, the kaon quark-mass threshold for these ensembles is unexpectedly small. Thus, in order to clarify finite-volume effects in other quantities, we use the value of m_{Q_K} determined for A hyp for both ensembles B hyp and C hyp. Similarly, A's value for m_{Q_K} is used for ensembles B and C.

9.6 $2\alpha_8 - \alpha_5$

In order to determine the value of the GL coefficient combination $2\alpha_8 - \alpha_5$, we fit the correlator $C_{5,5;t}$ over a range of time separations t and valence quark masses m_V to the form predicted by pqChPT: (6.16), (6.19), and (6.20). The result is values for the fit's free parameters, one of which is $2\alpha_8 - \alpha_5$.

9.6.1   Valence-Quark-Mass Cutoff

pqChPT is expected to accurately model the behavior of the local pion only within some radius of convergence of the chiral limit. Thus, we should only fit the correlator to pqChPT's predictions at and below some cutoff in the valence quark mass Λ_{m_V}. While we expect the appropriate cutoff to be below the kaon quark-mass threshold, there is no clear a priori value. As such, we turn to the data to determine our cutoff.

Figure D.51 plots χ^2 per degree of freedom for fits of ensemble A hyp's correlator data to the predictions of pqChPT against various choices for the cutoff Λ_{m_V}. A diagonal correlation matrix was used in these fits. The error bars are the result of a jackknife analysis. We choose as our value for Λ_{m_V} the cutoff at which χ^2 per degree of freedom is closest to one: $\Lambda_{m_V} = 0.025$. In Figure D.51 the chosen cutoff is denoted by a filled diamond. This cutoff is then used for ensembles A hyp through C hyp, as well as for ensemble Q hyp.

We know from our study of the kaon quark-mass threshold m_{Q_K} that the quark-mass renormalization factor of the thin-link ensembles is significantly different than that of the hypercubic-blocked ensembles. Thus, it would not be appropriate to use the same valence-quark-mass cutoff for the thin-link ensembles. Instead we determine

a cutoff which is consistent between the thin-link and hypercubic-blocked ensembles using m_{Q_K}.

The ratio of the valence-quark-mass cutoff over the kaon quark-mass threshold for ensemble A hyp is $\Lambda_{m_V}/m_{Q_K} = 0.751$. We choose the cutoff for ensemble A to be that which gives the closest ratio beyond this value. We choose $\Lambda_{m_V} = 0.0125$, which corresponds to a ratio of $\Lambda_{m_V}/m_{Q_K} = 0.870$. This cutoff is then used for ensembles A through C. We select the cutoff for ensembles W hyp through Z hyp similarly, choosing $\Lambda_{m_V} = 0.06$. Between the four ensembles, this gives an average ratio of $\Lambda_{m_V}/\overline{m}_{Q_K} = 0.0763$. For ensembles W through Z, we use the cutoff $\Lambda_{m_V} = 0.055$, which between the four ensembles gives an average ratio of $\Lambda_{m_V}/\overline{m}_{Q_K} = 0.782$.

Given the evident correlation present in the data, and that our calculations of χ^2 do not take that correlation into account, it could be argued that, while clearly minimization of this χ^2 is appropriate, its actual value is meaningless. As such, there is no compelling reason to believe that a choice of valence-quark-mass cutoff which results in a χ^2 per degree of freedom of one is appropriate. However, as we are left with no other quantitative evidence as to an appropriate cutoff choice, we feel that it is important to at least use a consistent and systematic method for resolving the choice.

In section 9.6.7 we study the effect of these cutoff choices on the resulting value of $2\alpha_8 - \alpha_5$ and find that it is a significant source of systematic uncertainty.

9.6.2 Pion Mass and Decay Constant

Figures D.52 and D.53 present results from the fit of ensemble A hyp's correlator to the predictions of pqChPT. These plots of the dependence of the pion mass and decay

constant on the valence quark mass were generated by inserting the fit's determined values for its free parameters into (6.19) and (6.20). Recall that we use the pion-decay-constant normalization in which $f_\pi \simeq 92.4\,\mathrm{MeV}$.

The diamonds display the result of a set of independent fits of the correlator at separate valence quark masses, using the same method as was used in Section 9.4. The result is a value for the pion mass and decay constant at each valence quark mass at which the correlator was calculated. The valence-quark-mass values at which a filled diamond appears correspond to the set of values used in the full pqChPT fit; that is, those within the valence-quark-mass cutoff. Open diamonds correspond to valence-quark-mass values beyond the cutoff. We stress that the full pqChPT fit is not a fit to the filled diamonds. Rather, the fit curve and points are related only in that they are derived from the same correlator data. Their agreement, or lack thereof, demonstrates the correlator data's tendency to match the predictions of pqChPT.

Note that while two plots are used to present the results of the pqChPT fit, they are both the product of a single fit, encompassing the valence-quark-mass dependence of both the pion mass and decay constant, as well as the correlator's time dependence.

Error bars were determined via a jackknife analysis of the statistical error. The fit curve's one-sigma range appears in the plots bound by dotted lines. This range was determined by individual jackknife analyses of the curve's value at each point along the horizontal axis. Uncertainty in the lattice spacing and kaon quark-mass threshold are not taken into account. Instead, the plots' axes have simply been rescaled using their central value, so as not to obscure statistical error in the quantities of interest.

A diagonal correlation matrix was used in the fit, as the full matrix proved to not be positive definite in all cases.

Because the statistical error in Figure D.52 is too small to be visible, we have included, inset in the plot, close-ups at three values of the valence quark mass. These inset plots do not share a single scale. However, they do have a horizontal-to-vertical scale ratio which matches that of the main plot.

The fit's determined values for its free parameters appear in Table 9.5.

9.6.3 R_M

As is clear from Figure D.52, the dependence of the squared pion mass on the valence quark mass is very nearly linear. In such plots this strong linearity obscures the presence of higher-order effects. Thus, in order to accentuate non-linear terms, we include plots of a ratio first suggested in [69]:

$$R_M \equiv \frac{m_V M_{\pi_5}^2(m_S)}{m_S M_{\pi_5}^2(m_V)} \tag{9.8}$$

where $M_{\pi_5}(m_Q)$ represents the mass of the local pion containing valence quarks of mass m_Q.

The ratio R_M is designed to allow a visual assessment of the strength and nature of the squared pion mass's non-linearity. Were the dependence of $M_{\pi_5}^2$ on m_V linear, with a massless pion in the chiral limit, a plot of R_M would be flat at $R_M = 1$. If the dependence were quadratic with no constant term, and did not include any higher-order or non-polynomial terms, an R_M plot would be linear. In both cases a small non-zero pion mass at the chiral limit introduces a sharp downturn in R_M for small m_V. For larger m_V the behavior described above is unaffected.

Taking the points and curve from Figure D.52 and transforming them based on the definition of R_M results in Figure D.54.

In order not to cloud the statistical error of the fit results, a jackknife analysis of the quantity R_M has not been performed. As such, correlation between $M_{\pi_5}^2$ at a given valence quark mass and at the dynamical quark mass is not accounted for, nor is uncertainty in $M_{\pi_5}^2$ at the dynamical quark mass. Instead, the plot has simply been transformed using the central value for $M_{\pi_5}^2(m_S)$ as determined in Section 9.4. We feel that this gives a more appropriate representation of the statistical error present in the pqChPT fit. The goal of presenting an R_M plot is not to accurately determine R_M and its uncertainty, but rather to compare the non-linearity of the data and the resulting fit curve. If we were to account for correlation with and uncertainty in $M_{\pi_5}^2(m_S)$, it would obfuscate the points' error bars and the fit curve's one-sigma range. Furthermore, because the independent points and the fit curve do not necessarily agree on the value of $M_{\pi_5}^2(m_S)$, a jackknife analysis would generate a misleading relative shift between their values for R_M.

Note that we use R_M for plotting purposes only. For the pqChPT fit of the correlator data, the expressions for pion mass and decay constant, (6.19) and (6.20), are used directly. Additionally, we do not use the simplification of R_M suggested in [69].

9.6.4 Results

Figures D.55 through D.67 display the results of each ensemble's pqChPT fit. For each ensemble, three plots are presented: an R_M plot, a pion-mass plot, and a pion-decay-constant plot. The creation and presentation of these plots mirrors Figures D.52 through D.54, as discussed in Sections 9.6.2 and 9.6.3. For completeness, the plots

	Λ_{m_V}	a_0	$\check{z}$	$\check{f}$	α_5	$2\alpha_8 - \alpha_5$
A hyp	0.025	-	9.35(17)	0.05237(35)	0.240(33)	0.275(17)
B hyp	0.025	-	11.95(74)	0.0471(11)	0.857(58)	0.211(53)
C hyp	0.025	0.0979(77)	149.1(85)	0.00693(49)	5.02(14)	$-0.28(11)$
A	0.0125	-	9.60(15)	0.07778(50)	2.065(20)	0.360(17)
B	0.0125	-	10.17(32)	0.0758(11)	2.187(49)	0.356(41)
C	0.0125	0.0411(41)	43.7(20)	0.0317(14)	4.82(25)	0.55(13)
W hyp	0.06	-	2.867(15)	0.12036(26)	$-0.298(15)$	0.2472(66)
X hyp	0.06	-	3.104(19)	0.11481(29)	$-0.066(21)$	0.2749(82)
Y hyp	0.06	-	3.281(23)	0.11086(31)	0.111(16)	0.3004(90)
Z hyp	0.06	-	3.778(29)	0.10221(32)	0.491(17)	0.3271(89)
W	0.055	-	0.7649(20)	0.23635(26)	$-0.527(26)$	0.278(14)
X	0.055	-	0.8069(23)	0.23049(27)	$-0.351(27)$	0.304(13)
Y	0.055	-	0.8430(26)	0.22548(28)	$-0.089(23)$	0.348(11)
Z	0.055	-	0.9176(29)	0.21596(28)	0.254(25)	0.4385(99)
Q hyp	0.025	-	9.05(21)	0.05250(46)	$-0.014(53)$	0.223(30)

Table 9.5: Results from the pqChPT correlator fits and corresponding valence-quark-mass cutoff values.

for ensemble A hyp are repeated. The values determined for the fits' free parameters are compiled in Table 9.5.

Comparison of the pqChPT-predicted curve to the individual points in each ensemble's R_M plot demonstrates that the correlator data is systematically missing the predictions of pqChPT. This is most evident in the results for ensembles W hyp through Z hyp, and their thin-link counterparts. It is telling that these are the same ensembles which have the coarsest lattice spacing, and thus the largest expected flavor-symmetry breaking. It is likely that a majority of the data's systematic deviation from the predictions of pqChPT is due to our failure to account for the effects of the staggered formulation's inherent flavor symmetry breaking. As will be discussed

in Section 11.3, any future work in this area will require a more robust handling of flavor-symmetry-breaking effects.

Our results for the GL coefficient combination $2\alpha_8 - \alpha_5$ are relatively stable between ensembles. Comparing ensembles A hyp, A, B hyp, and W hyp demonstrates that, while the corresponding systematic effects are strong, they are not beyond control. A detailed analysis of the systematic error present in our calculation of $2\alpha_8 - \alpha_5$ is presented in Section 10.1.1.

Results for α_5, which controls the polynomial NLO term in the pion decay constant, are much less consistent. This is interesting when we note that the data generally follow pqChPT's predictions for the form of the pion decay constant better than its predictions for the form of the pion mass.

The determined values for $2\alpha_8 - \alpha_5$ from ensembles W hyp through Z hyp show a definite trend, demonstrating an apparent dependence on the dynamical quark mass. This trend can be explained if we recall the m_S-dependent term which was dropped between the true predictions of pqChPT (6.17) and the form used in our single-dynamical-quark-mass fits (6.19). This term is accounted for in our simultaneous fit over these four ensembles, which is presented in Section 9.7.

9.6.5 Polynomial Fits

For comparison we include the R_M plot for both a quadratic and a cubic polynomial fit of the squared pion mass of ensemble A hyp. These can be found in Figures D.68 and D.69. The quadratic fit is taken directly from Section 9.5, while the cubic fit uses the same methods as Section 9.5, replacing the fit's form for the squared pion

	a_0	a_1	a_2	a_3
A hyp	0.001576(82)	3.815(28)	$-8.12(81)$	78.0(81)

Table 9.6: Results for a subset of the fit parameters from the cubic fit of the pion mass's valence-quark-mass dependence.

mass (9.6) with:

$$\check{M}^2_{\pi_5} = a_0 + a_1 m_V + a_2 m_V^2 + a_3 m_V^3 \tag{9.9}$$

The resulting values for the fit parameters of the cubic fit are given in Table 9.6. The agreement between the independent mass points and the fit curve, even in the quadratic case, is strikingly good, especially when compared to the results of the corresponding pqChPT fit, Figure D.54.

9.6.6   Finite Volume

The fit results of ensembles C hyp and C are given last, as their analyses required special attention. The small volume of these ensembles significantly affects their correlator data, a fact which is made most clear by the large non-zero value obtained for the constant term a_0 in the calculation of their kaon quark-mass thresholds. The reader is directed to Table 9.4 and Figure D.47. These finite-volume effects overwhelm the forms predicted by infinite-volume pqChPT, such that attempts to fit these ensembles' correlator data to pqChPT's forms either fail completely or generate nonsensical results.

In order to produce an even moderately reasonable fit, we added a constant term a_0 to pqChPT's predictions for the form of the squared pion mass. Thus, in these

fits, the standard pqChPT form (6.19) was replaced with:

$$\check{M}^2_{\pi_5} = a_0 + \check{z}m_V(4\pi\check{f})^2\left\{1 + \frac{\check{z}}{N_f}\left(2m_V - m_S\right)\ln\check{z}m_V + \frac{\check{z}}{N_f}\left(m_V - m_S\right)\right.$$
$$\left. + \check{z}m_V\left(2\alpha_8 - \alpha_5\right)\right\} \tag{9.10}$$

where a_0 is an additional fit parameter. Comparing Table 9.4 and 9.5, it is interesting to note the similarity between the values obtained for the constant term a_0 in the quadratic and pqChPT-predicted forms.

Even after the addition of a constant term, the results of the fits, Figures D.70 and D.71, remain questionable, especially in the case of ensemble C hyp. Luckily, our study of these ensembles has no purpose other than to elucidate the effects of finite volume.

9.6.7 Dependence on Λ_{m_V}

In order to study the dependence of our results for $2\alpha_8 - \alpha_5$ on the choice of valence-quark-mass cutoff Λ_{m_V}, the pqChPT fits were repeated using a range of cutoff values. The results of this investigation are presented in Figures D.72 through D.76. Figure D.72 displays the Λ_{m_V} dependence of all four parameters of the fit of ensemble A hyp, while Figures D.73 through D.76 display only the dependence of the parameter $2\alpha_8 - \alpha_5$ for all ensembles.

These plots clearly demonstrate that the cutoff choice is a significant source of systematic error. The strong dependence of $2\alpha_8 - \alpha_5$ on Λ_{m_V} is a direct result of the failure of the theoretical forms to closely match the data. As the mass cutoff is increased, and additional valence-quark-mass values are added to the fit range, the additional correlator data consistently fails to match the values predicted for it by

previous lower-cutoff fits. As such, each addition of correlator data significantly alters the fit results.

We expect this sort of behavior for large cutoffs which fall beyond the range of pqChPT. However, below some threshold value for Λ_{m_V}, we expect the value of $2\alpha_8 - \alpha_5$ to level off. This threshold would indicate the outer limit of pqChPT's domain. Yet, in our data we see no clear plateau. Instead, we observe a strong dependence on Λ_{m_V} down to the smallest valence quark masses studied.

Two possible reasons for this behavior are readily available. First, it is possible that the valence quark masses under study are too large for pqChPT to generate accurate predictions. That is, our entire study lies beyond the threshold. However, as the mass of our local pion reaches values well below the physical kaon mass, we feel that this possibility is unlikely. Second, the behavior of our correlator data may be significantly skewed by flavor-symmetry-breaking effects, rendering the predictions of continuum pqChPT inaccurate.

While the choice of valence-quark-mass cutoff is clearly a significant source of systematic error, the variation of $2\alpha_8 - \alpha_5$ is not so great as to render our results meaningless. In Section 10.1.1 we incorporate this quantitative analysis of this source of systematic error into an estimate for the full systematic uncertainty of our result.

While the utility of an analysis of the Λ_{m_V} dependence of the results of ensembles C hyp and C is not clear, it has been included for completeness. Because, for these ensembles, we are using a pion mass form with three free parameters, the smallest cutoff which generates sensible results is one which leaves us with three valence-quark-mass values within the cutoff. As such, the range of Λ_{m_V} studied for these ensembles does not reach as low as for other ensembles.

177

	$\check{z}$	$\check{f}$	$2\alpha_8 - \alpha_5$	α_5	$2\alpha_6 - \alpha_4$	α_4
hyp	2.500(16)	0.12993(41)	0.3860(63)	−0.119(19)	−0.2703(74)	−1.446(33)
thin	0.6970(26)	0.24780(39)	0.2292(88)	−0.093(29)	0.006(14)	−3.207(59)

Table 9.7: Results from the simultaneous pqChPT fits of the correlators of ensemble sets hyp, which includes ensembles W hyp through Z hyp, and thin, which includes ensembles W through Z.

9.7 $2\alpha_6 - \alpha_4$

Four of our ensembles, ensembles W through Z, are constructed to have the same lattice spacing and volume, such that the only variation between them is their dynamical quark mass. Through these ensembles we are granted the opportunity to fit lattice data to the predictions of pqChPT over a block of pqQCD's two-dimensional quark-mass plane.

We fit the correlator $C_{5,5;t}$ over a range of time separations t, valence quark masses m_V, and dynamical quark masses m_S to the form predicted by pqChPT: (6.16), (6.17), and (6.18). Because we are working over a range of dynamical quark masses, we do not need to drop the unknown m_S dependence from these forms, as was done in Section 9.6. The result is values for the fit's free parameters, which include the GL coefficient combinations $2\alpha_8 - \alpha_5$, $2\alpha_6 - \alpha_4$, α_5, and α_4.

The fit was carried out twice, once for the hypercubic-blocked ensemble set, and once for the corresponding thin-link set. The resulting fit parameter values can be found in Table 9.7, with the ensemble set hyp containing ensembles W hyp through Z hyp and the ensemble set thin containing ensembles W through Z. The corresponding fit curves are displayed in Figures D.77 through D.80. These curves are generated

using the fits' resulting parameter values in equations (6.17) and (6.18) and constructing the R_M curves as described in Section 9.6.3. Each plot includes four cross sections through the quark-mass plane, each along a different line of constant dynamical quark mass. Note that while eight fit curves are shown for each ensemble set, four in each plot, they together represent the results of a single fit.

The plots' diamonds represent the results of a set of independent fits of the correlator data at separate valence- and dynamical-quark-mass values, using the same method as was used in Section 9.4. From this we obtain a value for the pion mass and decay constant at each valence and dynamical quark mass at which the correlator was calculated. The quark-mass values at which a filled diamond appears correspond to the set of values used in the full pqChPT fit. Open diamonds correspond to quark-mass values beyond the valence-quark-mass cutoff. The full pqChPT fit of an ensemble set is not a fit to the filled diamonds. Rather, the fit curve and diamonds are related only in that they are derived from the same correlator data. Their agreement, or lack thereof, demonstrates the correlator's tendency to match the predictions of pqChPT.

Error bars were determined via a jackknife analysis of the statistical error. The fit curves' one-sigma range appears in the plots bound by dotted lines. This range was determined by individual jackknife analyses at each point along the horizontal axis. Uncertainty in the lattice spacing and kaon quark-mass threshold are not taken into account. Instead, the plots' axes have simply been rescaled using the average central value between the ensembles.

A diagonal correlation matrix was used in the fit, as the large number of correlator values generated a matrix which was far from positive definite.

For illustrative purposes we have compiled the results of the independent pqChPT fits of ensembles W hyp through Z hyp and W through Z from Section 9.6 into plots whose formats mirror Figures D.77 through D.80. These compiled plots of the independent fits can be found in Figures D.81 through D.84. Comparison between these plots makes clear the difference in results between the independent and simultaneous correlator fits.

We also present the results of the simultaneous fits using a cross section through the quark-mass plane along the unquenched line, $m_Q \equiv m_V = m_S$. The plots are found in Figures D.85 and D.86. Other than the choice of cross section, these plots were generated in the same fashion as described above. Because the definition of R_M is meaningful only along lines of constant dynamical quark mass, we introduce a new ratio:

$$R'_M \equiv \frac{m_Q M^2_{\pi_5}(m_R)}{m_R M^2_{\pi_5}(m_Q)} \tag{9.11}$$

For our plots we use a reference quark mass of $m_R = 0.025$.

From all the plots presented, we can clearly see that the correlator data systematically misses the predictions of pqChPT. As discussed in Section 9.6.4, this is most likely due to strong flavor-symmetry-breaking effects, a consequence of these ensembles' coarse lattice spacing. Because of the computational expense involved in the generation of a set of four reasonably long partially quenched Markov chains, we were forced to use small lattice extents. Thus, a very coarse lattice spacing was required in order to maintain a reasonable lattice volume. The spacing is coarser than what is generally deemed acceptable by the community. As such, this calculation of $2\alpha_6 - \alpha_4$ can only be taken as a preliminary study. Yet, as ours is the first attempt at such a calculation, such a preliminary study is not without value.

The preliminary nature of this study is further emphasized by the fact that only a single ensemble set is available to us. As such, we do not have the ability to generate estimates for the magnitude of the various systematic errors we know are present in our result.

9.7.1 Dependence on Λ_{m_V}

In order to study the dependence of our results on the choice of valence-quark-mass cutoff Λ_{m_V}, we repeated the fits using a range of cutoff values. The results of this investigation are shown in Figures D.87 and D.88. Just as was seen in the independent fits of Section 9.6, there is a strong dependence on Λ_{m_V} down to small quark mass. We would hope that in a more complete study using a smaller lattice spacing, this dependence would disappear for small quark mass.

CHAPTER 10

RESULTS

The primary result of our study is a value for the Gasser-Leutwyler coefficient combination $2L_8 - L_5$ (10.3), along with its corresponding value for the light-quark-mass ratio m_u/m_d (10.9). The secondary results include a value for the the GL coefficient L_5 with very large systematic errors (10.11) and values for L_4 and L_6 with large and unestimated systematic errors, (10.12) and (10.13).

A subset of these results were presented in [1]. Their account here is significantly more comprehensive and incorporates several improvements in our analysis techniques.

10.1   Primary Results

We take the central value of our quoted result for the GL coefficient combination $2\alpha_8 - \alpha_5$ from the correlator data of our primary ensemble, ensemble A hyp. This produces the value $2\alpha_8 - \alpha_5 = 0.275 \pm 0.017$, where the given uncertainty accounts only for statistical error.

10.1.1   Systematic Error

An important aspect of our study is the ability to make a quantitative estimate of our systematic error. Past theoretical estimates for the GL coefficient combination

$2\alpha_8 - \alpha_5$ have suffered from an inability to quantify the systematic error resulting from the approximations they require. Our first-principles approach, however, allows for such an investigation. All of the systematics which separate our calculation's result from the true value of $2\alpha_8 - \alpha_5$ are known and open to investigation.

To determine our systematic error, we note the variation in $2\alpha_8 - \alpha_5$ due to four changes in our calculation: reducing the lattice volume, hypercubic blocking, doubling the lattice spacing, and shifting the valence-quark-mass cutoff. While it is likely that several of the variations are correlated — for example, both the removal of hypercubic blocking and doubling the lattice spacing increase a single systematic-error source: flavor and Lorentz symmetry breaking — in order to generate a generous estimate of our error, we will add the variations in quadrature, as if uncorrelated.

Our study of ensemble B hyp grants us insight into the effects of finite volume on our result. Ensemble B hyp produces values for the fit parameters similar to those of ensemble A hyp, indicating that finite-volume effects in our primary ensemble are well under control. We estimate the uncertainty due to finite volume using the shift in value of $2\alpha_8 - \alpha_5$ between the volumes: ± 0.064.

Hypercubic blocking has been shown to reduce the flavor symmetry breaking inherent in staggered calculations. In order to estimate the strength of flavor-symmetry-breaking effects on our result, we compare our result to the value obtained from the thin-link version of our primary ensemble, ensemble A. We take the resulting shift in value as our estimate of flavor-symmetry-breaking error: ± 0.085.

The lattice spacing has a direct impact on the accuracy of our lattice calculations, controlling the strength of unwanted Lorentz- and flavor-symmetry-breaking terms in our action. To estimate the strength of these finite-lattice-spacing effects, we compare

our value for $2\alpha_8 - \alpha_5$ to that obtained from an ensemble with approximately double the lattice spacing, ensemble W hyp. This shift gives us a qualitative estimate for the corresponding systematic error: ± 0.028.

The investigation of Section 9.6.7 demonstrated that the choice of valence-quark-mass cutoff is a significant source of systematic uncertainty. While this uncertainty is likely related to flavor symmetry breaking, we will add in quadrature the variation due to changing our valence-quark-mass cutoff as if it were an independent error source. It was determined in Section 9.6.7 that shifting the valence-quark-mass cutoff Λ_{m_V}/m_{Q_K} by ± 0.15 results in a variation of $2\alpha_8 - \alpha_5$ equal to ± 0.13. We will use this variation as our estimate of the systematic error due to our somewhat arbitrary choice of valence-quark-mass cutoff.

Presenting all error sources together, our result becomes:

$$2\alpha_8 - \alpha_5 \;=\; 0.275 \;\pm\; 0.017 \;\pm\; 0.064 \;\pm\; 0.085 \;\pm\; 0.028 \;\pm\; 0.13 \qquad (10.1)$$

Adding all sources in quadrature gives our final result:

$$2\alpha_8 - \alpha_5 = 0.28 \pm 0.17 \qquad (10.2)$$

In terms of the standard GL coefficient normalization, this corresponds to:

$$2L_8 - L_5 = \left(0.22 \pm 0.14\right) \times 10^{-3} \qquad (10.3)$$

Note that this lies outside the range in which a massless up quark is allowed (3.42).

The compiled results for $2\alpha_8 - \alpha_5$ from all ensembles, as well as both our final result and the range which allows a massless up quark, can be found in Figure 10.1.
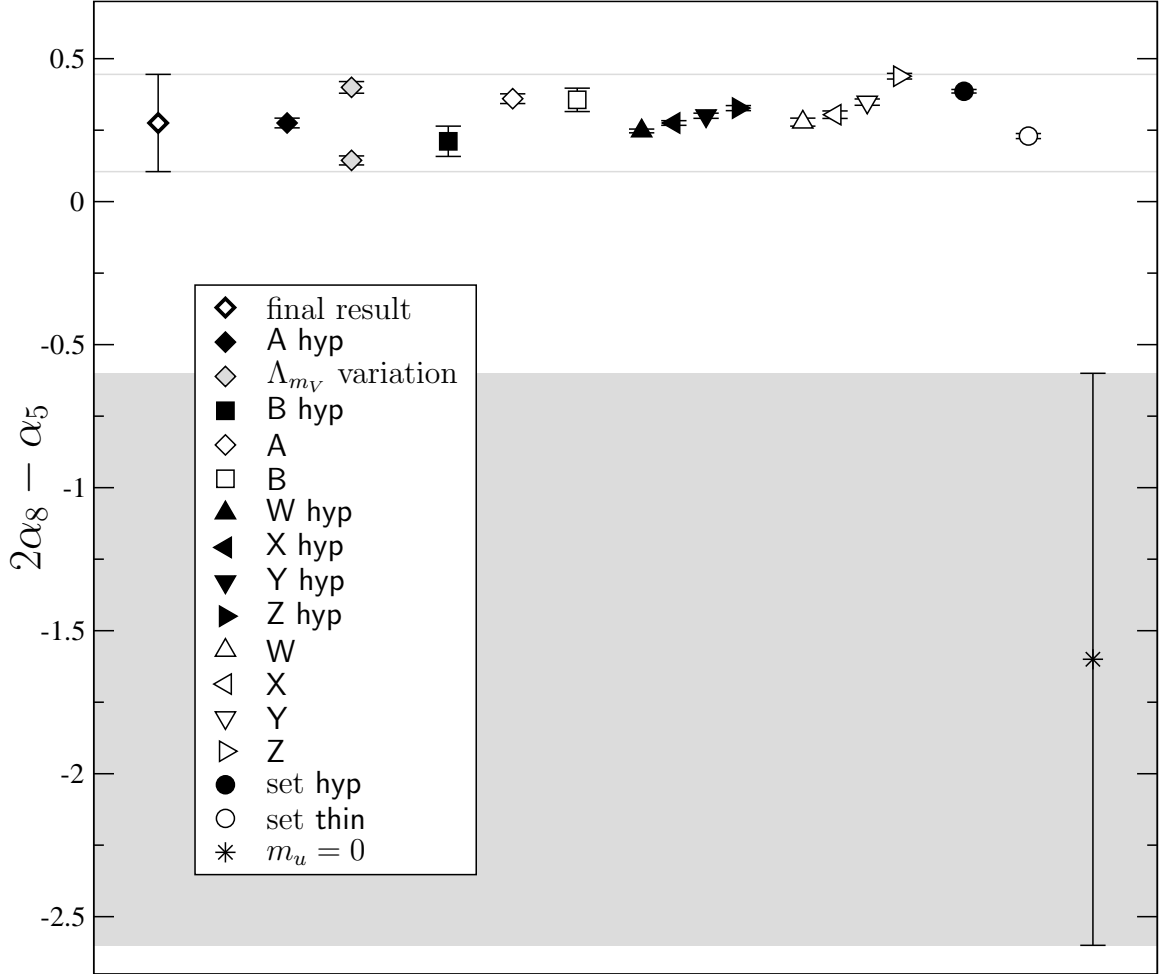
Figure 10.1: The compiled results for $2\alpha_8 - \alpha_5$. The bold open diamond corresponds to our final result and our quoted statistical and systematic error. All other error bars are statistical. The gray diamonds correspond to the result from ensemble A hyp after shifting the valence-quark-mass cutoff Λ_{m_V}/m_{Q_K} by ± 0.015. The filled and open circles correspond to the results of the simultaneous fits of ensembles W hyp through Z hyp and W through Z respectively. The burst corresponds to the range of values which allow a massless up quark (3.44). All other points represent the values obtained for $2\alpha_8 - \alpha_5$ from their corresponding ensemble.

10.1.2 Light-Quark-Mass Ratio

As discussed in Section 6.6, the GL coefficients of our partially quenched calculation are the same coefficients that appear in the physical chiral Lagrangian. As such, we can use our partially quenched results for $2L_8 - L_5$, along with NLO ChPT as presented in Chapter 3, to determine the light-quark-mass ratio of the Standard Model.

Using our result (10.3) in (3.35) generates a value for the NLO correction Δ_M:

$$\Delta_M \; = \; -0.0919 \; \pm \; 0.029 \; \pm \; 0.0084 \tag{10.4}$$

where the first uncertainty is due to error in our result and the second is based on an assumption that the unaccounted for NNLO corrections are on the order of Δ_M^2. Error in other inputs to the calculation of Δ_M are overwhelmed by the uncertainties given. Using Dashen's Theorem to account for the QED contributions to the physical meson masses, instead of (3.29), does not affect Δ_M at this level of precision.

Using our result for $2L_8 - L_5$ (10.3) in (3.40) allows us to generate a value for the light-quark-mass ratio:

$$\frac{m_u}{m_d} \; = \; 0.408 \; \pm \; 0.027 \; \pm \; 0.008 \; \pm \; 0.021 \tag{10.5}$$

where the first uncertainty is due to error in our calculated result, the second comes from an assumption that the NNLO corrections to Δ_M are on the order of Δ_M^2, and the third is due to uncertainty in Δ_E.

Summarizing the repercussions of our calculated value for $2L_8 - L_5$:

$$\Delta_M = 0.092 \pm 0.030 \tag{10.6}$$

$$2L_8 - L_5 = \left(0.22 \pm 0.14\right) \times 10^{-3} \tag{10.7}$$

$$L_7 = \left(-0.23 \pm 0.09\right) \times 10^{-3} \qquad L_8 = \left(0.36 \pm 0.24\right) \times 10^{-3} \tag{10.8}$$

$$\frac{m_u}{m_d} = 0.408 \pm 0.035 \tag{10.9}$$

where the error given in (10.4) and (10.5) has been added in quadrature. In order to determine L_7 and L_8, we have used the value for L_5 determined from the physical meson-decay-constant ratio (3.51) and the value for $12L_7 + 6L_8 - L_5$ determined from the physical deviation from the Gell-Mann-Okubo relation (3.55), adding in quadrature the experimental uncertainty in those values to the error in our calculation. Note that we do not use our calculated value for L_5 as presented in Section 10.2.1.

These numbers can be compared to the generally accepted set of values, (3.91) through (3.94), which are obtained using various model-dependent assumptions and data from beyond the light-meson sector.

The light-quark-mass ratio which results from using Dashen's theorem, instead of (3.29), is $m_u/m_d = 0.482 \pm 0.026$, where there is now no uncertainty due to Δ_E.

Our result for the light-quark-mass ratio (10.9) can be compared with the prediction generated by the generally accepted value for Δ_M (3.91): $m_u/m_d = 0.608 \pm 0.056$. The literature provides additional predictions. Leutwyler [70] gives a ratio of $m_u/m_d = 0.553 \pm 0.043$, while Amoros et al. [19] give a ratio of $m_u/m_d = 0.46 \pm 0.09$ (3.99). Our result is similar to these values, yet somewhat smaller in each case. Note

that our error bars are smaller than all quoted cases. In addition, we are of the opinion that our error bars are the first that can be well trusted, as all others are attempts to account for uncontrolled systematic error due to theoretical assumptions.

The *Review of Particle Physics* [68] quotes a very broad range for the light-quark-mass ratio: $0.2 < m_u/m_d < 0.7$. We fall well within this range.

Our first-principles calculation of the low-energy constants of ChPT demonstrates that the relevant coefficients are too low to allow for the scenario in which the up quark is massless and strong NLO terms emulate a non-zero mass. As the massless-quark solution is seen here to be unlikely, the strong CP problem remains unanswered.

10.2   Secondary Results

The secondary results of our study include values for the GL coefficients L_5, L_4, and L_6.

10.2.1 L_5

Our results for the GL coefficient L_5 are extremely vulnerable to systematic error and vary significantly across the ensembles studied. Estimating the systematic error using the same method as Section 10.1.1 results in:

$$\alpha_5 \;=\; 0.240 \;\pm\; 0.033 \;\pm\; 0.62 \;\pm\; 1.8 \;\pm\; 0.54 \;\pm\; 0.008 \qquad (10.10)$$

where the listed uncertainties are due to statistical error, reducing the lattice volume, hypercubic blocking, doubling the lattice spacing, and shifting the valence-quark-mass cutoff. While it is not clear with such large variation that adding in quadrature is justified, doing so results in $\alpha_5 = 0.2 \pm 2.0$. In terms of the standard GL coefficient

normalization, this corresponds to:

$$L_5 = \left(0.2 \pm 1.6\right) \times 10^{-3} \tag{10.11}$$

This value falls within the range obtained for L_5 from the meson-decay-constant ratio (3.51).

10.2.2 L_4 and L_6

Due to the coarse lattice spacing of ensembles W through Z, our results for the GL coefficient combinations $2\alpha_6 - \alpha_4$ and α_4 are guaranteed to be contaminated by strong systematic error. However, with only a single ensemble set to work with, we are unable to make any qualitative estimates of the error. Thus we present our values for these coefficients only as preliminary results, using the values from the hypercubic-blocked ensemble set and quoting only their statistical error bars:

$$L_4 = \left(-1.145 \pm 0.026^{(\text{stat})}\right) \times 10^{-3} \tag{10.12}$$

$$L_6 = \left(-0.680 \pm 0.013^{(\text{stat})}\right) \times 10^{-3} \tag{10.13}$$

These values both miss their generally accepted ranges, $L_4 = (-0.3 \pm 0.5) \times 10^{-3}$ and $L_6 = (-0.2 \pm 0.3) \times 10^{-3}$, which are determined using large-N_c considerations [17].

10.3   Quenching Effects

Analyzing the results produced by ensemble Q hyp, we see that quenching had a smaller systematic effect on $2\alpha_8 - \alpha_5$ and α_5 than any other source of systematic error studied. Clearly, at this level of precision, quenched and partially quenched ensembles do not generate distinctly different valence-quark-mass dependencies for

189

the pion mass and decay constant, despite the differing predictions of quenched and partially quenched ChPT. This indicates that, while the N_f dependence of ChPT is not explicit and thus the GL coefficients are unknown functions of the number of dynamical quark flavors, that functional dependence is very slight.

CHAPTER 11

SUMMARY AND OUTLOOK

The low-energy constants of the chiral Lagrangian, the Gasser-Leutwyler coefficients, are a critical element in the understanding of low-energy QCD. Yet current theoretical estimates and experimental measurements of the GL coefficients, even those unaffected by the Kaplan-Manohar ambiguity, have errors from 10% to 160% [23]. For many of the coefficients, their current error bars remain as large as they were at the first instance of their calculation [17]. Given LQCD's capacity to calculate these coefficients directly, with no uncontrolled approximations, it is clear that work in this area is warranted. This may in fact prove to be one of those rare, yet increasingly common, situations in which lattice techniques have some chance of providing the greater community with the most trusted predictions available.

Our study definitively calculates a single combination of the GL coefficients, determining a value for $2L_8 - L_5$ which rules out the massless-up-quark solution to the strong CP problem. The culmination of our study is a value for the light-quark-mass ratio:

$$\frac{m_u}{m_d} = 0.408 \pm 0.035 \tag{11.1}$$

This work is far from the closing word in the lattice study of Gasser-Leutwyler coefficients. In truth it is just the first step in what will likely be a long-term and comprehensive study of the coefficients by the lattice community.

From a short-term and more pragmatic perspective, there are several aspects of our study ripe for improvement. In addition, new theoretical work is on the horizon which should dramatically improve lattice calculations of the GL coefficients.

11.1 Improved Systematics

Clearly, future calculations would do well to improve on the systematics of our study through superior ensembles, utilizing either more sophisticated actions or simply more sophisticated computers.

Despite the large uncertainty in the QED contribution, the greatest source of error in the light-quark-mass ratio (10.5) remains the systematic error in our calculation of $2L_8 - L_5$. Improved systematics thus have the potential to reduce the error bars by up to a factor of root two.

Additionally, a reduction in systematic error may prove to bring the fluctuations in L_5 under control, leading to a result in which we could have reasonable confidence. As L_5 is not subject to the KM ambiguity, this would allow for a comparison between lattice and experimental results.

In the case of the coefficients L_4 and L_6, our study was not broad enough to estimate the magnitude of our error. Producing results with reasonable and well-estimated systematic error would require the availability of a number of quality ensemble sets, with each set including ensembles across a range of dynamical quark masses.

11.1.1 High-Quality Publicly Available Ensembles

When our study began, high-quality ensembles at $N_f = 3$ were not publicly available. We had no choice but to use our relatively limited computer resources to generate the requisite ensembles. As a consequence the resulting ensembles, with their mediocre lattice extent and unimproved action, are far from cutting edge.

Today however, thanks to the MILC collaboration [71] in conjunction with the Gauge Connection [72], a set of ten $20^3 \times 64$, $N_f = 3$ ensembles are available for public use. These ensembles span a range of dynamical quark masses and were generated using an improved gauge action and the highly improved a^2-tad staggered action [73]. The application of our analysis to these ensembles would not only produce reduced systematic error in the calculation of $2L_8 - L_5$, but as the ensembles have matched lattice spacings, would also allow for an accurate calculation of L_4 and L_6.

Such a spirit of sharing is extremely valuable to those of us who do not lead the community in computational resources. Beyond that, the community itself profits, as the number of individuals capable of significant and impacting research is dramatically increased.

11.2 Dynamical Hypercubic Blocking

In our study we reduced the systematic error due to flavor symmetry breaking by hypercubic blocking after the generation of our ensembles. In effect we used hypercubic-blocked valence quarks in conjunction with thin-link dynamical quarks. While this technique has merit, clearly a more consistent approach would be to use hypercubic-blocked dynamical quarks during ensemble creation. This approach should also further decrease flavor-symmetry-breaking error.

Following this logic, Flemming [74] has plans for a direct continuation of our work via the creation of ensembles using practical algorithms for dynamical hypercubic-blocked fermions, which are only now becoming available [50, 51, 52].

11.3   Staggered Chiral Perturbation Theory

A recent and very exciting theoretical development germane to the connection between LQCD and ChPT is staggered Chiral Perturbation Theory (sChPT) [75, 76].

In standard ChPT only a single structure breaks flavor symmetry: the quark mass matrix. In the context of staggered fermions, however, the theory contains additional flavor-breaking structures which arise at finite lattice spacing. In sChPT these new flavor-breaking elements are accounted for through the introduction of additional terms to the Lagrangian at each order. The chiral Lagrangian becomes an expansion in three parameters instead of two: meson momentum, meson mass, and lattice spacing.

A complication arises in sChPT when work is done at $N_f \neq 4$. At the core of the staggered formulation are four flavors. Thus, even when a fractional power of the fermionic determinant is used to set $N_f \neq 4$, as discussed in Section 5.3.9, the flavor symmetry breaking due to finite lattice spacing retains its four-flavor structure. As a consequence, sChPT can only be constructed for theories which include some multiple of four flavors. In order to apply the results of sChPT to theories with some other number of flavors, such as $N_f = 3$, the strength of meson-loop graphs must be adjusted by hand.

As discussed in Section 5.3.6, flavor symmetry breaking in staggered fermions leads to a non-degeneracy of the sixteen light mesons, splitting them into five levels.

The sChPT expression for the local pion mass conforms to this scenario, containing additional terms which are the result of meson loops failing to cancel exactly, as they would in the degenerate continuum case. As such, Bernard [75] demonstrates that accounting for a majority of the new finite-lattice-spacing terms does not require the calculation of a full set of fresh low-energy constants. Instead, it requires only a calculation of the four meson-mass splittings.

However, two of these new terms, those which allow mesons to switch flavor content via insertions into a propagator, have coefficients which can not be directly measured. Thus, they must be left as free parameters in a fit. Preliminary attempts at such fits of the local pion mass [76] have proved unstable, with the two parameters running to unnaturally large and opposite values. Introducing priors to the fit could stabilize results. Also, as the same two coefficients appear in all sChPT expressions, fitting multiple quantities simultaneously, such as the pion mass and decay constant, may bind their values. It is worth noting that these coefficients can not be determined once and for all, unlike the GL coefficients, as they are a function of the action. Different improved actions have different flavor symmetry breaking, and thus the coefficients will take on different values.

Because the lattice-spacing dependence of the staggered chiral Lagrangian is known and explicit up to whatever order we chose, and because in the continuum limit staggered quarks are equivalent to continuum quarks, a calculation of the low-energy constants of sChPT corresponds exactly to a calculation of physical ChPT's GL coefficients.

Preliminary results for sChPT are promising [76]. They demonstrate that in cases where the local pion mass's dependence on the quark mass does not follow the

195

form predicted by continuum ChPT, a phenomenon clearly evident in our data, the dependence matches closely the predictions of sChPT. As such, use of sChPT should result in a drastic reduction of the systematic errors in lattice calculations of the GL coefficients.

In fact the advent of sChPT has an impact beyond simply the accurate measurement of GL coefficients. sChPT provides, for any quantities to which it is relevant, the appropriate simultaneous extrapolation from numerically-favorable quark masses and finite lattice spacing to physical quark masses and the continuum limit.

11.4   Quantum Electrodynamic Corrections

A significant percentage of the uncertainty in the light-quark-mass ratio is due to uncertainty in the magnitude of the QED contribution to the pion mass. While not addressed in this study, lattice techniques exist which allow for the calculation of this contribution [77, 78]. In a situation where attempts to significantly reduce the systematic error in $2L_8 - L_5$ are successful, an accurate lattice calculation of Δ_E may prove valuable.

APPENDIX A

NOTATION

So as to leave the main text uncluttered, we list several notational conventions here.

Throughout, we use the pion decay constant normalization $f_\pi \simeq 92.4\,\mathrm{MeV}$. This differs from the other common normalization by a factor of root two, $\sqrt{2}f_\pi \simeq 130.7\,\mathrm{MeV}$.

When the standard normalization for the GL coefficients is being used, they are denoted by L_i. While this is the normalization which generally appears in a chiral Lagrangian, most NLO expressions for observable quantities are made cleaner through the use of a second normalization which we denote by α_i. The normalizations are related by the expression:

$$\alpha_i = 8(4\pi)^2 L_i \tag{A.1}$$

Traces over color indices are denoted by tr, while traces over other indices, generally flavor indices, are denoted by Tr.

Integration over all space is denoted by:

$$\int_x \equiv \iiiint d^4 x \tag{A.2}$$

while integration over all momenta is denoted by:

$$\int_k \equiv \iiiint \frac{d^4 k}{(2\pi)^4} \tag{A.3}$$

197

When denoting dimensionful quark masses, we use a lower-case subscript such as m_q. When denoting a dimensionless lattice quark mass, we use a corresponding upper-case subscript such as m_Q. For all quantities other than quark mass, we use a check over the variable to denote its unitless counterpart. For example in the case of the local pion mass, $M_{\pi_5} = a\check{M}_{\pi_5}$.

The generators of the various $SU(N)$ Lie algebras are represented by λ^a for color transformations and τ^a for flavor transformations. They are traceless Hermitian $N \otimes N$ matrices, which are normalized according to:

$$\mathrm{Tr}\left[\tau^a\tau^b\right] = \frac{1}{2}\delta^{ab} \qquad\qquad \mathrm{tr}\left[\lambda^a\lambda^b\right] = \frac{1}{2}\delta^{ab} \qquad (A.4)$$

and satisfy the commutation relations:

$$\left[\tau^a, \tau^b\right] = if^{abc}\tau^c \qquad\qquad \left[\lambda^a, \lambda^b\right] = ig^{abc}\lambda^c \qquad (A.5)$$

where f^{abc} and g^{abc} are the appropriate structure constants of the algebras, which are completely antisymmetric and real. λ^a should not be confused with the $SU(N)$ Gell-Mann matrices, as $\lambda^a = \frac{1}{2}\lambda^a_{\text{Gell-Mann}}$.

The Lorentz tensor $\epsilon_{\mu\nu\alpha\beta}$ is defined to be totally antisymmetric, with:

$$\epsilon_{1234} = 1 \qquad (A.6)$$

The Euclidean-space Dirac matrices γ^μ are defined to satisfy the anticommutation relation:

$$\{\gamma^\mu, \gamma^\nu\} = 2g_E^{\mu\nu} = 2\delta^{\mu\nu} \qquad (A.7)$$

where $g_E^{\mu\nu}$ is the flat Euclidean-space metric. Unlike the Minkowski-space Dirac matrices, the Euclidean-space matrices are Hermitian:

$$\gamma^\mu = \gamma^{\mu\dagger} \qquad (A.8)$$

198

The Dirac matrices can be used to construct the generators of a spinor representation of the Lorentz group. Given a Lorentz transformation:

$$x^\mu \quad \rightarrow \quad x'^\mu = \Lambda^\mu_\nu x^\nu \tag{A.9}$$

$$\Lambda^\mu_\nu = e^{-\frac{i}{2}\omega_{\alpha\beta}(\mathcal{J}^{\alpha\beta})^\mu_\nu} \in O(4)_{\mathrm{Lorentz}} \tag{A.10}$$

where $\mathcal{J}^{\alpha\beta}$ are the generators of Lorentz rotations on Lorentz 4-vectors and $\omega_{\alpha\beta}$ is an antisymmetric tensor which parameterizes the transformation, a spinor transforms as:

$$\psi \quad \rightarrow \quad \psi' = S(\Lambda)\psi \tag{A.11}$$

$$\bar{\psi} \quad \rightarrow \quad \bar{\psi}' = \bar{\psi}S^{-1}(\Lambda) \tag{A.12}$$

$$S(\Lambda) = e^{-\frac{1}{8}\omega_{\alpha\beta}[\gamma^\alpha,\gamma^\beta]} \in O(4)_{\mathrm{spin}} \tag{A.13}$$

The Dirac matrices themselves transform correctly under the Lorentz group both as Lorentz 4-vectors and as spin space matrices:

$$S(\Lambda)\gamma^\mu S^{-1}(\Lambda) = \Lambda^\mu_\nu \gamma^\nu \tag{A.14}$$

Using the Dirac matrices, the matrix γ^5 is defined as:

$$\gamma^5 = \gamma^1\gamma^2\gamma^3\gamma^4 \tag{A.15}$$

which anticommutes with the other four Dirac matrices:

$$\{\gamma^5,\gamma^\mu\} = 0 \qquad\qquad \gamma^5\gamma^5 = \mathbb{1} \tag{A.16}$$

We define the discretized directional derivative Δ_μ as:

$$
\begin{aligned}
\Delta_\mu \varphi(x) &\equiv \frac{\varphi(x + a\hat{\mu}) - \varphi(x - a\hat{\mu})}{2a} \\
&= \frac{1}{2a}\left(e^{a\partial_\mu} - e^{-a\partial_\mu}\right)\varphi(x) \\
&= \frac{1}{a}\left(\sinh a\partial_\mu\right)\varphi(x) \\
&= \partial_\mu \varphi(x) + O(a^2)
\end{aligned}
\tag{A.17}
$$

while we defined the second discretized directional derivative Δ_μ^2 as:

$$
\begin{aligned}
\Delta_\mu^2 \varphi(x) &\equiv \frac{\varphi(x + a\hat{\mu}) - 2\varphi(x) + \varphi(x - a\hat{\mu})}{a^2} \\
&= \frac{1}{a^2}\left(e^{a\partial_\mu} - 2 + e^{-a\partial_\mu}\right)\varphi(x) \\
&= \frac{1}{a^2}\left(1 + a\partial_\mu + \tfrac{1}{2}a^2\partial_\mu^2 - 2 + 1 - a\partial_\mu + \tfrac{1}{2}a^2\partial_\mu^2\right)\varphi(x) + O(a^4) \\
&= \partial_\mu^2 \varphi(x) + O(a^4)
\end{aligned}
\tag{A.18}
$$

APPENDIX B

STAGGERED IDENTITIES

B.1 Bilinear Sum

For the sources of our bilinear correlators, we use a linear combination of all bilinears with a given distance binary four-vector $\mathcal{D}_{\mathcal{S},\mathcal{F}} = \mathcal{D}$. Such a combination has a simple form when expressed in terms of χ and $\bar{\chi}$:

$$
\begin{aligned}
\sum_{\mathcal{R}} \mathcal{J}_{\mathcal{R}+\mathcal{D},\mathcal{R};h} &= \sum_{\mathcal{R}} \bar{Q}_h \big(\gamma_{\mathcal{D}} \gamma_{\mathcal{R}} \otimes \xi_{\mathcal{R}} \big) Q_h \\
&= \sum_{\mathcal{R}} \mathrm{Tr} \big[\bar{Q}_h \gamma_{\mathcal{D}} \gamma_{\mathcal{R}} Q_h \gamma_{\mathcal{R}}^{\dagger} \big] \\
&= 4 \mathrm{Tr} \big[\bar{Q}_h \gamma_{\mathcal{D}} \big] \mathrm{Tr} \big[Q_h \big] \\
&= \sum_A \sum_B \mathrm{Tr} \big[\Gamma_A^{\dagger} \gamma_{\mathcal{D}} \big] \mathrm{Tr} \big[\Gamma_B \big] \bar{\chi}_{h+A} \chi_{h+B} \\
&= 16 \sum_A \sum_B \delta_{A,\mathcal{D}} \delta_{B,0} \bar{\chi}_{h+A} \chi_{h+B} \\
&= 16 \bar{\chi}_{h+\mathcal{D}} \chi_h
\end{aligned}
\tag{B.1}
$$

where we have used the identity

$$
\sum_C \big(\Gamma_C^{\dagger} \big)_{b\beta} \big(\Gamma_C \big)_{\alpha a} = 4 \delta_{b,a} \delta_{\beta,\alpha}
\tag{B.2}
$$

or equivalently

$$
\sum_C \Gamma_A^{\dagger} \Gamma_C \Gamma_B \Gamma_C^{\dagger} = 4 \Gamma_A^{\dagger} \, \mathrm{Tr} \, \Gamma_B
\tag{B.3}
$$

The linear combination leaves only a single contraction, that between $\bar{\chi}$ at the corner of the hypercube offset from the lowest corner by $\mathcal{D}$ and χ at the lowest corner. Adding the gauge links required by an interacting theory, we have:

$$\sum_{\mathcal{R}} \mathcal{J}_{\mathcal{R},\mathcal{R}+\mathcal{D};h} = 16\bar{\chi}_{h+\mathcal{D}}\mathcal{U}_{\mathcal{D},0;h}\chi_h \tag{B.4}$$

where $\mathcal{U}_{A,B;h}$ is defined after (5.62). In the case of local bilinears, $\mathcal{D} = 0$, the contraction is contained completely by the lowest corner of the hypercube:

$$\sum_{\mathcal{R}} \mathcal{J}_{\mathcal{R},\mathcal{R};h} = 16\bar{\chi}_h\chi_h \tag{B.5}$$

B.2   Transpose of the Staggered Interaction Matrix

The transpose of the staggered fermion interaction matrix $M^S[U]^T$ arises as the antiquark propagator in our calculation of bilinear correlators. The adjoint matrix can be expressed in terms of $M^S[U]$ in a manner similar to that used for the naive interaction matrix (5.28):

$$
\begin{aligned}
M^S[U]^\dagger_{n,m} &= \frac{1}{2}\sum_\mu \eta_{\mu;m}\left[U_{\mu;m}\delta_{m;n-\hat{\mu}} - U^\dagger_{\mu;m-\hat{\mu}}\delta_{m,n+\hat{\mu}}\right] + m_Q\delta_{m,n} \\
&= -\frac{1}{2}\sum_\mu \left[\eta_{\mu;n-\hat{\mu}}U^\dagger_{\mu;m-\hat{\mu}}\delta_{m;n+\hat{\mu}} - \eta_{\mu;n+\hat{\mu}}U_{\mu;m}\delta_{m;n-\hat{\mu}}\right] + m_Q\delta_{n,m} \\
&= -\frac{1}{2}\sum_\mu \eta_{\mu;n}\left[U^\dagger_{\mu;n}\delta_{n,m-\hat{\mu}} - U_{\mu;n-\hat{\mu}}\delta_{n;m+\hat{\mu}}\right] + m_Q\delta_{n,m} \\
&= \epsilon_n\epsilon_m\left\{\frac{1}{2}\sum_\mu \eta_{\mu;n}\left[U^\dagger_{\mu;n}\delta_{n,m-\hat{\mu}} - U_{\mu;n-\hat{\mu}}\delta_{n;m+\hat{\mu}}\right] + m_Q\delta_{n,m}\right\} \\
&= \epsilon_n M^S_{n,m}[U]\epsilon_m \tag{B.6}
\end{aligned}
$$

This mirrors closely the result for naive fermions, with ϵ_n filling the roll of γ_5.

B.3 Non-Local Bilinear Correlators

In order to study the non-local staggered mesons, the correlators between non-local bilinears must be calculated. We now express non-local bilinear correlators explicitly in terms of quantities which are straightforward to calculate using lattice techniques. That is, the inverse staggered fermion interaction matrix applied to various fermion field vectors. A similar discussion limited to local bilinears is found in Section 5.8.1.

Our general bilinear correlator, using a wall sink to overlap only with zero momentum states, is:

$$\left\langle \sum_{\substack{\vec{g} \\ g_4=t}} \mathcal{J}_{\mathcal{S},\mathcal{F};g} \mathcal{J}_{\mathcal{S},\mathcal{F};0} \right\rangle \tag{B.7}$$

We replace the bilinear in our source with a linear combination of all bilinears with distance vector $\mathcal{D} = \mathcal{D}_{\mathcal{S},\mathcal{F}} = \mathcal{S} + \mathcal{F}$:

$$\frac{1}{16}\left\langle \sum_{\substack{\vec{g} \\ g_4=t}} \mathcal{J}_{\mathcal{S},\mathcal{F};g} \sum_{\mathcal{R}} \mathcal{J}_{\mathcal{R}+\mathcal{D},\mathcal{R};0} \right\rangle \tag{B.8}$$

We replace our single-bilinear source with a wall of bilinears at the appropriate time slice:

$$C_{\mathcal{S},\mathcal{F};t} = \frac{1}{16}\left\langle \sum_{\substack{\vec{g} \\ g_4=t}} \mathcal{J}_{\mathcal{S},\mathcal{F};g} \sum_{\substack{\vec{h} \\ h_4=0}} \sum_{\mathcal{R}} \mathcal{J}_{\mathcal{R}+\mathcal{D},\mathcal{R};h} \right\rangle \tag{B.9}$$

Using (5.62), (5.63), and (B.4), we express the correlator in terms of χ and $\bar{\chi}$:

$$C_{\mathcal{S},\mathcal{F};t} = \left\langle \sum_{\substack{\vec{g} \\ g_4=t}} \sum_{B} (-)^{\varphi_{\mathcal{S},\mathcal{F};B}} \right.$$
$$\left. \times \sum_{\substack{\vec{h} \\ h_4=0}} \sum_{a,b,c,d} \bar{\chi}_{g+B} \mathcal{U}_{B,B+\mathcal{D};g} \chi_{g+B+\mathcal{D}} \bar{\chi}_{h+\mathcal{D}} \mathcal{U}_{\mathcal{D},0;h} \chi_{h} \right\rangle \tag{B.10}$$

203

Integrating over the Grassmann variables using Wick contractions, we express the correlator in terms of the inverse of the interaction matrix:

$$
C_{\mathcal{S},\mathcal{F};t} = \Big\langle \sum_{\substack{\vec{g} \\ g_4=t}} \sum_{B} (-)^{\varphi_{\mathcal{S},\mathcal{F};B}}
$$

$$
\times \sum_{\substack{\vec{h} \\ h_4=0}} \sum_{a,b,c,d} \bar{\chi}_{g+B}\, \underset{a,b}{\mathcal{U}_{B,B+\mathcal{D};g}}\, \underset{b}{\chi_{g+B+\mathcal{D}}}\, \underset{d}{\bar{\chi}_{h+\mathcal{D}}}\, \underset{d,c}{\mathcal{U}_{\mathcal{D},0;h}}\, \underset{c}{\chi_h} \Big\rangle
$$

$$
= \Big\langle \sum_{\substack{\vec{g} \\ g_4=t}} \sum_{B} (-)^{\varphi_{\mathcal{S},\mathcal{F};B}}
$$

$$
\times \sum_{\substack{\vec{h} \\ h_4=0}} \sum_{a,b,c,d} \underset{a,b}{\mathcal{U}_{B,B+\mathcal{D};g}}\, \underset{d,c}{\mathcal{U}_{\mathcal{D},0;h}}\, M^S[U]^{-1}_{\underset{a,c}{g+B,h}} (M^S[U]^T)^{-1}_{\underset{b,d}{g+B+\mathcal{D},h+\mathcal{D}}} \Big\rangle
$$

$$
= \Big\langle \sum_{\substack{\vec{g} \\ g_4=t}} \sum_{B} (-)^{\varphi_{\mathcal{S}+5,\mathcal{F}+5;B}}
$$

$$
\times \sum_{\substack{\vec{h} \\ h_4=0}} \sum_{a,b,c,d} \underset{a,b}{\mathcal{U}_{B,B+\mathcal{D};g}}\, \underset{d,c}{\mathcal{U}_{\mathcal{D},0;h}}\, M^S[U]^{-1}_{\underset{a,c}{g+B,h}}\, M^S[U]^{-1*}_{\underset{b,d}{g+B+\mathcal{D},h+\mathcal{D}}} \Big\rangle \qquad (B.11)
$$

In order to reduce the number of required applications of the inverse interaction matrix, we calculate the $2N_c$ field vectors $X^{(c)}$ and $Y^{(c)}$:

$$
\underset{a}{X^{(c)}_n} = \sum_{\substack{\vec{h} \\ h_4=0}} M^S[U]^{-1}_{\underset{a,c}{n,h}} \qquad (B.12)
$$

$$
\underset{b}{Y^{(c)}_m} = \sum_{d} \sum_{\substack{\vec{h} \\ h_4=0}} M^S[U]^{-1}_{\underset{b,d}{m,h+\mathcal{D}}} \underset{d,c}{\mathcal{U}^*_{\mathcal{D},0;h}} \qquad (B.13)
$$

To calculate $X^{(c)}$ we construct the field vector $W^{(c)}$, which equals one only at color c in the lowest corner of each hypercube on the time slice $n_4 = 0$ and zero elsewhere. The result of applying the inverse interaction matrix to $W^{(c)}$ is $X^{(c)}$:

$$
\underset{a}{X^{(c)}_n} = \big(M^S[U]^{-1} W^{(c)} \big)_{\underset{a}{n}} \qquad (B.14)
$$

To calculate $Y^{(c)}$ we first apply a swap operator $S_{\mathcal{D}}$ to $W^{(c)}$ and then the inverse interaction matrix. The resulting field vector is $Y^{(c)}$:

$$Y^{(c)}_{\substack{m\\b}} = \left(M^S[U]^{-1} S_{\mathcal{D}} W^{(c)} \right)_{\substack{m\\b}} \tag{B.15}$$

The swap operator $S_{\mathcal{D}}$ is similar to the bilinear operator $\left(\gamma_S \otimes \xi_{\mathcal{F}} \right)$ defined by (5.75), but does not apply phase factors to the field vector. It swaps corners separated by the offset vector $\mathcal{D}$ within each hypercube, and applies the appropriate color matrix for that movement:

$$\left(S_{\mathcal{D}} \right)_{n,m} = \delta_{h+A+\mathcal{D},m} \mathcal{U}^*_{A,A+\mathcal{D};h} \tag{B.16}$$

where h denotes the hypercube containing n, and A denotes its position within that hypercube:

$$h = 2 \left\lfloor \frac{n}{2} \right\rfloor \qquad\qquad A = n - h \tag{B.17}$$

The unique random phase associated with each lattice site due to local gauge freedom washes out the position-off-diagonal terms in the product of $X^{(c)}$ and $Y^{(c)}$:

$$\begin{aligned}
Y^{(c)*}_{\substack{m\\b}} X^{(c)}_{\substack{n\\a}} &= \sum_d \sum_{\substack{\vec{h}\\h_4=0}} M^S[U]^{-1*}_{\substack{m,h+\mathcal{D}\\b,d}} \mathcal{U}_{\substack{\mathcal{D},0;h\\d,c}} \sum_{\substack{\vec{f}\\f_4=0}} M^S[U]^{-1}_{\substack{n,f\\a,c}} \\
&= \sum_d \sum_{\substack{\vec{h}\\h_4=0}} M^S[U]^{-1*}_{\substack{m,h+\mathcal{D}\\b,d}} \mathcal{U}_{\substack{\mathcal{D},0;h\\d,c}} M^S[U]^{-1}_{\substack{n,h\\a,c}}
\end{aligned} \tag{B.18}$$

Thus, once $X^{(c)}$ and $Y^{(c)}$ have been calculated, we can construct our correlator:

$$\begin{aligned}
C_{\mathcal{S},\mathcal{F};t} &= \left\langle \sum_c \sum_{\substack{\vec{g}\\g_4=t}} \sum_B (-)^{\varphi_{\mathcal{S}+5,\mathcal{F}+5;B}} \sum_{a,b} \mathcal{U}_{\substack{B,B+\mathcal{D};g\\a,b}} Y^{(c)*}_{\substack{g+B+\mathcal{D}\\b}} X^{(c)}_{\substack{g+B\\a}} \right\rangle \\
&= \left\langle \sum_c \sum_{\substack{\vec{g}\\g_4=t}} \sum_B (-)^{\varphi_{\mathcal{S}+5,\mathcal{F}+5;B}} \sum_{a,b} X^{(c)}_{\substack{g+B\\a}} \mathcal{U}_{\substack{B,B+\mathcal{D};g\\a,b}} Y^{(c)*}_{\substack{g+B+\mathcal{D}\\b}} \right\rangle
\end{aligned} \tag{B.19}$$

or more concisely

$$
\begin{aligned}
C_{\mathcal{S},\mathcal{F};t} &= \left\langle \sum_{c} \sum_{\substack{\vec{g} \\ g_4=t}} \sum_{B} (-)^{\varphi_{\mathcal{S}+5,\mathcal{F}+5;B}} \sum_{a,b} X^{(c)}_{g+B}(S^*_{\mathcal{D}})_{\substack{g+B,g+B+\mathcal{D} \\ a,b}} Y^{(c)*}_{\substack{g+B+\mathcal{D} \\ b}} \right\rangle \\
&= \left\langle \sum_{c} \sum_{\substack{\vec{g} \\ g_4=t}} \sum_{B} (-)^{\varphi_{\mathcal{S}+5,\mathcal{F}+5;B}} \sum_{a} X^{(c)}_{\substack{g+B \\ a}}(S_{\mathcal{D}}Y^{(c)})^*_{\substack{g+B \\ a}} \right\rangle
\end{aligned}
\tag{B.20}
$$

The correlator is a contraction of $X^{(c)}$ and $S_{\mathcal{D}}Y^{(c)}$ summed only over the time slices t and $t+1$.

Note that the field vectors $X^{(c)}$ and $S_{\mathcal{D}}Y^{(c)}$ are independent of t and depend only on the distance vector of the bilinear, $\mathcal{D} = \mathcal{S}+\mathcal{F}$. Thus, once they are known, we can calculate all bilinear correlators of distance vector $\mathcal{D}$ at every time separation with no additional inversions.

APPENDIX C

$SU(3)$ **PROJECTION**

The application of hypercubic blocking, as discussed in Section 5.6, requires the projection of an arbitrary 3×3 matrix onto the group $SU(3)$. We describe here the algorithm used for this projection. For clarity we will use capital letters to denote 3×3 matrices and lower-case letters to denote 2×2 matrices.

Given the 3×3 complex matrix M, we wish to find the nearest $SU(3)$ matrix G:

$$\underset{SU(3)}{\text{proj}}\big[M\big] \equiv G \tag{C.1}$$

We define the nearest group element to be the one which maximizes:

$$\text{tr}\big[GM^{\dagger}\big] \tag{C.2}$$

In order to maximize this trace, we must choose a G such that $GM^{\dagger}$ is as nearly proportional to identity as possible. For $SU(2)$ this problem can be solved in closed form. While this is not true for $SU(3)$, we can break the problem down into an iterative procedure of repeatedly applying the closed-form solution on $SU(2)$ subgroups. If we use a set of subgroups which span the full $SU(3)$ group, the process will converge on the correct G.

We begin with a guess for G:

$$G_1 = \mathbb{1} \tag{C.3}$$

This then gives us an initial residual matrix R:

$$R_1 = G_1 M^\dagger = M^\dagger \tag{C.4}$$

The residual matrix is the matrix we wish to make proportional to identity.

We now enter an iterative process in which each iteration pushes R closer to identity and leads us to a more refined value for G. At the start of each iteration we choose an $SU(2)$ subgroup to work within. In practice we choose from among three $SU(2)$ subgroups, using each in turn. We extract the appropriate 2×2 matrix r from R:

$$r = r^{(a)} \tag{C.5}$$

$$r^{(1)} = \begin{bmatrix} R_{n;11} & R_{n;12} \\ R_{n;21} & R_{n;22} \end{bmatrix} \quad r^{(2)} = \begin{bmatrix} R_{n;11} & R_{n;13} \\ R_{n;31} & R_{n;33} \end{bmatrix} \quad r^{(3)} = \begin{bmatrix} R_{n;22} & R_{n;23} \\ R_{n;32} & R_{n;33} \end{bmatrix} \tag{C.6}$$

where a identifies the subgroup chosen.

In the context of the $SU(2)$ subgroup, there exists a closed-form expression for the group element u nearest the matrix r. We calculate directly the unnormalized coefficients $\tilde{\alpha}_\mu$ of the matrix u:

$$\tilde{\alpha}_4 = \mathrm{Re}\left\{ \frac{1}{2}\mathrm{Tr}[r] \right\} \qquad\qquad \tilde{\alpha}_i = \mathrm{Re}\left\{ -\frac{i}{2}\mathrm{Tr}[r\sigma_i] \right\} \tag{C.7}$$

where σ_i are the Pauli matrices:

$$\sigma_1 \equiv \begin{bmatrix} 0 & 1 \\ 1 & 0 \end{bmatrix} \qquad\qquad \sigma_2 \equiv \begin{bmatrix} 0 & -i \\ i & 0 \end{bmatrix} \qquad\qquad \sigma_3 \equiv \begin{bmatrix} 1 & 0 \\ 0 & -1 \end{bmatrix} \tag{C.8}$$

After normalizing the coefficients:

$$\alpha_\mu = \frac{\tilde{\alpha}_\mu}{|\tilde{\alpha}|} \tag{C.9}$$

u is constructed:

$$u = \alpha_4 \mathbb{1} + i \sum_i \alpha_i \sigma_i \tag{C.10}$$

Clearly, if u is the closest $SU(2)$ group element to r, applying the inverse of u to r will result in a matrix as near to proportional to identity as is possible.

We now return to the full 3×3 matrices in order to complete the iteration:

$$
U = \begin{cases}
\begin{bmatrix} u_{11} & u_{12} & 0 \\ u_{21} & u_{22} & 0 \\ 0 & 0 & 1 \end{bmatrix} & a = 1 \\[2em]
\begin{bmatrix} u_{11} & 0 & u_{12} \\ 0 & 1 & 0 \\ u_{21} & 0 & u_{22} \end{bmatrix} & a = 2 \\[2em]
\begin{bmatrix} 1 & 0 & 0 \\ 0 & u_{11} & u_{12} \\ 0 & u_{21} & u_{22} \end{bmatrix} & a = 3
\end{cases} \tag{C.11}
$$

We move R closer to identity, and refine our value for G, by applying to G the inverse of U. As U is unitary, its inverse is simply its adjoint:

$$G_{n+1} = U^\dagger G_n \tag{C.12}$$

$$R_{n+1} = U^\dagger R_n = G_{n+1} M^\dagger \tag{C.13}$$

At this point we have completed one iteration. The process is now repeated using our refined guess for G.

When the trace of R stops improving, we have reached our final value for G. We end the iterative process when:

$$\left| \text{Tr} \, R_{n+1} - \text{Tr} \, R_n \right| < \epsilon \tag{C.14}$$

where ϵ is our error tolerance. In practice we only perform this test after using all three $SU(2)$ subgroups in turn, as it is possible that the trace may be flat with respect to one subgroup, while improvement is still possible along the other directions.

APPENDIX D

FIGURES
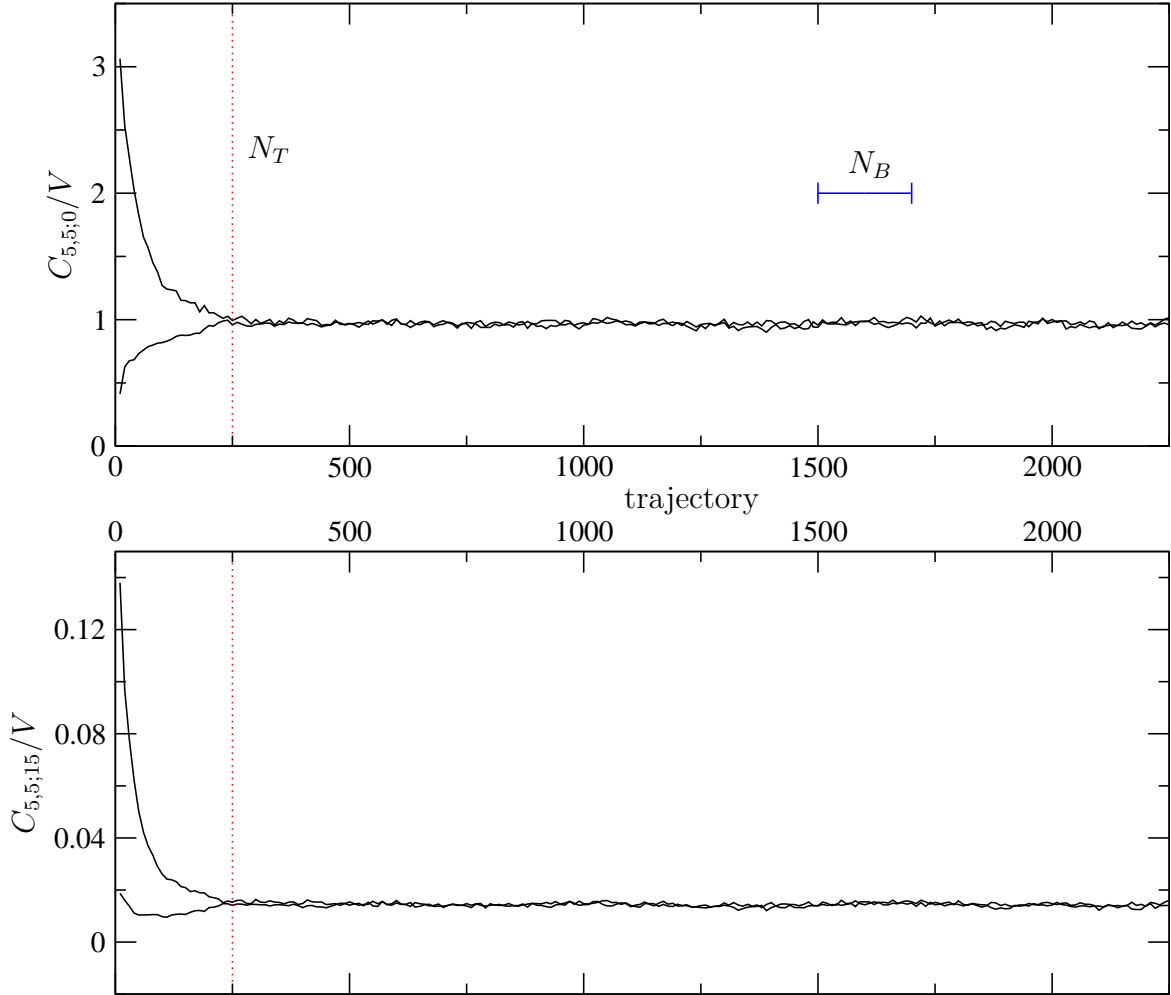
Figure D.1: Markov chain of ensemble A with thermalization point N_T and block length N_B shown. The correlator $C_{5,5;t}$ is calculated using $m_V = 0.01$. Of the ensemble's two Markov chains, the chain which begins above the equilibrium value has a disordered initial condition. The second has an ordered initial condition.
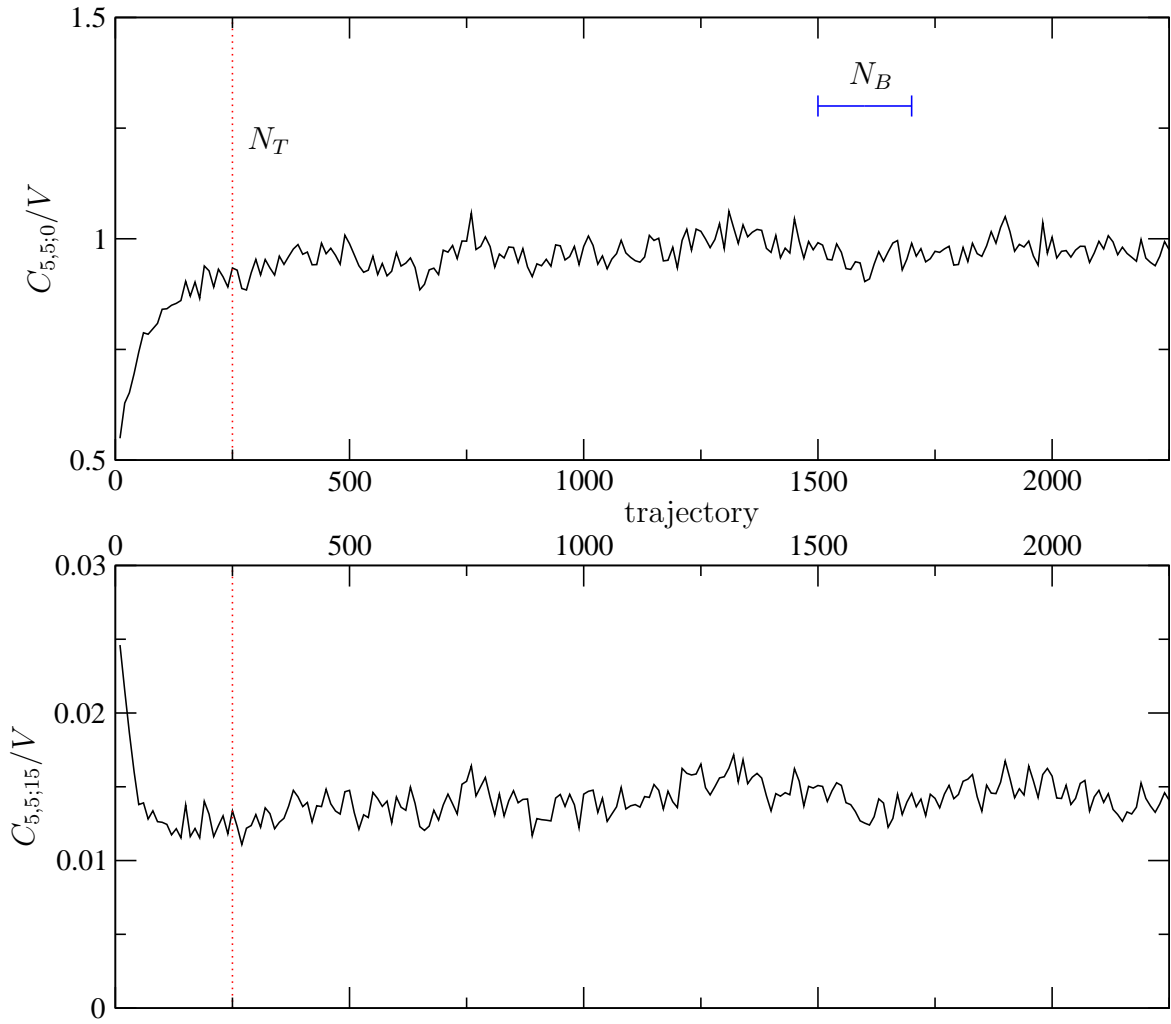
Figure D.2: Markov chain of ensemble B with thermalization point N_T and block length N_B shown. The correlator $C_{5,5;t}$ is calculated using $m_V = 0.01$. The Markov chain has an ordered initial condition.
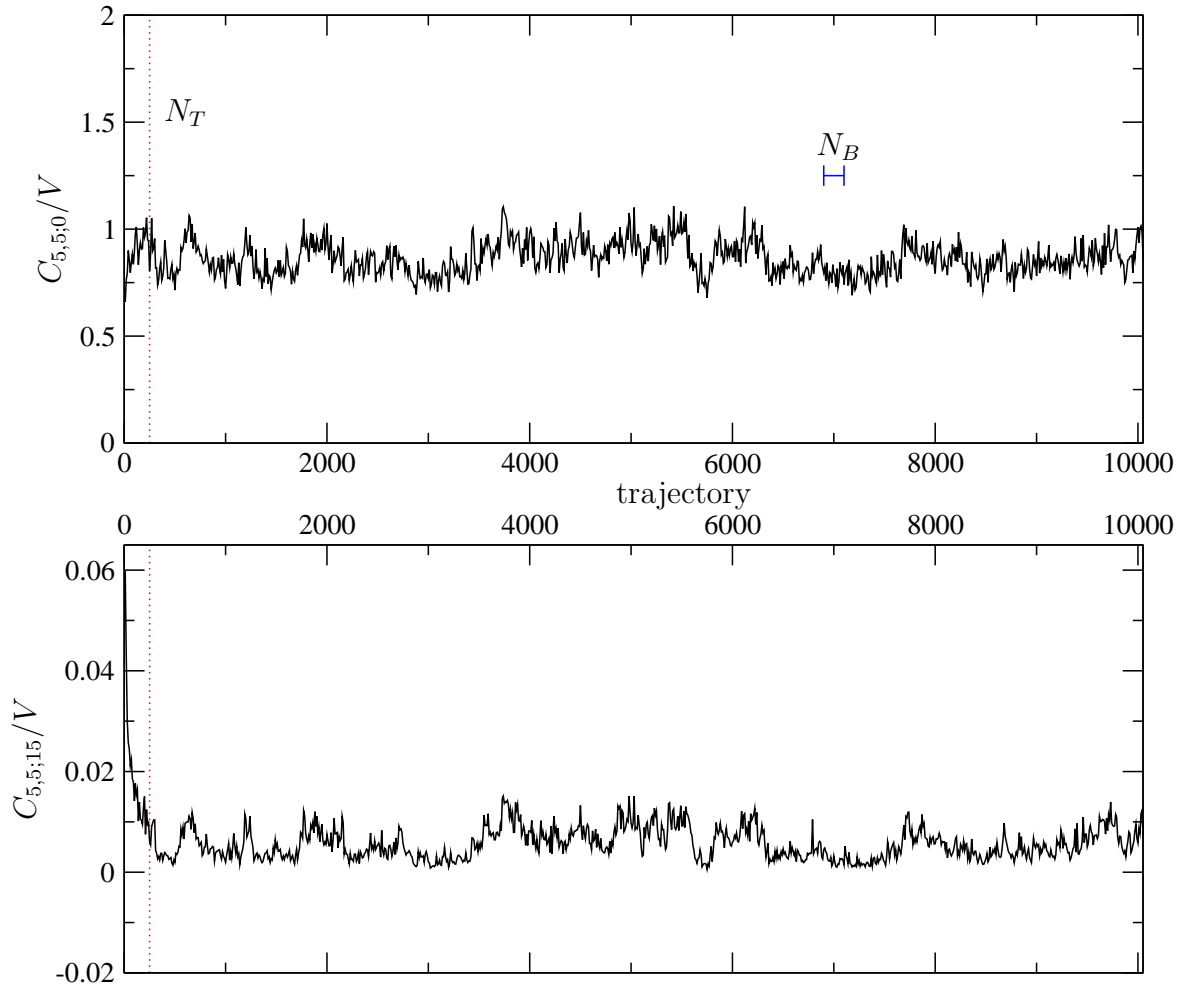
Figure D.3: Markov chain of ensemble C with thermalization point N_T and block length N_B shown. The correlator $C_{5,5;t}$ is calculated using $m_V = 0.01$. The Markov chain has an ordered initial condition.
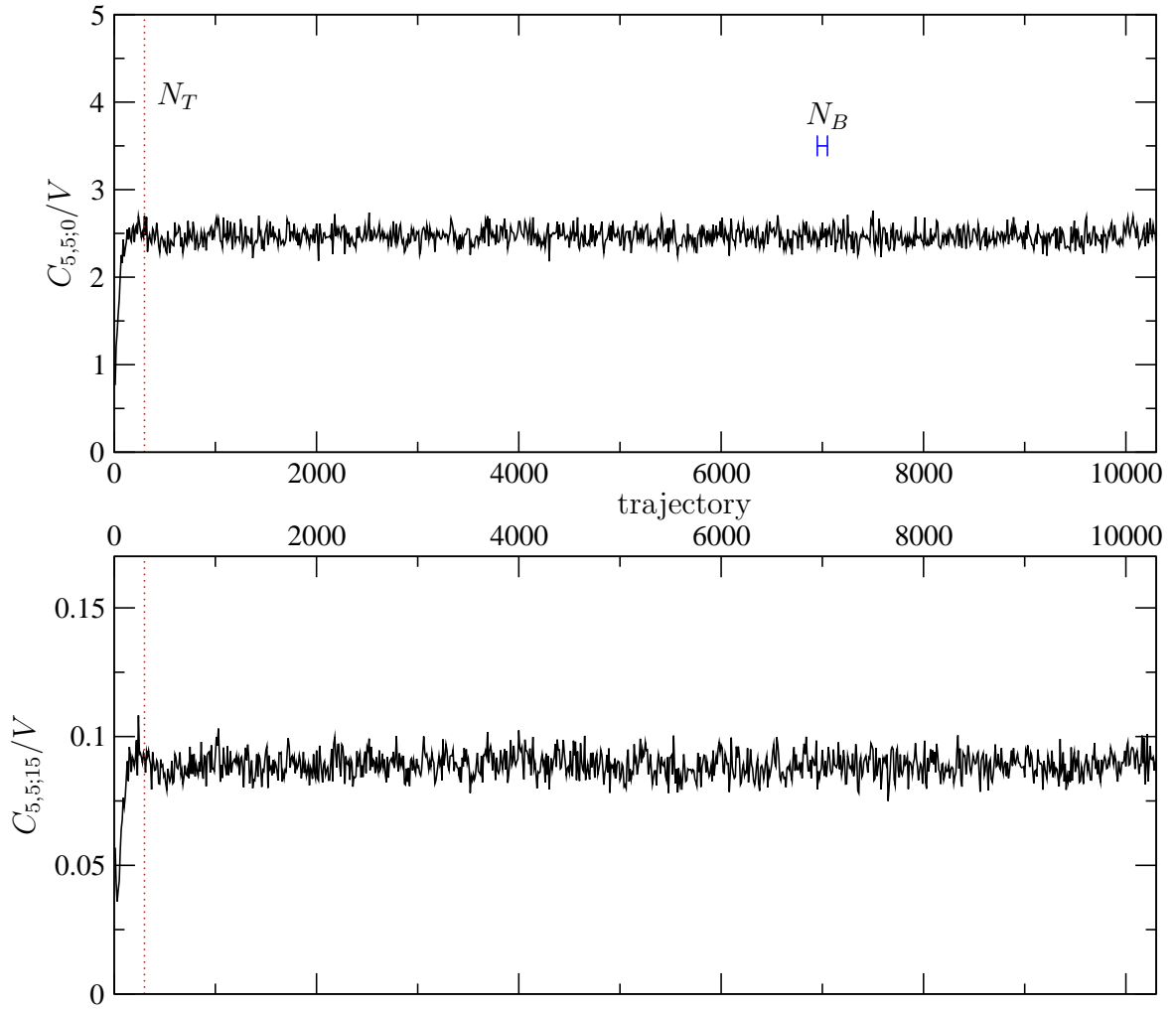
Figure D.4: Markov chain of ensemble W with thermalization point N_T and block length N_B shown. The correlator $C_{5,5;t}$ is calculated using $m_V = 0.01$. The Markov chain has an ordered initial condition.
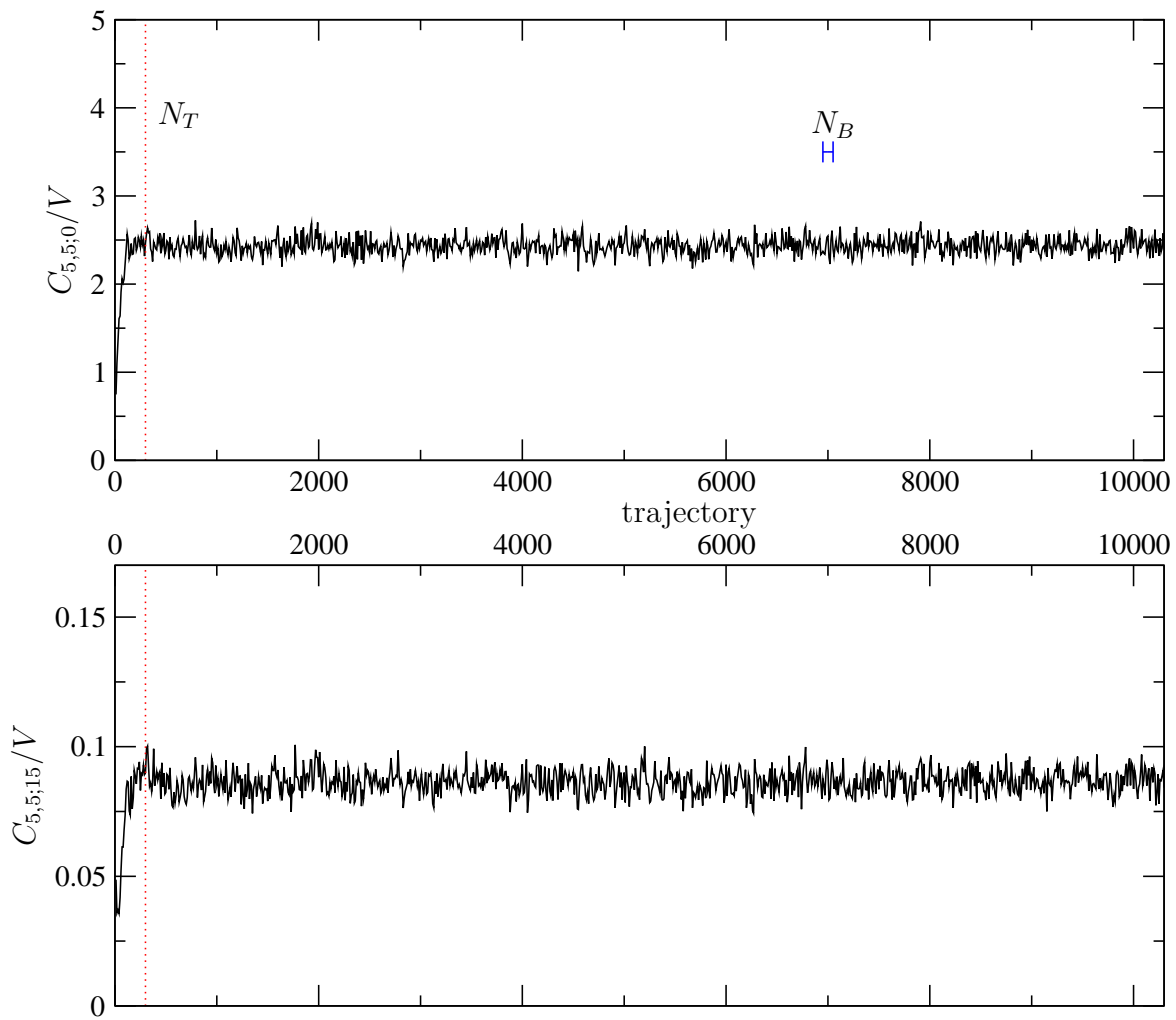
Figure D.5: Markov chain of ensemble X with thermalization point N_T and block length N_B shown. The correlator $C_{5,5;t}$ is calculated using $m_V = 0.01$. The Markov chain has an ordered initial condition.
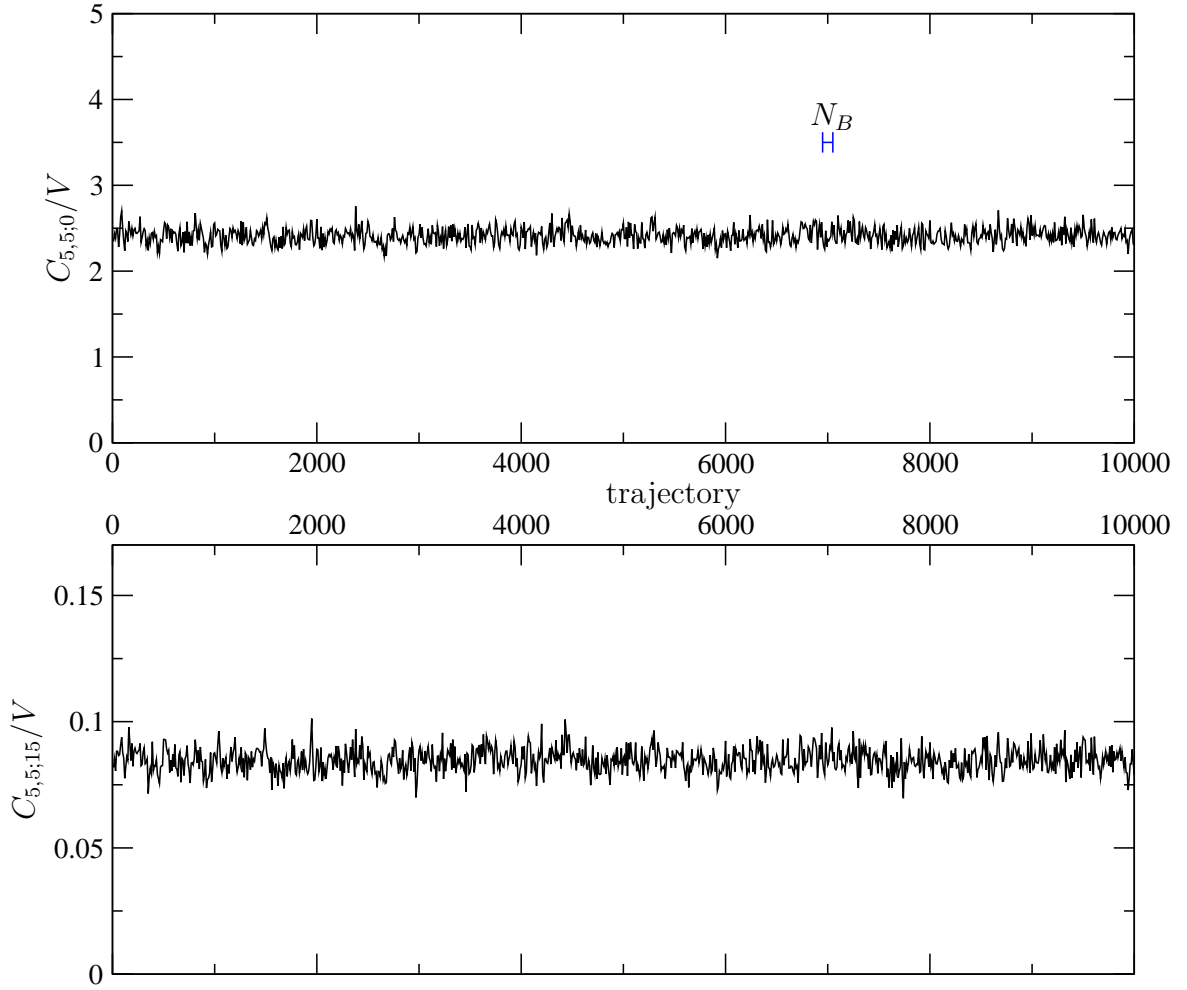
Figure D.6: Markov chain of ensemble Y with thermalization point N_T and block length N_B shown. The correlator $C_{5,5;t}$ is calculated using $m_V = 0.01$. The Markov chain has an ordered initial condition.
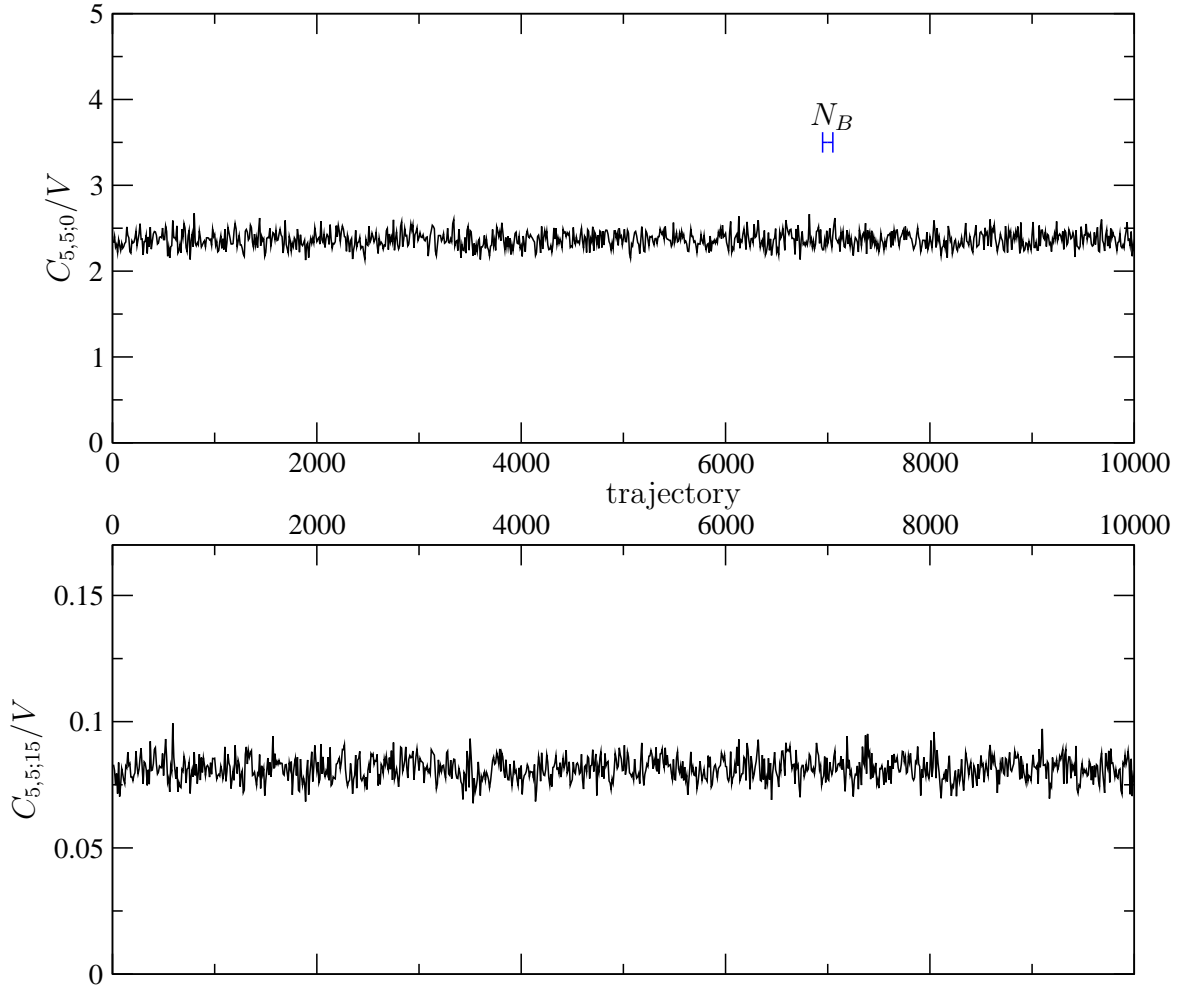
Figure D.7: Markov chain of ensemble Z with thermalization point N_T and block length N_B shown. The correlator $C_{5,5;t}$ is calculated using $m_V = 0.01$. The Markov chain has an ordered initial condition.
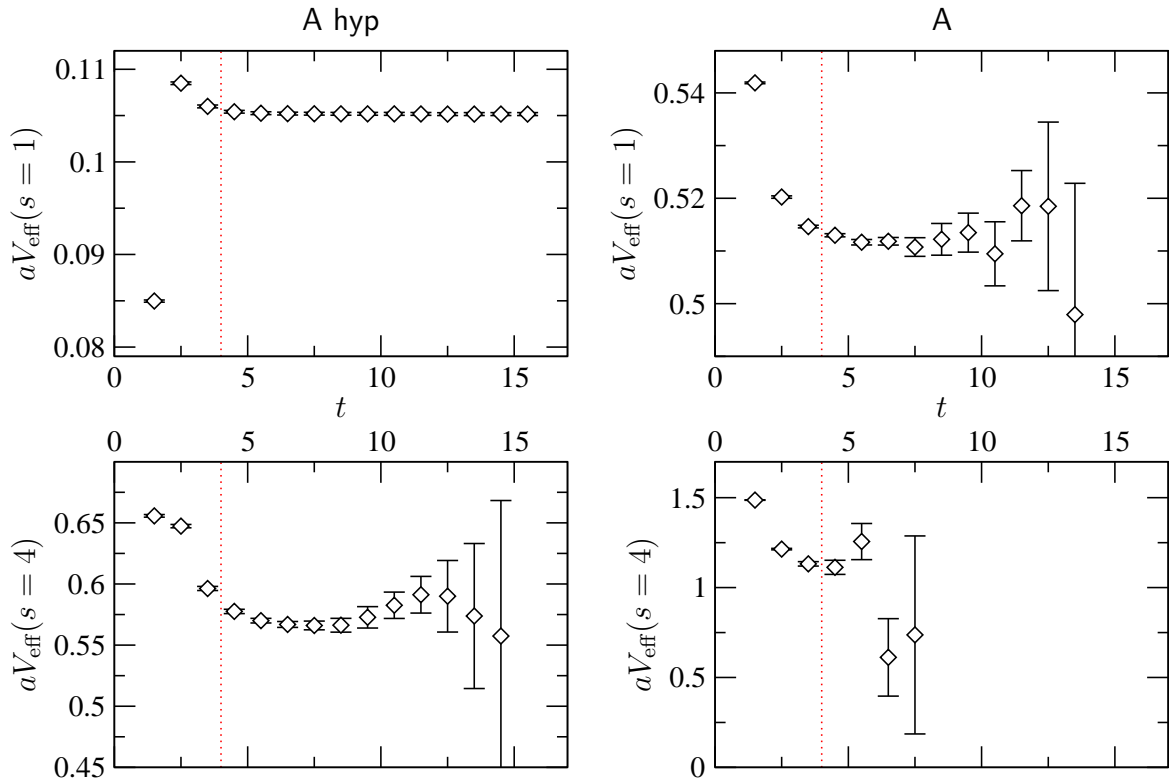
Figure D.8: Effective potential for ensembles A hyp and A. The minimum time separation chosen is $t_{\min} = 4$.
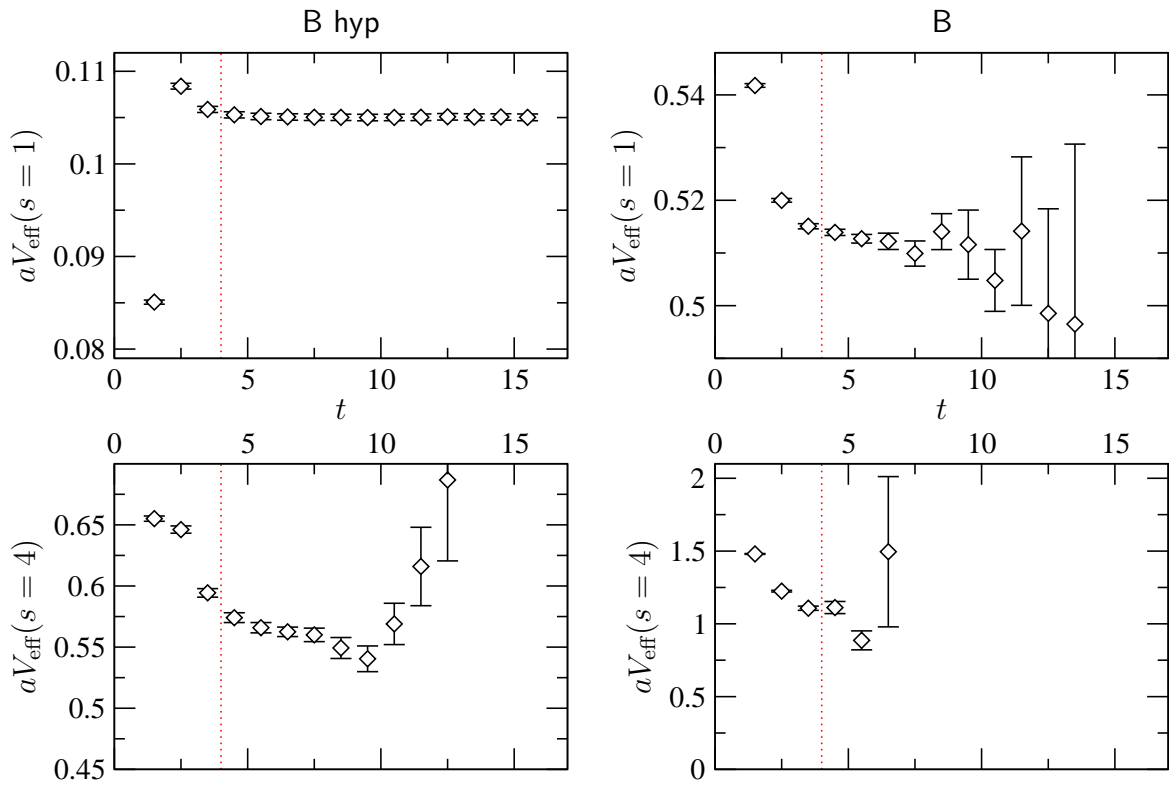
Figure D.9: Effective potential for ensembles B hyp and B. The minimum time separation chosen is $t_{\min} = 4$.
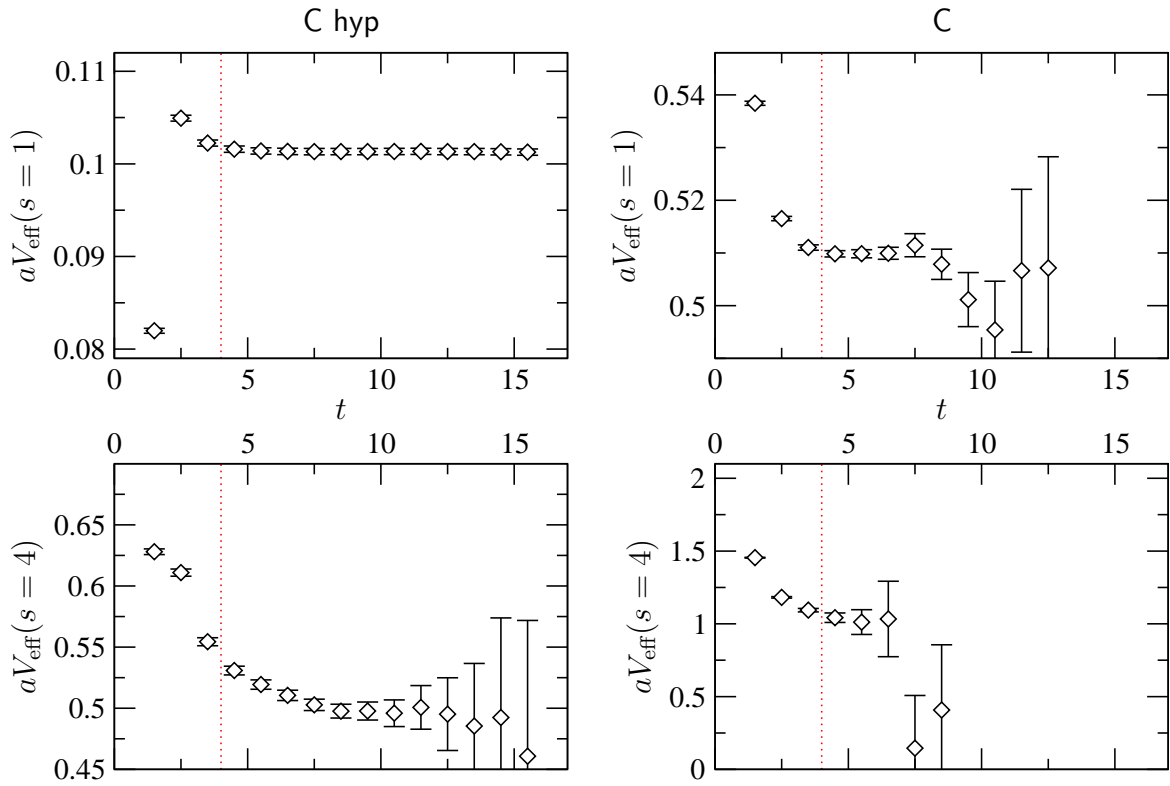
Figure D.10: Effective potential for ensembles C hyp and C. The minimum time separation chosen is $t_{\min} = 4$.

Figure D.11: Effective potential for ensembles W hyp and W. The minimum time separation chosen is $t_{\min} = 2$.
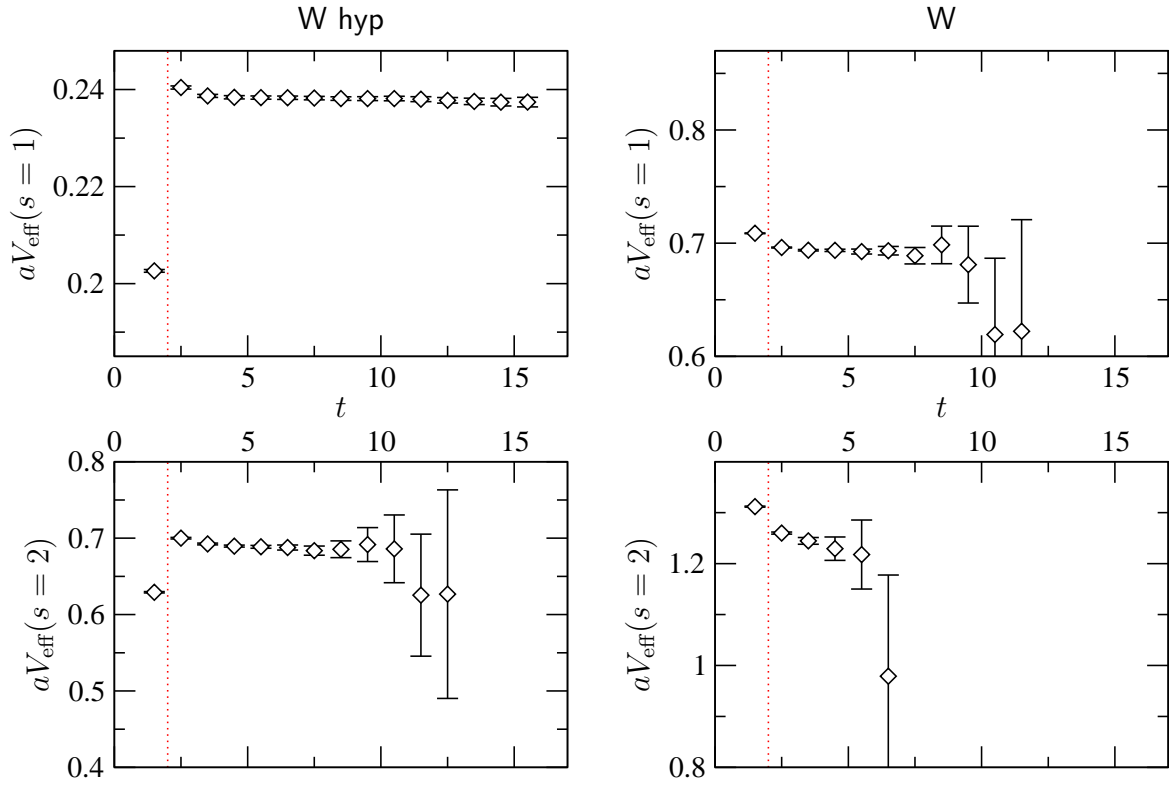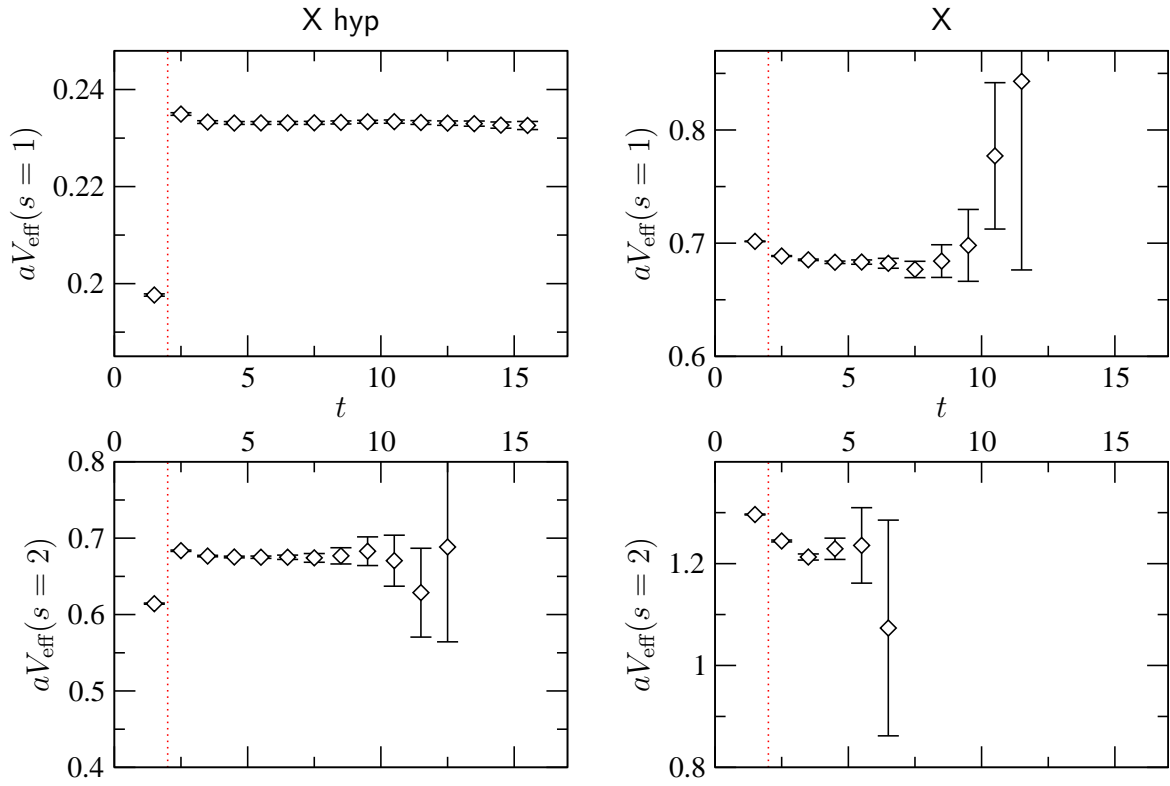
Figure D.12: Effective potential for ensembles X hyp and X. The minimum time separation chosen is $t_{\min} = 2$.
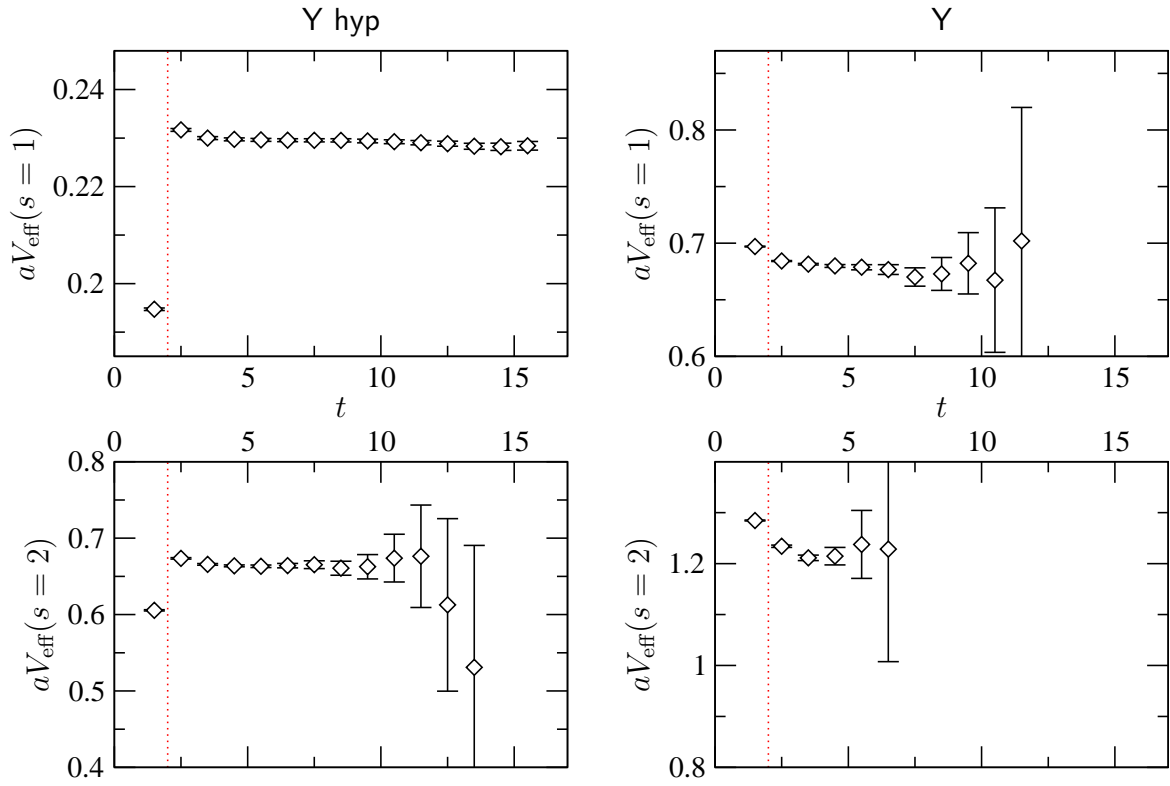
Figure D.13: Effective potential for ensembles Y hyp and Y. The minimum time separation chosen is $t_{\min} = 2$.
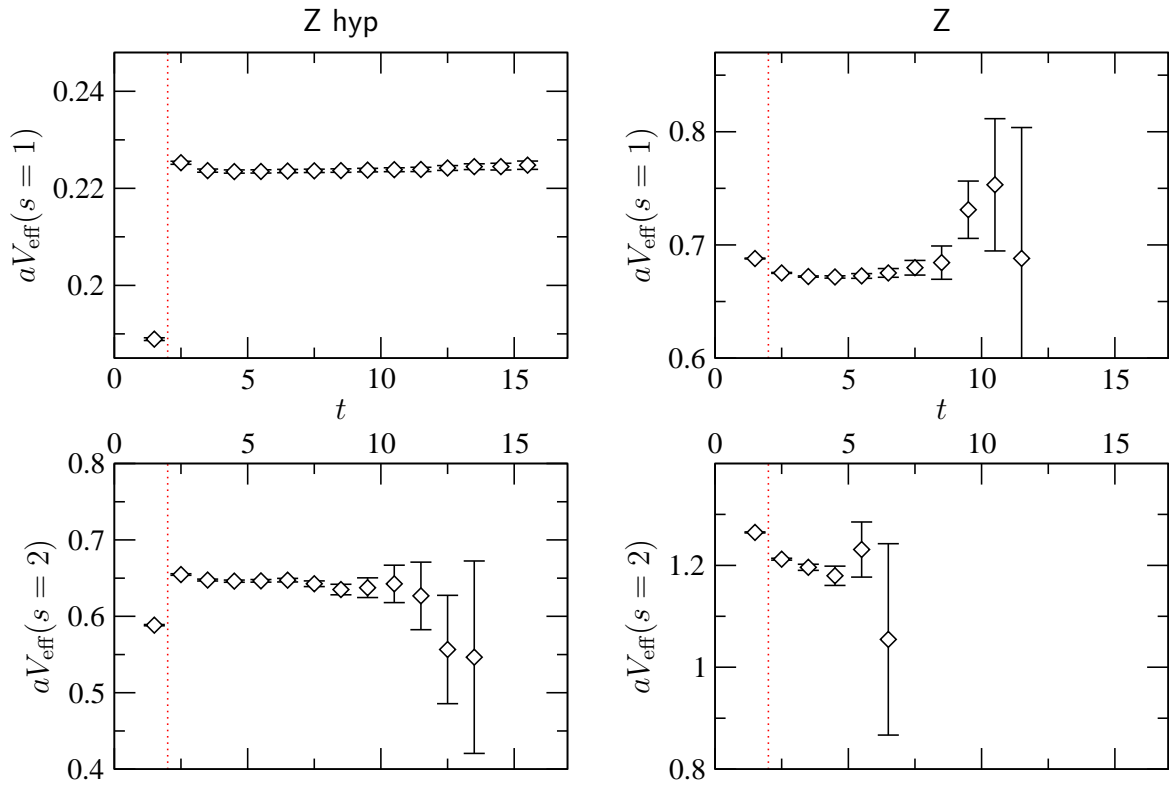
Figure D.14: Effective potential for ensembles Z hyp and Z. The minimum time separation chosen is $t_{\mathrm{min}} = 2$.
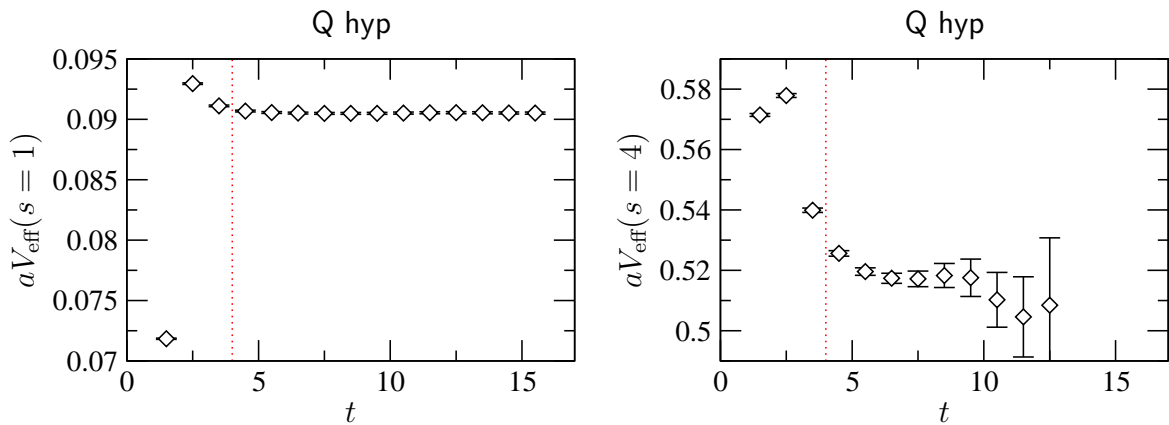
Figure D.15: Effective potential for ensemble Q hyp. The minimum time separation chosen is $t_{\mathrm{min}} = 4$.
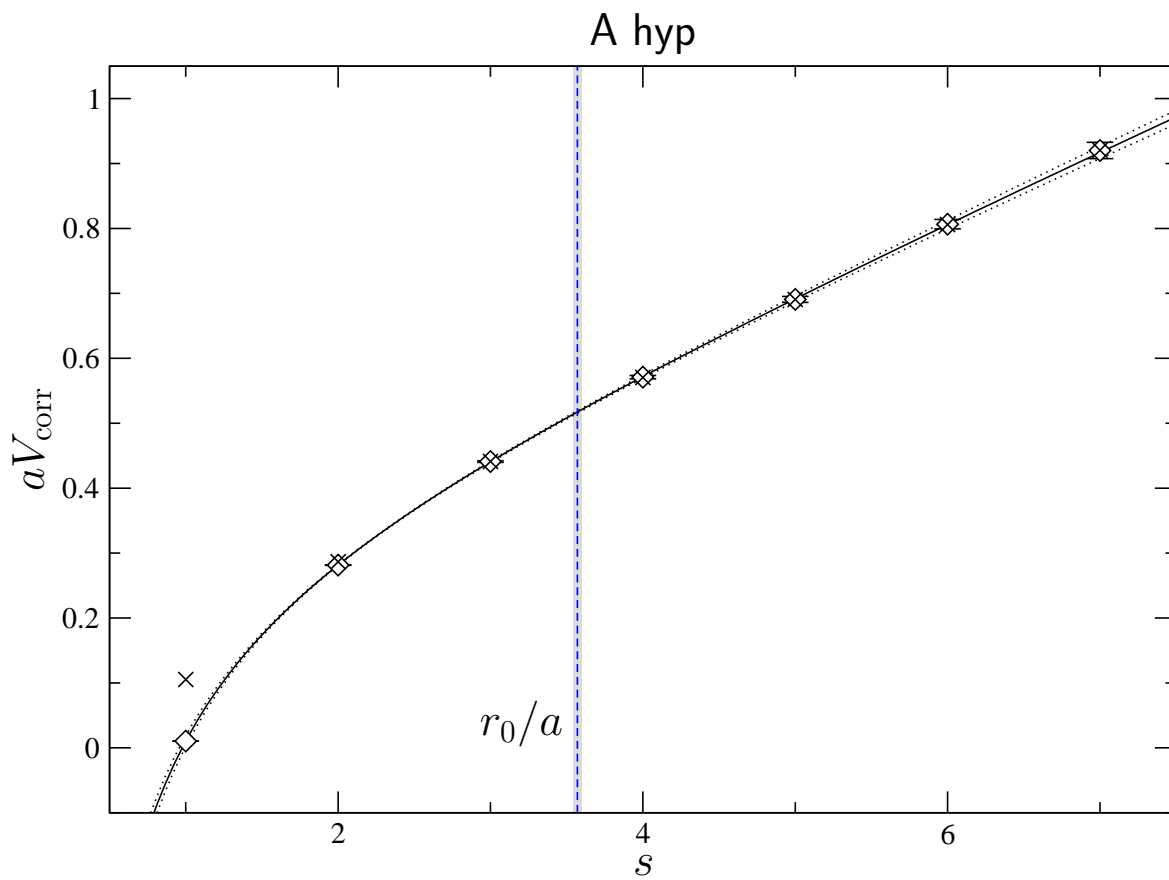
Figure D.16: Static quark potential for ensemble A hyp. The ×'s correspond to the un-corrected static quark potential, while the diamonds correspond to the corrected potential. The result is $r_0/a = 3.570(27)$.
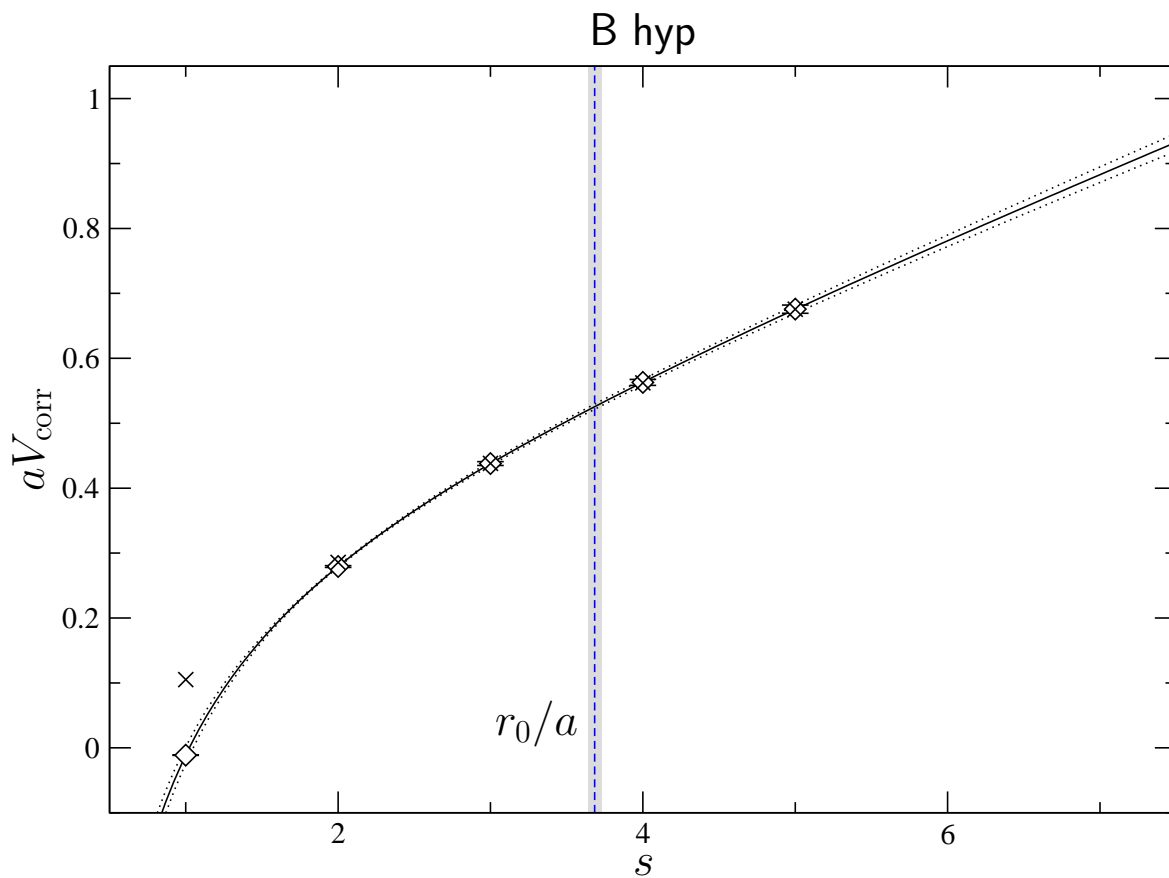
Figure D.17: Static quark potential for ensemble B hyp. The ×'s correspond to the uncorrected static quark potential, while the diamonds correspond to the corrected potential. The result is $r_0/a = 3.684(44)$.
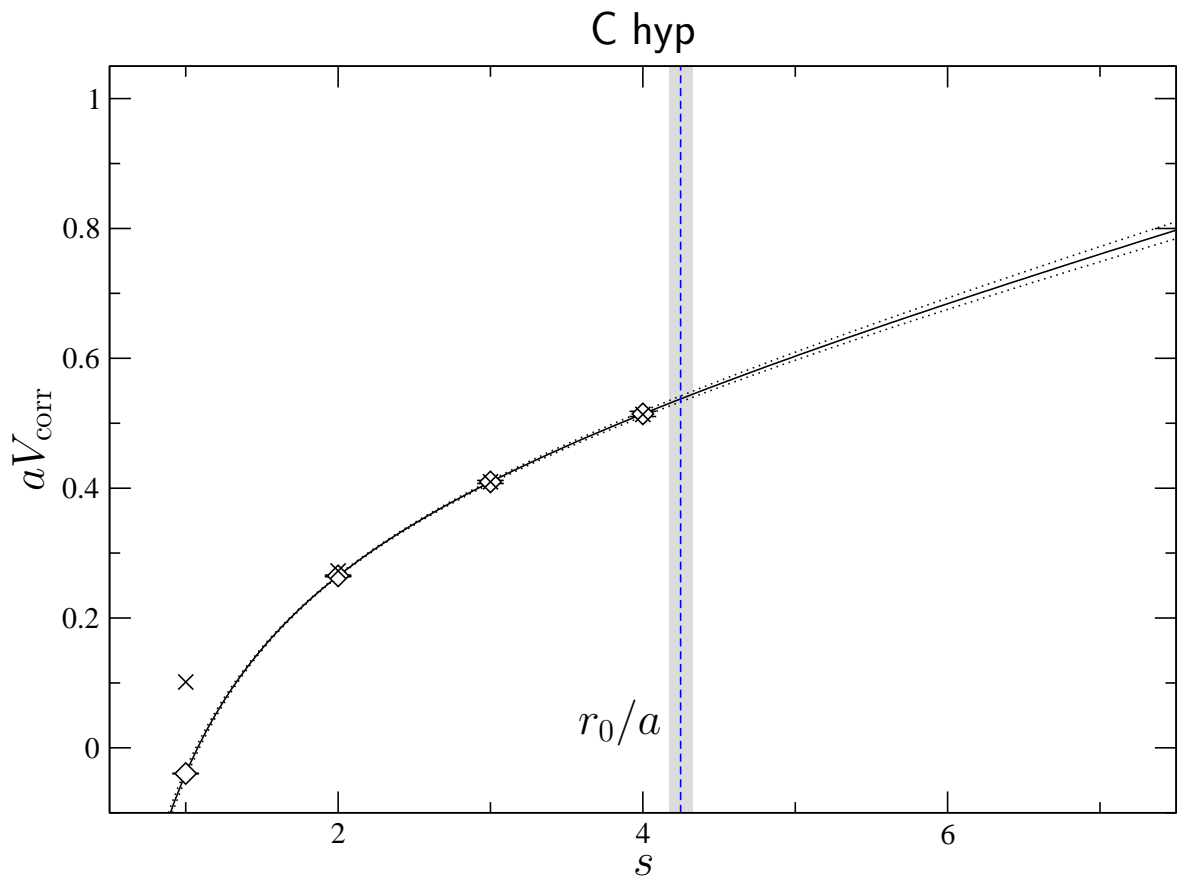
Figure D.18: Static quark potential for ensemble C hyp. The ×'s correspond to the uncorrected static quark potential, while the diamonds correspond to the corrected potential. The result is $r_0/a = 4.248(78)$.
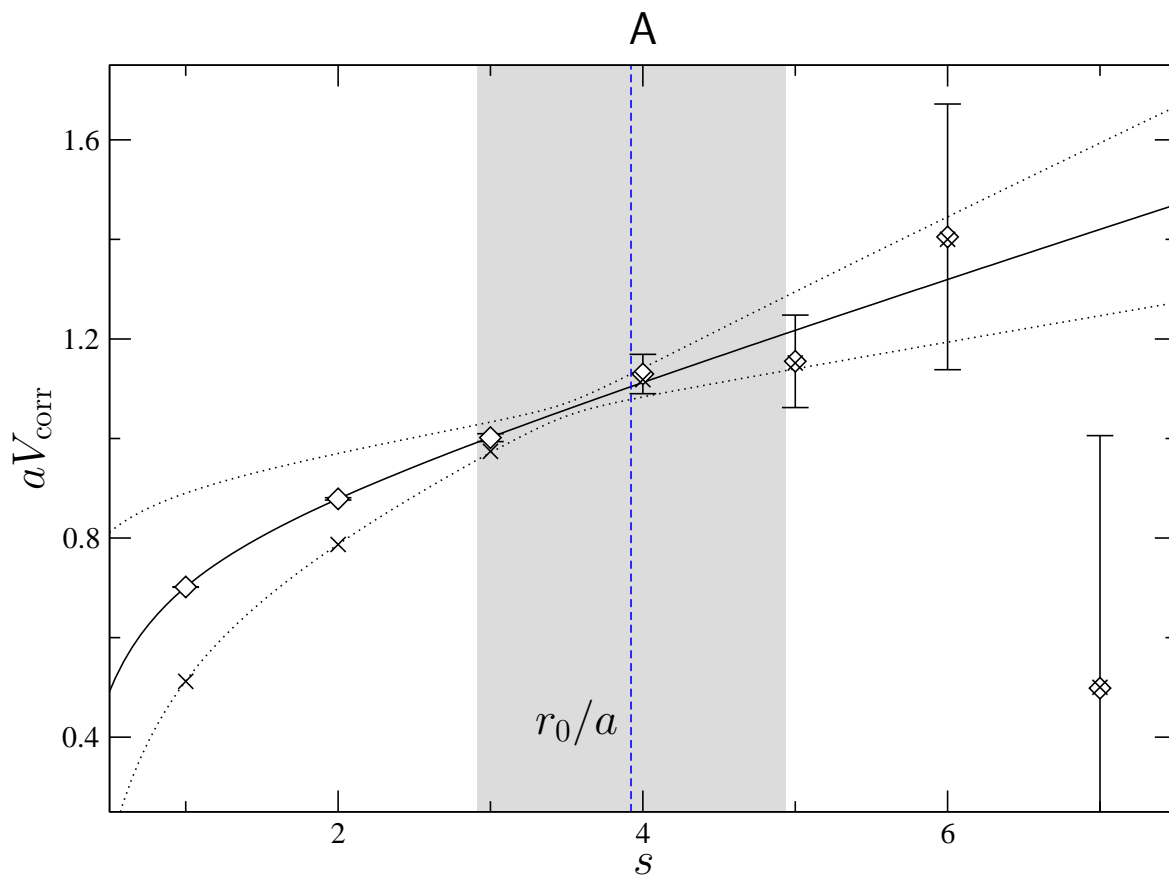
Figure D.19: Static quark potential for ensemble A. The ×'s correspond to the uncorrected static quark potential, while the diamonds correspond to the corrected potential. The result is $r_0/a = 3.9(10)$.
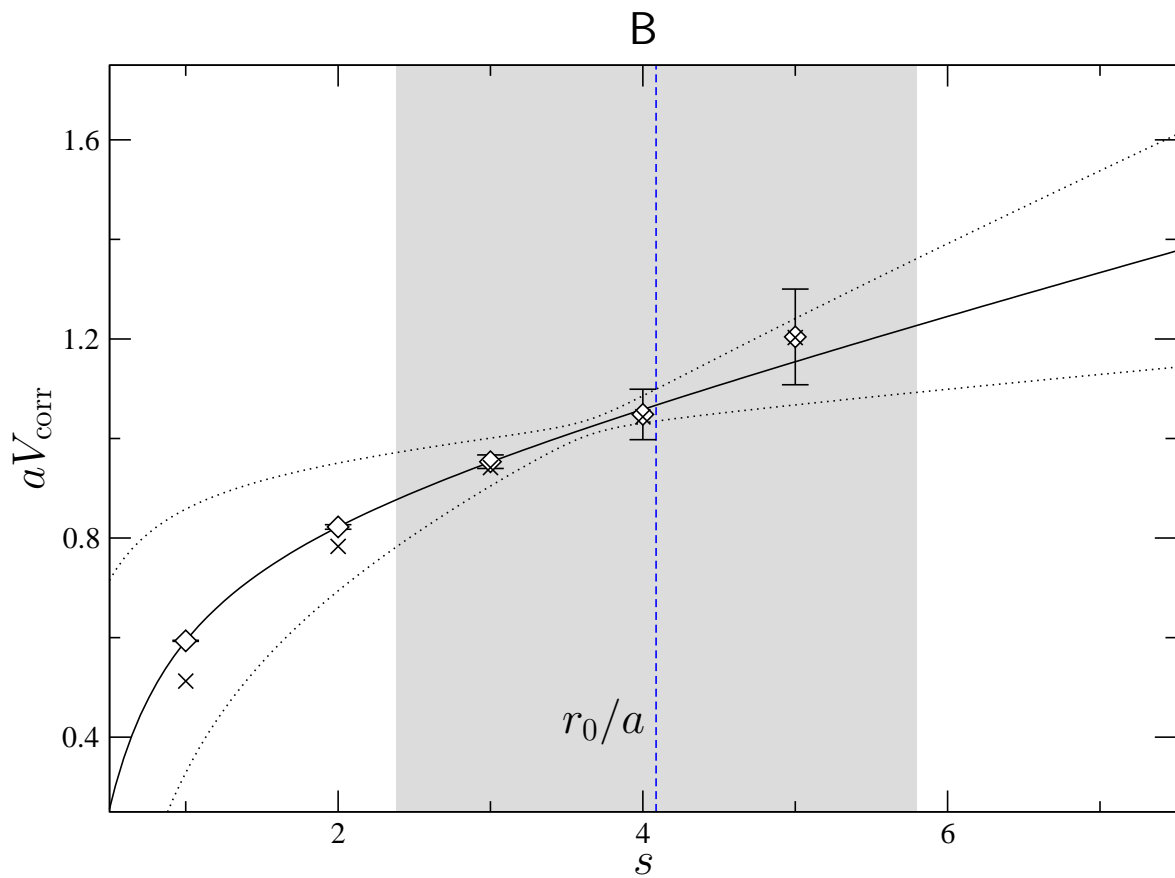
Figure D.20: Static quark potential for ensemble B. The $\times$'s correspond to the uncorrected static quark potential, while the diamonds correspond to the corrected potential. The result is $r_0/a = 4.1(17)$.
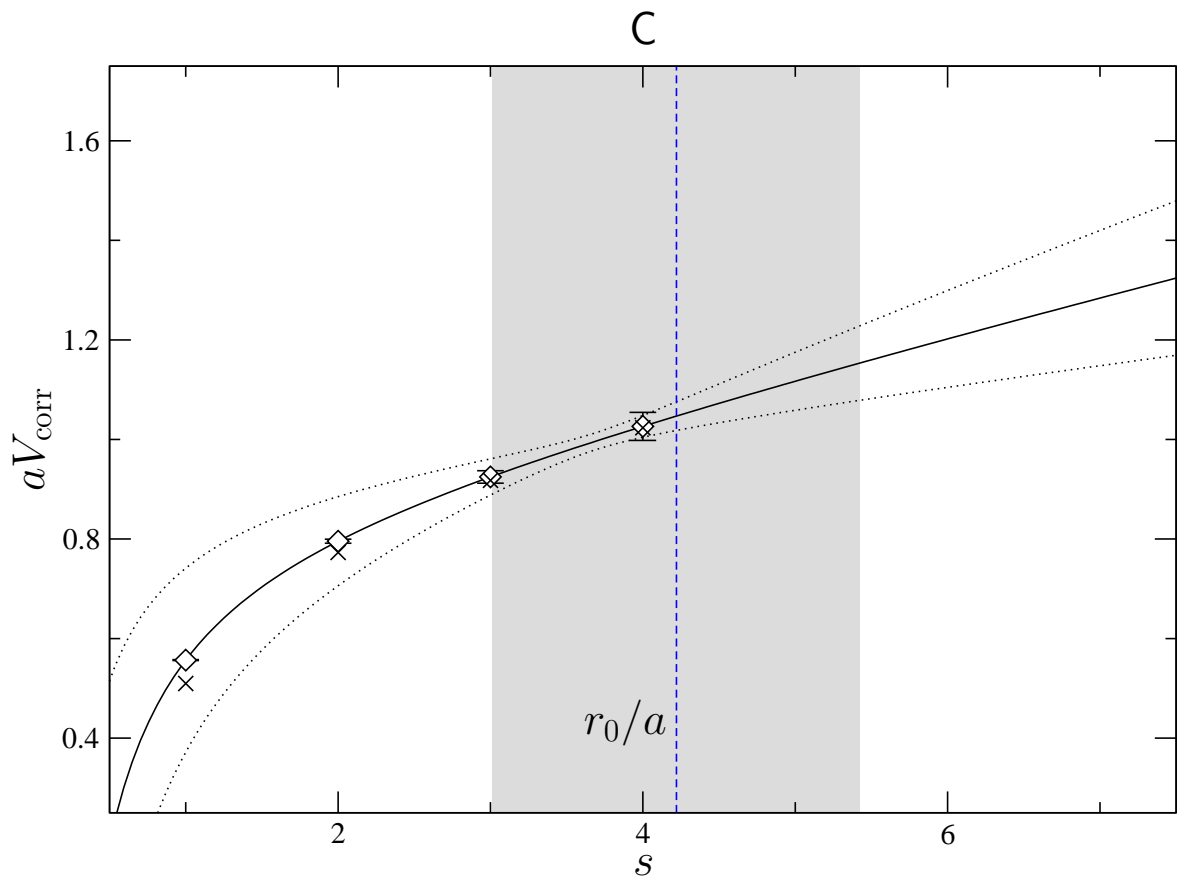
Figure D.21: Static quark potential for ensemble C. The ×'s correspond to the uncorrected static quark potential, while the diamonds correspond to the corrected potential. The result is $r_0/a = 4.2(12)$.
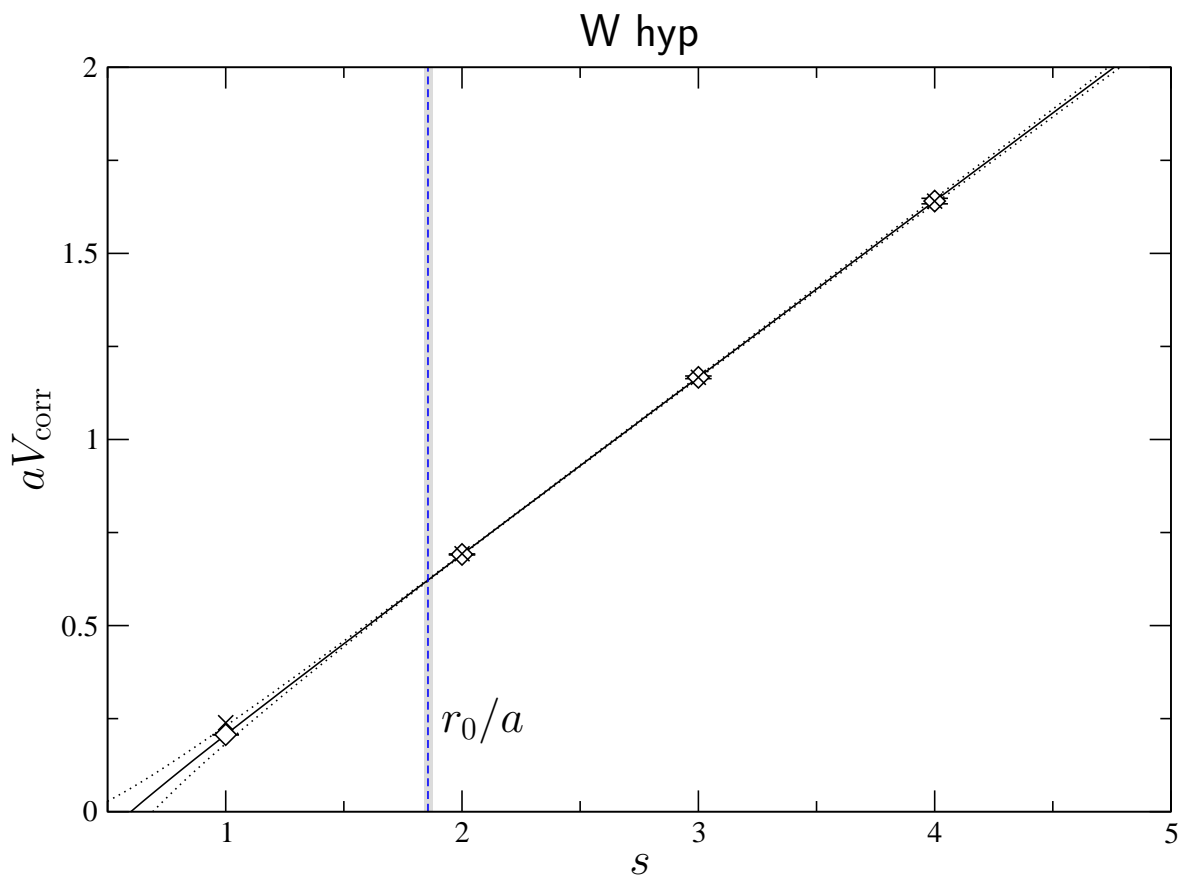
Figure D.22: Static quark potential for ensemble W hyp. The ×'s correspond to the uncorrected static quark potential, while the diamonds correspond to the corrected potential. The result is $r_0/a = 1.856(19)$.
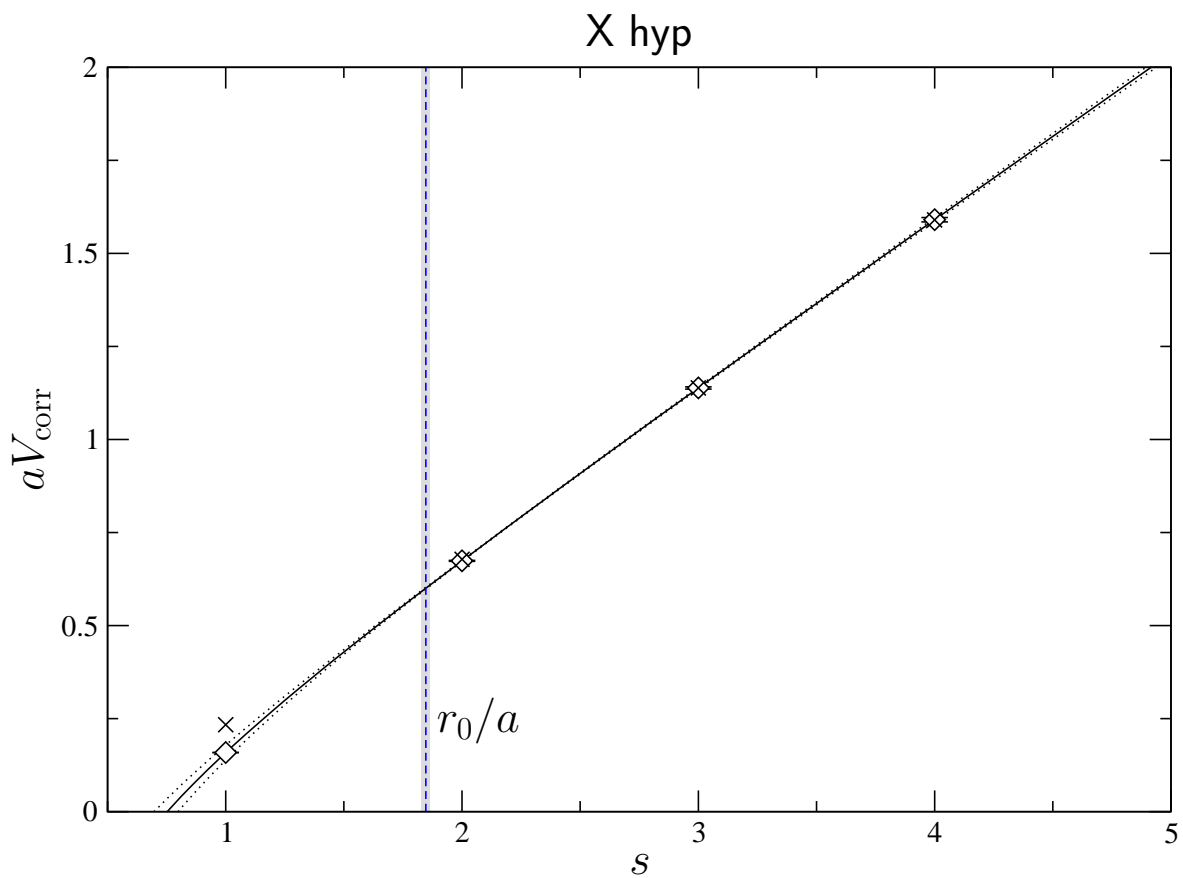
Figure D.23: Static quark potential for ensemble X hyp. The $\times$'s correspond to the un-corrected static quark potential, while the diamonds correspond to the corrected potential. The result is $r_0/a = 1.847(17)$.
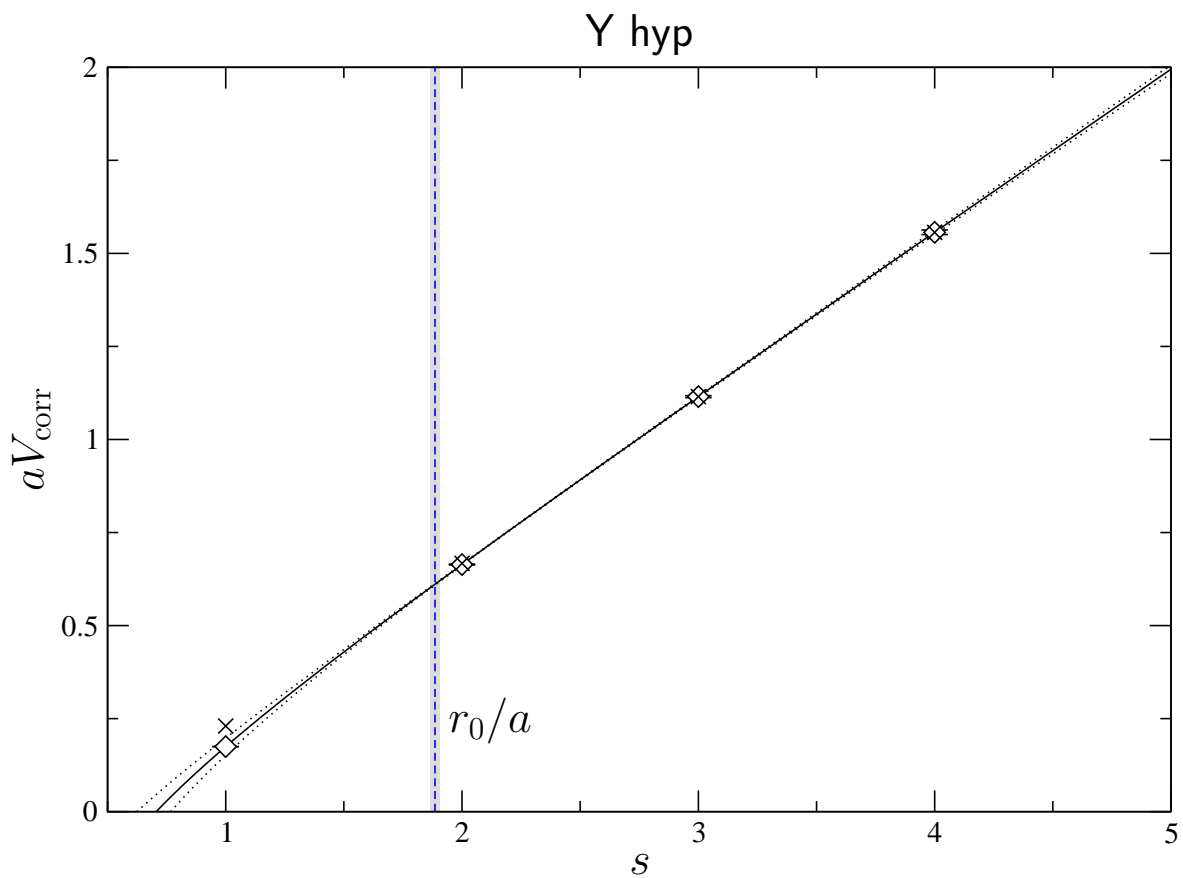
Figure D.24: Static quark potential for ensemble Y hyp. The ×'s correspond to the un-corrected static quark potential, while the diamonds correspond to the corrected potential. The result is $r_0/a = 1.885(19)$.
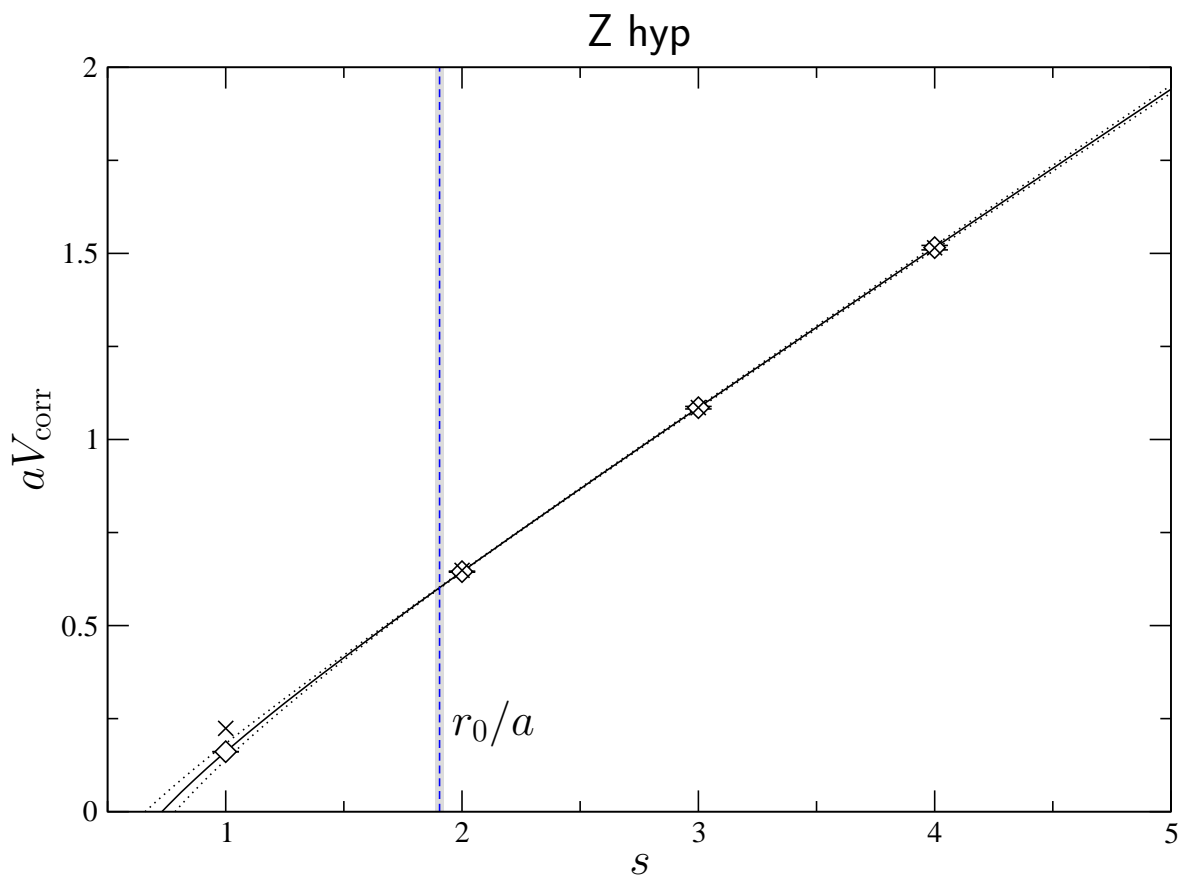
Figure D.25: Static quark potential for ensemble Z hyp. The ×'s correspond to the un-corrected static quark potential, while the diamonds correspond to the corrected potential. The result is $r_0/a = 1.905(19)$.

W

aV_{corr}

r_0/a

s

PSfrag replacements
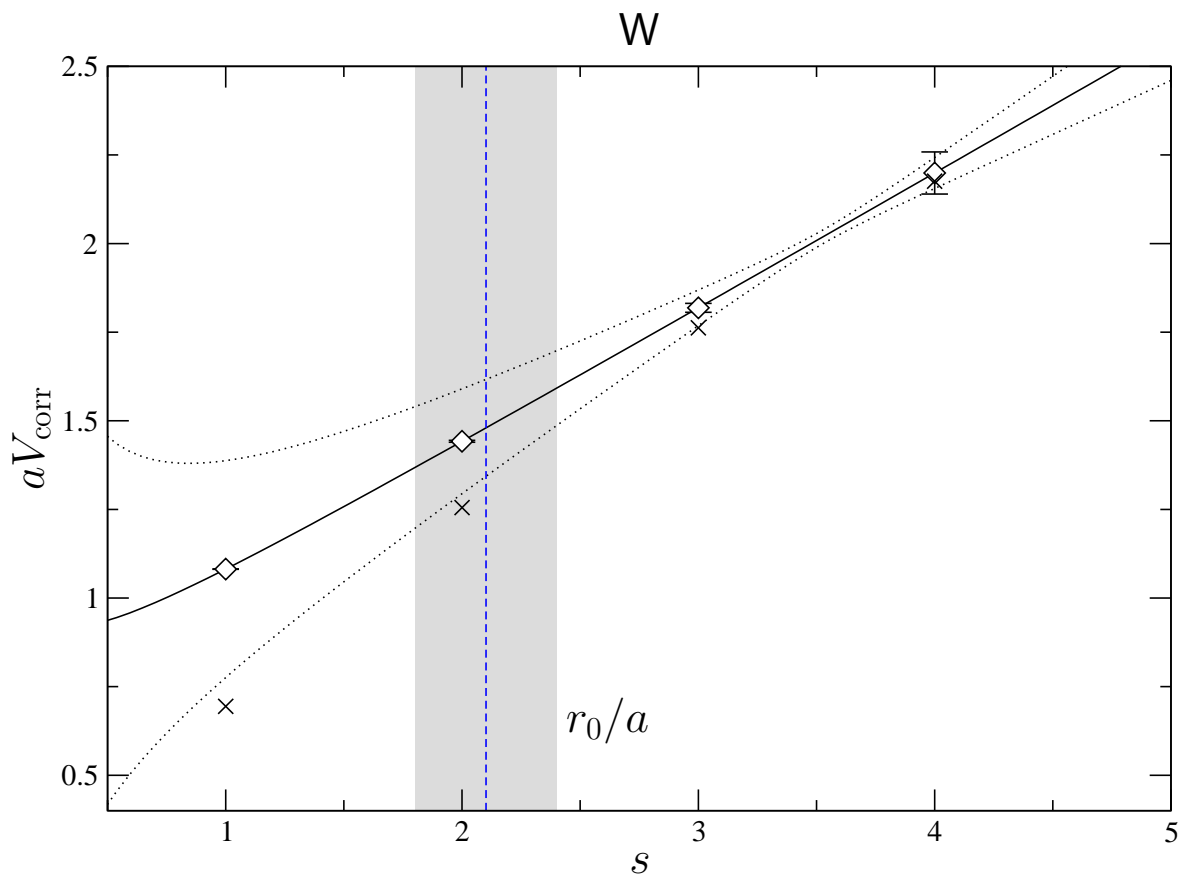
Figure D.26: Static quark potential for ensemble W. The ×'s correspond to the uncorrected static quark potential, while the diamonds correspond to the corrected potential. The result is $r_0/a = 2.10(30)$.
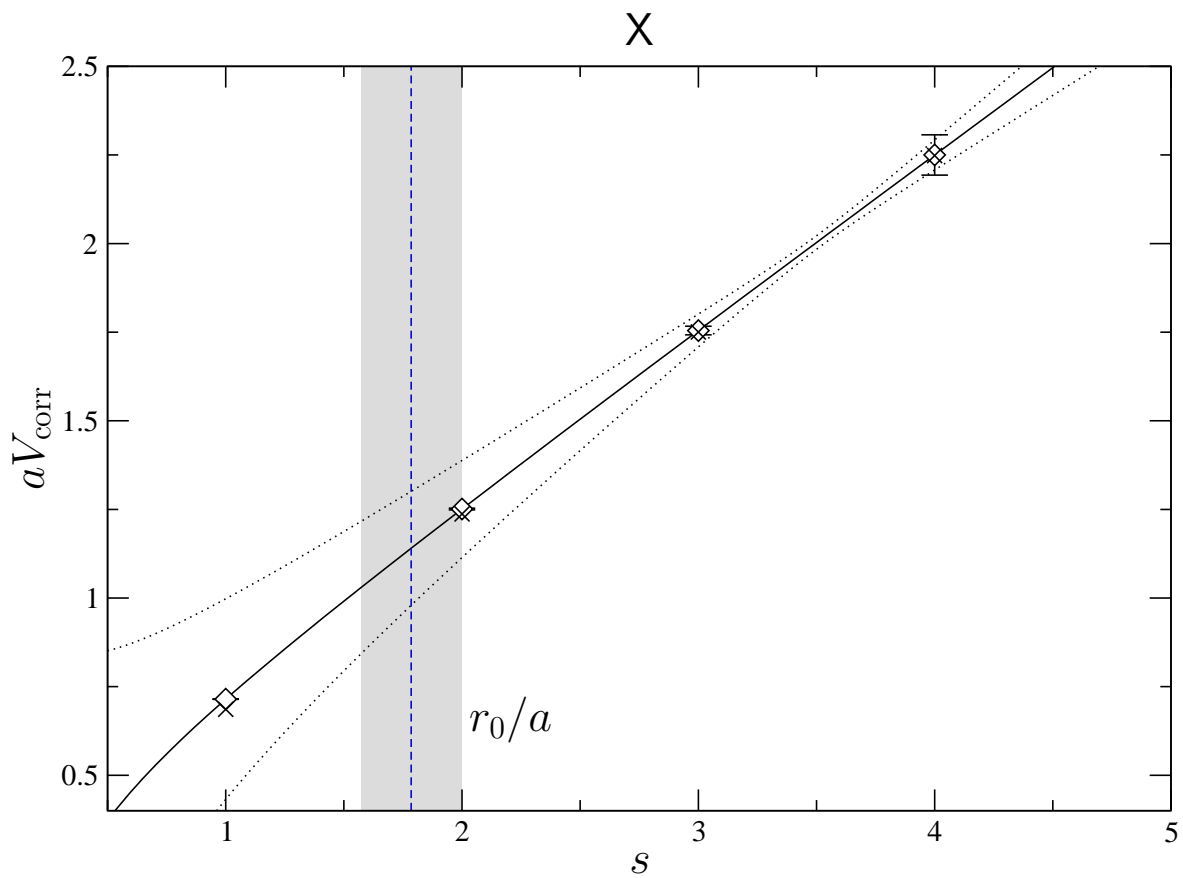
Figure D.27: Static quark potential for ensemble X. The ×'s correspond to the uncorrected static quark potential, while the diamonds correspond to the corrected potential. The result is $r_0/a = 1.78(21)$.
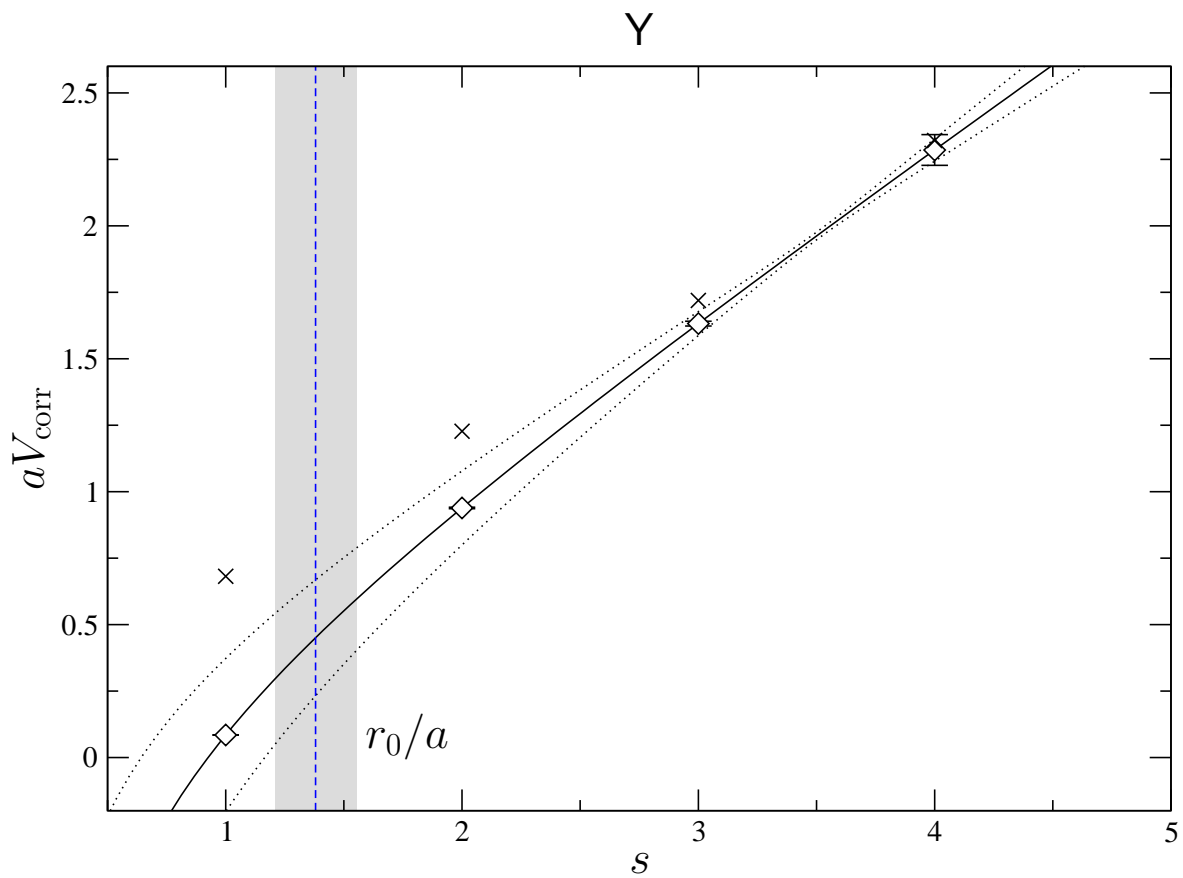
Figure D.28: Static quark potential for ensemble Y. The ×'s correspond to the uncorrected static quark potential, while the diamonds correspond to the corrected potential. The result is $r_0/a = 1.38(17)$.
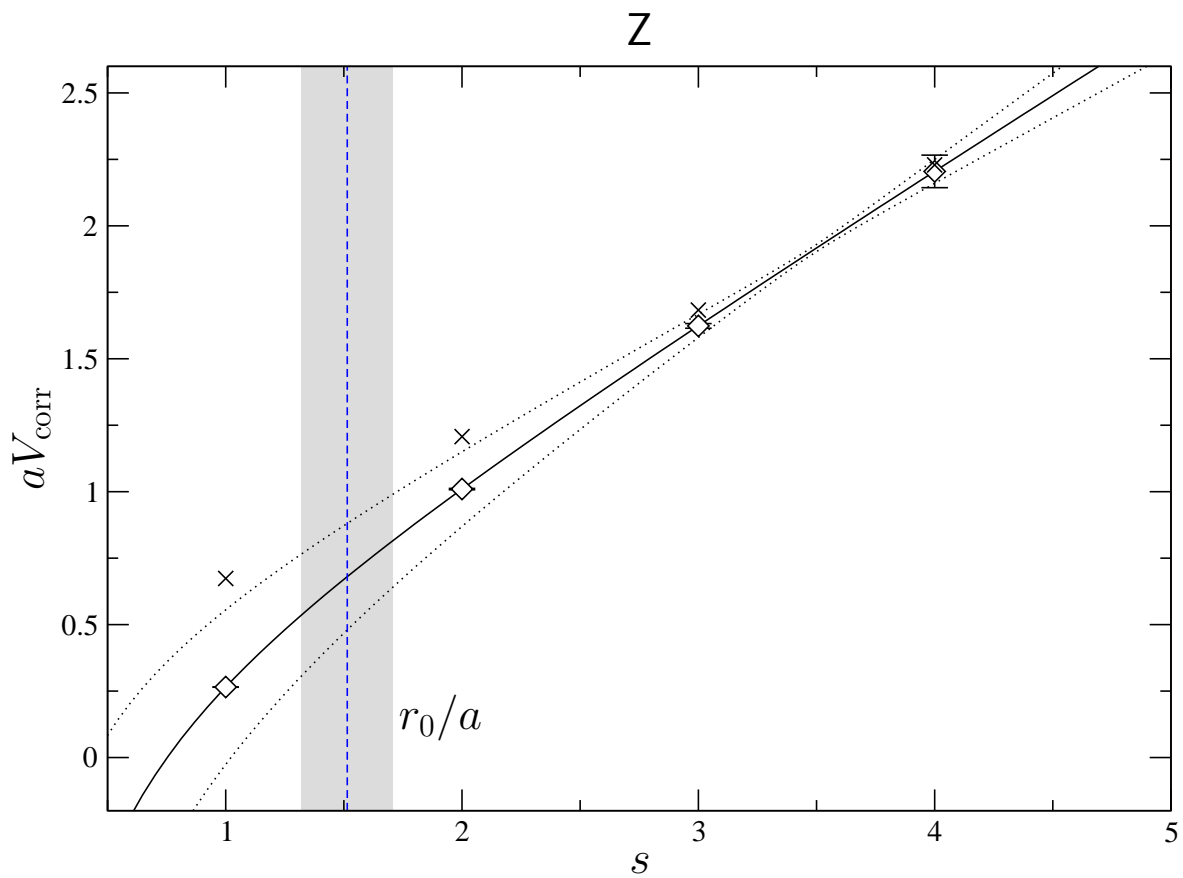
Figure D.29: Static quark potential for ensemble Z. The ×'s correspond to the uncorrected static quark potential, while the diamonds correspond to the corrected potential. The result is $r_0/a = 1.51(19)$.
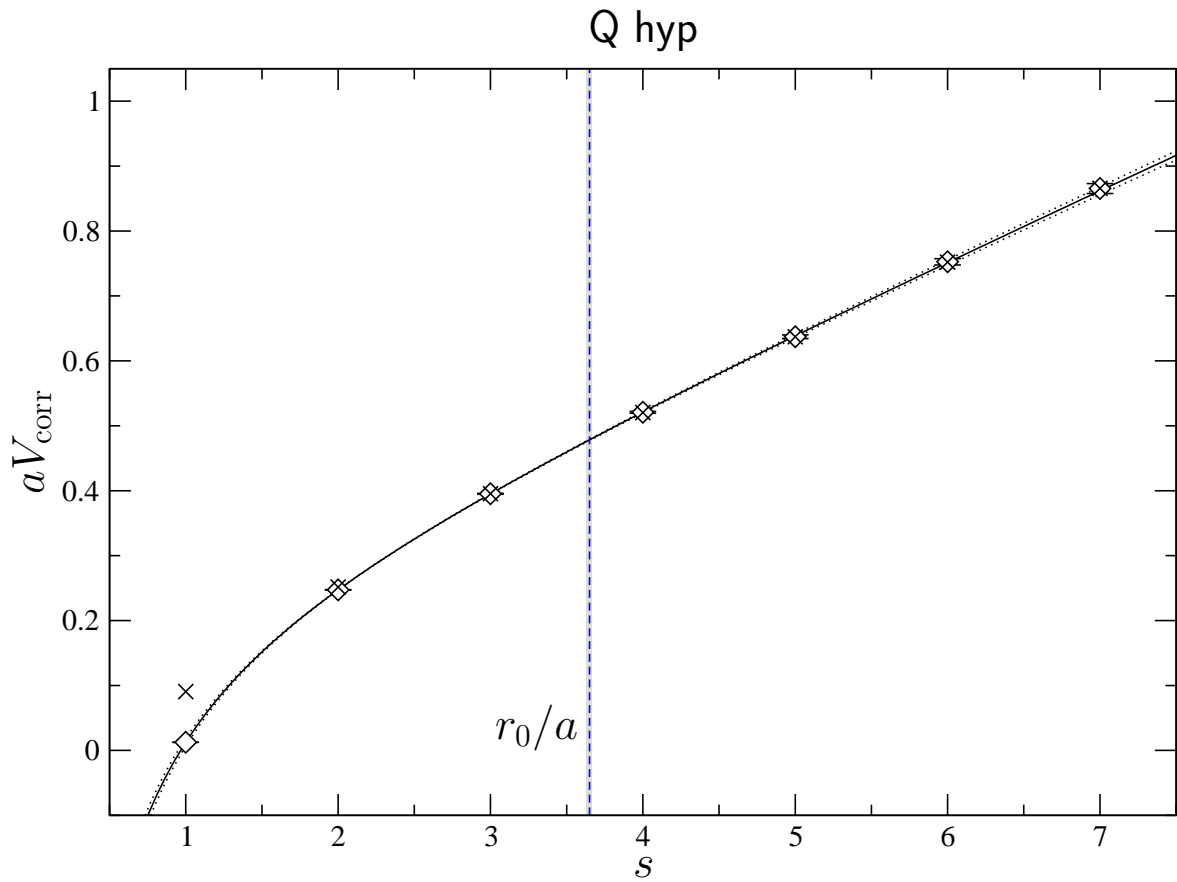
Figure D.30: Static quark potential for ensemble Q hyp. The ×'s correspond to the un-corrected static quark potential, while the diamonds correspond to the corrected potential. The result is $r_0/a = 3.650(19)$.
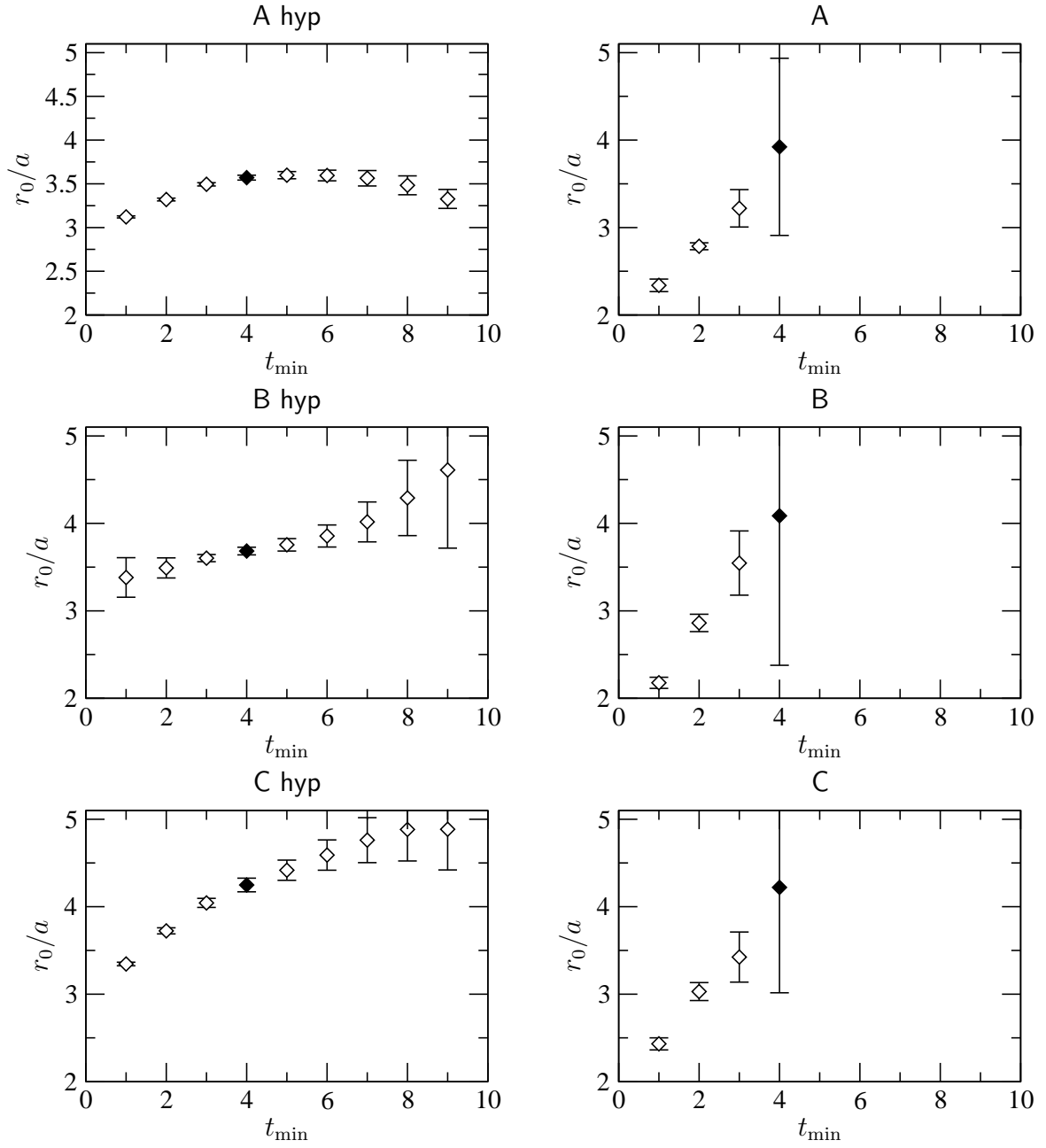
Figure D.31: Dependence of the Sommer scale on $t_{\min}$ for ensembles A hyp, A, B hyp, B, C hyp, and C. The filled diamond corresponds to $t_{\min}$ used in the final fit.
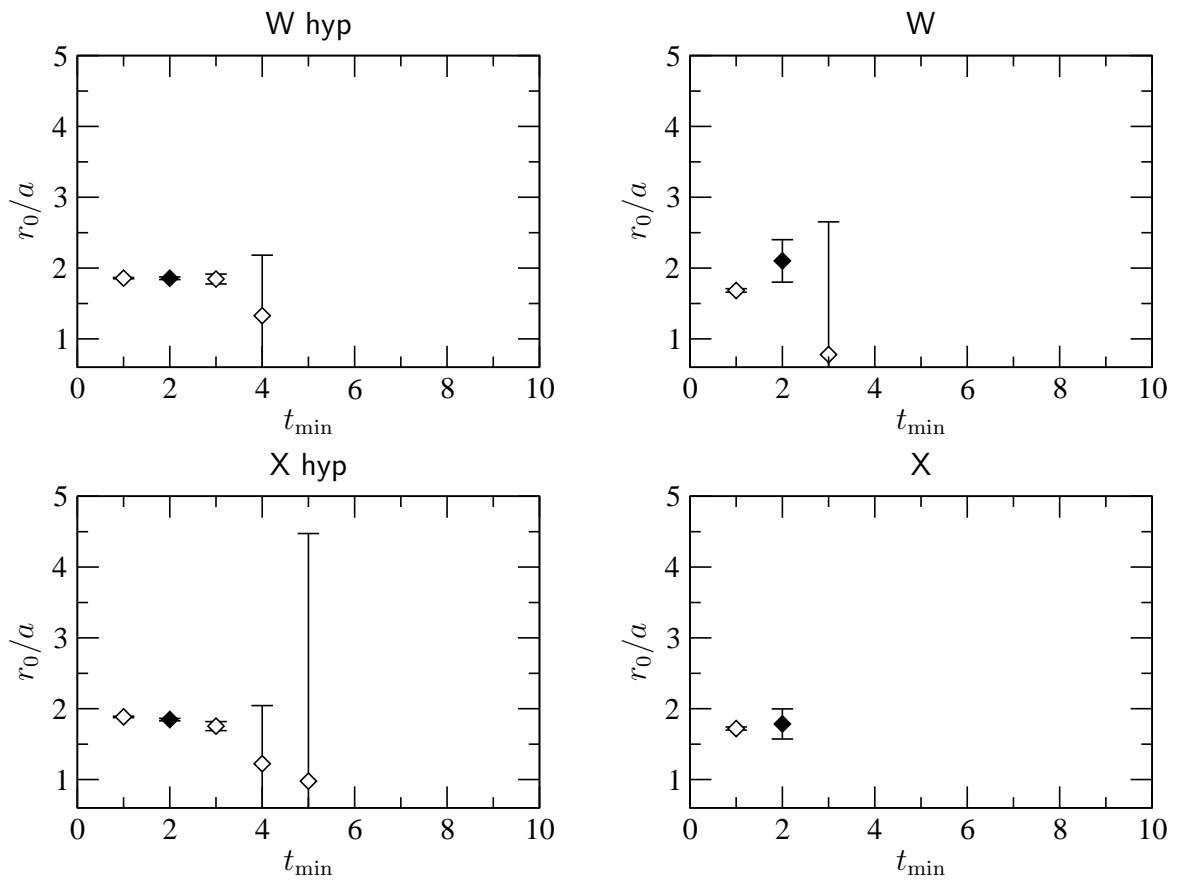
Figure D.32: Dependence of the Sommer scale on $t_{\min}$ for ensembles W hyp, W, X hyp, and X. The filled diamond corresponds to $t_{\min}$ used in the final fit.
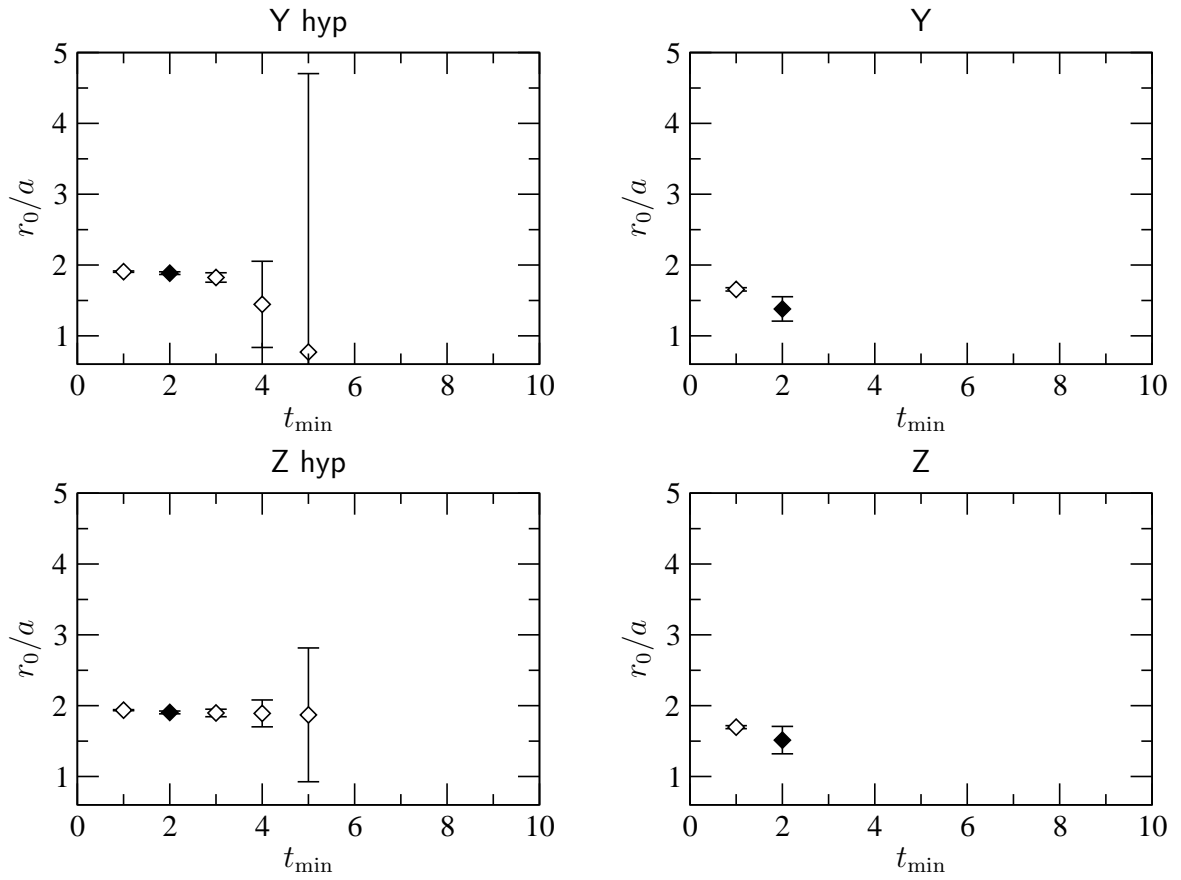
Figure D.33: Dependence of the Sommer scale on $t_{\min}$ for ensembles Y hyp, Y, Z hyp, and Z. The filled diamond corresponds to $t_{\min}$ used in the final fit.
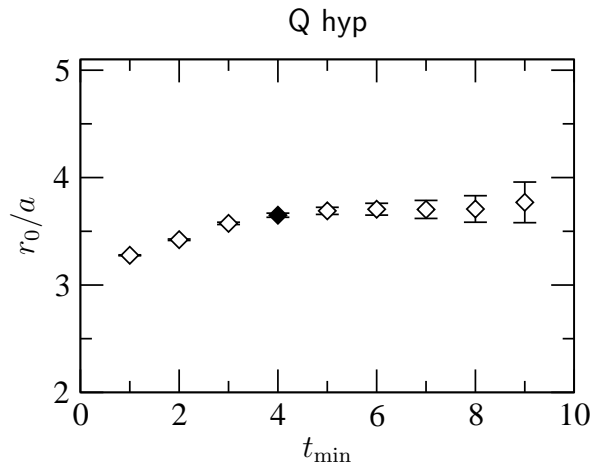
Figure D.34: Dependence of the Sommer scale on $t_{\min}$ for ensemble Q hyp. The filled diamond corresponds to $t_{\min}$ used in the final fit.
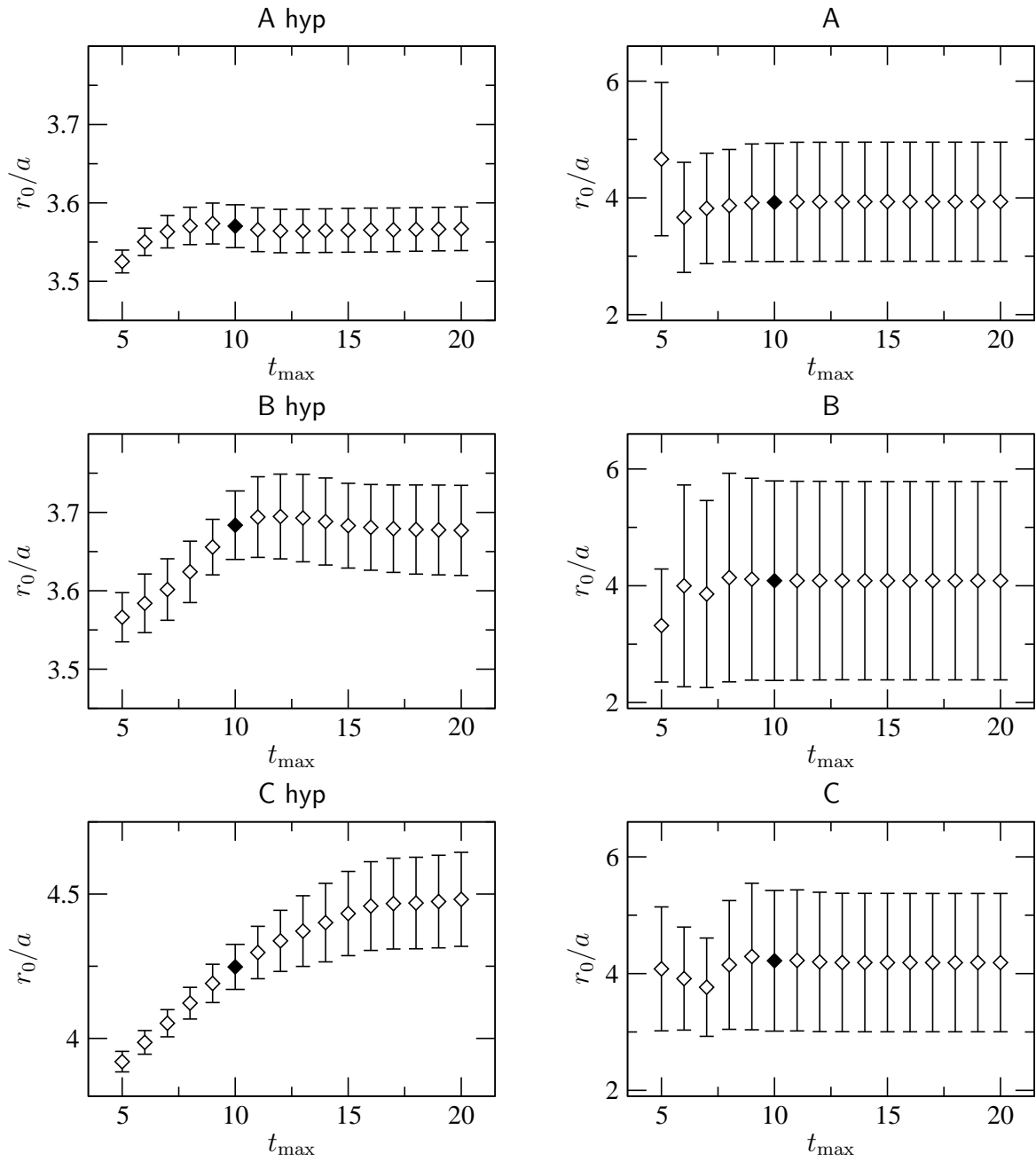
Figure D.35: Dependence of the Sommer scale on $t_{\max}$ for ensembles A hyp, A, B hyp, B, C hyp, and C. The filled diamond corresponds to $t_{\max}$ used in the final fit.
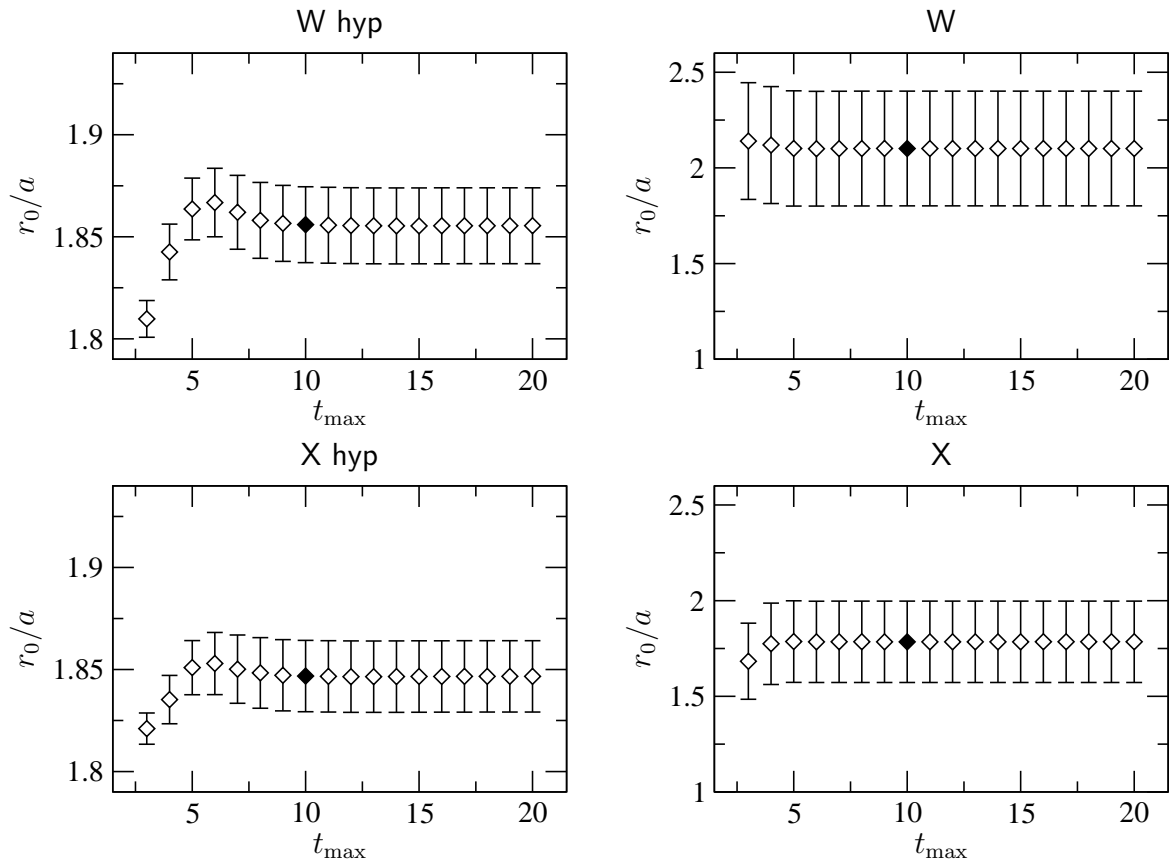
Figure D.36: Dependence of the Sommer scale on t_{max} for ensembles W hyp, W, X hyp, and X. The filled diamond corresponds to t_{max} used in the final fit.
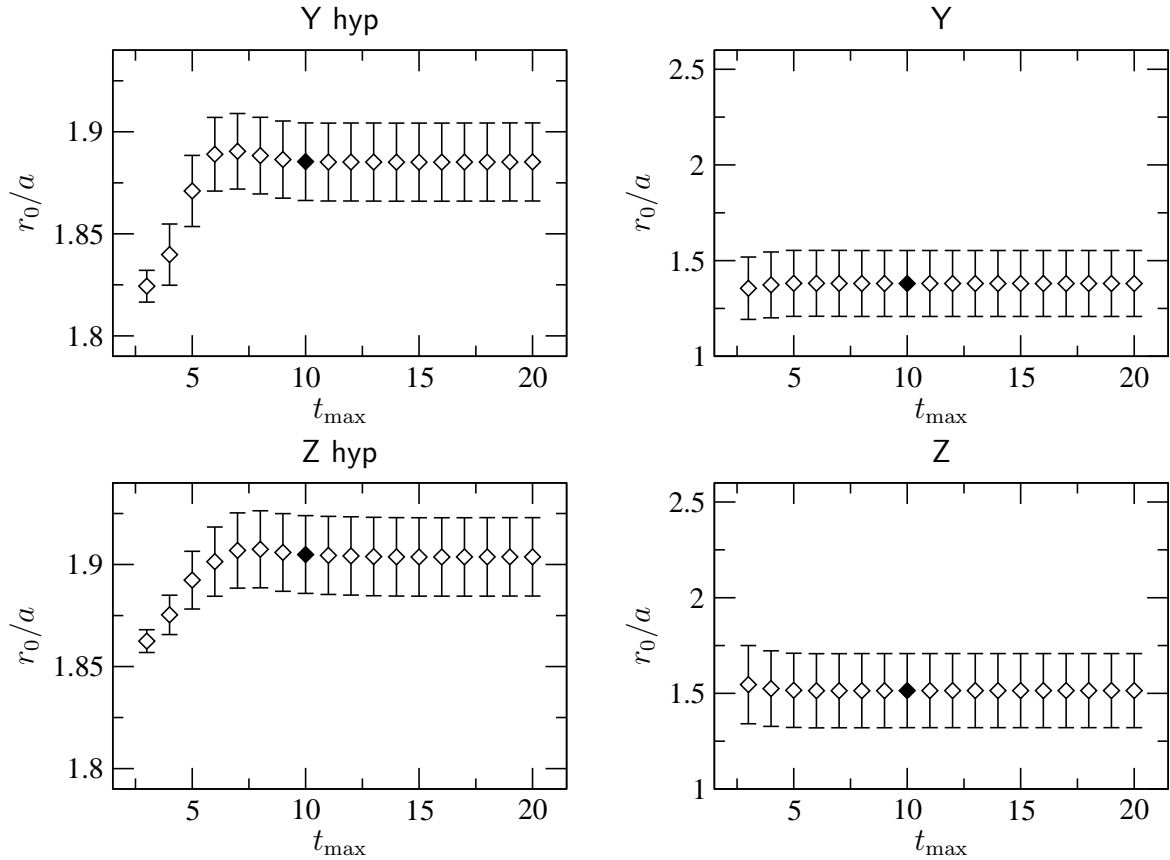
Figure D.37: Dependence of the Sommer scale on $t_{\max}$ for ensembles Y hyp, Y, Z hyp, and Z. The filled diamond corresponds to $t_{\max}$ used in the final fit.
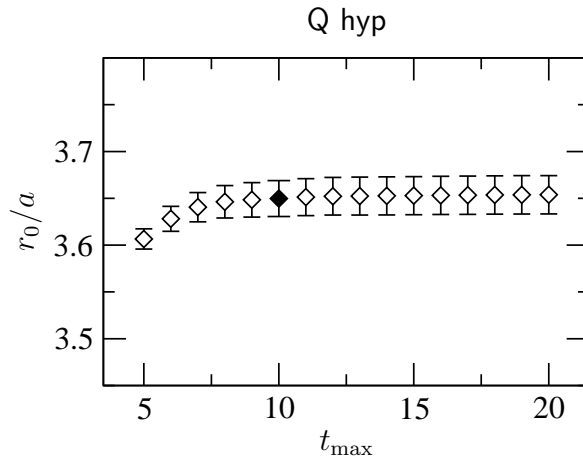
Figure D.38: Dependence of the Sommer scale on $t_{\max}$ for ensemble Q hyp. The filled diamond corresponds to $t_{\max}$ used in the final fit.
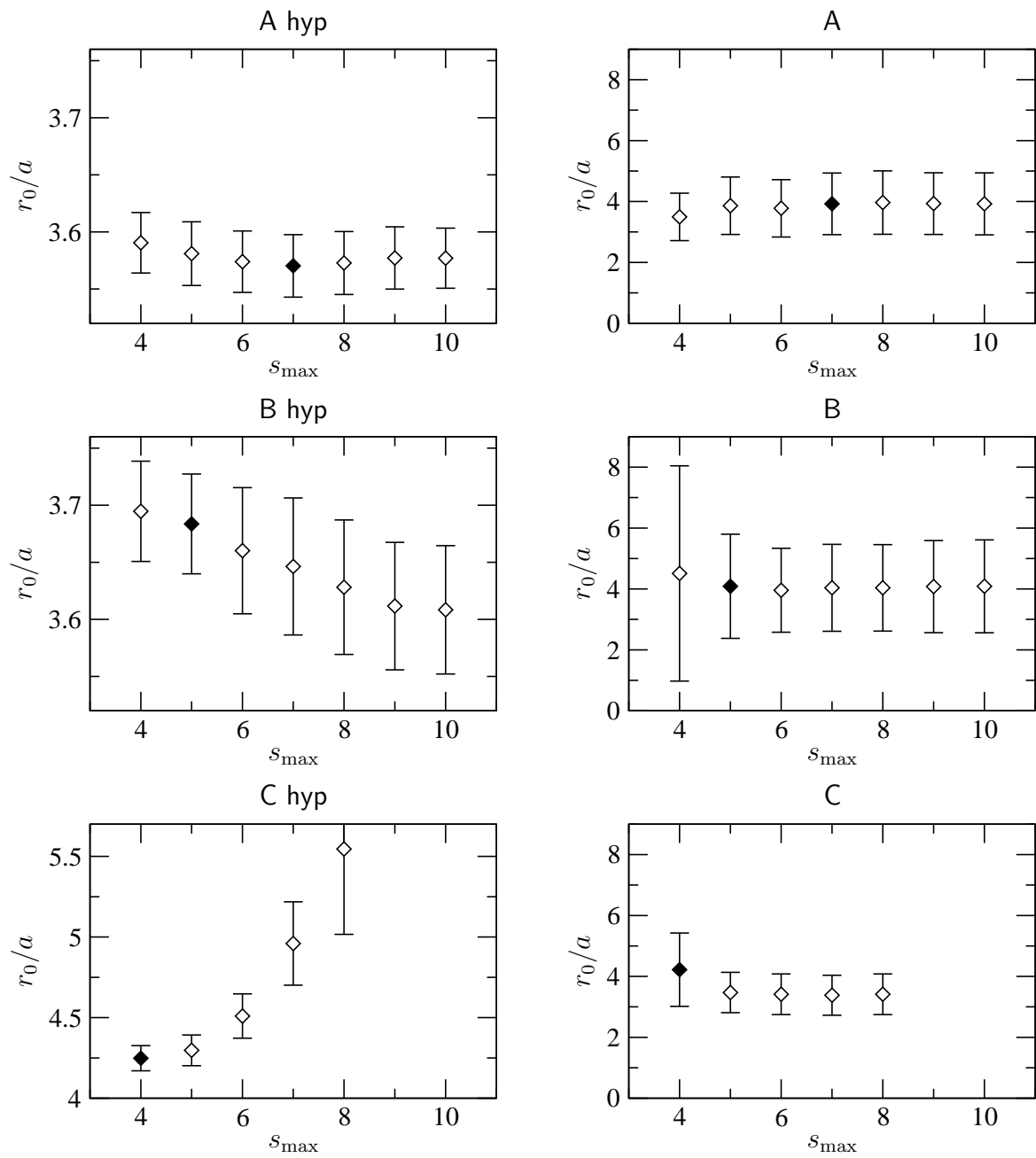
Figure D.39: Dependence of the Sommer scale on $s_{\min}$ for ensembles A hyp, A, B hyp, B, C hyp, and C. The filled diamond corresponds to $s_{\max}$ used in the final fit.
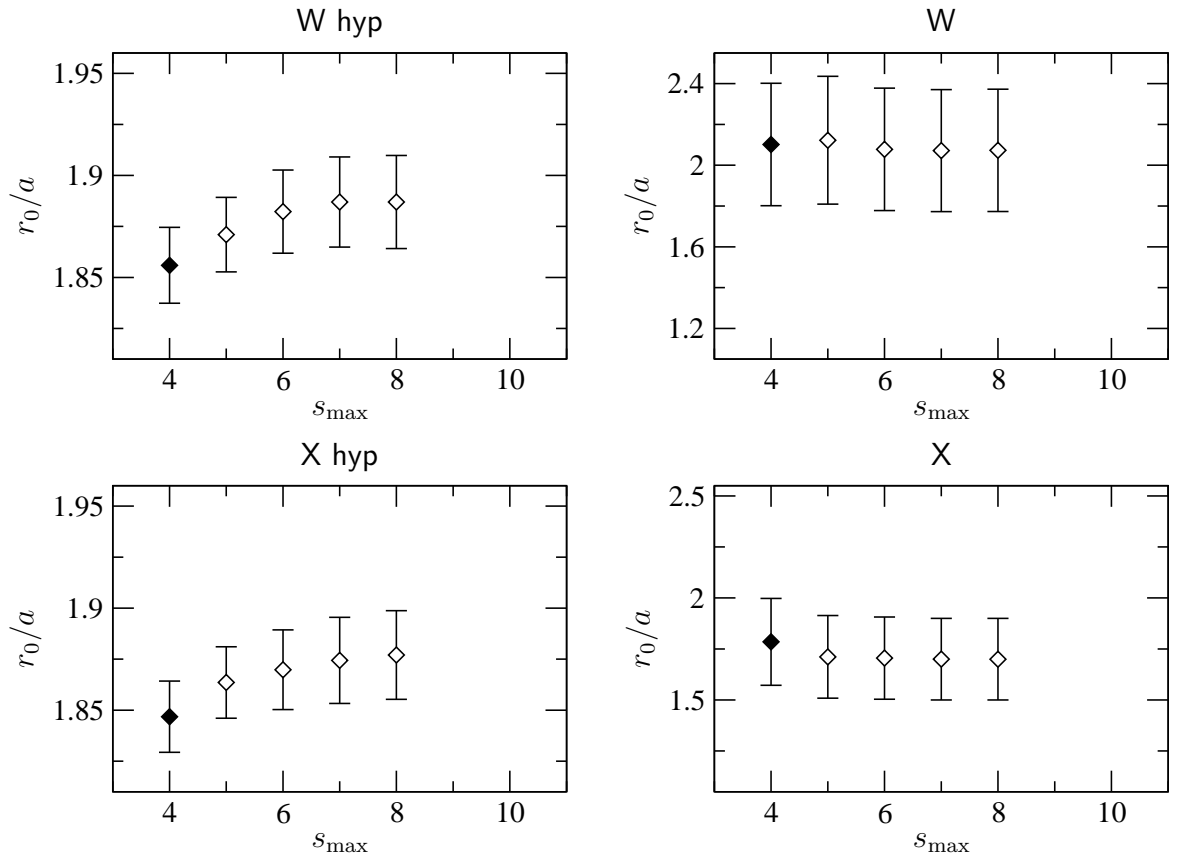
Figure D.40: Dependence of the Sommer scale on s_{min} for ensembles W hyp, W, X hyp, and X. The filled diamond corresponds to s_{max} used in the final fit.
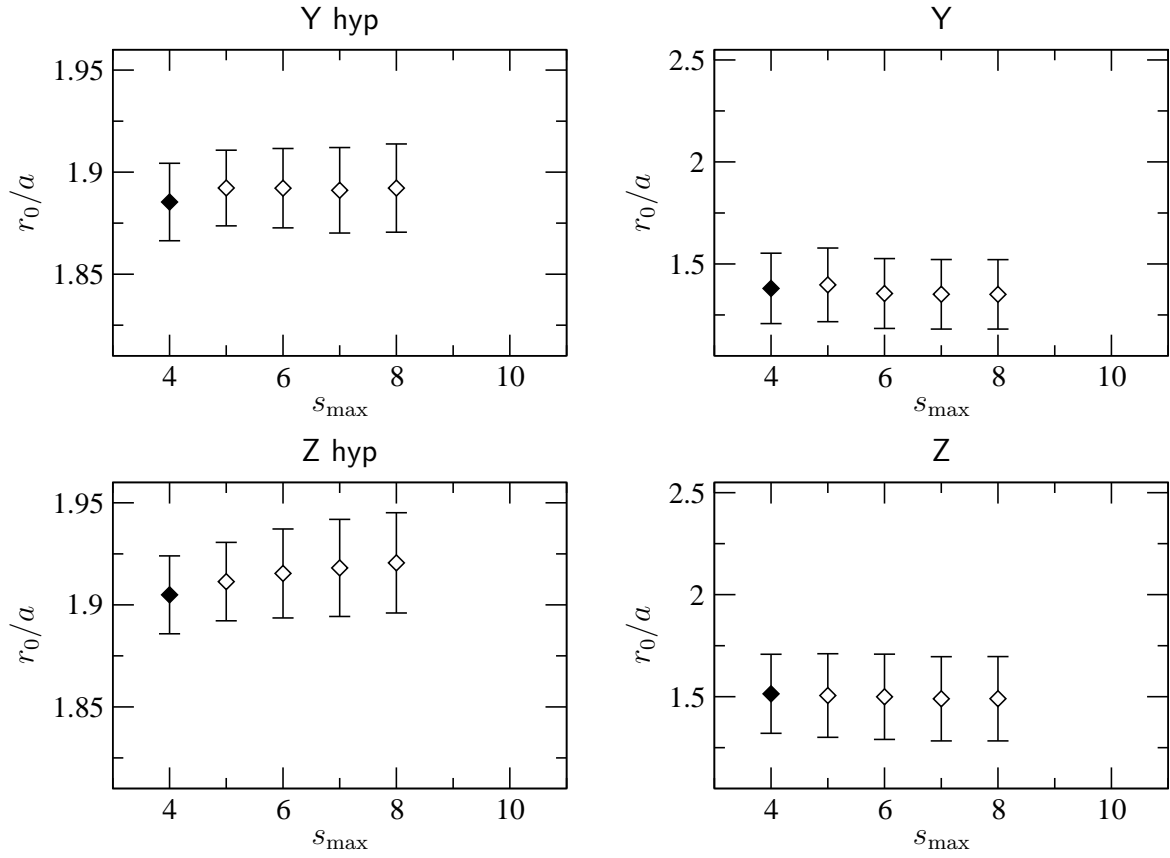
Figure D.41: Dependence of the Sommer scale on $s_{\min}$ for ensembles Y hyp, Y, Z hyp, and Z. The filled diamond corresponds to $s_{\max}$ used in the final fit.
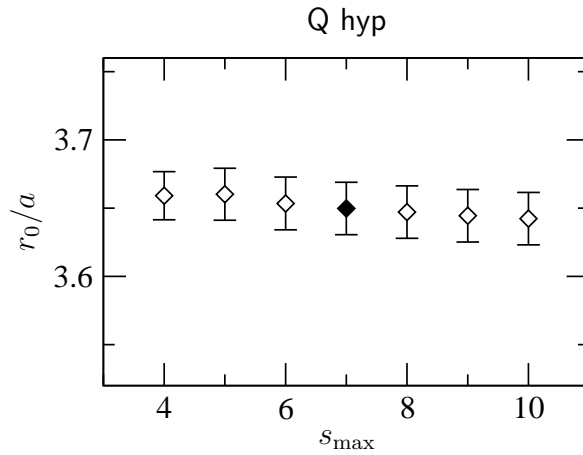
Figure D.42: Dependence of the Sommer scale on $s_{\min}$ for ensemble Q hyp. The filled diamond corresponds to $s_{\max}$ used in the final fit.
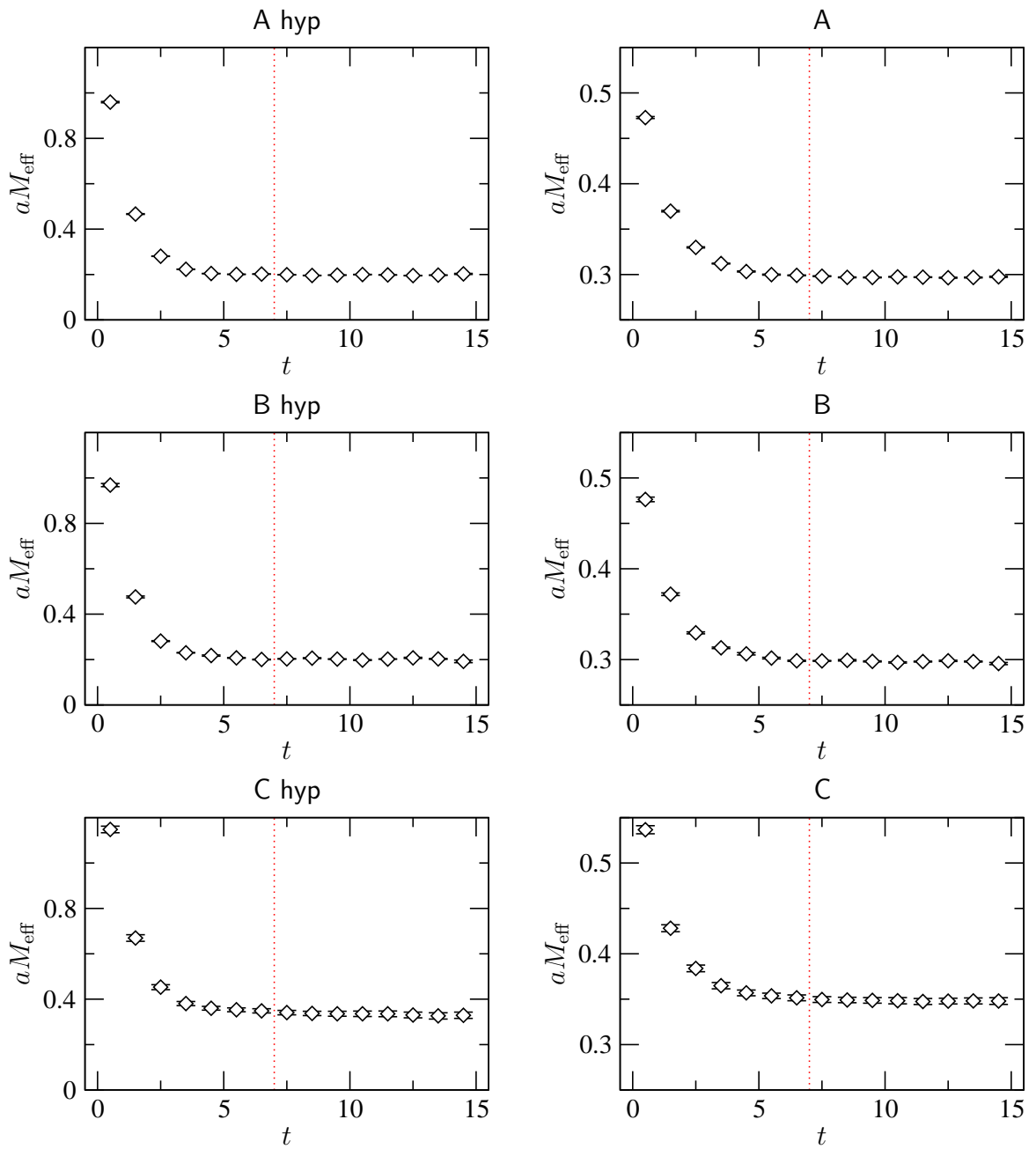
Figure D.43: Effective pion mass for ensembles A hyp, A, B hyp, B, C hyp, and C at $m_V = 0.01$. The minimum time separation chosen is $t_{\min} = 7$.
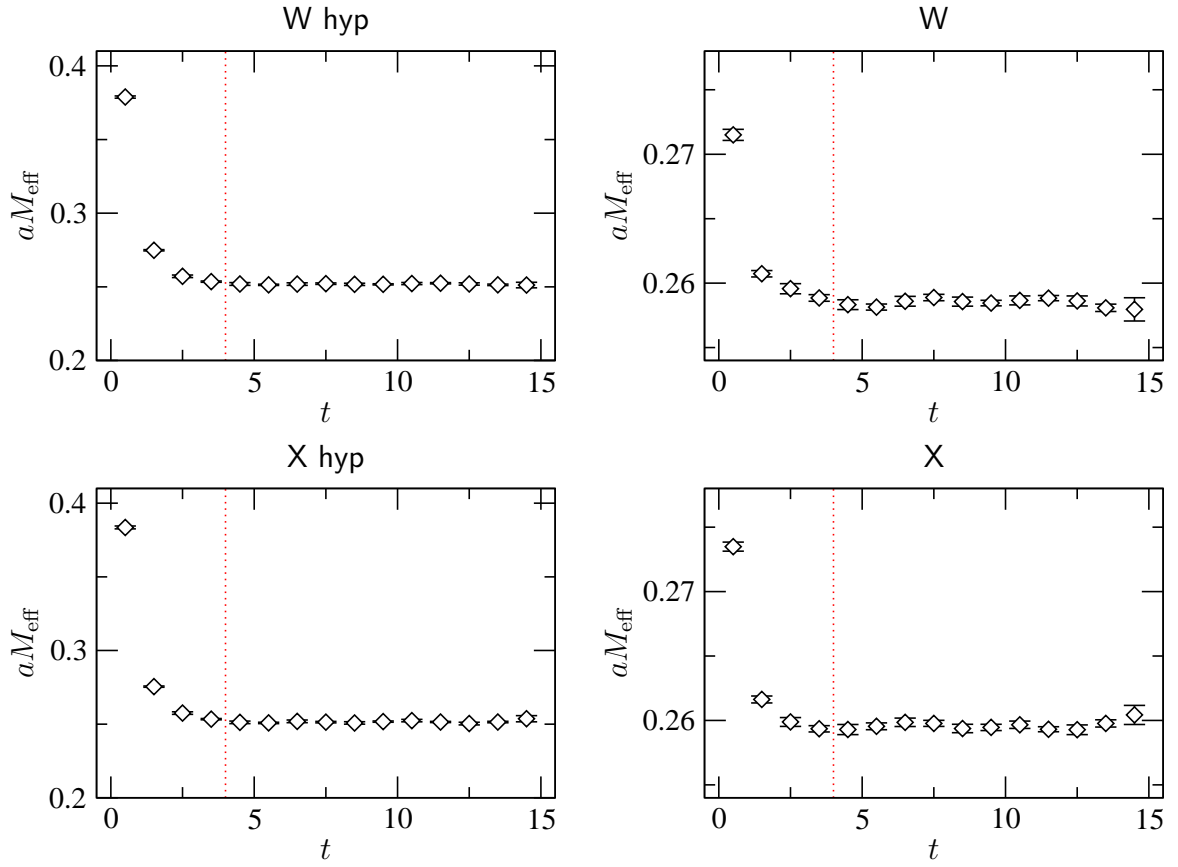
Figure D.44: Effective pion mass for ensembles W hyp, W, Z hyp, and Z at $m_V = 0.01$. The minimum time separation chosen is $t_{\min} = 4$.
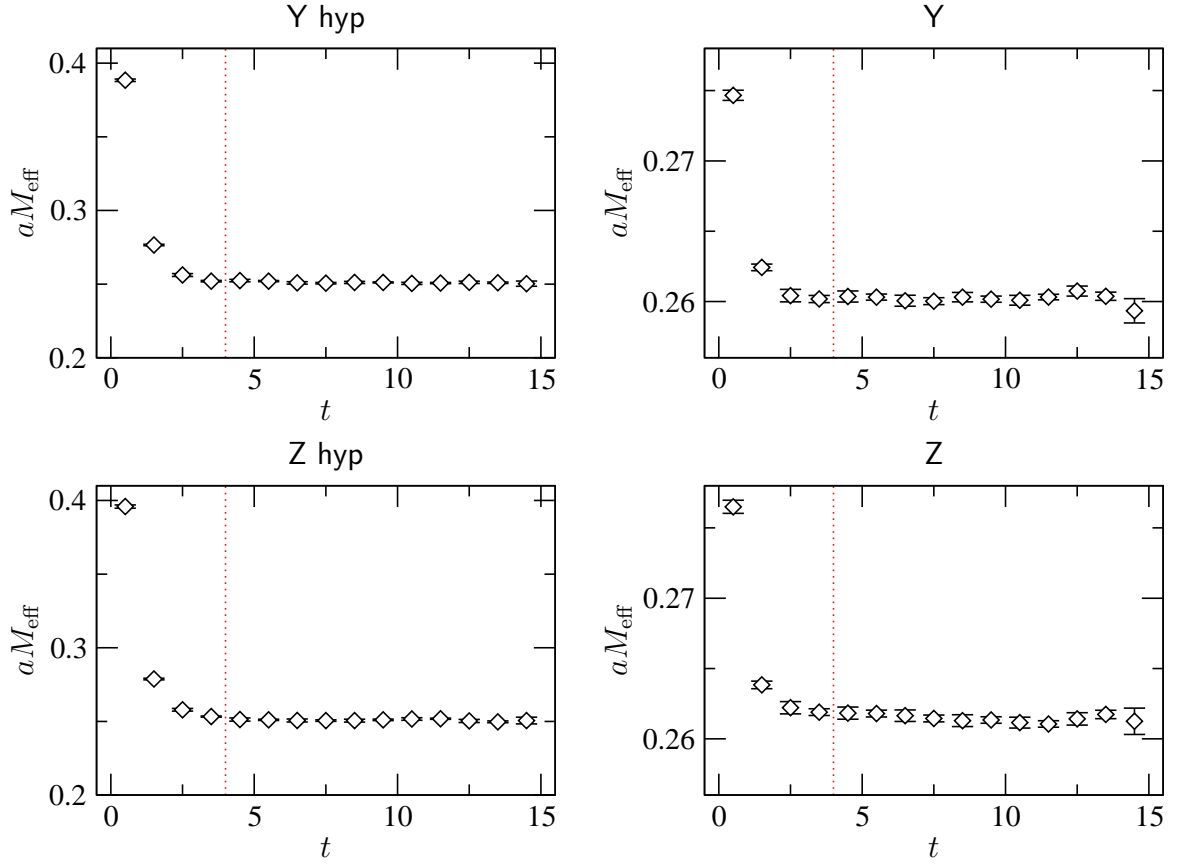
Figure D.45: Effective pion mass for ensembles Y hyp, Y, Z hyp, and Z at $m_V = 0.01$. The minimum time separation chosen is $t_{\min} = 4$.
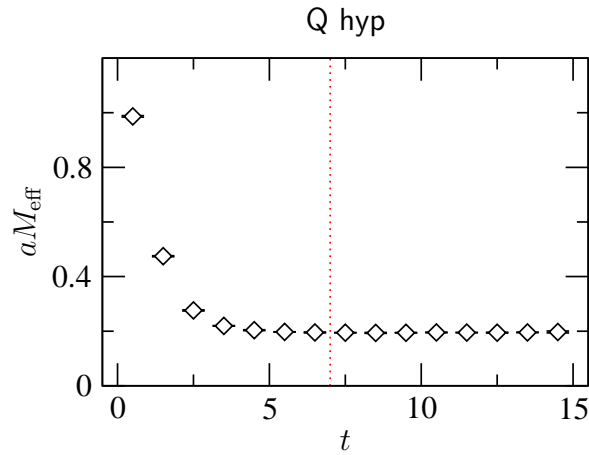
Figure D.46: Effective pion mass for ensemble Q hyp at $m_V = 0.01$. The minimum time separation chosen is $t_{\min} = 7$.
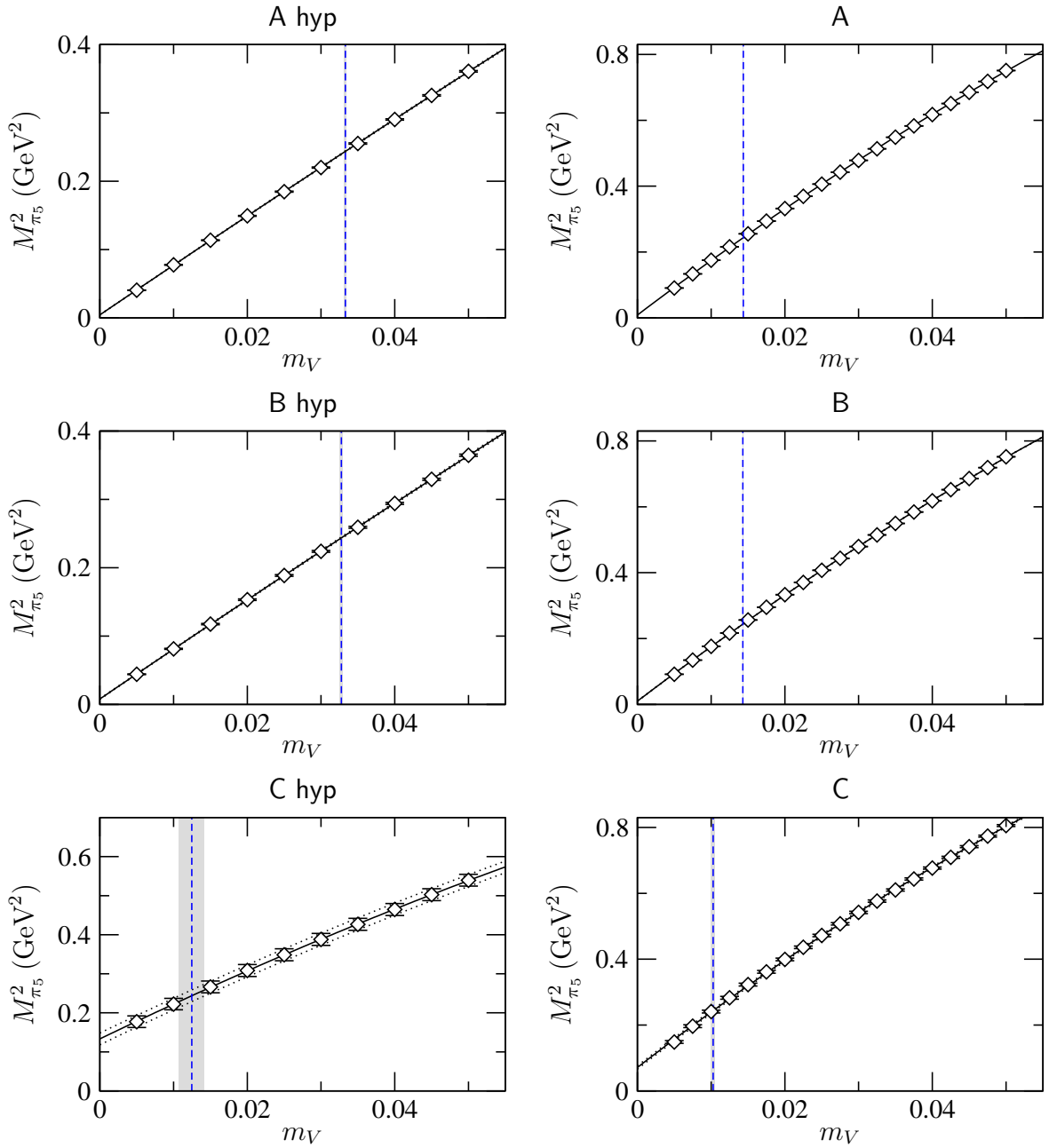
Figure D.47: Quadratic pion-mass fit and kaon quark-mass threshold for ensembles A hyp, A, B hyp, B, C hyp, and C. The dotted vertical lines correspond to the determined values of m_{Q_K}.
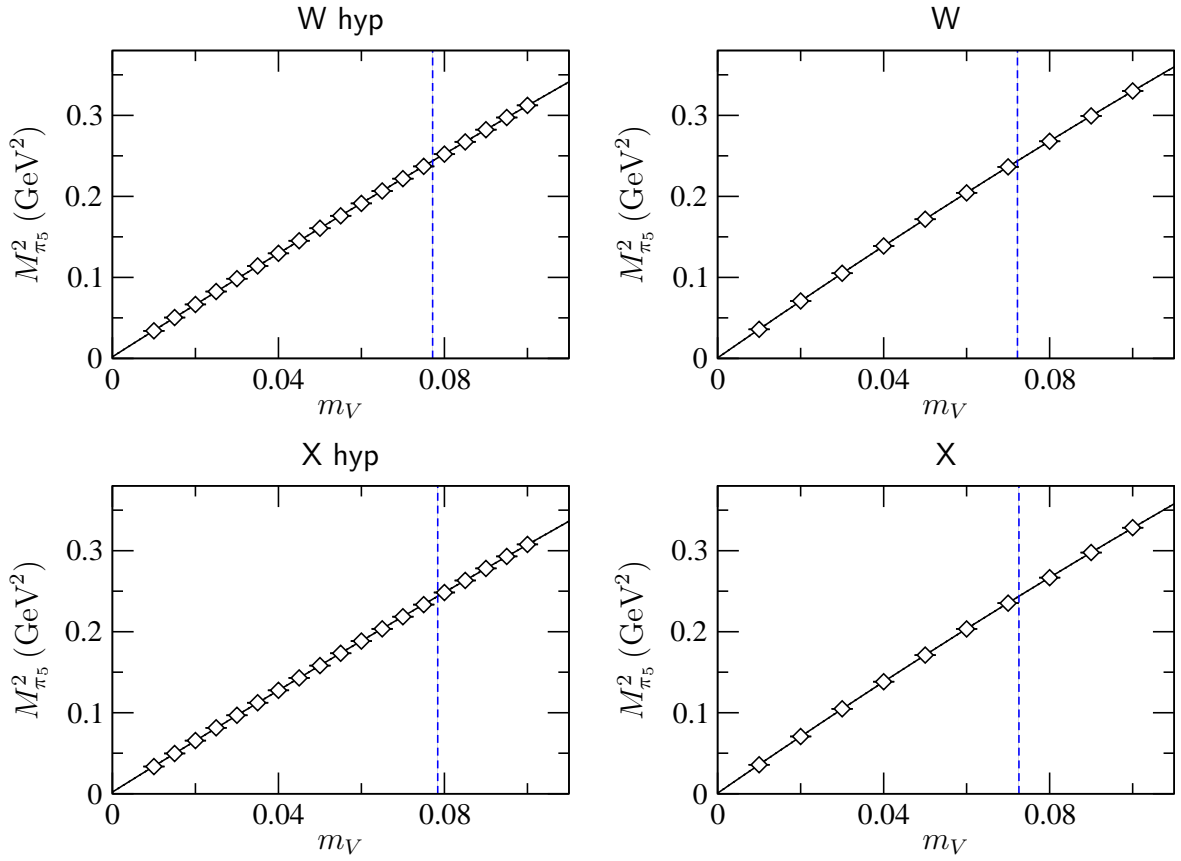
Figure D.48: Quadratic pion-mass fit and kaon quark-mass threshold for ensembles W hyp, W, X hyp, and X. The dotted vertical lines correspond to the determined values of m_{Q_K}.
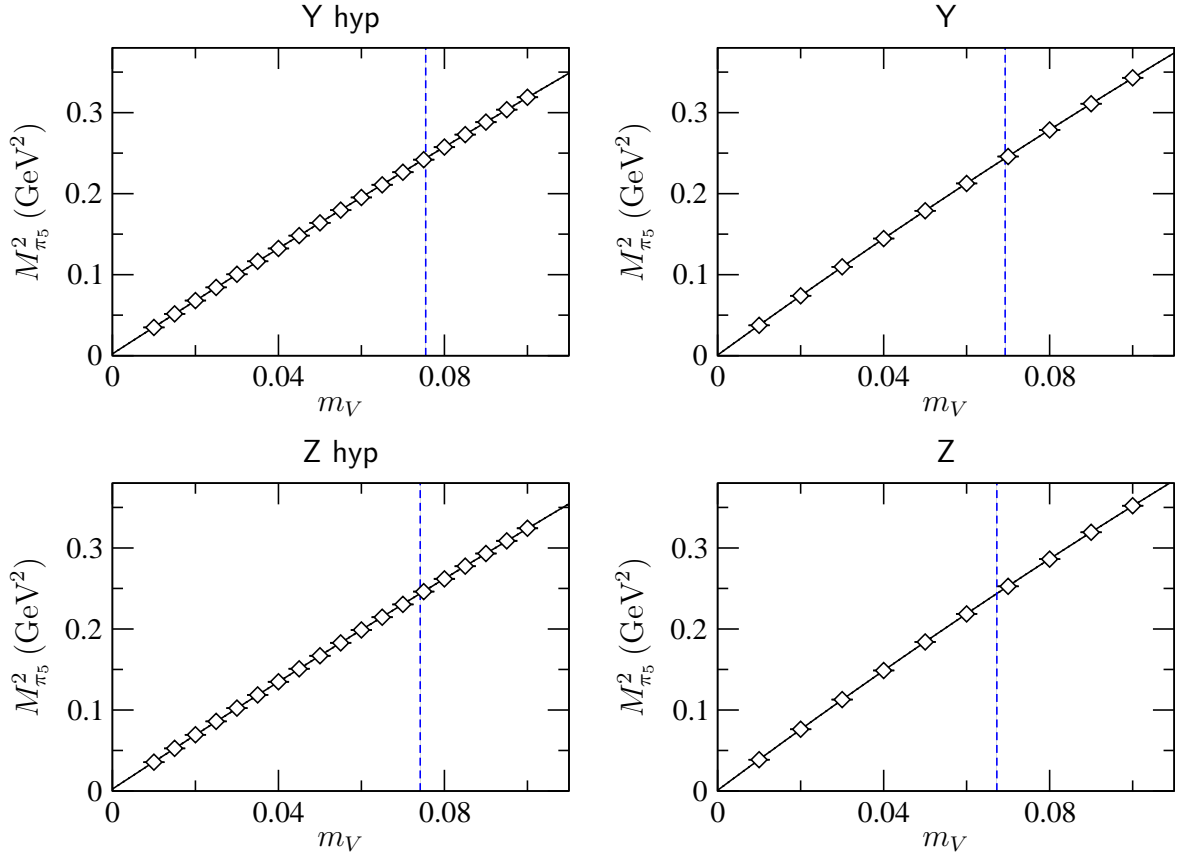
Figure D.49: Quadratic pion-mass fit and kaon quark-mass threshold for ensembles Y hyp, Y, Z hyp, and Z. The dotted vertical lines correspond to the determined values of m_{Q_K}.
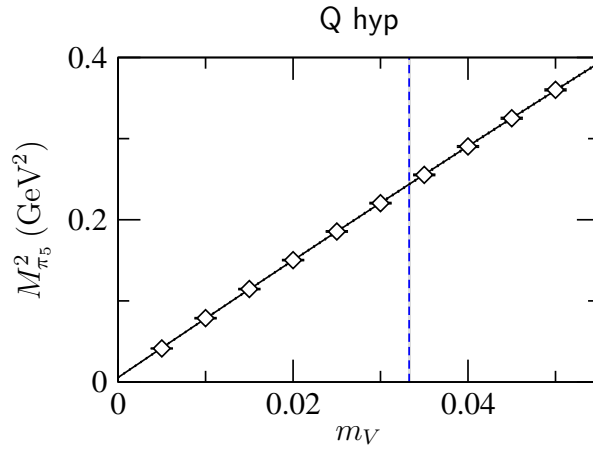
Figure D.50: Quadratic pion-mass fit and kaon quark-mass threshold for ensemble Q hyp. The dotted vertical line corresponds to the determined value of m_{Q_K}.
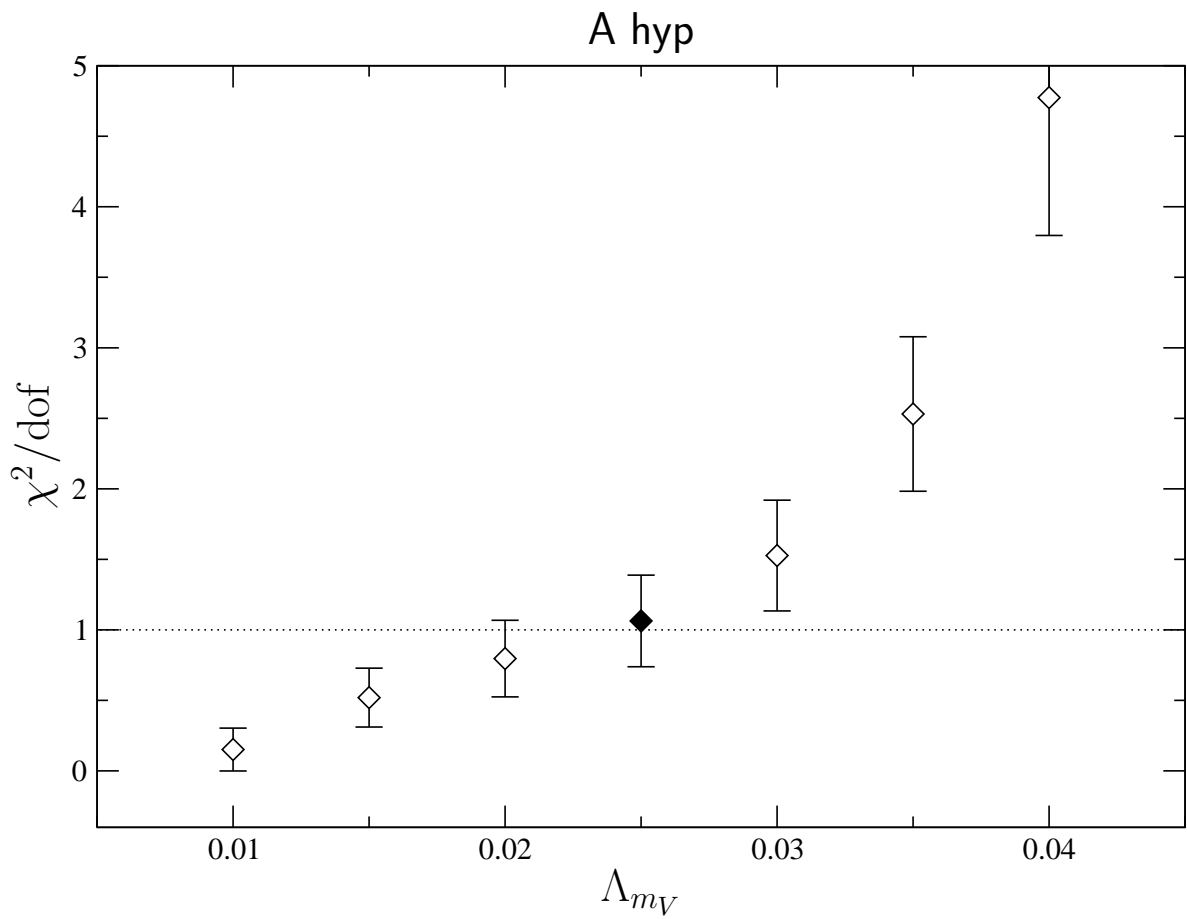
Figure D.51: χ^2 per degree of freedom over a range of valence-quark-mass cutoffs for ensemble A hyp. The filled diamond corresponds to the cutoff used in the final fit.
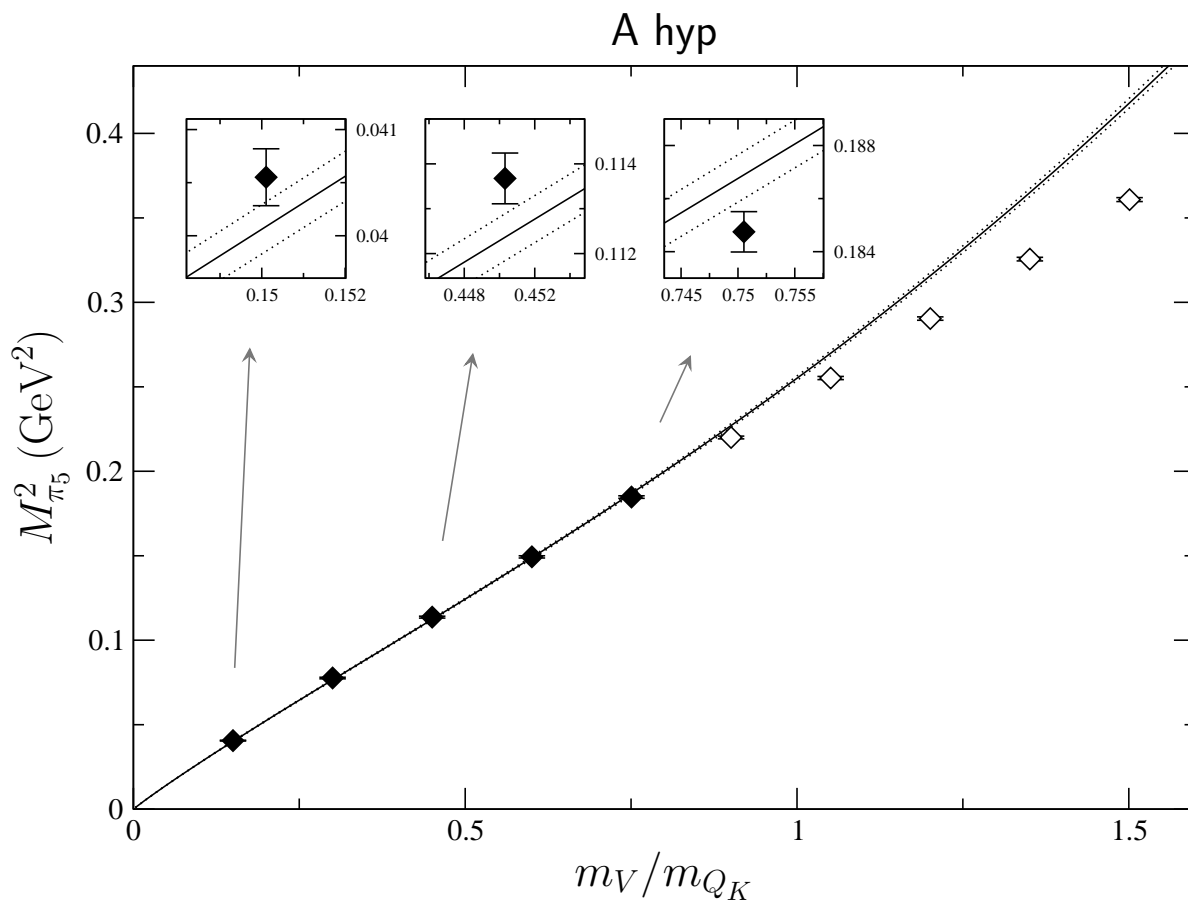
Figure D.52: Pion mass squared versus valence quark mass from the pqChPT fit of ensemble A hyp. Filled diamonds correspond to valence-quark-mass values within the fit range, while open diamonds correspond to those values beyond it.
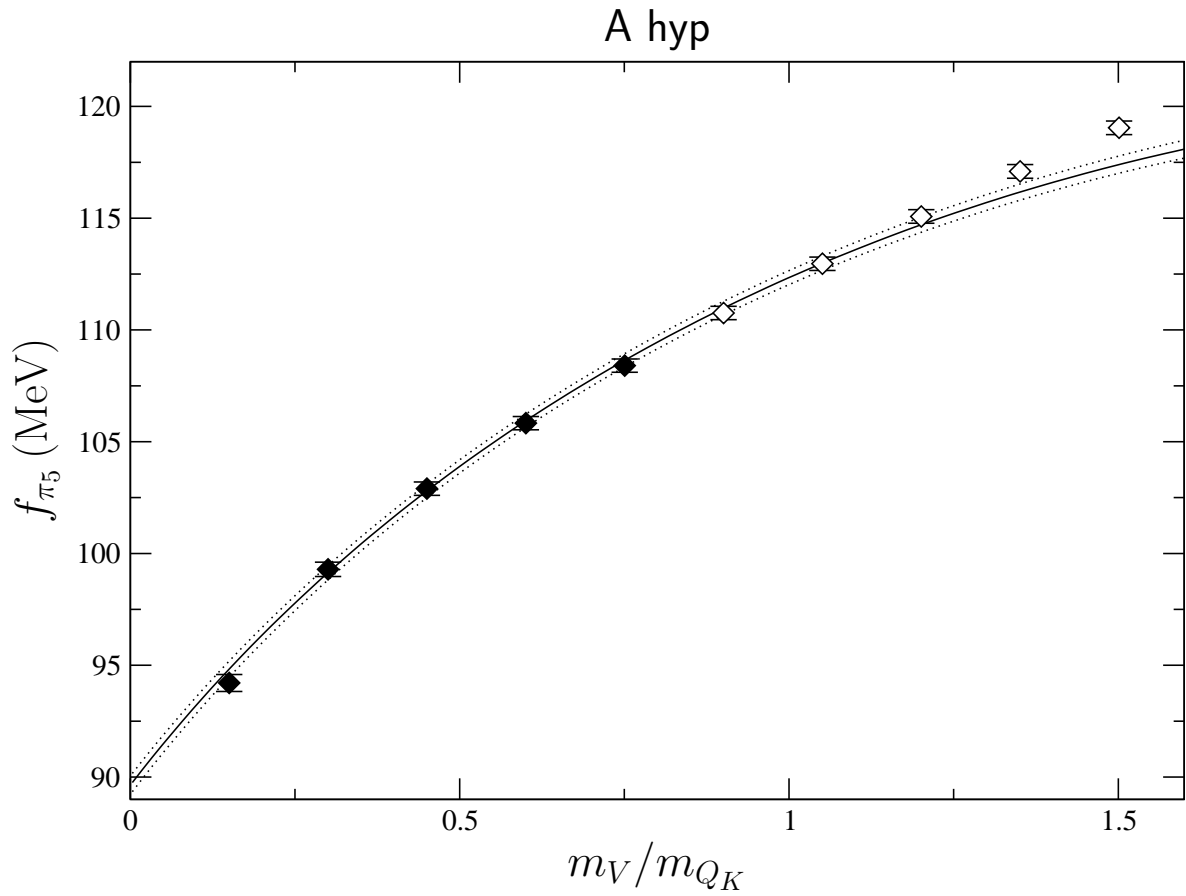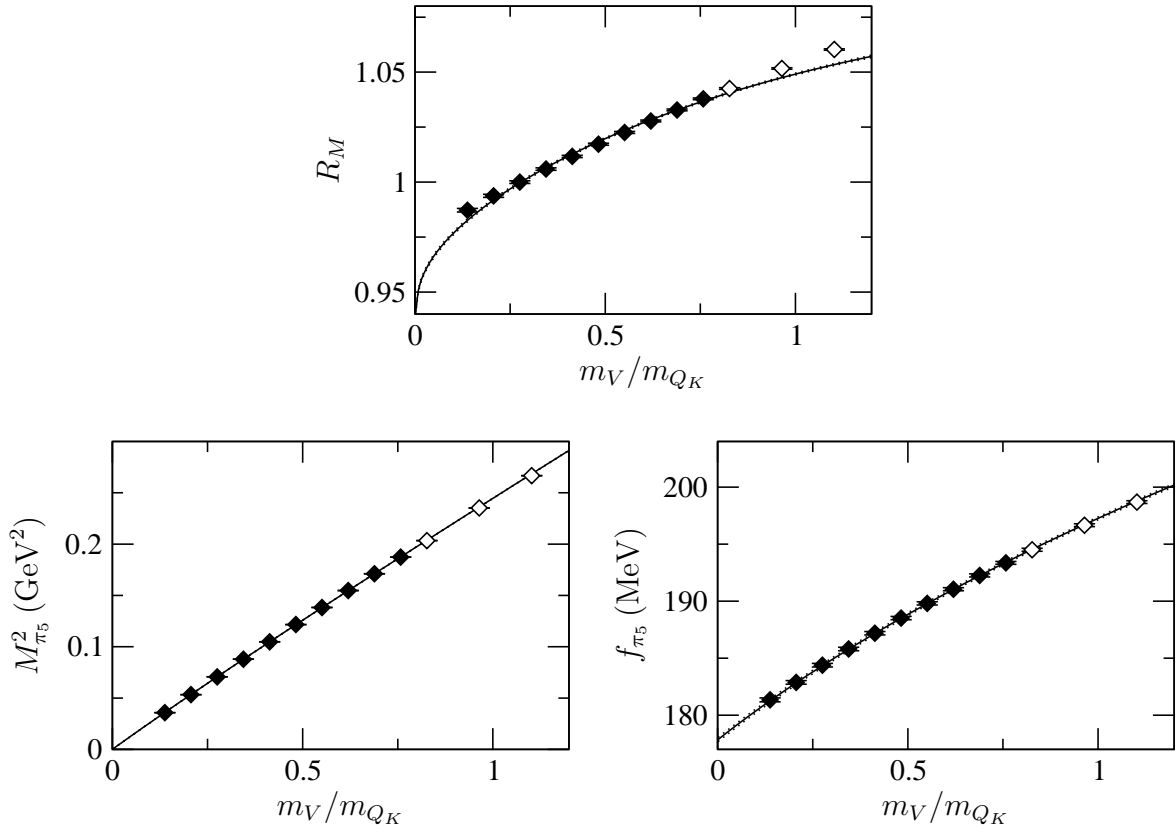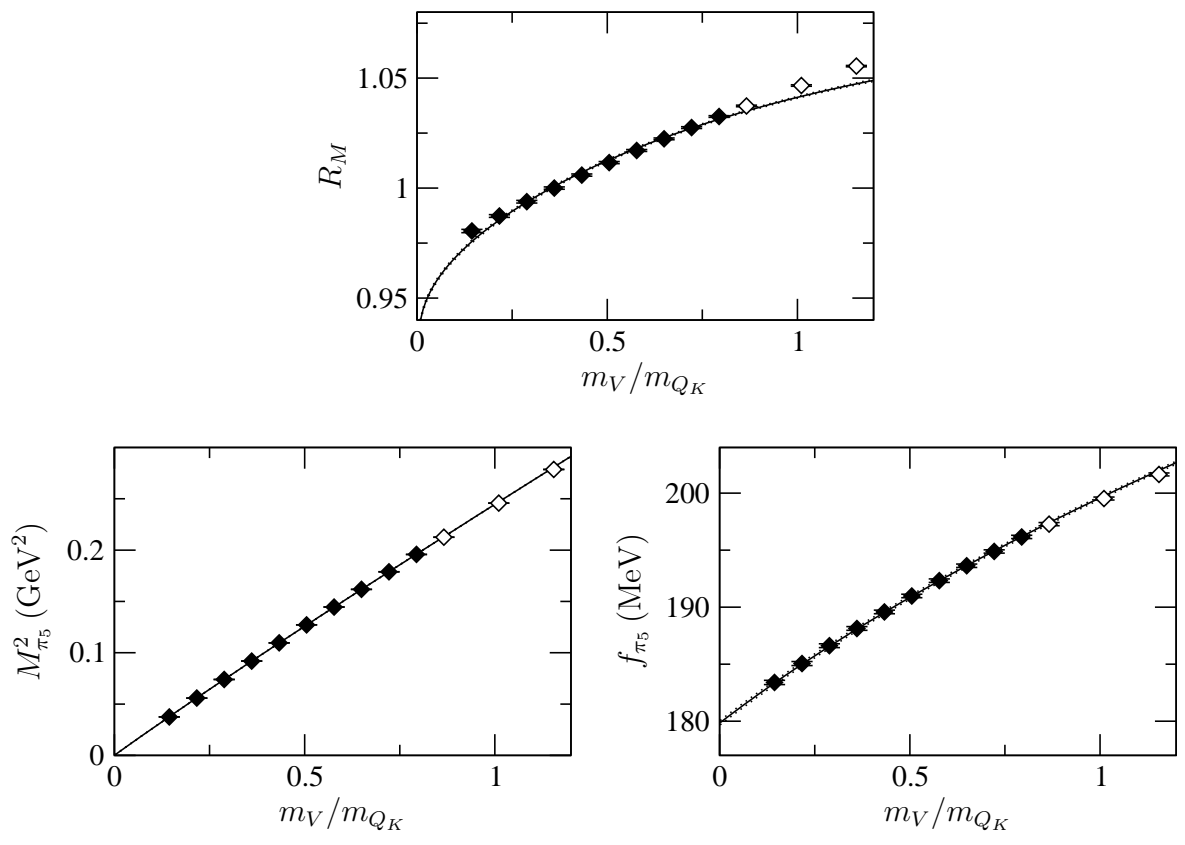
Figure D.53: Pion decay constant versus valence quark mass from the pqChPT fit of ensemble A hyp. Filled diamonds correspond to valence-quark-mass values within the fit range, while open diamonds correspond to those values beyond it.
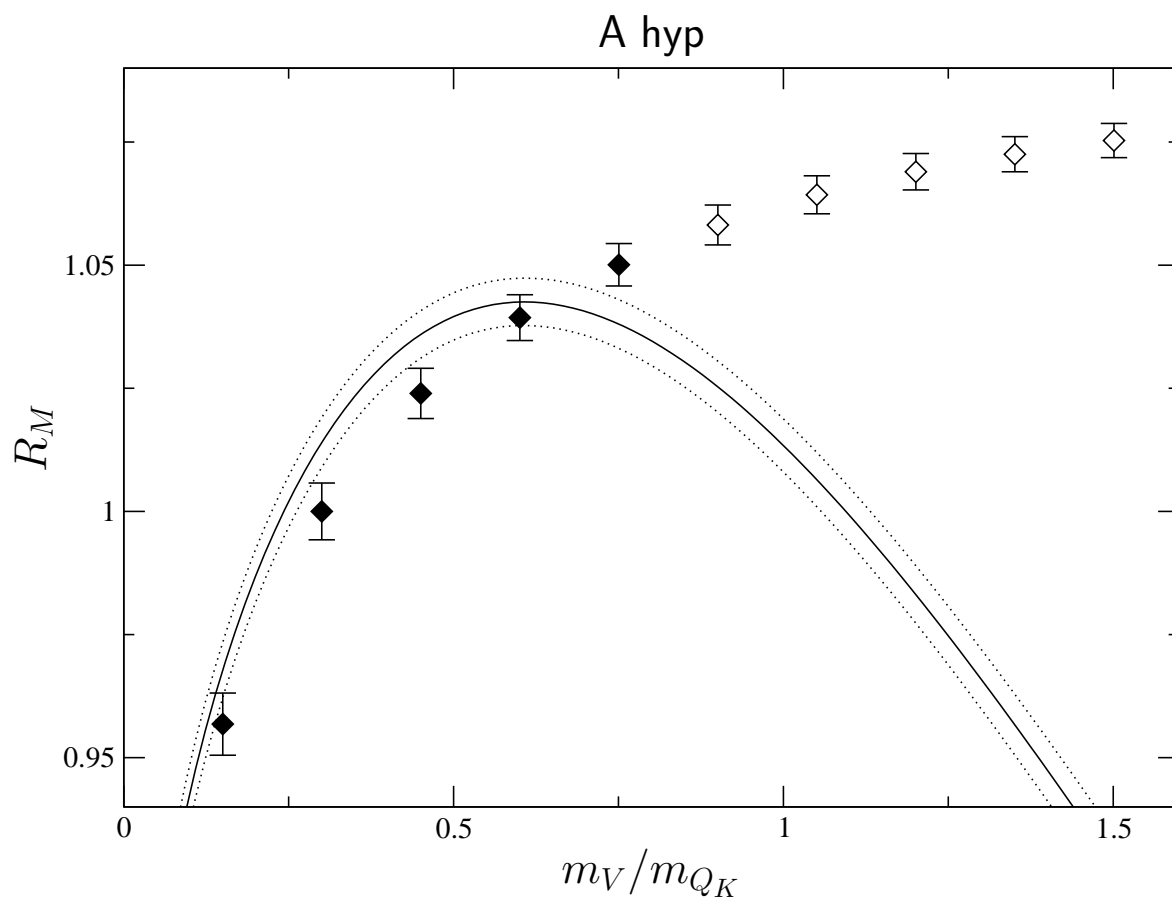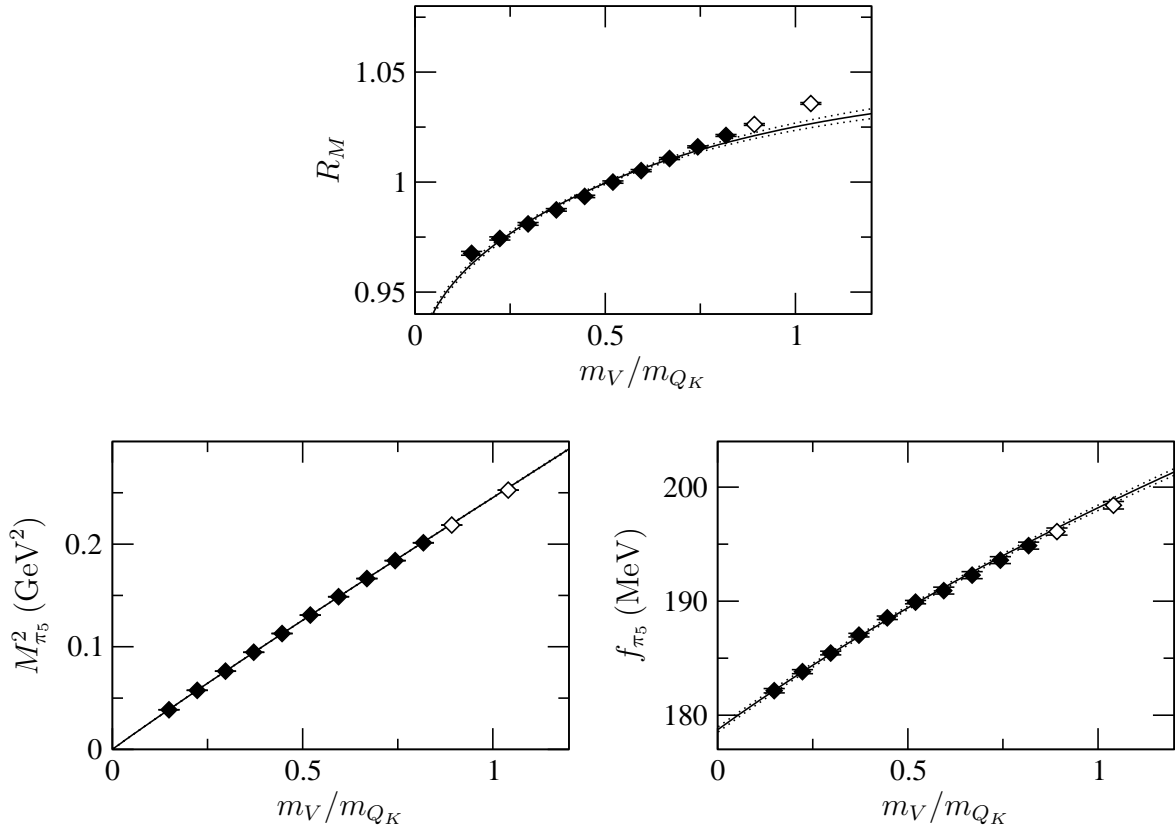
Figure D.54: R_M versus valence quark mass from the pqChPT fit of the correlator of ensemble A hyp. Filled diamonds correspond to valence-quark-mass values within the fit range, while open diamonds correspond to those values beyond it.
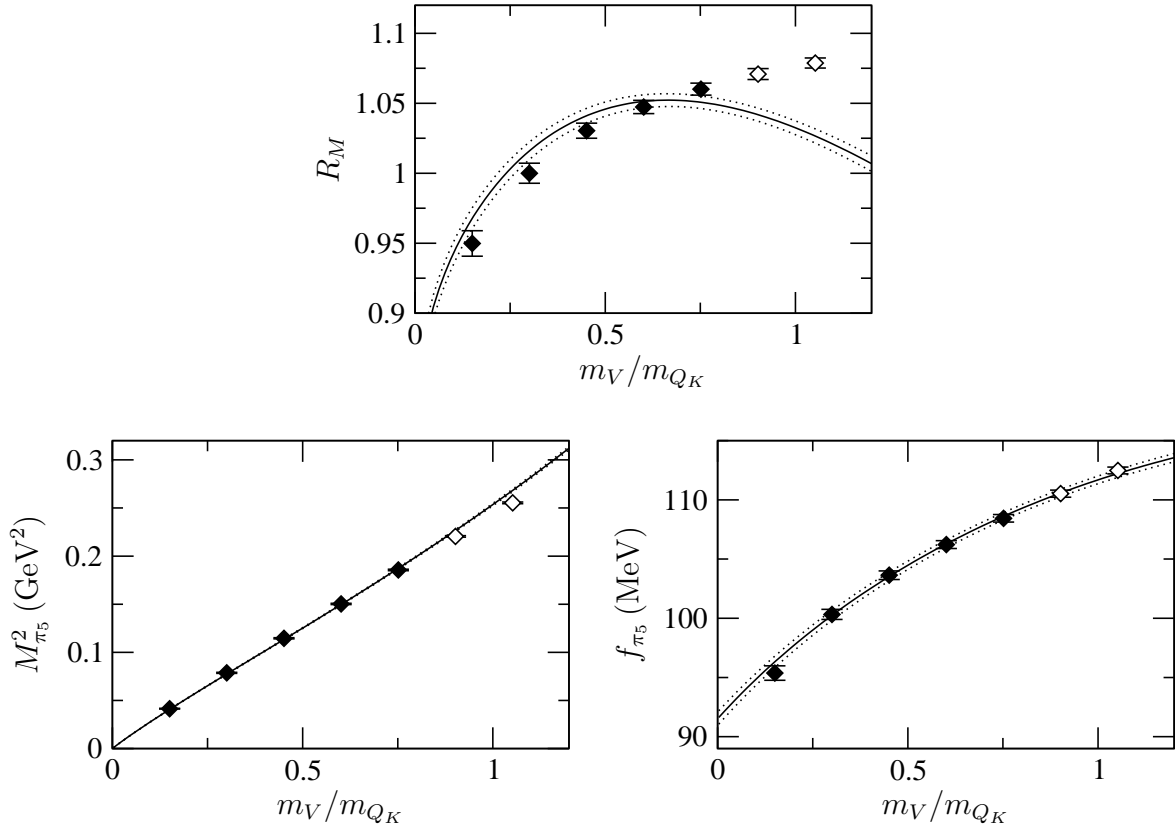
A hyp
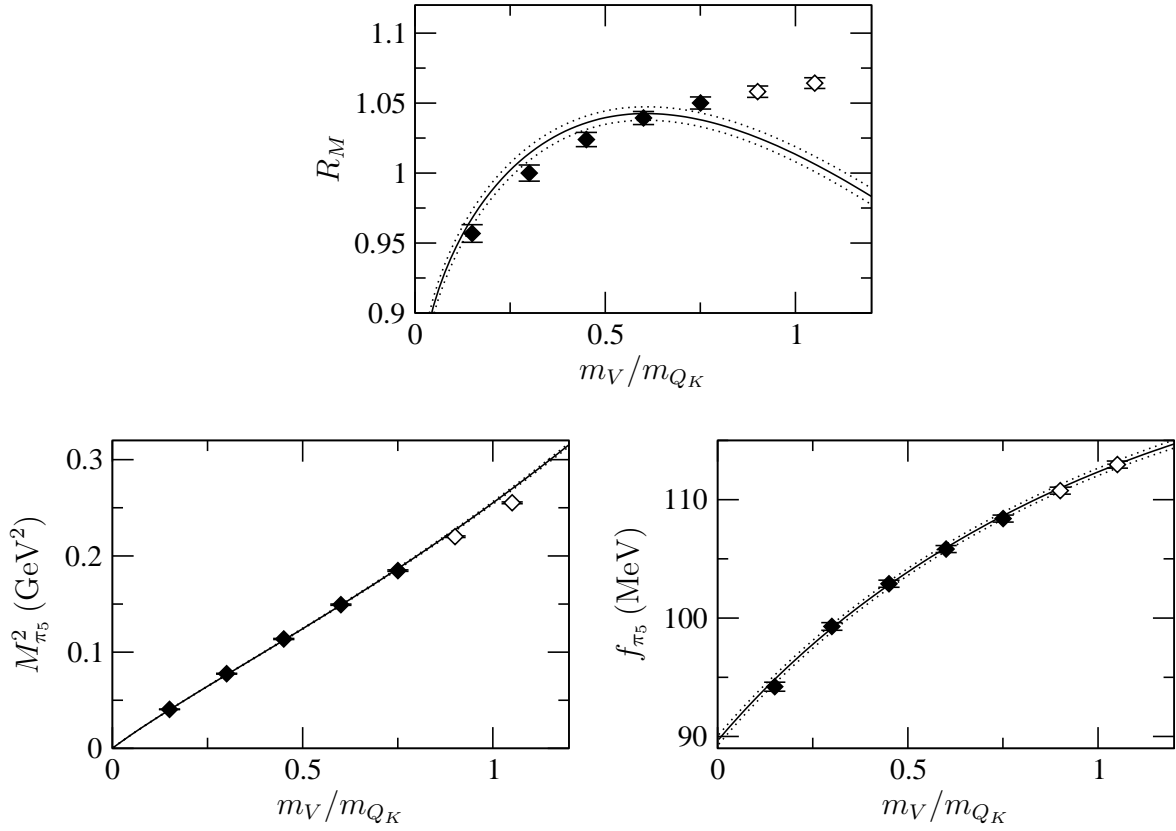
Figure D.55: Results from the pqChPT fit of ensemble A hyp. Filled diamonds correspond to valence-quark-mass values within the fit range, while open diamonds correspond to those values beyond it.

B hyp
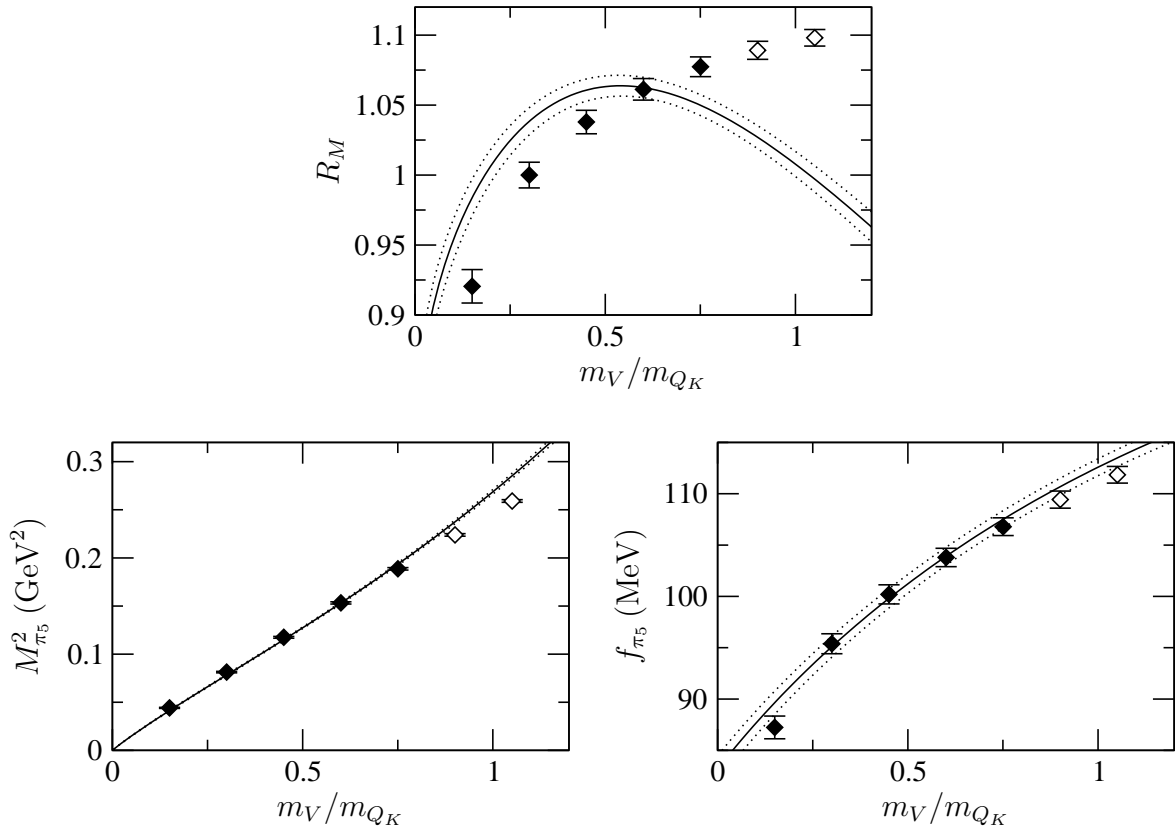
Figure D.56: Results from the pqChPT fit of ensemble B hyp. Filled diamonds correspond to valence-quark-mass values within the fit range, while open diamonds correspond to those values beyond it.
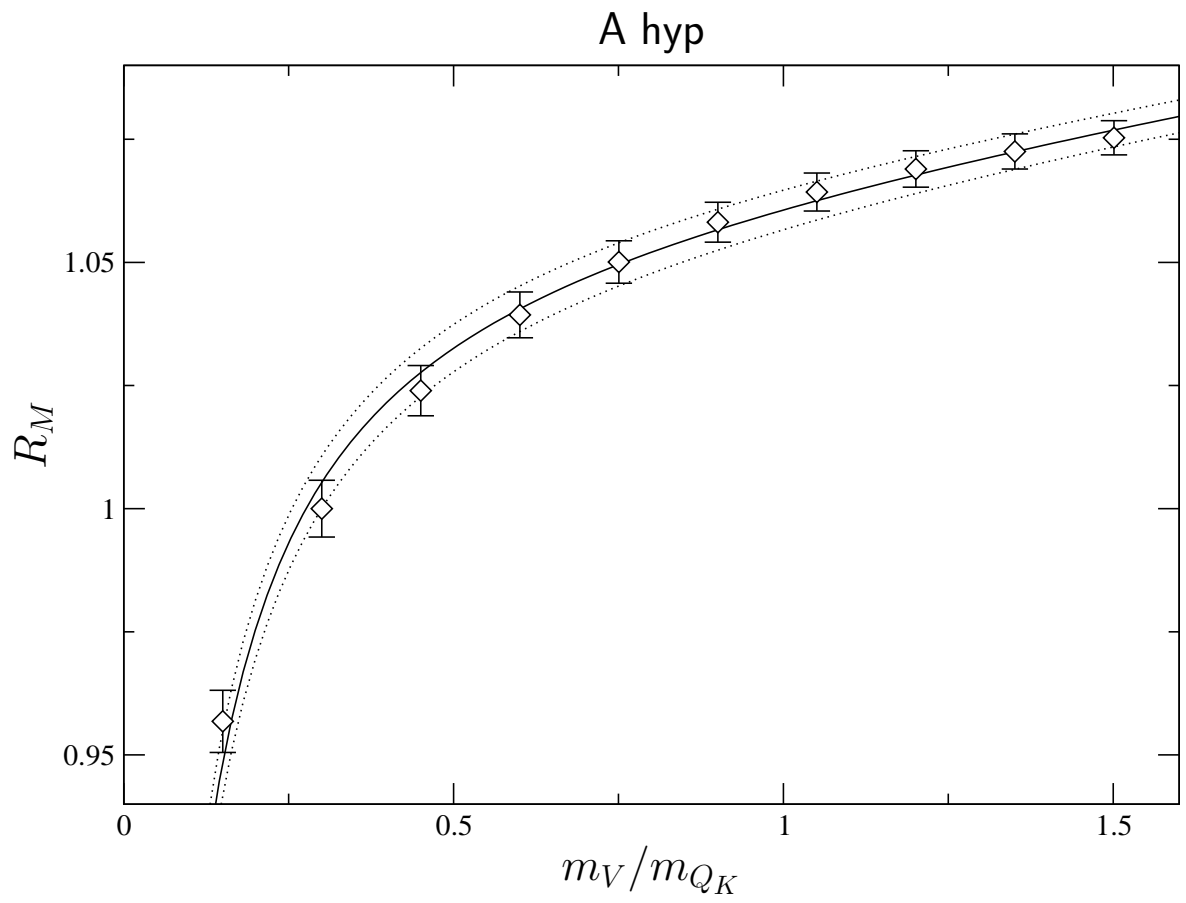
A
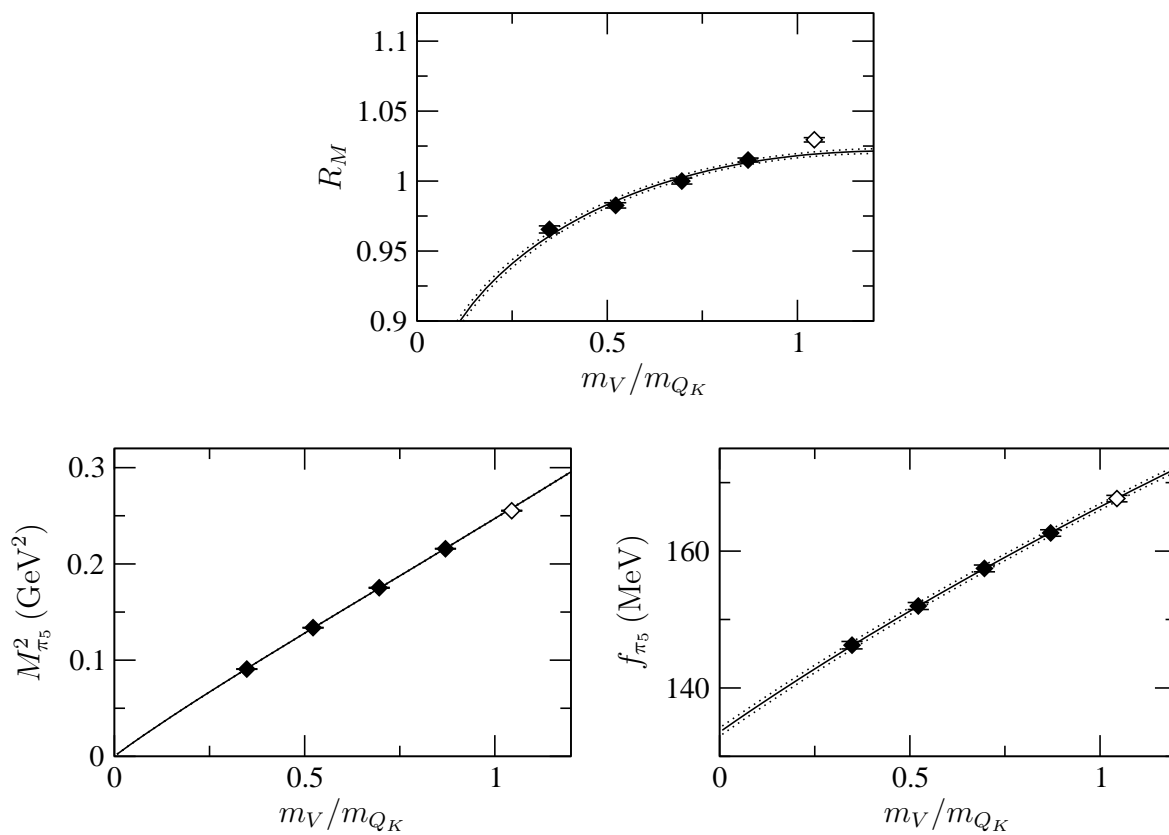
Figure D.57: Results from the pqChPT fit of ensemble A. Filled diamonds correspond to valence-quark-mass values within the fit range, while open diamonds correspond to those values beyond it.

B
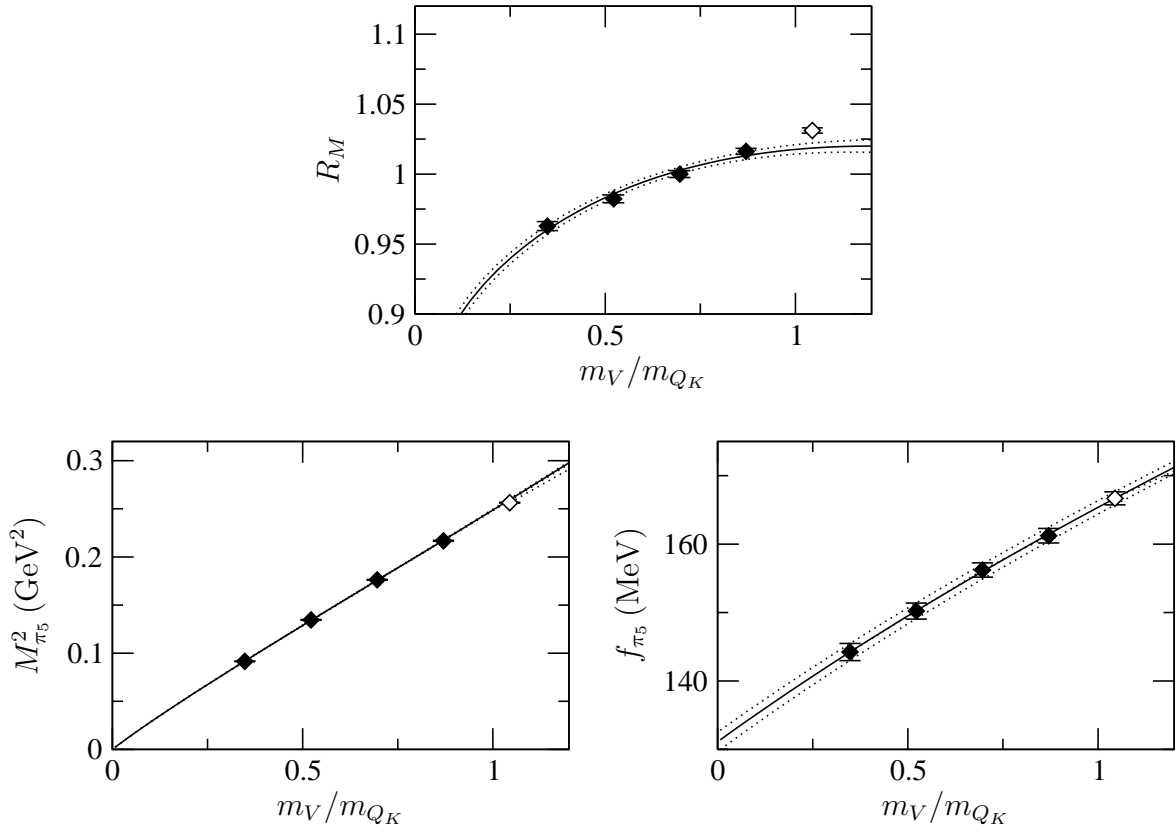
Figure D.58: Results from the pqChPT fit of ensemble B. Filled diamonds correspond to valence-quark-mass values within the fit range, while open diamonds correspond to those values beyond it.
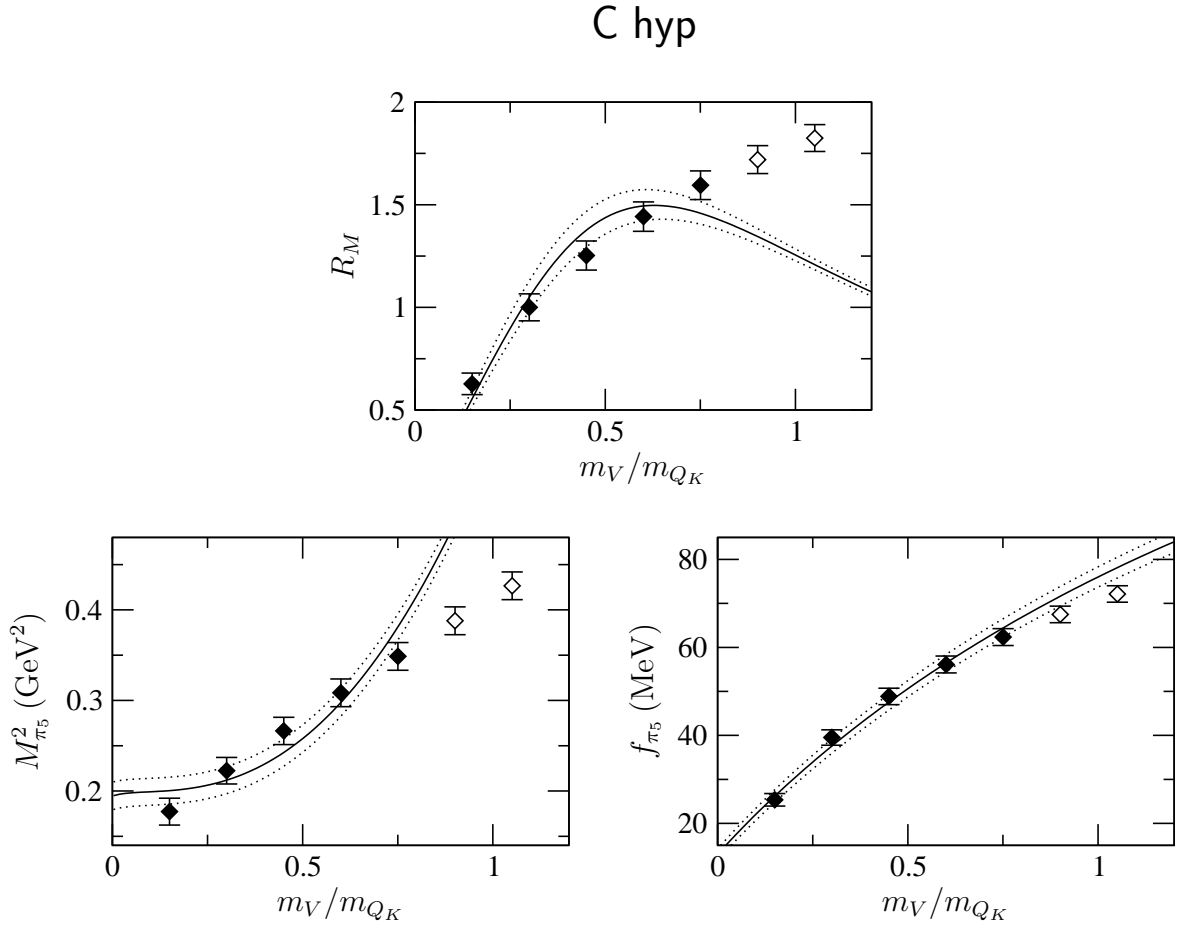
W hyp
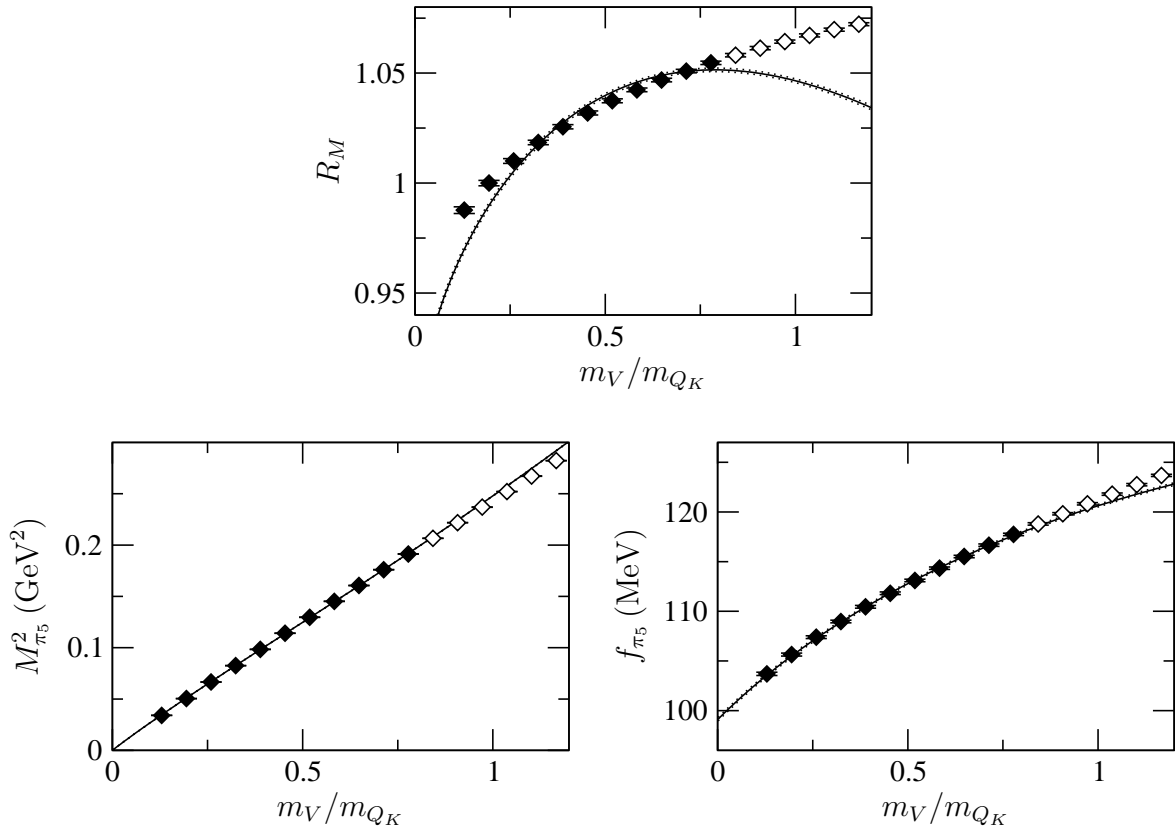
Figure D.59: Results from the pqChPT fit of ensemble W hyp. Filled diamonds correspond to valence-quark-mass values within the fit range, while open diamonds correspond to those values beyond it.

263
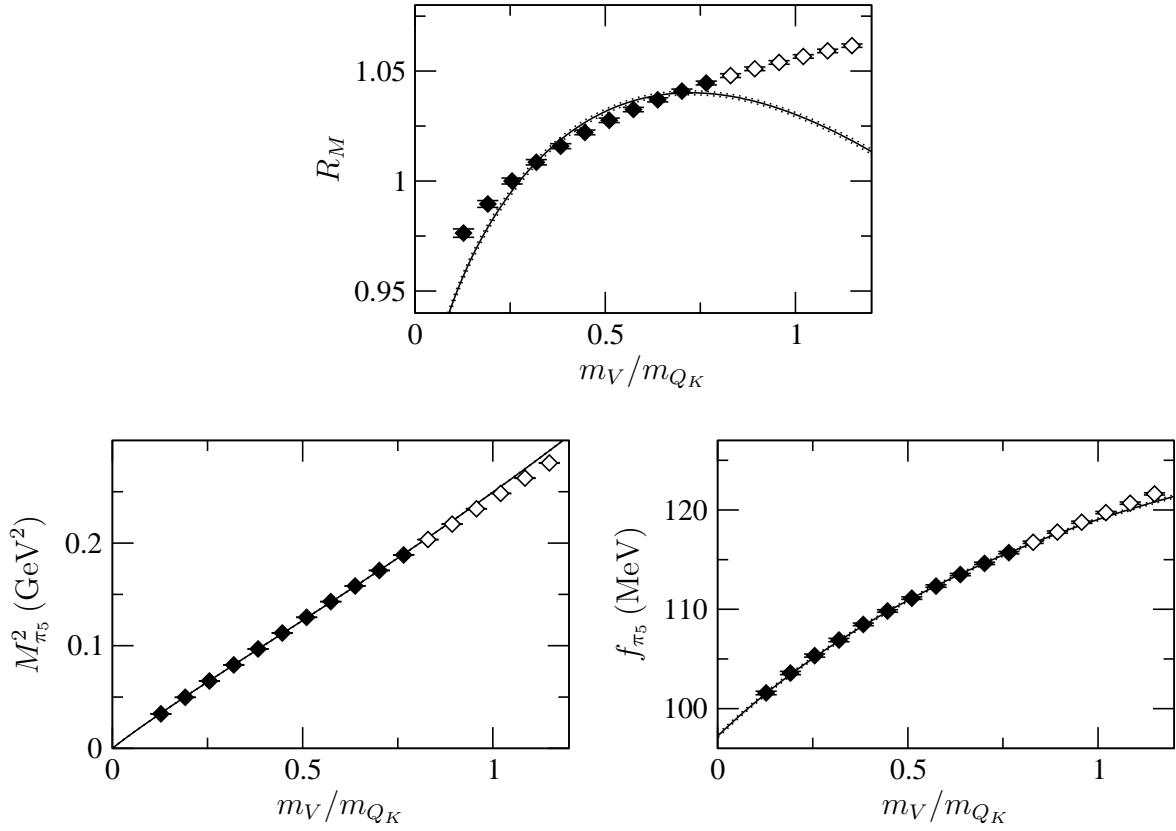
X hyp

Figure D.60: Results from the pqChPT fit of ensemble X hyp. Filled diamonds correspond to valence-quark-mass values within the fit range, while open diamonds correspond to those values beyond it.
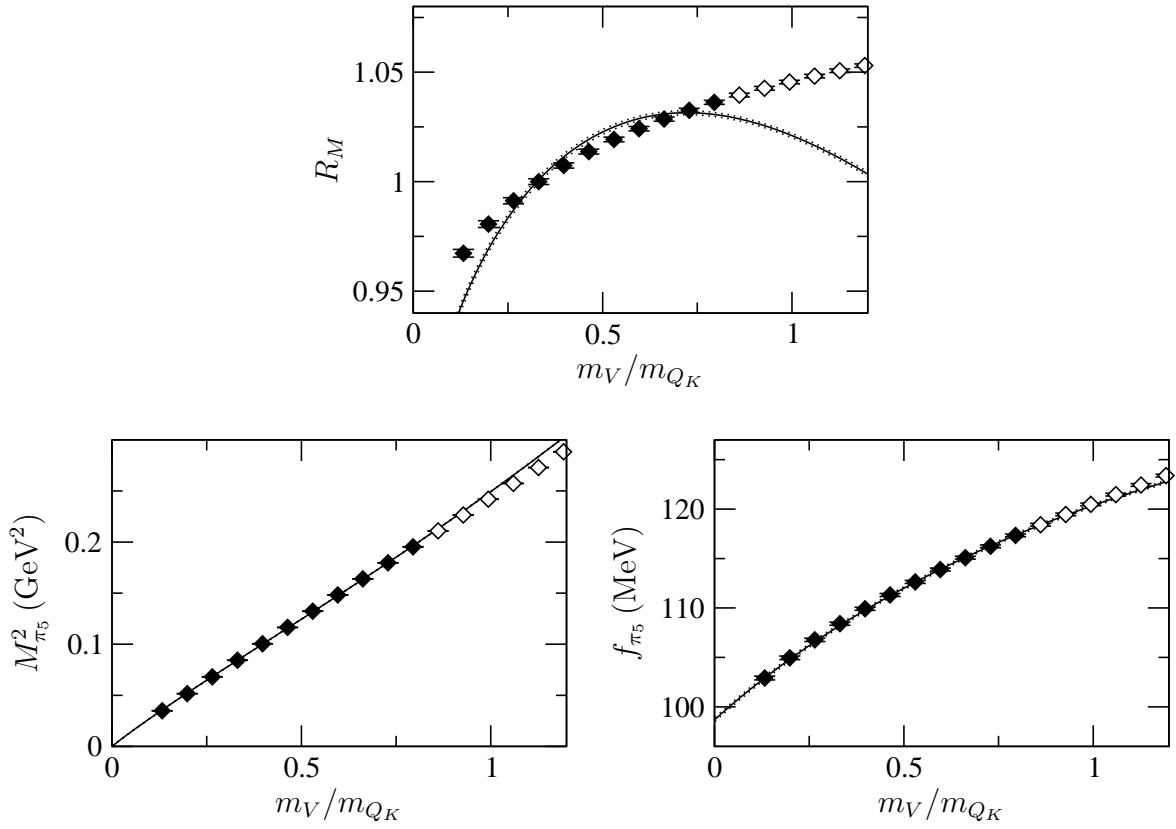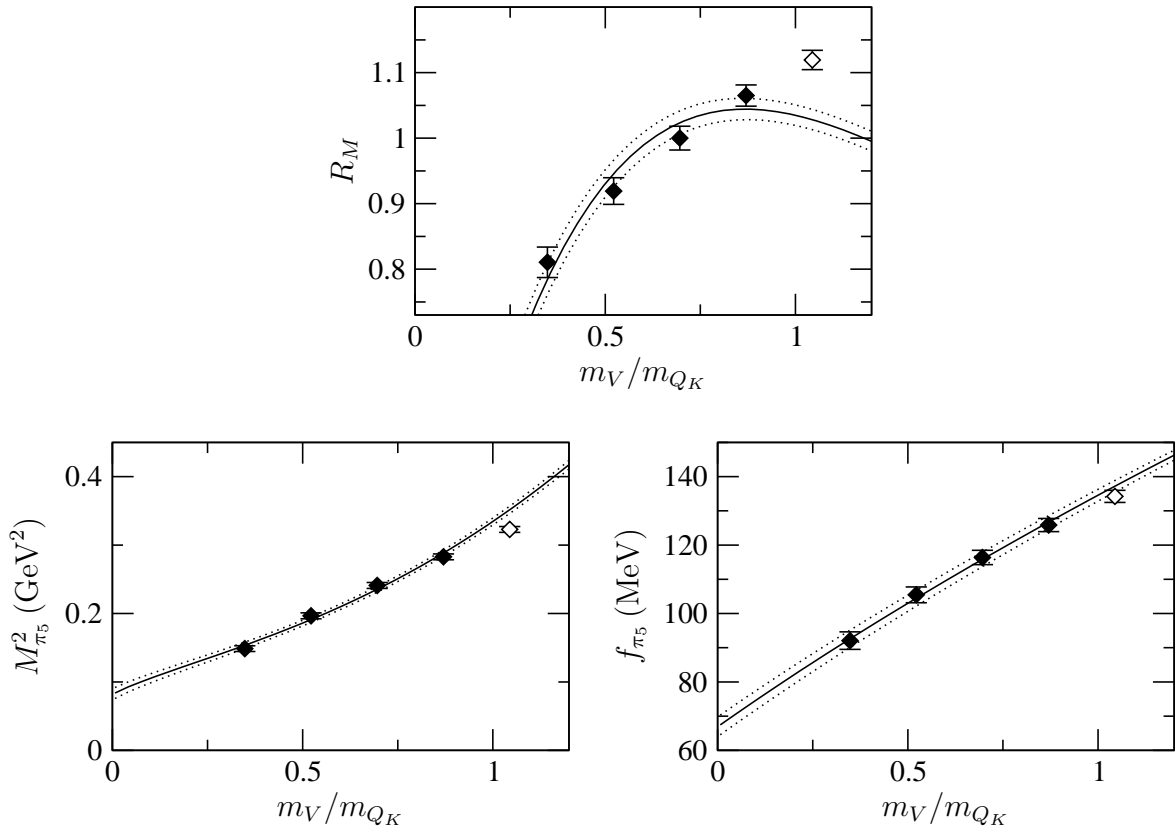
Figure D.61: Results from the pqChPT fit of ensemble Y hyp. Filled diamonds correspond to valence-quark-mass values within the fit range, while open diamonds correspond to those values beyond it.

Z hyp
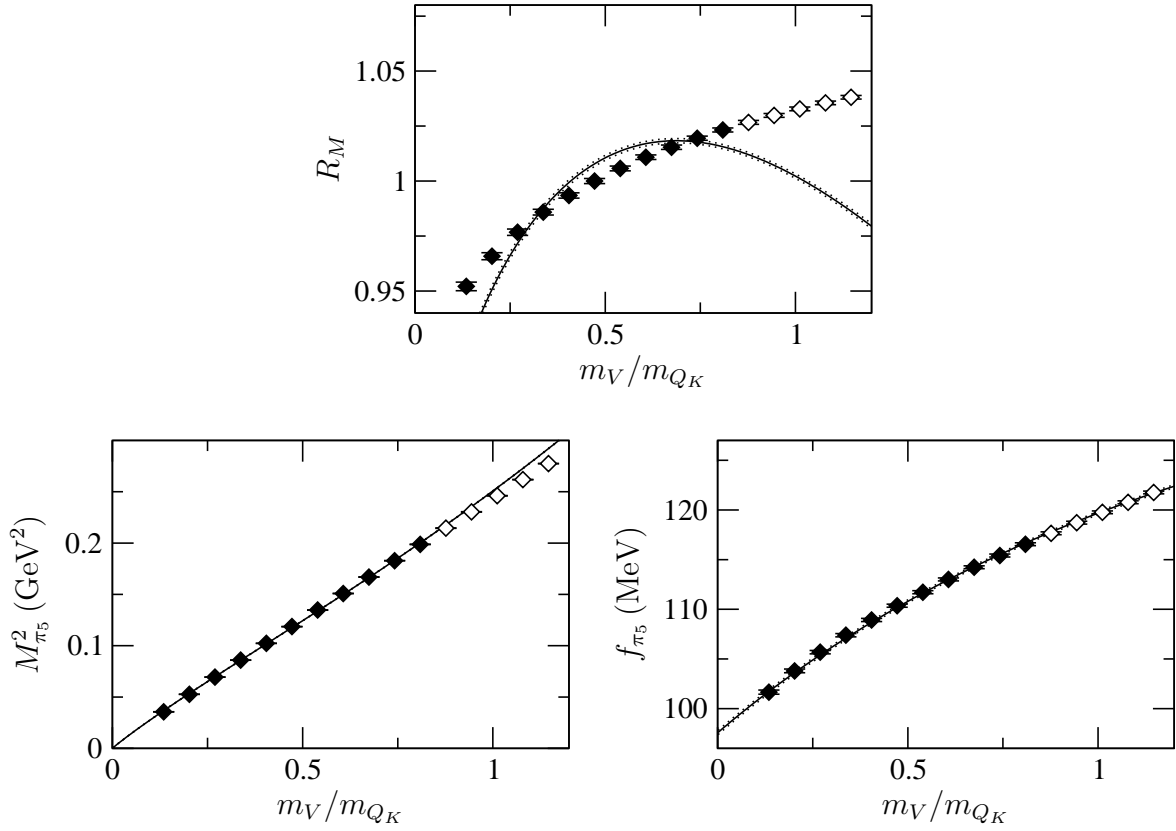
Figure D.62: Results from the pqChPT fit of ensemble Z hyp. Filled diamonds correspond to valence-quark-mass values within the fit range, while open diamonds correspond to those values beyond it.

266

W
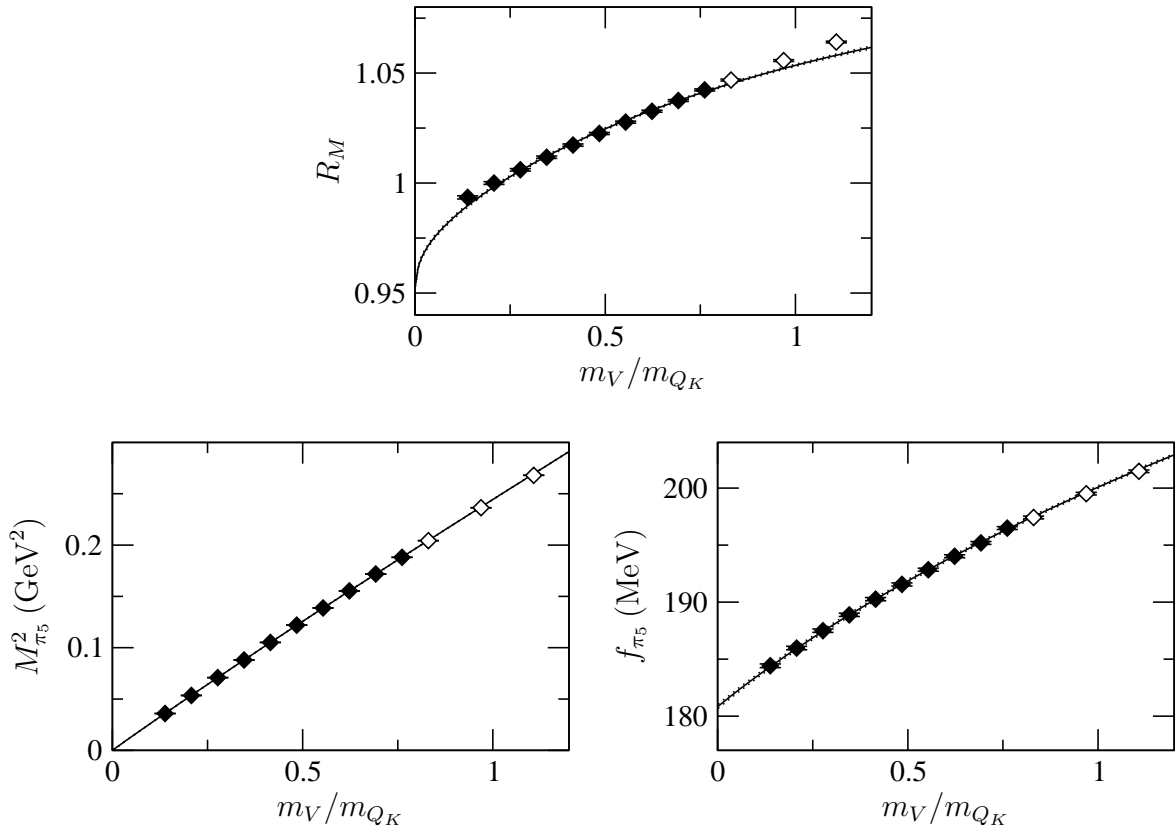
Figure D.63: Results from the pqChPT fit of ensemble W. Filled diamonds correspond to valence-quark-mass values within the fit range, while open diamonds correspond to those values beyond it.
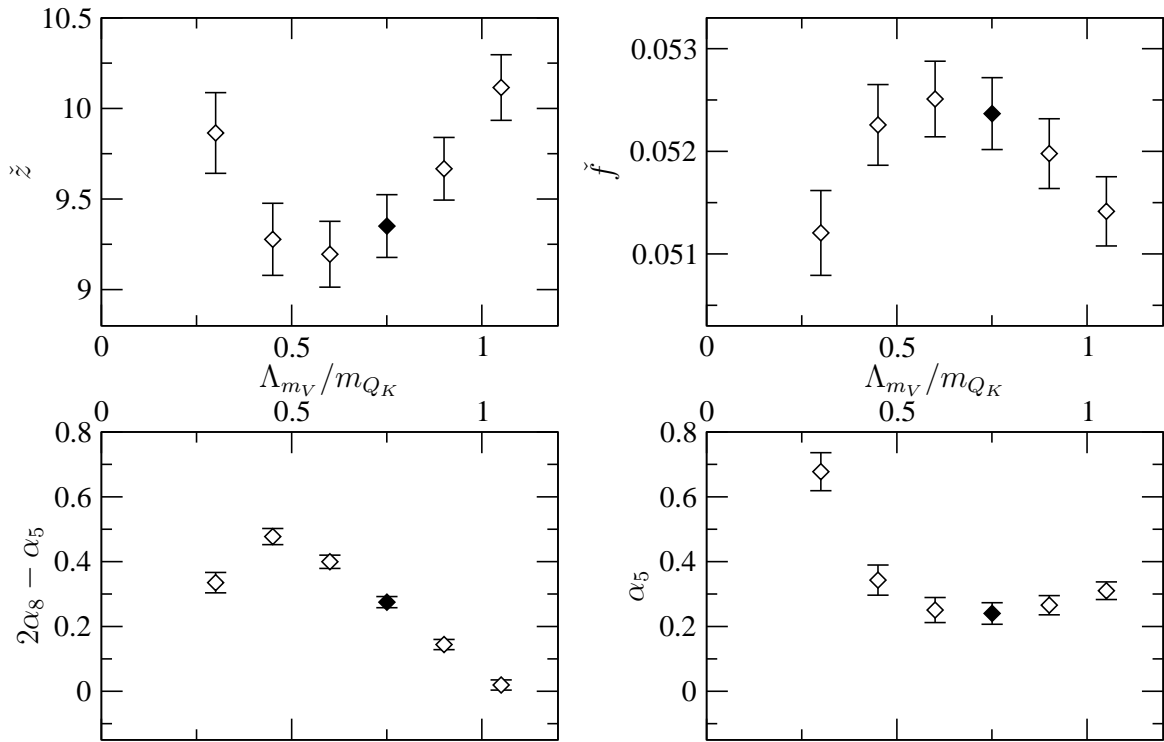
Figure D.64: Results from the pqChPT fit of ensemble X. Filled diamonds correspond to valence-quark-mass values within the fit range, while open diamonds correspond to those values beyond it.

Figure D.65: Results from the pqChPT fit of ensemble Y. Filled diamonds correspond to valence-quark-mass values within the fit range, while open diamonds correspond to those values beyond it.

Figure D.66: Results from the pqChPT fit of ensemble Z. Filled diamonds correspond to valence-quark-mass values within the fit range, while open diamonds correspond to those values beyond it.

Q hyp

Figure D.67: Results from the pqChPT fit of ensemble Q hyp. Filled diamonds correspond to valence-quark-mass values within the fit range, while open diamonds correspond to those values beyond it.

PSfrag replacements

Figure D.68: R_M versus valence quark mass from the quadratic fit of the correlator of ensemble A hyp.
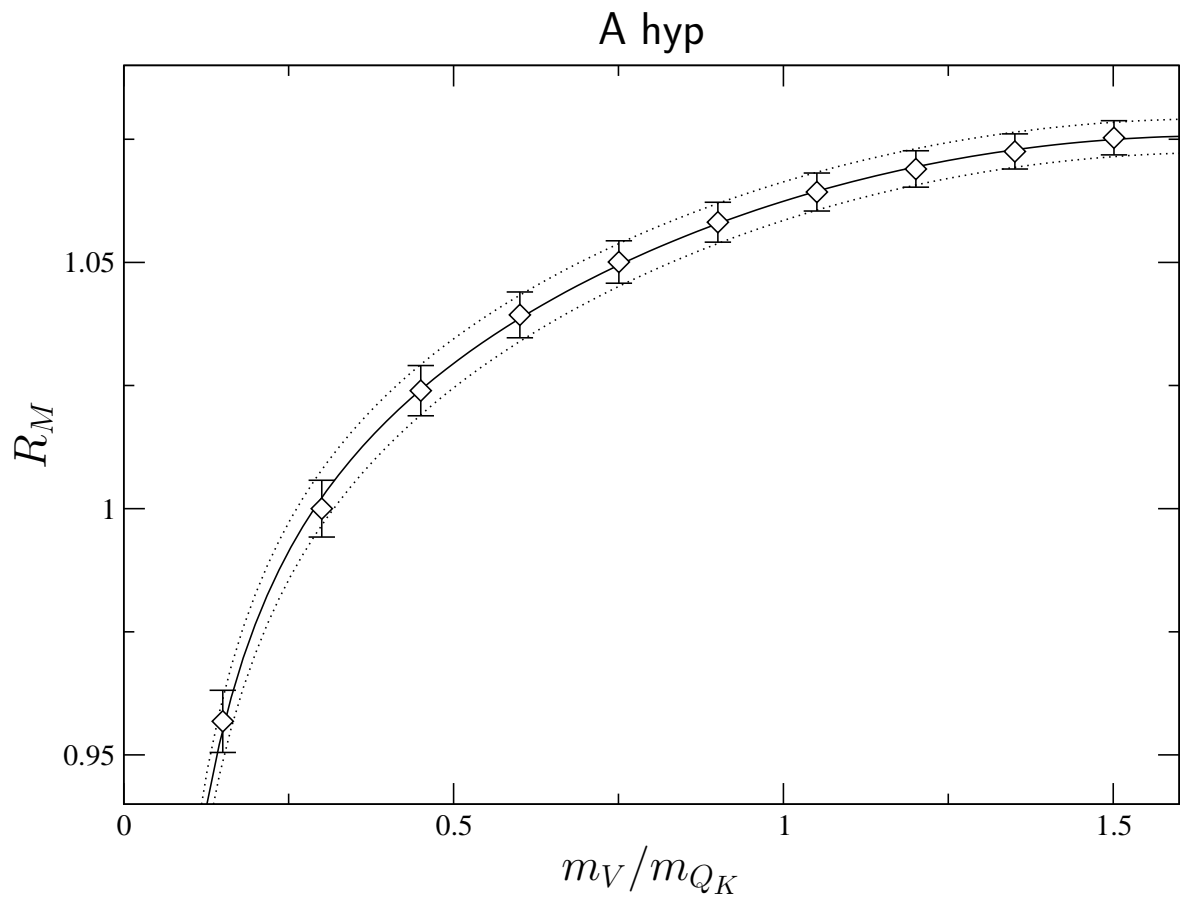
Figure D.69: R_M versus valence quark mass from the cubic fit of the correlator of ensemble A hyp.

C hyp

Figure D.70: Results from the pqChPT fit of ensemble C hyp. Filled diamonds correspond to valence-quark-mass values within the fit range, while open diamonds correspond to those values beyond it.

C

Figure D.71: Results from the pqChPT fit of ensemble C. Filled diamonds correspond to valence-quark-mass values within the fit range, while open diamonds correspond to those values beyond it.

Figure D.72: Dependence of the results of the pqChPT fit of ensemble A hyp on the valence-quark-mass cutoff. The filled diamond corresponds to the cutoff used in the final fit.
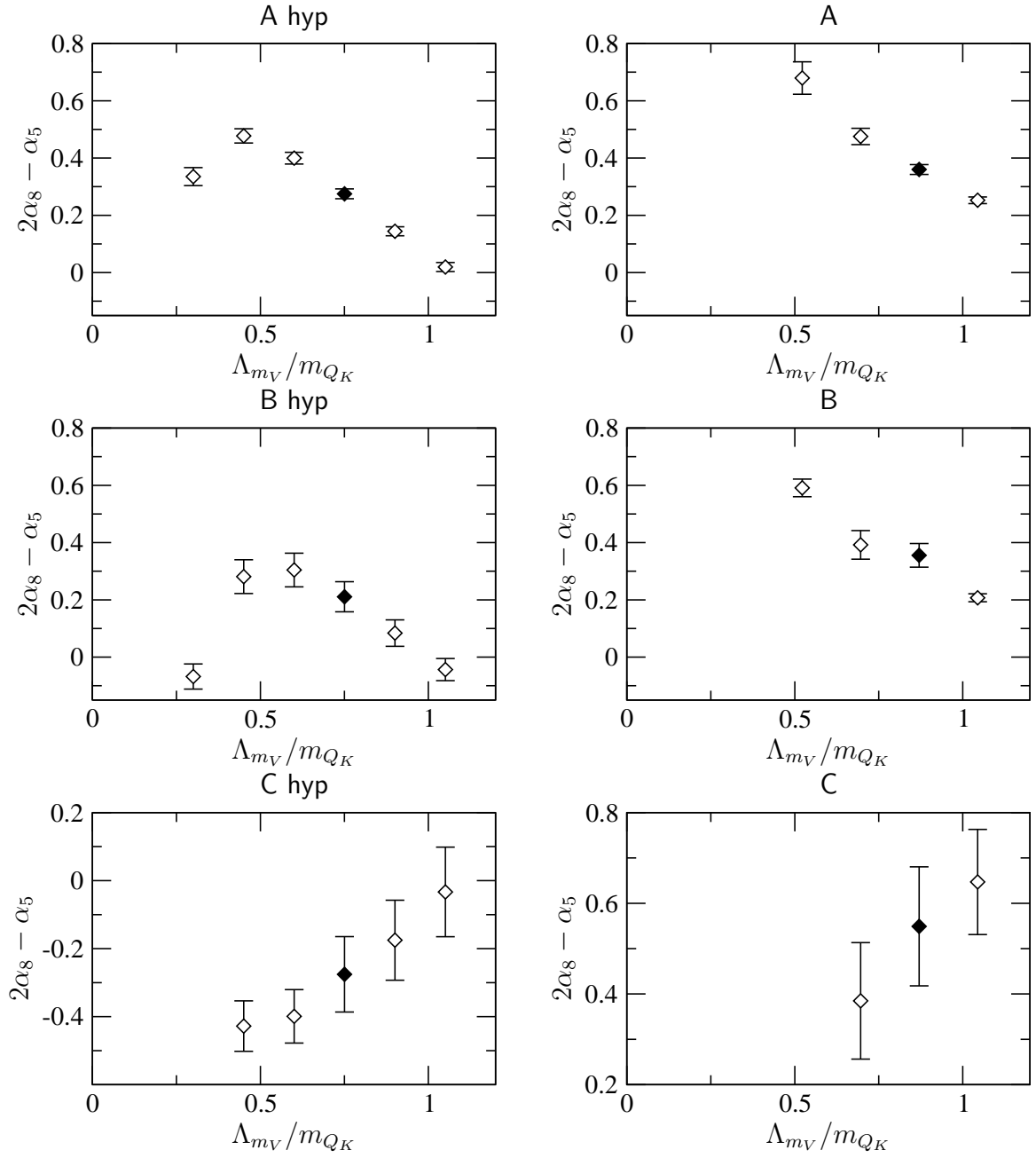
Figure D.73: Dependence of the results of the pqChPT fit of ensembles A hyp, A, B hyp, B, C hyp, and C on the valence-quark-mass cutoff. The filled diamond corresponds to the cutoff used in the final fit.
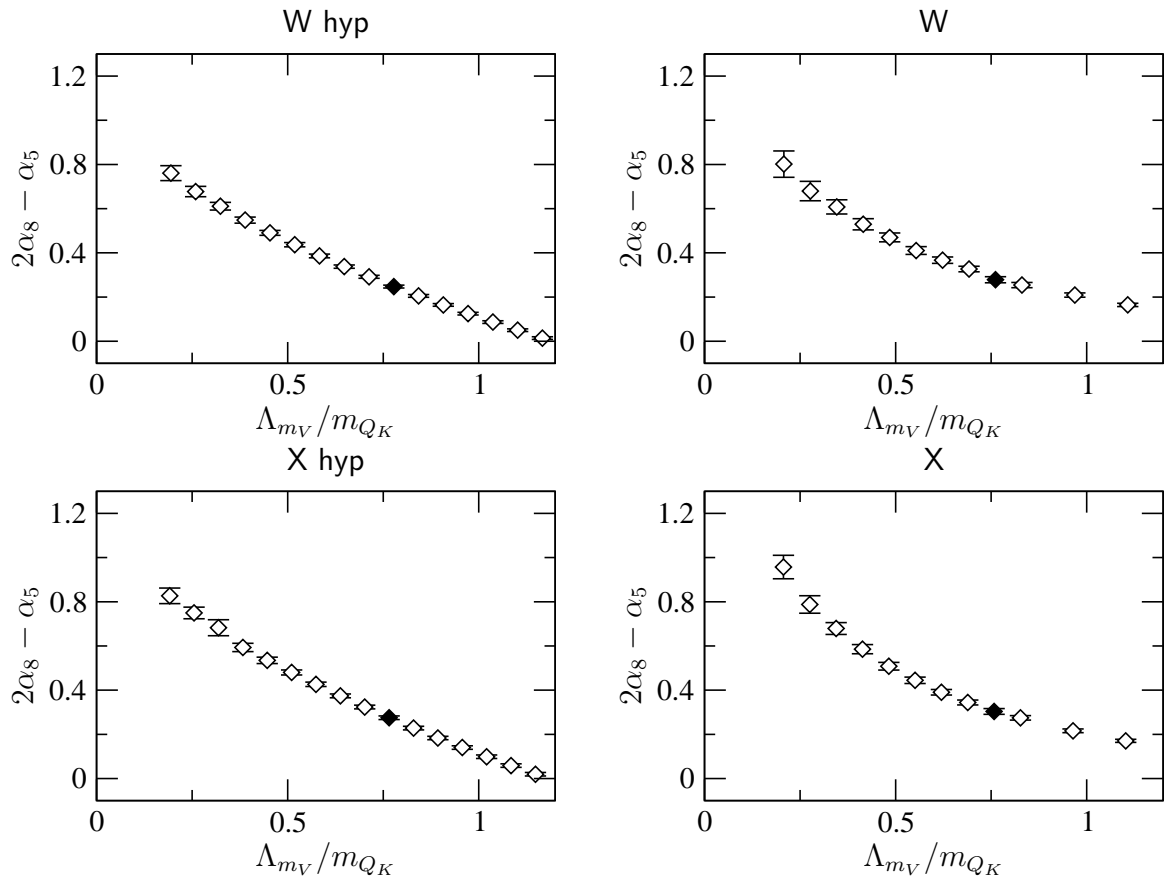
Figure D.74: Dependence of the results of the pqChPT fit of ensembles W hyp, Z, W hyp, and W on the valence-quark-mass cutoff. The filled diamond corresponds to the cutoff used in the final fit.
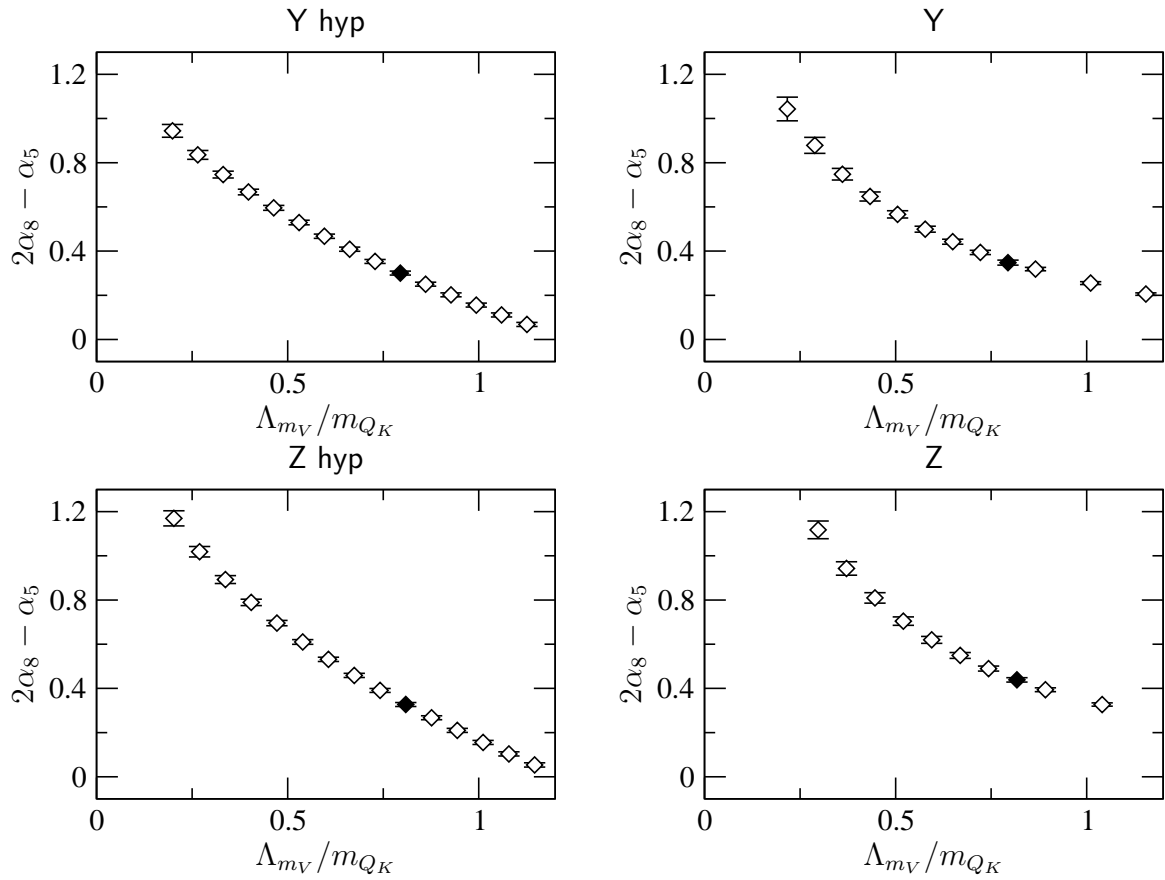
Figure D.75: Dependence of the results of the pqChPT fit of ensembles Y hyp, Y, Z hyp, and Z on the valence-quark-mass cutoff. The filled diamond corresponds to the cutoff used in the final fit.
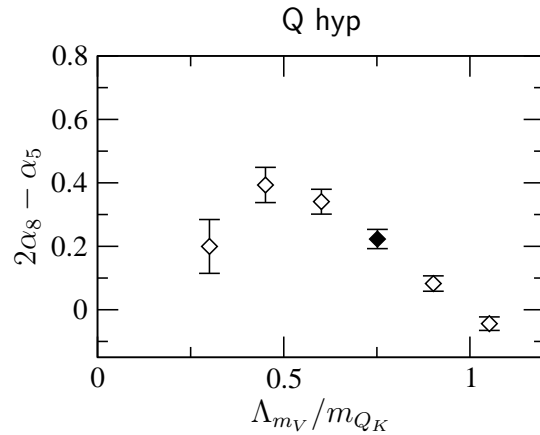
Figure D.76: Dependence of the results of the pqChPT fit of ensemble Q hyp on the valence-quark-mass cutoff. The filled diamond corresponds to the cutoff used in the final fit.
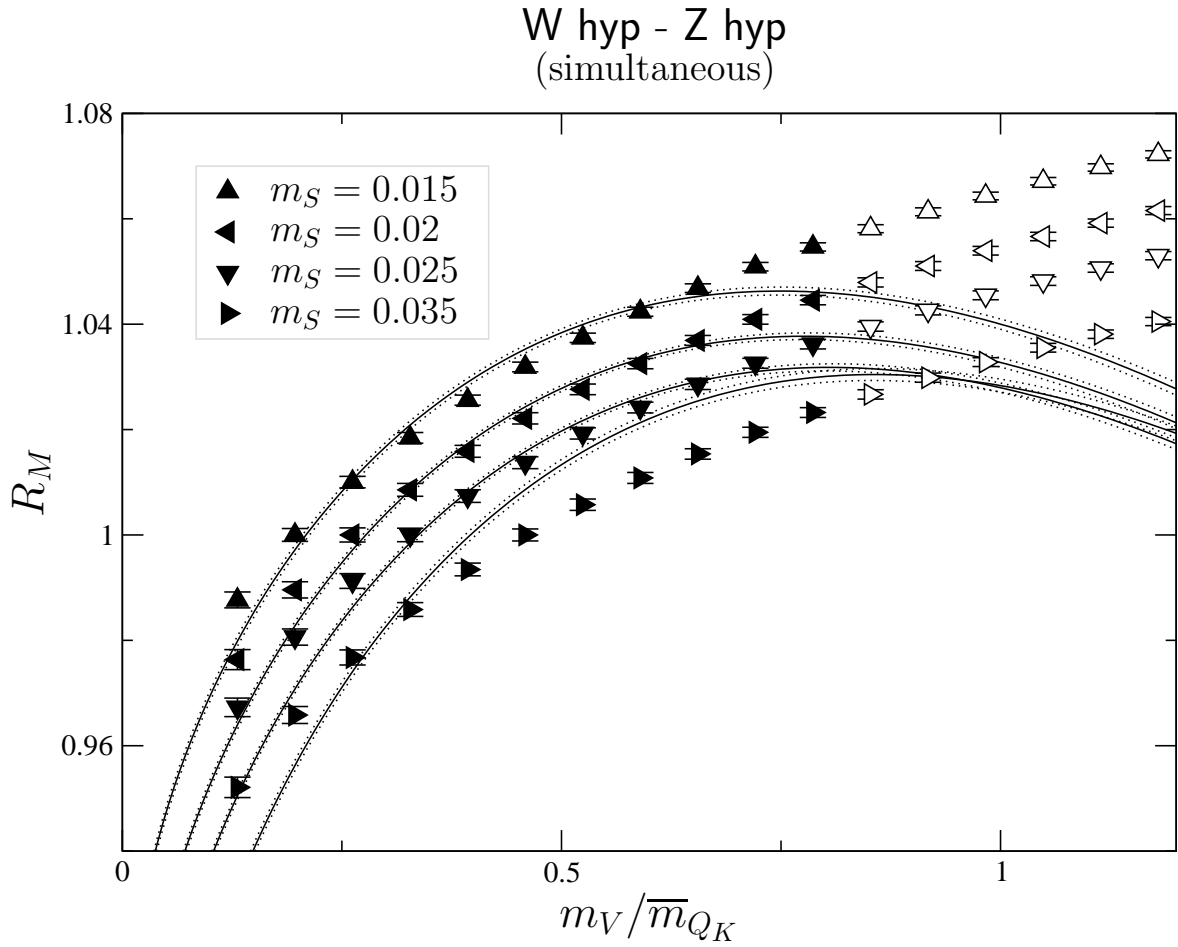
Figure D.77: R_M versus valence quark mass from the simultaneous pqChPT fit of the correlators of ensembles W hyp through Z hyp. Filled diamonds correspond to valence-quark-mass values within the fit range, while open diamonds correspond to those values beyond it. An average of the ensembles' values for m_{Q_K} is used.
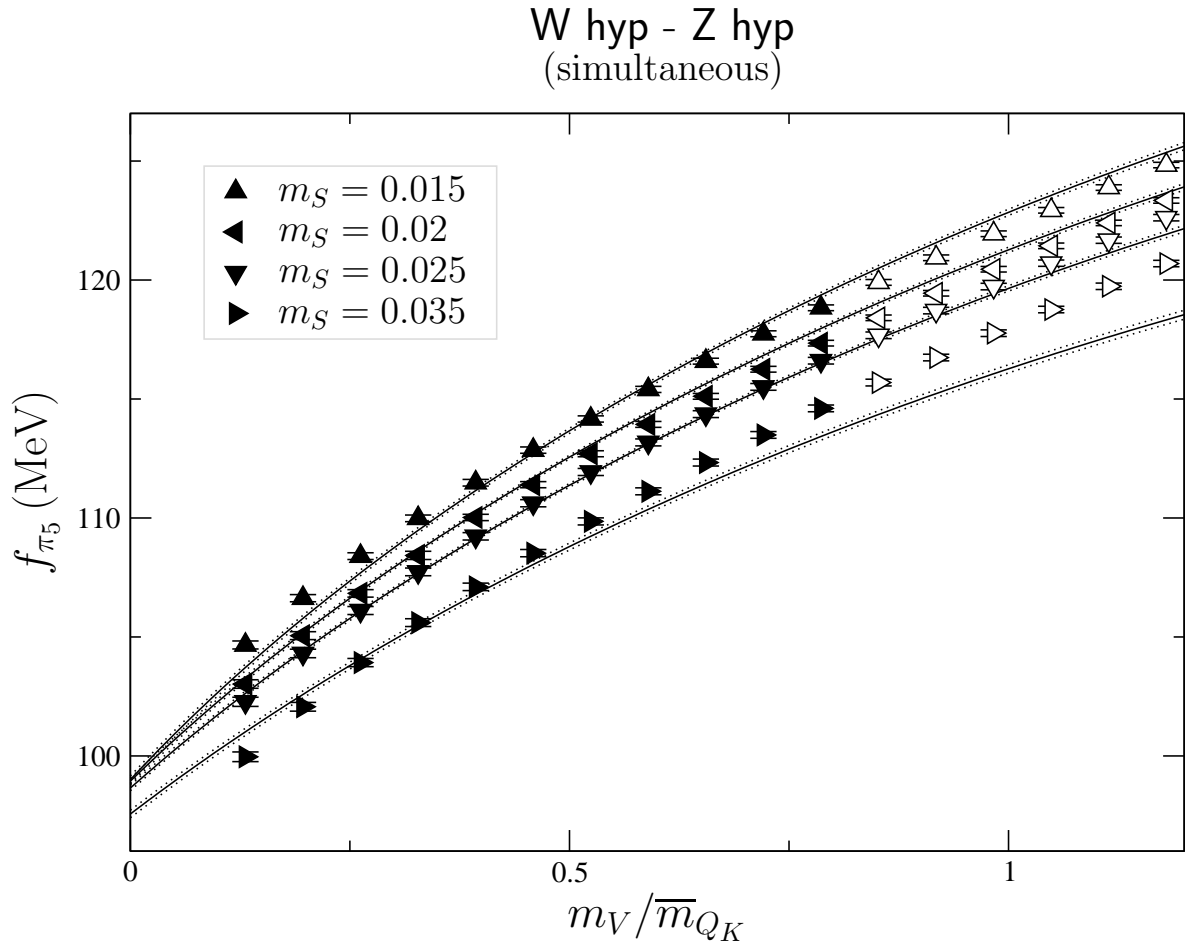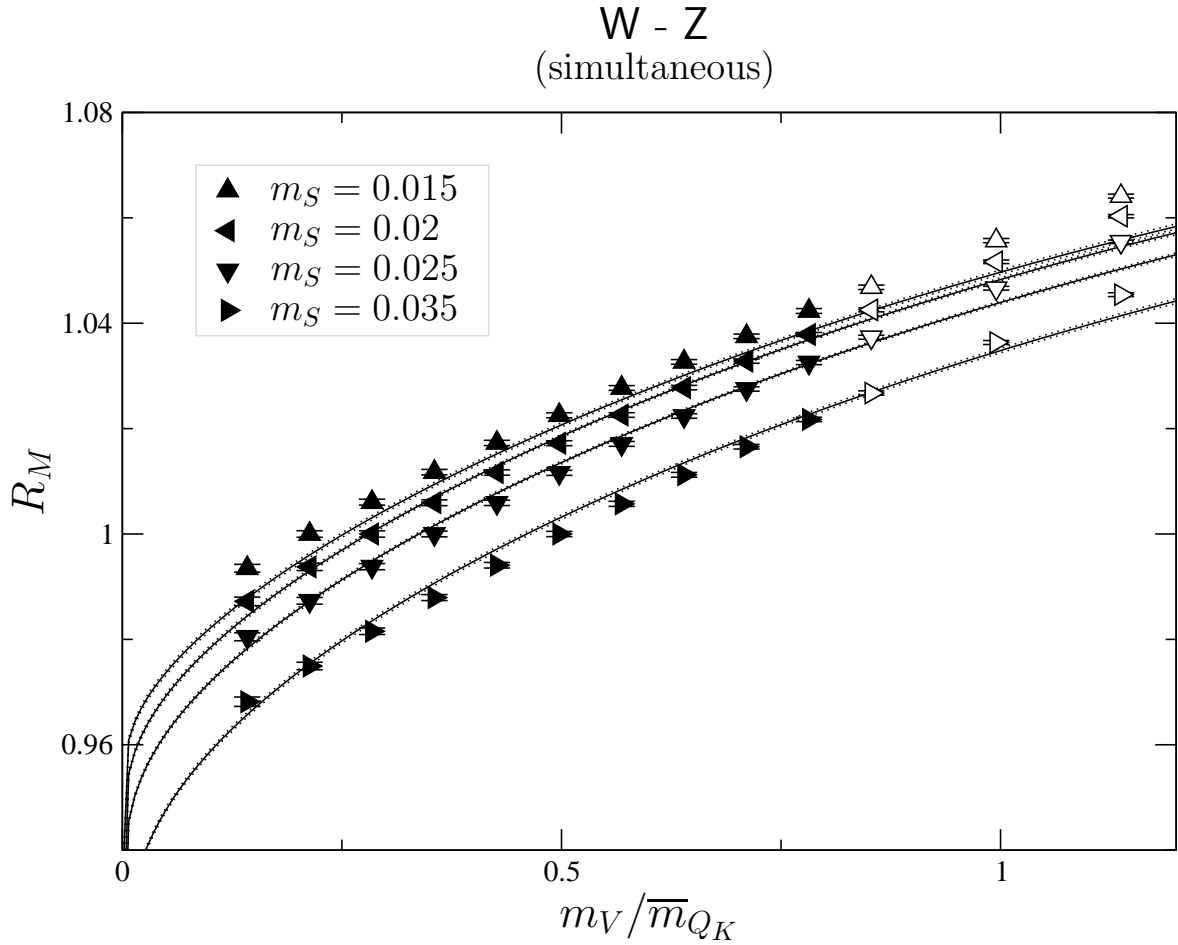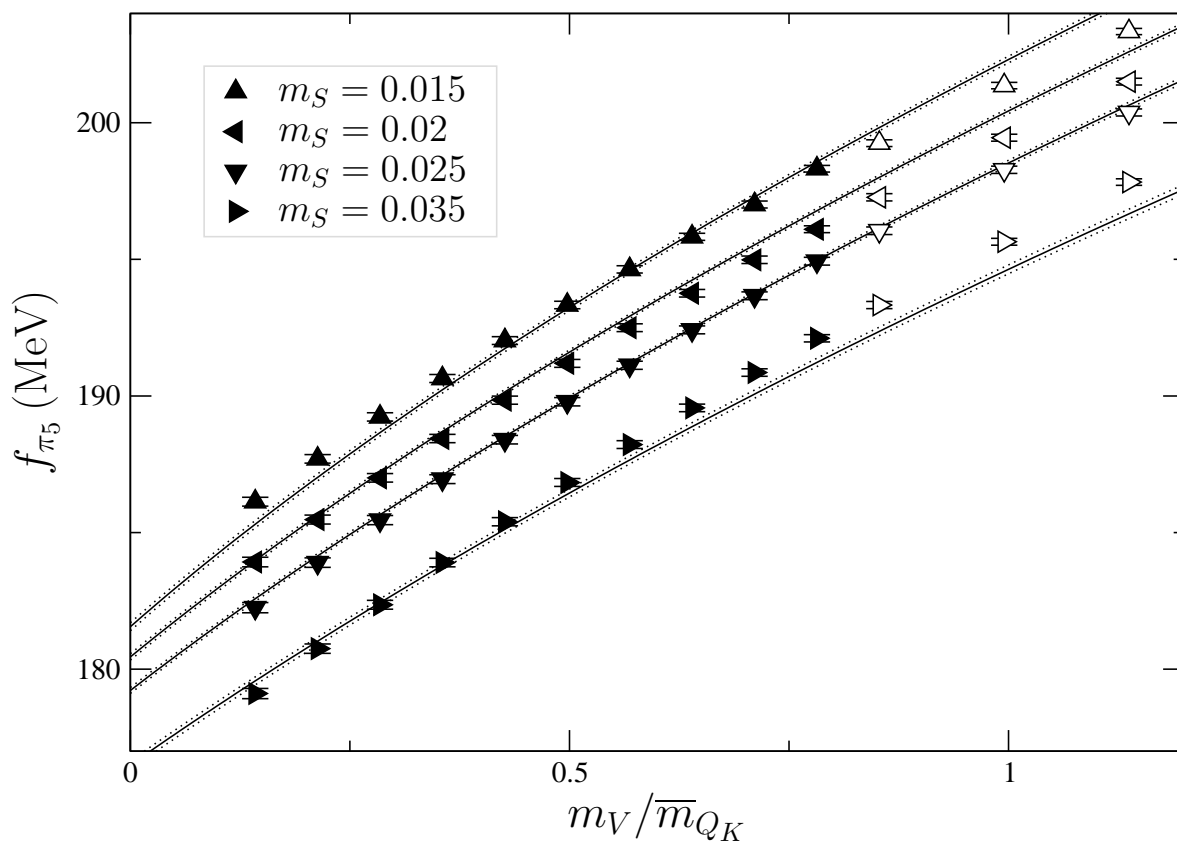
Figure D.78: Pion decay constant versus valence quark mass from the simultaneous pqChPT fit of ensembles W hyp through Z hyp. Filled diamonds correspond to valence-quark-mass values within the fit range, while open diamonds correspond to those values beyond it. An average of the ensembles' values for m_{Q_K} and lattice spacing are used.

Figure D.79: Pion decay constant versus valence quark mass from the simultaneous pqChPT fit of ensembles W through Z. Filled diamonds correspond to valence-quark-mass values within the fit range, while open diamonds correspond to those values beyond it. An average of the ensembles' values for m_{Q_K} and lattice spacing are used.
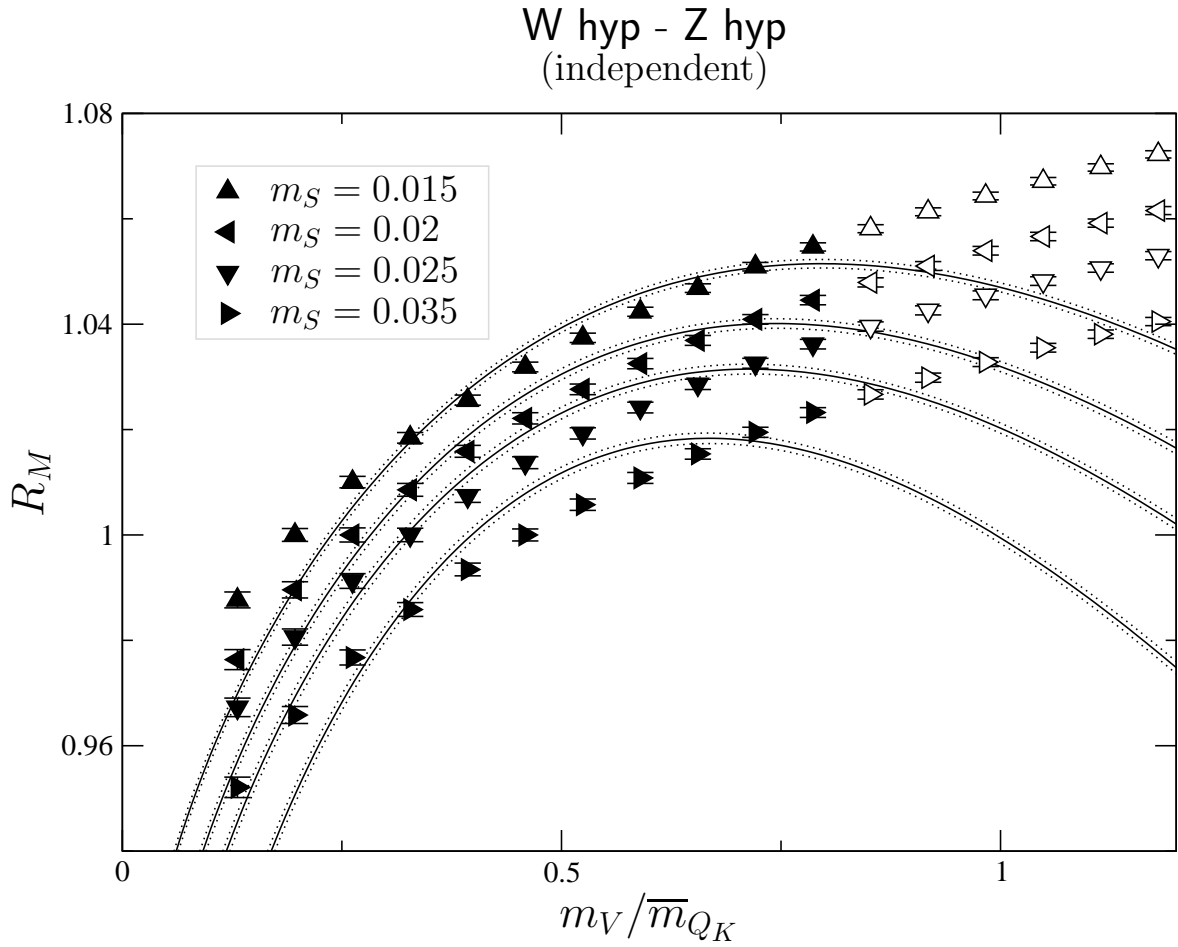
Figure D.80: Pion decay constant versus valence quark mass from the simultaneous pqChPT fit of ensembles W through Z. Filled diamonds correspond to valence-quark-mass values within the fit range, while open diamonds correspond to those values beyond it. An average of the ensembles' values for m_{Q_K} and lattice spacing are used.

Figure D.81: R_M versus valence quark mass from the four independent pqChPT fits of ensembles W hyp through Z hyp. Filled diamonds correspond to valence-quark-mass values within the fit range, while open diamonds correspond to those values beyond it. An average of the ensembles' values for m_{Q_K} is used.
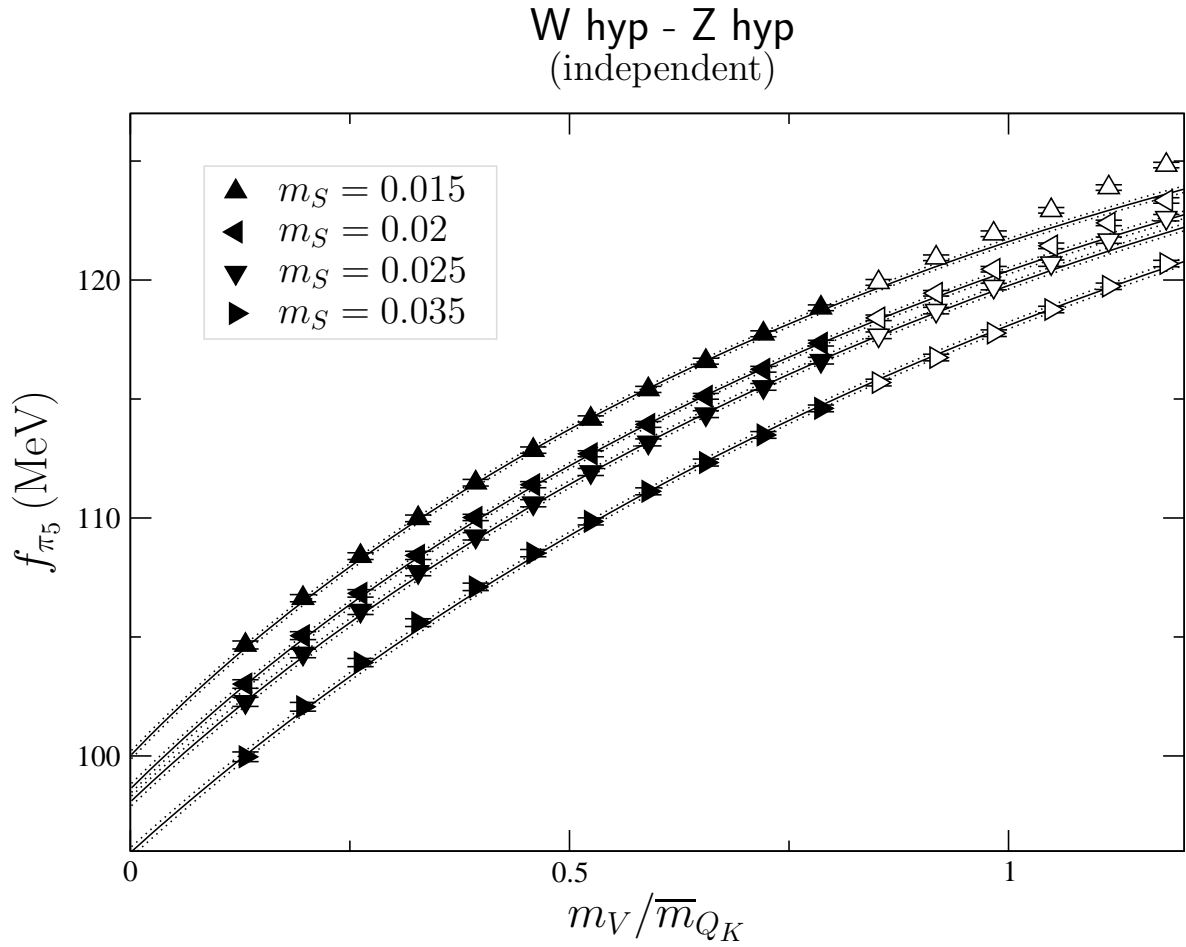
Figure D.82: Pion decay constant versus valence quark mass from the four independent pqChPT fits of ensembles W hyp through Z hyp. Filled diamonds correspond to valence-quark-mass values within the fit range, while open diamonds correspond to those values beyond it. An average of the ensembles' values for m_{Q_K} and lattice spacing are used.
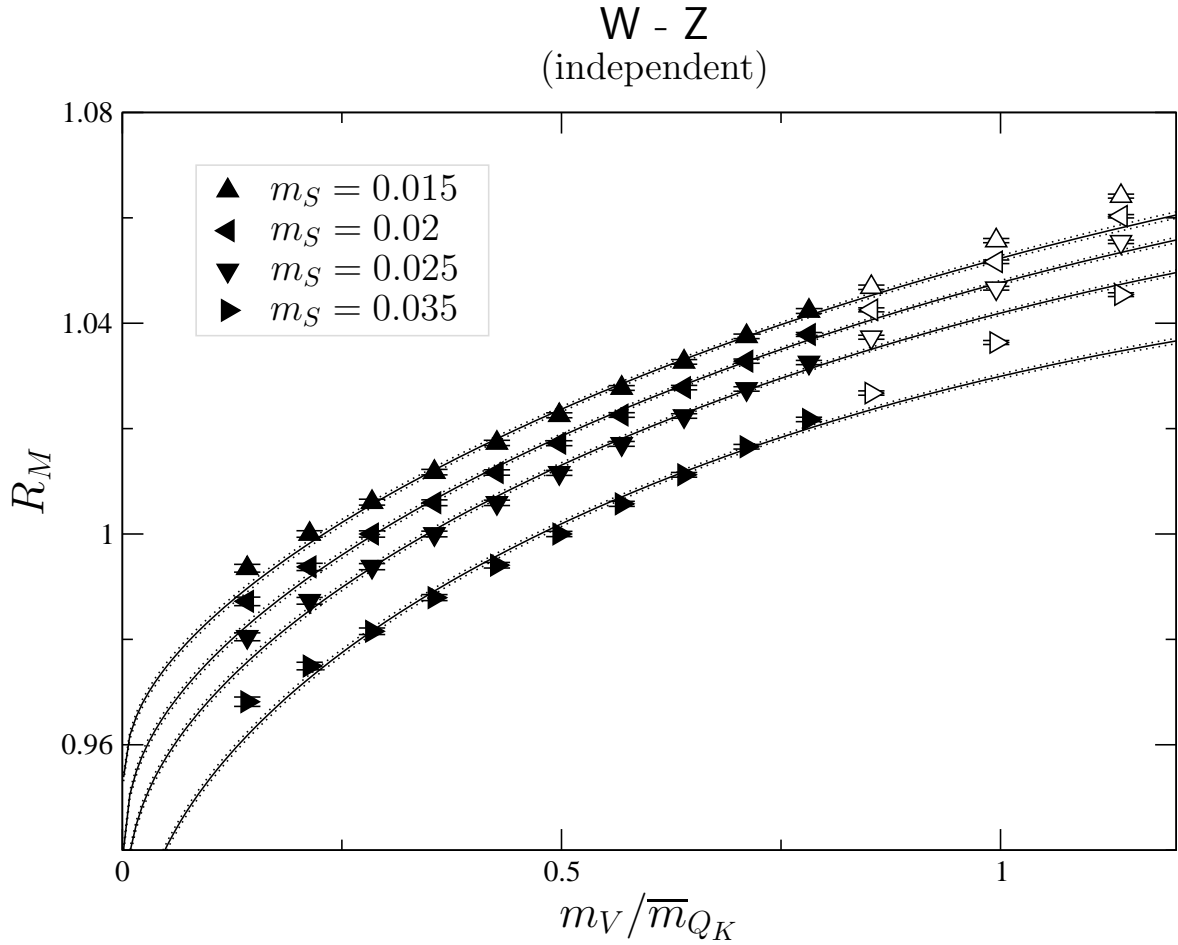
Figure D.83: R_M versus valence quark mass from the four independent pqChPT fits of ensembles W through Z. Filled diamonds correspond to valence-quark-mass values within the fit range, while open diamonds correspond to those values beyond it. An average of the ensembles' values for m_{Q_K} is used.
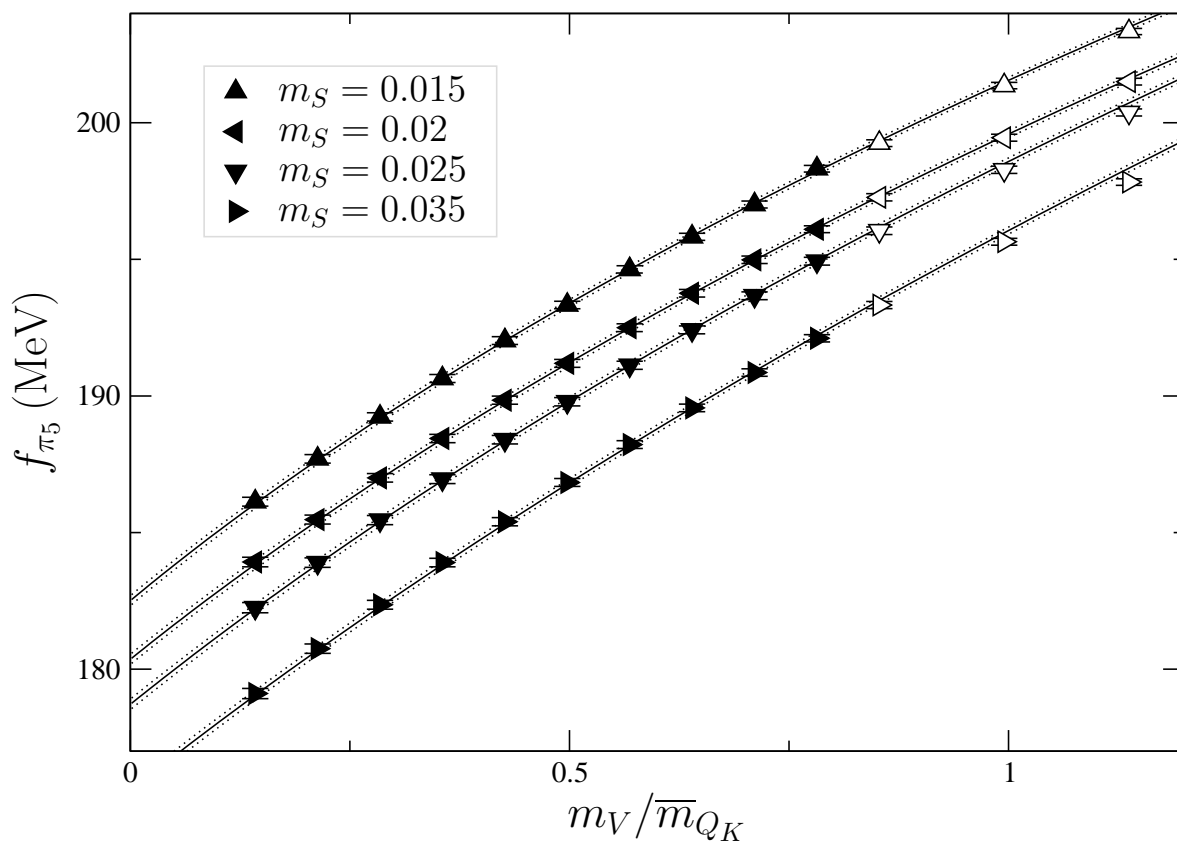
Figure D.84: Pion decay constant versus valence quark mass from the four independent pqChPT fits of ensembles W through Z. Filled diamonds correspond to valence-quark-mass values within the fit range, while open diamonds correspond to those values beyond it. An average of the ensembles' values for m_{Q_K} and lattice spacing are used.
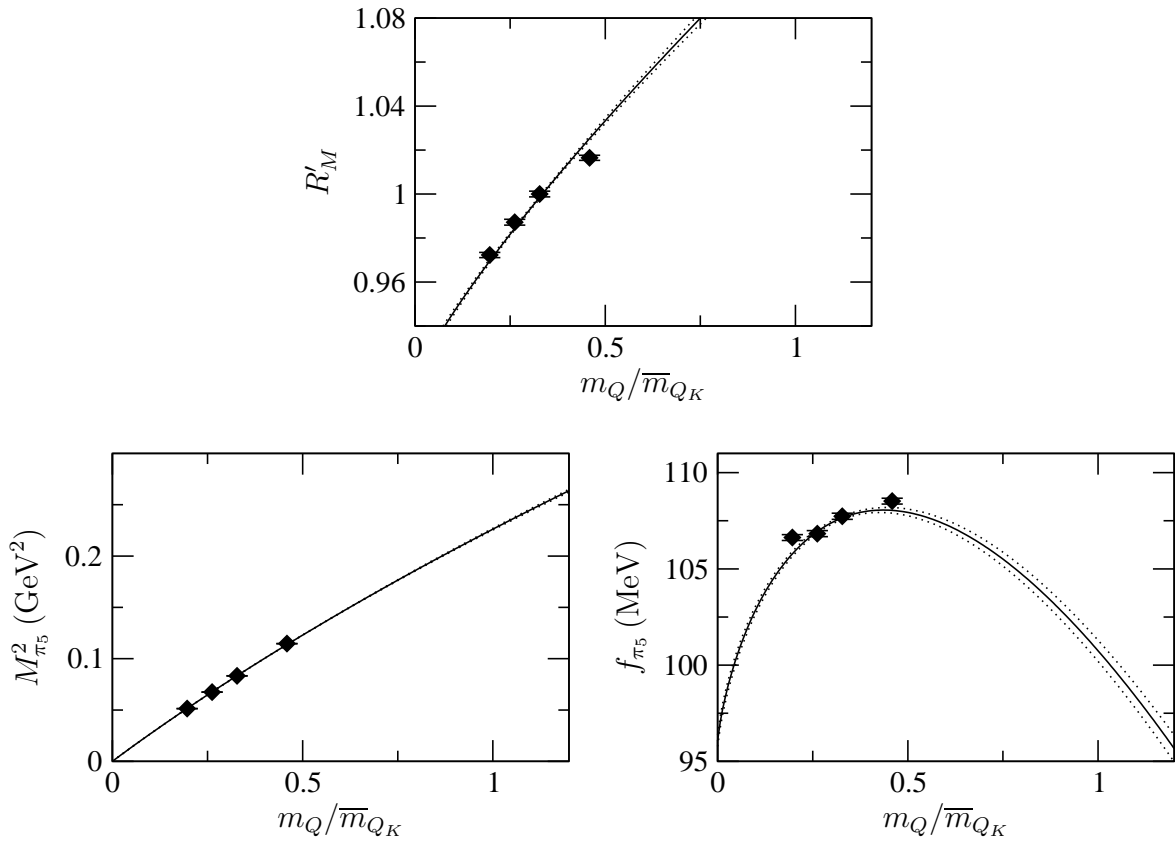
Figure D.85: Results from the simultaneous pqChPT fit of ensembles W hyp through Z hyp, displayed along the unquenched line of the quark-mass plane. An average of the ensembles' values for m_{Q_K} and lattice spacing are used.
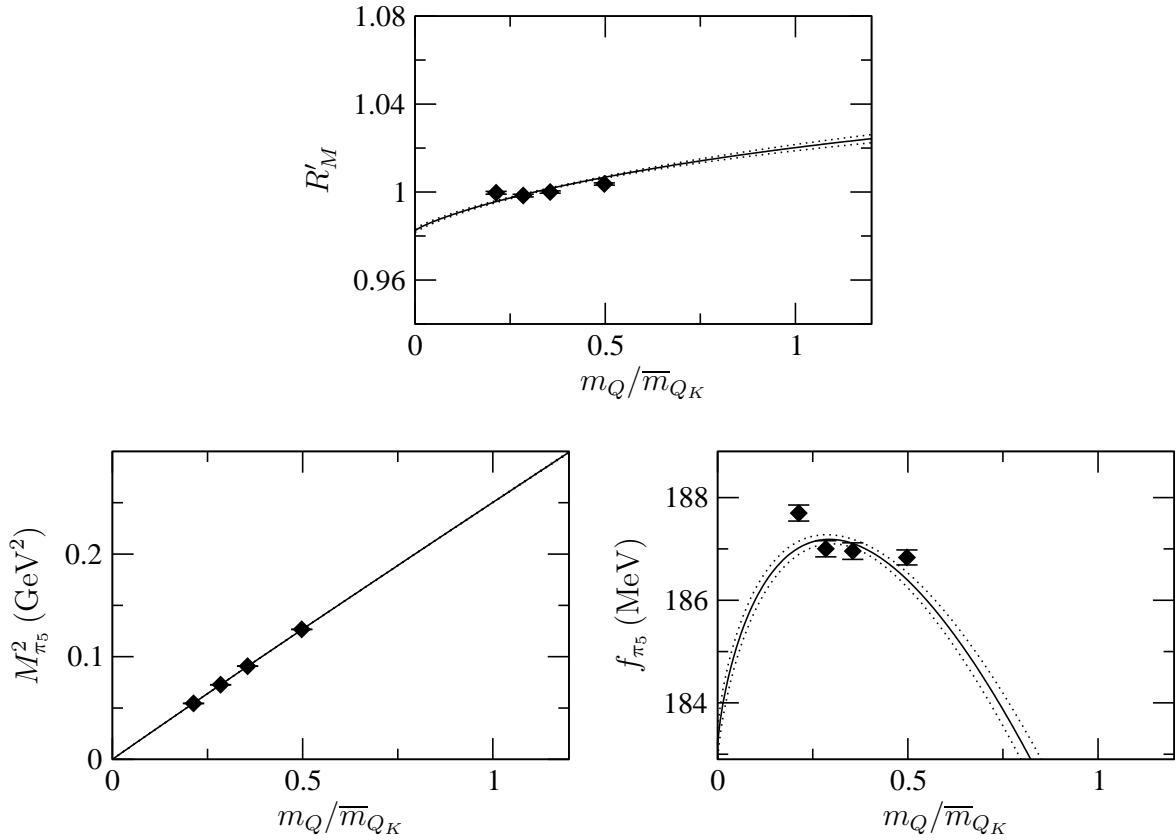
W - Z
(simultaneous)

Figure D.86: Results from the simultaneous pqChPT fit of ensembles W through Z, displayed along the unquenched line of the quark-mass plane. An average of the ensembles' values for m_{Q_K} and lattice spacing are used.
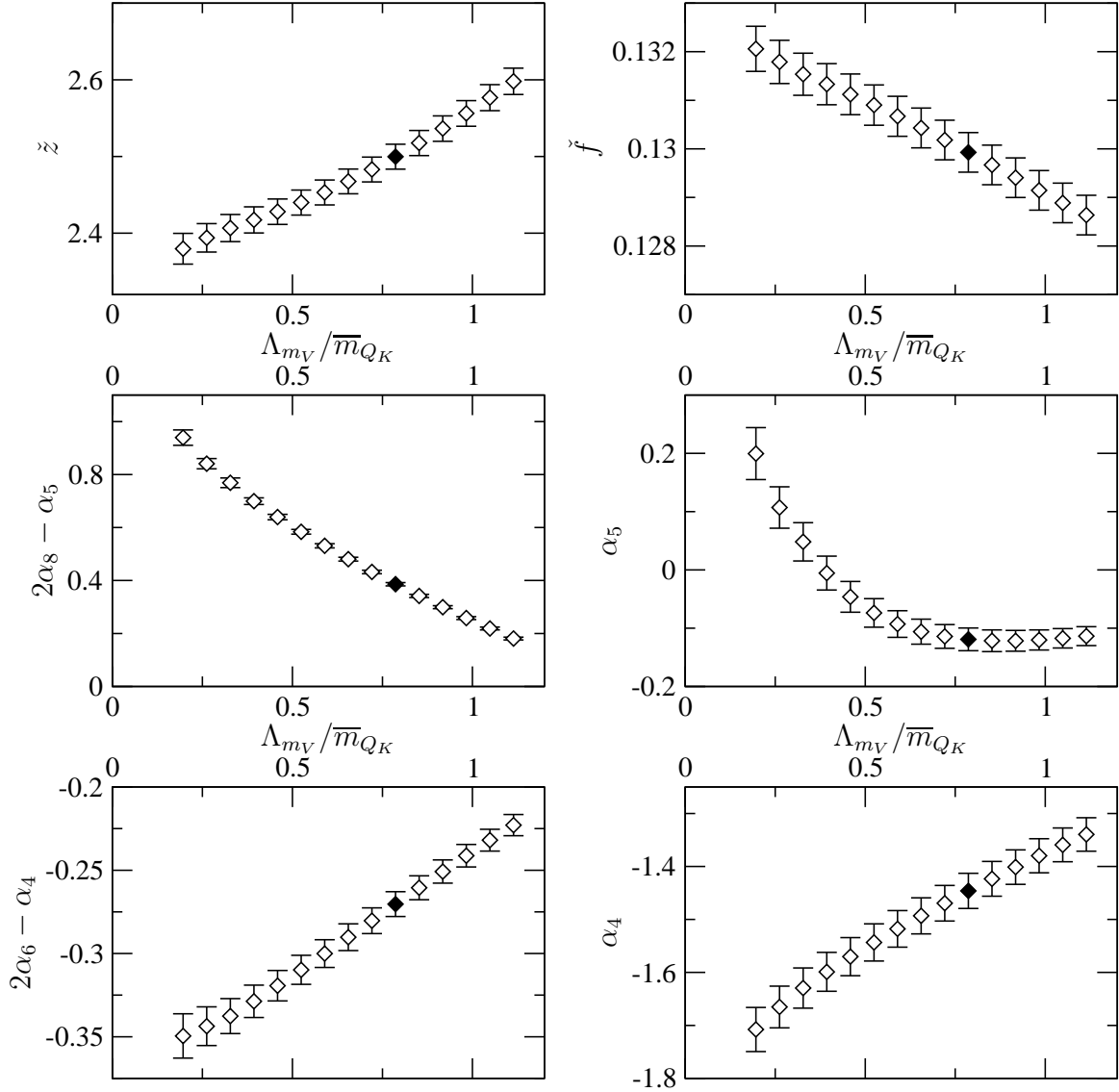
W hyp - Z hyp
(simultaneous)

Figure D.87: Dependence of the results of the simultaneous pqChPT fit of ensembles W hyp through Z hyp on the valence-quark-mass cutoff. The filled diamond corresponds to the cutoff used in the final fit. An average of the ensembles' values for m_{Q_K} is used.
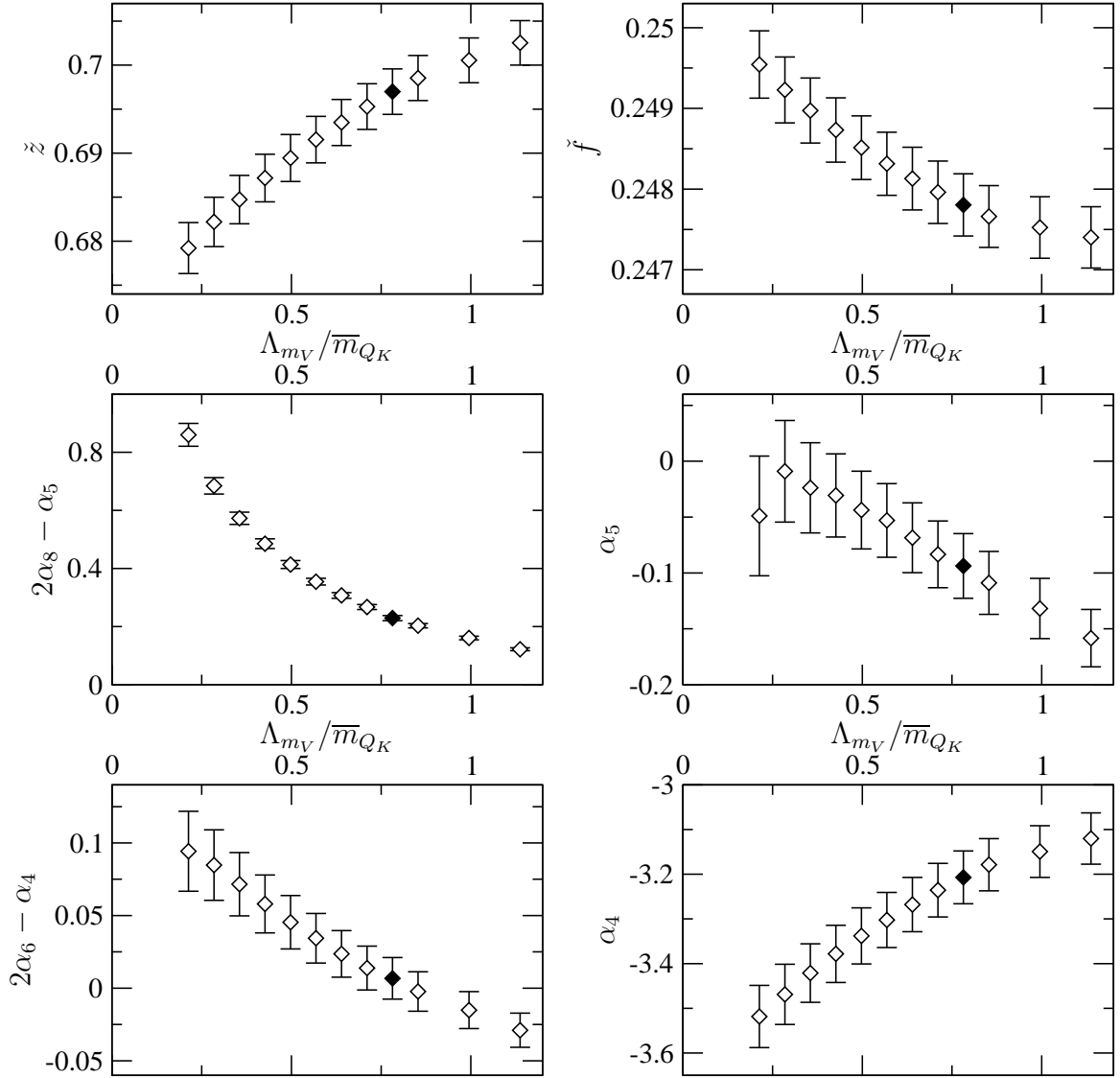
Figure D.88: Dependence of the results of the simultaneous pqChPT fit of ensembles W through Z on the valence-quark-mass cutoff. The filled diamond corresponds to the cutoff used in the final fit. An average of the ensembles' values for m_{Q_K} is used.

BIBLIOGRAPHY

[1] D.R. Nelson, G.T. Fleming and G.W. Kilcup, (2001), hep-lat/0112029.

[2] UKQCD, A.C. Irving et al., Phys. Lett. B518 (2001) 243, hep-lat/0107023.

[3] S. Weinberg, Phys. Rev. D11 (1975) 3583.

[4] J.B. Kogut and L. Susskind, Phys. Rev. D11 (1975) 3594.

[5] G. 't Hooft, Phys. Rev. D14 (1976) 3432.

[6] P.G. Harris et al., Phys. Rev. Lett. 82 (1999) 904.

[7] Y. Nir, (2001), hep-ph/0109090.

[8] G. 't Hooft, Adv. Ser. Math. Phys. 19 (1994) 1.

[9] R.D. Peccei and H.R. Quinn, Phys. Rev. D16 (1977) 1791.

[10] A.E. Nelson, Phys. Lett. B136 (1984) 387.

[11] S.M. Barr, Phys. Rev. Lett. 53 (1984) 329.

[12] M. Leurer, Y. Nir and N. Seiberg, Nucl. Phys. B420 (1994) 468, hep-ph/9310320.

[13] T. Banks, Y. Nir and N. Seiberg, (1994), hep-ph/9403203.

[14] D.E. Kaplan et al., Phys. Rev. D60 (1999) 055003, hep-ph/9806430.

[15] R.F. Dashen, Phys. Rev. 183 (1969) 1245.

[16] S. Weinberg, Trans. New York Acad. Sci. 38 (1977) 185.

[17] J. Gasser and H. Leutwyler, Nucl. Phys. B250 (1985) 465.

[18] J. Bijnens and J. Prades, Nucl. Phys. B490 (1997) 239, hep-ph/9610360.

[19] G. Amoros, J. Bijnens and P. Talavera, Nucl. Phys. B602 (2001) 87, hep-ph/0101127.

[20] D.B. Kaplan and A.V. Manohar, Phys. Rev. Lett. 56 (1986) 2004.

[21] A.G. Cohen, D.B. Kaplan and A.E. Nelson, JHEP 11 (1999) 027, hep-lat/9909091.

[22] S.R. Sharpe and N. Shoresh, Int. J. Mod. Phys. A16S1C (2001) 1219, hep-lat/0011089.

[23] J. Bijnens, G. Ecker and J. Gasser, (1994), hep-ph/9411232.

[24] G. Ecker et al., Nucl. Phys. B321 (1989) 311.

[25] H. Leutwyler, (1996), hep-ph/9609465.

[26] E. Witten, Ann. Phys. 128 (1980) 363.

[27] H. Leutwyler, Phys. Lett. B374 (1996) 163, hep-ph/9601234.

[28] B.L. Ioffe and M.A. Shifman, Phys. Lett. B95 (1980) 99.

[29] J.F. Donoghue and D. Wyler, Phys. Rev. D45 (1992) 892.

[30] M.A. Luty and R. Sundrum, Phys. Lett. B312 (1993) 205, hep-ph/9304258.

[31] R. Urech, Phys. Lett. B355 (1995) 308, hep-ph/9504238.

[32] J. Gasser and H. Leutwyler, Phys. Rept. 87 (1982) 77.

[33] L.H. Karsten and J. Smit, Nucl. Phys. B183 (1981) 103.

[34] H.B. Nielsen and M. Ninomiya, Nucl. Phys. B185 (1981) 20.

[35] H.B. Nielsen and M. Ninomiya, Nucl. Phys. B193 (1981) 173.

[36] K.G. Wilson, New Phenomena In Subnuclear Physics. Part A. Proceedings of the First Half of the 1975 International School of Subnuclear Physics, Erice, Sicily, July 11 - August 1, 1975, ed. A. Zichichi, Plenum Press, New York, 1977, p. 69, CLNS-321.

[37] J.B. Kogut and L. Susskind, Phys. Rev. D11 (1975) 395.

[38] T. Banks, L. Susskind and J.B. Kogut, Phys. Rev. D13 (1976) 1043.

[39] L. Susskind, Phys. Rev. D16 (1977) 3031.

[40] H.S. Sharatchandra, H.J. Thun and P. Weisz, Nucl. Phys. B192 (1981) 205.

[41] C. van den Doel and J. Smit, Nucl. Phys. B228 (1983) 122.

[42] M.F.L. Golterman and J. Smit, Nucl. Phys. B245 (1984) 61.

[43] M.R. Hestenes and E. Stiefel, J. Res. Nat. Bur. Stds. B49 (1952) 409.

[44] J.R. Shewchuk, Pittsburgh, USA: School of Computer Science, Carnegie Mellon University (1994), `http://www-2.cs.cmu.edu/~quake-papers`.

[45] S. Gottlieb et al., Phys. Rev. D35 (1987) 2531.

[46] MILC, K. Orginos, D. Toussaint and R.L. Sugar, Phys. Rev. D60 (1999) 054503, hep-lat/9903032.

[47] MILC, K. Orginos and D. Toussaint, Phys. Rev. D59 (1999) 014501, hep-lat/9805009.

[48] G.P. Lepage, Phys. Rev. D59 (1999) 074502, hep-lat/9809157.

[49] A. Hasenfratz and F. Knechtli, Phys. Rev. D64 (2001) 034504, hep-lat/0103029.

[50] A. Alexandru and A. Hasenfratz, (2002), hep-lat/0207014.

[51] A. Alexandru and A. Hasenfratz, (2002), hep-lat/0209070.

[52] A. Hasenfratz and A. Alexandru, (2002), hep-lat/0209071.

[53] R. Sommer, Nucl. Phys. B411 (1994) 839, hep-lat/9310022.

[54] ALPHA, M. Guagnelli, R. Sommer and H. Wittig, Nucl. Phys. B535 (1998) 389, hep-lat/9806005.

[55] A. Hasenfratz, R. Hoffmann and F. Knechtli, Nucl. Phys. Proc. Suppl. 106 (2002) 418, hep-lat/0110168.

[56] R.G. Edwards, U.M. Heller and T.R. Klassen, Nucl. Phys. B517 (1998) 377, hep-lat/9711003.

[57] G.W. Kilcup and S.R. Sharpe, Nucl. Phys. B283 (1987) 493.

[58] C.W. Bernard and M.F.L. Golterman, Phys. Rev. D46 (1992) 853, hep-lat/9204007.

[59] C.W. Bernard and M.F.L. Golterman, Phys. Rev. D49 (1994) 486, hep-lat/9306005.

[60] S.R. Sharpe and N. Shoresh, Phys. Rev. D64 (2001) 114510, hep-lat/0108003.

[61] S.R. Sharpe, Phys. Rev. D56 (1997) 7052, hep-lat/9707018.

[62] S.R. Sharpe and N. Shoresh, Phys. Rev. D62 (2000) 094503, hep-lat/0006017.

[63] W.H. Press et al., Numerical Recipes: The Art of Scientific Computing, 2nd ed. (Cambridge University Press, Cambridge (UK) and New York, 1992).

[64] J.A. Nelder and R. Mead, The Computer Journal 7 (1965) 308.

[65] D.W. Marquardt, Journal of the Society for Industrial and Applied Mathematics 11 (1963) 431.

[66] `http://www.phys.columbia.edu/~cqft/`.

[67] X. Liao, (2001), hep-lat/0111013.

[68] K. Hagiwara et al., Physical Review D 66 (2002) 010001+.

[69] ALPHA, J. Heitger, R. Sommer and H. Wittig, Nucl. Phys. B588 (2000) 377, hep-lat/0006026.

[70] H. Leutwyler, Phys. Lett. B378 (1996) 313, hep-ph/9602366.

[71] `http://media4.physics.indiana.edu/~sg/milc.html`.

[72] `http://qcd.nersc.gov/`.

[73] C.W. Bernard et al., Phys. Rev. D64 (2001) 054506, hep-lat/0104002.

[74] G.T. Fleming, D.R. Nelson and G.W. Kilcup, (2002), hep-lat/0209141.

[75] MILC, C. Bernard, Phys. Rev. D65 (2002) 054031, hep-lat/0111051.

[76] C. Aubin et al., (2002), hep-lat/0209066.

[77] A. Duncan, E. Eichten and H. Thacker, Phys. Rev. Lett. 76 (1996) 3894, hep-lat/9602005.

[78] A. Duncan, E. Eichten and H. Thacker, Nucl. Phys. Proc. Suppl. 53 (1997) 295, hep-lat/9609015.

[79] S. Coleman, Cambridge, UK: Univ. Pr. (1985) 402 p.

[80] e. DeGrand, T. and e. Toussaint, D., Singapore, Singapore: World Scientific (1990) 750 p.

[81] G. Ecker, Prog. Part. Nucl. Phys. 35 (1995) 1, hep-ph/9501357.

[82] R. Gupta, (1997), hep-lat/9807028.

[83] H. Georgi, Menlo Park, USA: Benjamin/Cummings (1984) 165 p.

[84] M. Kaku, New York, USA: Oxford Univ. Pr. (1993) 785 p.

[85] e. Kilcup, G. and e. Sharpe, S. R., Singapore, Singapore: World Scientific (1995) 332 p.

[86] I. Montvay and G. Munster, Cambridge, UK: Univ. Pr. (1994) 491 p (Cambridge Monographs on Mathematical Physics).

[87] D.R. Nelson, G.T. Fleming and G.W. Kilcup, Nucl. Phys. Proc. Suppl. 106 (2002) 221, hep-lat/0110112.

[88] M.E. Peskin and D.V. Schroeder, Reading, USA: Addison-Wesley (1995) 842 p.

[89] A. Pich, (1993), hep-ph/9308351.